Processing of calcium and magnesium phosphate cements for bone substitution

Dissertation zur Erlangung des naturwissenschaftlichen
Doktorgrades der Julius-Maximilians-Universität Würzburg

vorgelegt von

Susanne Meininger geb. Christ

aus Aura im Sinngrund

Würzburg 2018

Eingereicht bei der Fakultät für Chemie und Pharmazie am

_____

Gutachter der schriftlichen Arbeit

1. Gutachter: Prof. Dr. rer. nat. Jürgen Groll

2. Gutachter: Prof. Dr.-Ing. Frank A. Müller

Prüfer des öffentlichen Promotionskolloquiums

1. Prüfer: Prof. Dr. rer. nat. Jürgen Groll

2. Prüfer: Prof. Dr.-Ing. Frank A. Müller

3. Prüfer: Prof. Dr. rer. nat. Uwe Gbureck

Datum des öffentlichen Promotionskolloquiums

_____

Doktorurkunde ausgehändigt am

_____

Wer kämpft, kann verlieren.

Wer nicht kämpft, hat schon verloren.

Verfasser unbekannt

Table of contents

List of abbreviations

Abbreviation	Full name
3DP	3D powder printing
ACP	Amorphous calcium phosphate
ALP	Alkaline phosphatase
AM	Additive manufacturing
BSP	Bone sialoprotein
CAD	Computer aided design
CaSR	Calcium sensing receptor
CDHA	Calcium-deficient hydroxyapatite
COX-2	Cyclooxygenase-2
CPC	Calcium phosphate cement
CS	Compressive strength
CSD	Calcium sulfate dihydrate
CT	Computed tomography
DCPA	Dicalcium phosphate anhydrous
DCPD	Dicalcium phosphate dihydrate
DDS	Drug delivery system
DMEM	Dulbecco's Modified Eagle's Medium
DTS	Diametral tensile strength
EqD	Pore equivalent diameter
ERK1/2	Extracellular signal-regulated kinase
FCS	Fetal calf serum
FDA	Food and Drug Administration
FS	Flexural strength
HA	Hydroxyapatite
HEMA	2-hydroxyethyl methacrylate
hFOB	Human fetal osteoblast cell line 1.19
HPLC	High performance liquid chromatrography
MAPK	Mitogen activated protein kinase

MOC	Magnesium oxychloride cement
MPC	Magnesium phosphate cement
MSD	Mean squared displacement
OC	Osteocalcin
OCP	Octacalcium phosphate
OPG	Osteoprotegerin
PA	Polyamide fiber fillers
PAN	Polyacrylonitrile fiber fillers
PAN-sc	Polyacrylonitrile short cut fibers
PBS	Phosphate buffered saline
PCL	Poly-ε-caprolactone
PDF	Probability density function
PLA	Poly(lactic acid)
PLGA	Poly(lactic-co-glycolic acid)
PLR	Powder-to-liquid ratio
PMMA	Poly(methyl methacrylate)
PS	Polystyrene
RANK	Protein receptor activator of the nuclear factor κB
RANKL	Protein receptor activator of the nuclear factor κB ligand
SD	Standard deviation
SEM	Scanning electron microscope
SrMPC	Strontium-substituted magnesium phosphate cement
TCP	Tricalcium phosphate
TTCP	Tetracalcium phosphate
wof	Work of fracture
WST	Water-soluble tetrazolium salt
XRD	X-ray diffraction

List of symbols

Symbol	Mathematical meaning
a	Centrifugal acceleration
c	Drug concentration
C	Concentration gradient
C_0	Initial drug concentration
C_s	Drug solubility
d	Diameter
D	Diffusion coefficient
d_a	Outer diameter
d_i	Inner diameter
d_m	Diffusion coefficient
E	Young's modulus
F	Ultimate force
F_c	Centrifugal force
h	Height
K	Constant
k	Constant
K_0	Zero-order release constant
K_1	First-order release constant
K_H	Higuchi dissolution constant
K_V	Drug specific volume
l	Length
l_c	Critical fiber length
l_D	Defect distance
M	Absolute cumulative amount of drug released
m	Weibull modulus
m	Mass
n	Release exponent

N	Number of tested samples
n_R	Rank number
P_f	Probability of failure
Q	Amount of drug dissolved
r	Radius
r_a	Outer radius
r_i	Inner radius
s	Wall thickness
s_p	Scale parameter
t	Time
V	Volume
V_C	Critical fiber volume fraction
V_D	Defect volume
x	Lognormal distribution variable
y	Probability density function
Δl	Real diffusion path
Δx	Unit length
ε	Porosity
μ	Location parameter
ρ	Density
ρ_D	Defect density
σ	Strength
σ_0	Scale parameter with a failure probability of 63.2 %
σ_f	Fiber strength
σ_t	Stress below which the probability of failure is zero
τ	Shear stress on the surface
τ_t	Tortuosity
ω	Angular velocity

1. Introduction

Critical size bone defects are a severe medical indication occurring after trauma or bone resection due to cancer or other diseases. They exceed a critical size between neighboring bone faces, which results in a defect that cannot heal appropriately. In contrast, fibrous soft tissue will grow into the untreated defect [1]. To avoid this ingrowth of fibrous tissue with its adverse effect on healing and to recover the natural functionality of bone, an adequate treatment of critical size defects is essential. The consequences of an untreated defect are engraving for the patient in terms of physiology as well as psychology. The skeleton loses functionalities like metabolic activity and regulation as well as its mechanical stability. Especially the latter can lead to a complete immobilization of the patient with further medical implications and pain. Although there is a great need for adequate bone replacement materials, there are still huge challenges to overcome. This includes the material and its properties as well as the processing of those materials. In the last few decades, development is heading from biocompatible but inert mono-functional materials towards bioactive multi-functional composites [2, 3]. One of the most promising approaches is the mimicking of human bone with respect to the structure, chemical composition, metabolic agent release and properties. Ceramic materials like calcium and magnesium phosphate cements approximate these requirements due to their similarity to human bone composition. However, bone itself is a composite material of mainly carbonated hydroxyapatite as inorganic matrix and collagen as organic reinforcement [4]. With this in mind, new material combinations were employed together with new manufacturing techniques to obtain patient-specific implants. Additive manufacturing, which is a relatively new field especially in medicine, gained more and more interest due to the ability to fabricate tailor-made implants with perfect fitting. However, not all materials and composites can be used in combination with every technique, which requires an adaption of the technique or a transfer to other manufacturing processes.

The aim of this thesis was the optimization of existing materials in terms of their mechanical and biological performance and the transfer of a new fabrication technique from construction industry [5, 6] to medical implant production. As a first step, 3D powder printing as a commercially available additive manufacturing technique was modified to optimize the green strength of as-printed samples. This technique is based on the reconstruction from computed tomography images of the patient's defect in a three-dimensional way [7, 8]. For the improvement of mechanical stability, the well-established fiber reinforcement [9] was used within the printing process for the first time. Since the layer-by-layer fabrication is highly dependent on smooth powder spreading, the optimization of fiber length and fiber content is essential for an adequate printing result. In a second project the transfer of centrifugally casting from construction industry to biomedical relevant materials was conducted accompanied by the optimization of the materials with respect to mechanical and biological performance. The manufacturing technique uses the centrifugation of cement slurries to form tubular structures. For the reconstruction of the diaphysis of long bones this technique seems to be suitable as demonstrated by the reconstruction of a non-centrosymmetric long bone. The hollow structures of these tubes involve additional advantages in bone replacement, e.g. hollow structures are favorable due to their low weight with simultaneously high mechanical stability. Additionally, the tubes can lead to an ingrowth of bone marrow and bone marrow derived cells supporting the healing and implant replacement process [10-15]. The technique of centrifugally casting was used for the fabrication of mechanically and biologically optimized materials. The mechanical performance was tuned by using both fiber reinforcement and dual setting cement systems to obtain damage tolerance necessary for the treatment of load bearing defects. On the other hand, materials for such tubular structures were improved regarding the biodegradation and biological behavior. This implicated the fabrication of graded structures, which is a huge challenge or even impossible for other manufacturing techniques. The graded structures could be employed for strontium release that supports new bone formation or adjustment of the degradation behavior by calcium addition in magnesium phosphate cements. Furthermore, the technique is

suitable for the incorporation of drugs, growth factors or proteins, since no elevated temperatures or other components harming the substances are involved. The graded structure enables a long-term release of the incorporated drug at the application site. The biological improvements were also transferred to 3D powder printing for the fabrication of a strontium-substituted magnesium phosphate cement. The high porosity and pore interconnectivity of 3D printed constructs is favorable for bone ingrowth, vascularization and nutrition supply [10, 11, 16, 17]. As this is a well-established additive manufacturing technique, the process is operator independent and yields in a high reliability of the mechanical properties. The addition of strontium not only influences the degradation behavior and imaging of the implant but also supports new bone formation [18-26]. This is even more important for patients with an imbalance in bone formation and resorption as it occurs for osteoporosis. The strontium release from the degrading implant can improve new bone formation by osteoblasts and simultaneously impede the bone resorption by osteoclasts. Together, a patient-specific implant can be fabricated that can be replaced by own bone tissue *in vivo*.

These studies provide a versatile tool box for the treatment of critical size bone defects with superior properties for each application site. Additionally, centrifugally casting as another alternative for the manufacturing of patient-specific implants was established for bone cement materials. The combination of a perfectly adapted material and the adequate manufacturing technique provides the opportunity to treat critical size defects with a long-term improvement of the patients' life.

2. Theoretical background

Parts of Section 2.3, 2.4 and 2.7 are submitted and accepted for publication as a book chapter. At the time of submission of this thesis, the book was not published yet.

2.1 Natural bone remodeling

To evaluate the healing and bone ingrowth into implant material, the natural remodeling and bone healing procedure have to be considered. Human bone structure can be divided into cortical bone and cancellous bone. Cortical bone has a dense structure and occurs primarily in long bones like the femur. The high strength and fracture resistance of cortical bone is needed for the outer surface of bones to protect the much softer cancellous bone inside. Cancellous bone is built of trabeculae oriented for maximum load bearing. This spongy tissue is very lightweight but optimized in the direction of external forces. Cancellous bone can also be divided in two categories: coarse and fine. Coarse cancellous bone can be found in healthy adults. Fine cancellous bone occurs in fetal bone or in the early fracture callus [27]. In general, a mature bone in the human body is subject of steady remodeling processes to maintain mechanical properties, adapt to new load situations and repair damaged regions. In general, this process is balanced by the activities of osteoblasts (bone forming cells) and osteoclasts (bone resorbing cells). Beside those two cell types, osteocytes and osteoblast-derived lining cells (both terminally differentiated osteoblasts) play an important role in bone remodeling. The latter two cell types are by far the most abundant cell types in bone. They build a network all over the bone volume (osteocytes) and the bone surface (lining cells), respectively, and communicate via gap junctions. The remodeling process follows several steps: activation, resorption, formation [28]. The bone resorption is initiated by the expression of different cytokines that stimulate osteoclasts. The cytokines are released by osteoblasts, lining cells and osteocytes triggered by external stimuli like microdamage in the bone

matrix. Those microcracks lead to a local osteocyte apoptosis initiating the repair cascade. The protein receptor activator of the nuclear factor κB ligand (RANKL) interacts with the receptor RANK, which is located on the surface of mononuclear hemopoietic osteoclast precursors. The interaction of RANKL and RANK stimulates the expression of fusion proteins for osteoclast progenitor fusion. To avoid an uncontrolled osteoclastogenesis, osteoblasts lineage releases the protein osteoprotegerin (OPG) that blocks the interaction of RANKL and RANK by binding to RANKL and, therefore, reducing free RANKL [29]. Osteoclast precursors are further guided by chemoattractants like osteocalcin. Those chemokines are secreted by osteoblasts and lead to chemotaxis of osteoclast precursors towards each other (for fusion) and towards bone surface. To prepare the bone surface for osteoclast resorption, cytokines promote lining cells to resorb the osteoid layer by the secretion of collagenase [30, 31]. Subsequently, lining cells detach from the surface and form the temporary bone remodeling compartment. Within this compartment, all further remodeling steps are performed. However, it is still unclear how the involved cells enter the compartment. The attachment of osteoclasts at the bone surface is realized by integrins that form a sealed lacuna. Osteoclasts pump H^+ ions into the lacuna and, therefore, reduce the pH value locally to around 5 [32]. Since the solubility of the mineral bone phase increases with reduced pH the mineral phase is resorbed. Additionally, lysosomal enzymes are released to degrade the organic component [33]. After completion of bone resorption, osteoclasts become apoptotic. The work of osteoblasts begins by sensing the pit created by the osteoclast activity. The size of the pit together with regulatory factors embedded in the bone matrix and released during resorption regulate new bone formation. One of the most important requirements is the communication between osteoblast cells via gap junctions and proteins. Bone formation by osteoblasts then starts with the deposition of an osteoid layer, which is not yet mineralized. In the early stage, preosteoblasts secrete type I collagen and bone sialoprotein. Later on, the mature osteoblasts express type I collagen, osteocalcin and alkaline phosphatase [28]. Formation of hard tissue is performed by the mineralization of the osteoid layer. Surrounding blood serum is the source of calcium and

phosphorous ions for the formation of a calcium phosphate layer. In the beginning of mineralization amorphous calcium phosphate crystals form within vesicles of bone-lining cells and are excreted and deposited. Then the amorphous calcium phosphate converts first into a metastable octacalcium phosphate phase and then into calcium-deficient carbonate hydroxyapatite [4, 34]. The formation of these intermediate phases is difficult to investigate, since they form in nanometer size, which is hard to detect via x-ray diffraction analysis. To date, the excretion from vesicles is the most probable explanation for the observations so far [27, 35]. The mineralization occurs in two steps, a primary and a secondary mineralization. The primary step includes the mineralization of the previously formed matrix. In the second step the crystals grow to their ultimate size and the amount of crystals is further enhanced [36]. At the end of bone formation osteoblasts differentiate into lining cells deposited on the bone surface or into osteocytes embedded in the bone matrix [31]. Beside the continuous remodeling process, the procedure of bone resorption and bone formation also occurs after fracture events. In this case, inflammation precedes the healing process. After a fracture event, disrupted blood vessels cause a local bleeding and, therefore, the invasion of inflammatory cells into the hematoma. Those cells secrete several cytokines and growth factors which again attract multipotent mesenchymal stem cells for repair [37]. This event always happens prior to the implantation of a bone replacement and, therefore, influences healing and ingrowth.

2.2 Response to bone replacement material

Bone replacement materials are required when the defect exceeds a critical size. The natural remodeling processes described above are in principle the same for bone fractures. However, a decisive factor is the contact of bone tissue with the opposite fracture site. Bone tissue and especially bone cells need mechanical stimulation for bone formation and remodeling processes [38]. In critical size defects, an implant has to undertake this task. Critical size defects are injuries where the contact is insufficient for natural healing processes like callus bridging. Such cases arise due to severe

fracture events with multiple cracking, surgical intervention like tumor resections or diseases of gradual bone loss. The application of an implant is, therefore, inevitable and causes biological response. This response is, of course, dependent on the implant material, implant properties and implantation site. However, some general reactions can be summarized occurring in connection with an implantation of foreign materials.

When an implant is in contact with tissue, body fluids and blood, proteins adsorb at the implant surface within seconds. The adsorption is proportional to the protein concentration but is also influenced by many factors. These proteins determine the further behavior within the body like inflammatory response or cell adhesion, proliferation and differentiation. A competition between cell colonization and bacterial biofilm formation may take place, commonly known as the "race for the surface". This race is dependent on initial bacteria concentration originating from the surgery or circulating body fluids [39]. The surface structure plays a decisive role in the adsorption process. Factors like roughness, particle size, pore size and porosity influence the surface area, which is direct proportional to the amount of protein adsorption. Furthermore, the nanoscale roughness of the surface affects the protein structure, which can alter the function and impact of the protein. On porous structures, proteins will adsorb in multi-layers, whereas on dense structures they build just a monolayer. Another influencing factor is the surface charge. Since proteins have charged groups, they can interact with the surface via electrostatic interactions. For calcium phosphate cements, the surface exhibits Ca^{2+} and PO_4^{3-} ions that can act as binding sites for the protein. The overall surface charge is then proportional to the amount of protein adsorption and the zeta potential delivers a hint which proteins will be adsorbed. Foreign ions can also alter the surface charge of the ceramic or cause vacancies and defects. All these factors alter the protein adsorption on the implant surface. But not just the implant itself has an influence on adsorption behavior, the pH of the surrounding media or body fluid favors or reduces the affinity for different proteins to adsorb. In the human body, the pH of body fluids can be altered for example by bacterial activity or dissolution of the implant. So a bacterial infection can

strongly affect foreign body reactions and implant ingrowth. The protein plays also a decisive role when being adsorbed. The primary structure determines the binding sites, e.g. functional groups, and the adsorption affinity of the whole protein. Larger proteins exhibit more binding sites than small proteins on average. This fact leads to the so-called Vroman effect: small proteins have a higher diffusion rate in the media and adsorb on the surface first. After a while the small proteins are replaced by larger ones, which have more binding sites and, therefore, bind stronger to the surface. By surface binding, the conformation of the whole protein can change influencing the function and possibly the cell attachment. However, the exact changes in conformation and their influence on cells and cell attachment is still not clear [40]. After protein adsorption on the implant surface, cells like osteoblasts and osteoclasts start to attach on this protein layer. This process is dependent on the proteins, their conformation and material properties of the implant beneath. The surface roughness and possible grooves that can act as guiding structures also influence cell attachment, orientation and morphology. Lampin et al. calculated the surface free energy depending on the surface roughness. The surface energy increased with increasing roughness especially after initial protein adsorption. This has also a strong impact on cell attachment [38, 41].

Apart from protein adsorption and cell attachment, the overall reaction to a bone replacement material can be described according to the bone formation. The most important terms describing the behavior and properties of the materials are listed in Table 1.

Table 1: Explanation of important terms related to the behavior of bone replacement materials within the human body [2, 42-45].

Term	Explanation
Osteoconductivity	A material that enables and facilitates bone ingrowth by providing a guiding structure
Osteoinductivity	A material that actively supports bone growth by activation of mesenchymal stem cells differentiating into osteoblasts
Osteogenesis	Formation of new bone
Osteointegration	Bonding between host bone and bone replacement material
Osteoproduction / Osteostimulation	Stimulation of new bone formation
Bioactivity	The ability of a material to actively influence biological reactions or tissue response; for bone replacement materials, bioactivity is usually measured by the induction of hydroxyapatite crystallization in simulated body fluid solutions
Biocompatibility	No negative influence of a material on living tissue, organs or the whole organism and causing no harmful reactions; no inflammatory or toxic mediators are released by the material

2.3 Bioceramics as bone replacement material

The biological application of ceramic materials gained momentum in the last decades. Although autologous bone is still the gold standard in bone replacement, synthetic materials exhibit some superior advantages meeting economical as well as individual requirements. A huge drawback of autologous bone grafts is the donor site morbidity and the related pain. For the extraction, a second surgery is necessary entailing the risk of infections and loss of function at the extraction site. Secondly, the availability of autologous bone is limited especially in elderly people with osteoporosis and multimorbidity. These drawbacks can be overcome by the use of synthetic materials

that mimic the natural tissue. They exhibit a broad diversity in application forms and can be produced for examples as coatings, nanoparticles or porous solids. Due to diverse composition of the different ceramics, the implant can be adapted to the special requirements of the implantation site or the patients' needs. According to the three generations of bioceramics, the interaction between implant material and the organism increased during development. The first generation intended to avoid all interactions of the ceramic material with surrounding tissue. Zirconia and alumina are two famous representatives, which were used for inlays or heads of hip prostheses. They exhibit an excellent wear resistance, hardness and inertness [3]. Since tissue formation within the artificial joint is not favorable, an inert material is essential for this application. However, when thinking of bone replacement, bioactivity would enable a better implant ingrowth and bone regeneration. Therefore, a second generation was developed to exhibit bioactive properties without negative side effects like fibrous tissue formation or inflammation. Additionally, a strong bonding between the artificial bioceramic and the natural bone could be achieved by the development of new formulations [2]. Bioceramics of this generation are often degradable giving space for new bone formation. Calcium phosphate cements (CPC) including hydroxyapatite, which is the main inorganic component of natural bone [46], are widely used for bone replacement. Another material exhibiting bioactivity are the bioactive glasses based on silica. The third generation of bioceramics even goes one step further and tries to interfere with the cellular mechanisms behind bone healing.

2.3.1. Bioactive glasses and its hybrids

Bioactive glasses can be used as bone replacement materials due to their good biocompatibility and especially the bioactivity. They favor cell adhesion and proliferation leading to enhanced bone tissue formation, ingrowth and regeneration. The third generation of bioceramics not only favors cellular activity but induces mechanisms for influencing cell activity and, therefore, bone healing [47]. This influence on the cells and the subsequent bone healing is called osteoproduction or

osteostimulation [2]. The influence on the cells can be exerted by the release of ions or agents affecting the natural cell metabolism [48]. Drug delivery systems (DDS) are part of this third generation, since they can be employed as carrier systems for specific proteins or drugs promoting bone regeneration. Drug loading, however, requires a certain extend of porosity where the drug can be stored and slowly released. Bioactive glasses based on silica or mesoporous silica scaffolds can provide a certain kind of porosity. Moreover, foams can be produced from bioactive glasses that serve as drug release scaffolds and mimic cancellous bone. Their pores are interconnected and vary from nano to micro scale [49-51]. Bioactive glasses are often termed bioglass, although the name "Bioglass®" is a trademark for the specific composition 45S5 (46.1 mol% SiO_2, 24.4 mol% Na_2O, 26.9 mol% CaO and 2.6 mol% P_2O_5). Hench invented a degradable glass of the general composition Na_2O-CaO-SiO_2-P_2O_5 that can strongly bind to bone tissue. The bonding is attributed to a hydroxycarbonate apatite layer that forms during dissolution of the implant material [52]. There are two major routes to produce bioactive glass scaffolds: quenching of a melt or sol-gel processing [47]. The firstly developed melt-quenching needs temperatures > 1300 °C to melt all reactant components and a subsequent quenching of the glass melt [52]. The reactant oxide or carbonate powders are mixed in the stoichiometric ratio, melted and transferred into a mold. Quenching hast to be very fast with a cooling rate of at least 10^6 K/s. After quenching, the glass frit is annealed at around 500 °C to relief stresses [53]. The sol-gel process is performed at much lower temperatures since it is a chemical synthesis with post-processing temperatures of some hundred degrees [47]. Moreover, the surface area as well as the porosity are very high [3, 53], whereas melt-quenched glasses have a dense structure. The Na_2O component is often omitted in the sol-gel process, since it acts as melting point lowering agent and increases the solubility. In the sol-gel process no melting is required and the solubility is primarily influenced by the high surface area and solid state diffusion processes [52]. The degradation of bioactive glass plays a decisive role in the bioactivity of the material. The bioactive glasses degrade in several steps. It starts with an ion exchange, where Na^+ or Ca^{2+} ions are replaced by H^+ ions. Due to a reduced pH, the silica dissolves leading to $Si(OH)_4$

groups at the surface. A polycondensation of silanols on the surface leads to the formation of a silica gel layer attracting Ca^{2+} ions from the surrounding media. Additionally, OH^- and PO_4^{2-} ions are also incorporated into this layer, which is a silica rich calcium phosphate phase. By further adsorption of ions from the media, the layer gradually converts into HA. This process starts at the glass surface and proceeds towards the bulk material [53-55]. The bioactive glasses are designed to maintain an ionic concentration that is always in an optimal range for osteoblast activity during release of bioactive Ca, Na, Si and P ions [48]. These ions increased the expression of growth factors responsible for osteoblast proliferation and, therefore, bone tissue formation [2, 56, 57]. Since silicon can be found in bone as a trace element, it is obvious that it has to have a positive influence on physiological processes. The impact of silicon on osteoblast and on bone formation was investigated not only by release from bioactive glass but also by incorporation of silicon in CPC. A promotion of osteoblast proliferation and differentiation, a regulation of osteoclast and resorption and an enhanced mineralization were found for release concentrations of 0.1 – 100 ppm [42, 53, 58, 59]. Calcium release also promotes bone formation by increasing osteoblast activity when released in a range of 13.1 – 90 ppm [53, 59]. Additionally to the promoting effect on bone formation, bioactive glass can increase the pH locally and act antibacterial similar to calcium hydroxide [60]. Therefore, these materials are already used in clinics as commercial product for example in jaw regeneration, orthopedics and middle ear prosthesis. However, the shape was for a long time limited to monoliths, before additive manufactured molds were produced to cast patient specific implants [52]. Among the bioactive glasses, the organic-inorganic hybrid materials are of great importance. They can be used to tailor mechanical properties, biological interaction like bioactivity or degradation behavior. The organic groups can also be utilized for drug binding and controlled release. Two classes of hybrid materials are distinguished: class I and class II hybrids. Class I hybrids exhibit just weak interactions between the two phases, whereas class II hybrids (called ormosils = organically modified silicates) have covalent or ion-covalent bonds [3]. An example of class I hybrids is the combination of bioactive glass with poly(vinyl alcohol) [61].

For ormosils or class II hybrids, polymers with silanol (Si-OH) groups are introduced into bioactive glass to combine the bioactivity of the inorganic bioactive glass matrix with the optimizing mechanical properties of the organic component. The formation of hydroxyapatite, the main inorganic component of bone, is promoted by silanol groups on the implant surface [62-64].

2.3.2 Mesoporous silica

Mesoporous silica in general describes a highly ordered structure with pores in the nanometer range based on silica or alumina. Here, the focus is on mesoporous structures based on bioactive glasses with the general composition SiO_2-CaO-P_2O_5 since their bioactivity is much higher than for other silica or alumina compositions. Therefore, the relevance in bone replacement material is given for those compositions. In the beginning of their invention they were used as catalysts, as they are an excellent material as host-guest system [65, 66]. Mesoporous silica glasses are synthesized by an evaporation-induced self-assembly of non-ionic triblock copolymer surfactants building the basic framework for the inorganic silica material. After removal of the surfactant, a highly ordered, mesoporous and inorganic structure remains [67]. During processing numerous factors can be modified to tailor the properties of the resulting scaffold. Among others, CaO and P_2O_5 addition can influence not just the glass composition but also the structure. Since Ca^{2+} is a network modifier, it alters the inorganic/organic ratio leading to a different orientation of the surfactants. Phosphorus content has a similar but indirect influence on the resulting structure. The P_2O_5 together with CaO leads to the formation of amorphous calcium phosphate on the surface. Therefore, the Ca^{2+} ions are bound and cannot interrupt the silica network. Without phosphorus ions Ca^{2+} ions can again alter the inorganic/organic ratio, which influences the structure. Further factors include temperature, solvent, additives and pH [68]. The resulting structures exhibit a high surface area, high pore volume, narrow pore size distribution, small pores (2 – 50 nm) and interconnectivity [47, 67, 69]. This high surface area causes a fast mineralization with calcium-deficient carbonate

hydroxyapatite. The mineralization is much faster when P_2O_5 is incorporated since the amorphous calcium phosphate crystals serve as nucleation sites for hydroxyapatite formation [68]. The hydroxyapatite formation of mesoporous silica exhibits a biomimetic behavior. Observations in simulated body fluid showed the formation of amorphous calcium phosphate within the first hour. This amorphous layer then converts into metastable octacalcium phosphate, which forms only at a pH below 7. To achieve such a pH value, a high CaO content and the highly porous structure are key factors. The Ca^{2+} / H_3O^+ exchange leads to a condensation of the silanol groups resulting in an acid hydrated silica layer with a pH below 7. After around 8 h the octacalcium phosphate layer converts into a calcium-deficient carbonate hydroxyapatite layer. Mesoporous silica materials can be modified with organic groups due to their high amount of silanol groups on the surface to improve drug, protein or growth factor loading with subsequent controlled release [3]. They can also be modified with hydrophobic groups to load the scaffold with a hydrophobic drug or amino groups for electrostatic interactions with phosphonate or carboxylate containing drugs. When used as a bone replacement material, the porous structure is a decisive factor. Mesoporous silica particles are characterized by their pores in the size range of nanometers, whereas pore sizes for bone ingrowth have to be in the micrometer range as it can be found in native bone tissue. The challenge is to introduce macroporous structures without the loss of mesoporosity. The combination of different porosities like macro-, meso- or micropores and tailoring of their interconnectivity gives a powerful tool to tune the mechanical properties along with the biological activity and the drug load and release capacity [68]. Apart from porosity, the size of mesoporous silica particles can be reduced to nanoparticles facilitating cellular uptake and, therefore, release within the cell [70].

2.4 Mineral bone cements

Another class of bioceramics are mineral bone cements, predominantly based on calcium and magnesium phosphate chemistry. The preparation of scaffolds from such

materials can be performed at high temperature via sintering of a green body [71] or low temperature [72]. When compared to sintered monoliths, low temperature fabricated cements imply a higher specific surface area due to crystal formation (up to 100 m^2/g compared to < 1 m^2/g for hydroxyapatite mineral) [73]. The low temperature preparation is based on a dissolution/precipitation reaction. Therefore, a powder of one or more components is mixed with an aqueous solution resulting in a paste. Depending on the pH and additional ions powders dissolve and undergo a setting reaction. The product precipitates due to a lower solubility in the supersaturated solution and forms a crystalline structure. By interlocking of growing crystals the cements gain mechanical strength. The aqueous solution involved in this process leaves a certain porosity in the set cement. This again means, that the porosity can be tuned by the powder-to-liquid ratio (PLR) with a lower PLR causing a higher porosity. The mechanical performance, which is often required for bone substitution, suffers from a highly porous structure. However, the porosity can be used for example for drug loading in DDS [74]. The reactant powder as well as the set product are all biocompatible and non-toxic. Since the setting can be done at body temperature, CPCs and magnesium phosphate cements (MPCs) are suitable for *in vivo* hardening. The set cements are chemically similar to human bone resulting in a strong and in some cases chemical bonding between bone and substitute material. The bone bonding is also favored by a very low shrinkage of less than 1 % [75]. The surgeon can mold the cement paste, which is easily mixable, within the defect cavity and adapt the shape to the patient's requirements. Depending on the specific properties of the cement paste applied, they are injectable and can be used in minimally invasive surgery. This again reduces the risk of infections, scars and pain for the patient. The dissolution/precipitation reaction has the additional advantage of a high specific surface area for hydroxyapatite cements, which is close to that of bone mineral (≈ 80 m^2/g). Since the protein adsorption and the following cell adhesion is strongly dependent on the specific surface area (see Section 2.2), the dissolution/precipitation reaction is superior to sintering. During degradation, the degrading products are also biocompatible, non-toxic and can be resorbed by the body or even used for the

formation of new bone. This facilitates the replacement with natural bone and a complete healing [76].

2.4.1 Calcium phosphate cements (CPC)

Mineral bone cements on the basis of calcium phosphates include various more or less stable phases. An overview of the most important phases in the biomedical field is given in Table 2. Among those, calcium-deficient HA ($Ca_9(HPO_4)(PO_4)_5OH$), dicalcium phosphate dihydrate (DCPD, brushite, $CaHPO_4 \cdot 2H_2O$) and dicalcium phosphate anhydrous (DCPA, monetite, $CaHPO_4$) are the main products of the dissolution/precipitation reaction [76, 77]. The solubility of such calcium phosphate cements (CPCs) strongly depends on the pH of the cement liquid (Figure 1), in which the cement powder dissolves due to a high solubility and forms a supersaturated gel. Depending on several factors such as pH and ionic concentration, a new calcium phosphate precipitates and forms an entangled crystalline cement matrix [78]. The great advantage is that the reaction can be performed under physiological conditions and, therefore, *in vivo*. In contrast, poly(methyl methacrylate) (PMMA), which is frequently used in bone replacement application, reaches temperatures of up to 120 °C causing severe tissue necrosis [79-82]. The dissolution/precipitation reaction of CPC is only slightly exothermic and rarely exceeds body temperature [83]. Bohner et al. investigated the enthalpy of the single reactions occurring during setting. For a brushite cement, the dissolution of β-TCP is exothermic with ΔH = -66.0 kJ/mol, the dissolution of MCPM is endothermic with ΔH = 23.0 kJ/mol and the precipitation of brushite is exothermic with ΔH = -10.0 kJ/mol. This yields in an overall exothermic reaction with an enthalpy of -83.0 kJ/mol [84]. This enables the patient-specific adaption of the cement paste to the defect shape without the risk of tissue necrosis due to heat. However, the solubility of synthetic CPCs is among others influenced by the crystallinity, morphology, porosity and outer dimensions. This opens up additional factors for the adjustment of an implant material. The different CPCs can be characterized by their Ca/P ratio (Table 2), which is on the one hand a result of the

ionic concentration during setting and on the other hand influences the stability of the ceramic. Since several years, a variety of CPCs are commercially available on the market, although investigation and improvement is still in progress [44]. Apart from pure CPC, there are numerous studies investigating ionically substituted CPCs for tuning the mechanical as well as the biological performance of the ceramic. Among others, these cements are substituted with magnesium [85-87], lithium [88, 89] or silicon ions [90-93].

Table 2: Selection of commonly used CPC ordered with decreasing solubility [76].

CPC	Abbreviation	Ca/P	Solubility K_{sp}	Solubility / mg/l
Monocalcium phosphate monohydrate	MCPM	0.5	$7.24 \cdot 10^{-2}$	$18 \cdot 10^{3}$
Monocalcium phosphate anhydrous	MCPA	0.5	$7.24 \cdot 10^{-2}$	$17 \cdot 10^{3}$
Dicalcium phosphate dihydrate; brushite	DCPD	1.0	$2.57 \cdot 10^{-7}$	88
Dicalcium phosphate anhydrous; monetite	DCPA	1.0	$1.26 \cdot 10^{-7}$	48
Octacalcium phosphate	OCP	1.33	$2.51 \cdot 10^{-97}$	8.1
Amorphous calcium phosphate	ACP	1.2 – 2.2	-	-
α-tricalcium phosphate	α-TCP	1.5	$3.16 \cdot 10^{-26}$	2.5
Tetracalcium phosphate	TTCP	2.0	10^{-38} - 10^{-44}	0.7
β-tricalcium phosphate	β-TCP	1.5	$1.26 \cdot 10^{-29}$	0.5
Hydroxyapatite	HA	1.67	$< 10^{-116}$	0.3

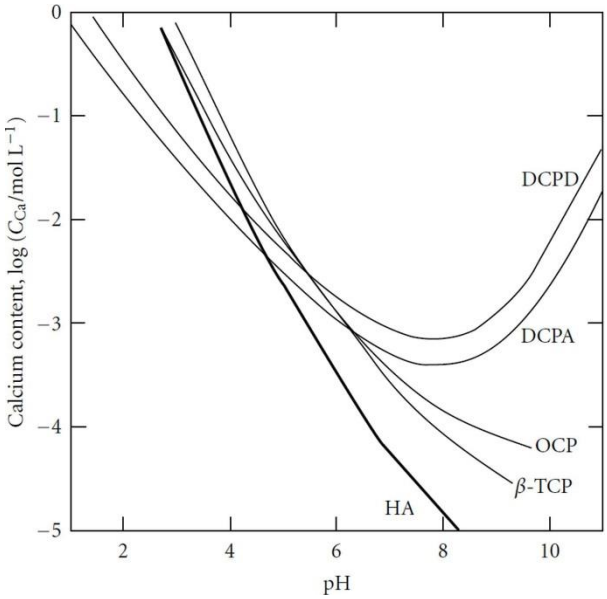

Figure 1: Solubility of different calcium phosphate cements: dicalcium phosphate anhydrous (DCPA), dicalcium phosphate dihydtrate (DCPD), octacalcium phosphate (OCP), β-tricalcium phosphate (β-TCP) and hydroxyapatite (HA). Copyright 2012 K. Kuroda and M. Okido [94].

Hydroxyapatite

The most investigated CPCs are forming HA as a suitable candidate for bone replacement since calcium-deficient carbonate HA it is the main inorganic component of bone [46]. Beside other routes, it can be formed by the dissolution/precipitation reaction of α-tricalcium phosphate (α-TCP) with water (eq. 2.1) or tetracalcium phosphate (TTCP) with dicalcium phosphate anhydrous (DCPA, monetite) (eq. 2.2).

$$3\ \alpha\text{-}Ca_3(PO_4)_2 + H_2O \rightarrow Ca_9(HPO_4)(PO_4)_5OH \quad (2.1)$$

$$2\ Ca_4(PO_4)_2O + 2\ CaHPO_4 \rightarrow Ca_{10}(PO_4)_6(OH)_2 \quad (2.2)$$

α-TCP has a higher solubility compared to HA, which favors the formation of HA crystals during cement setting at a physiological pH of 7.4. HA is the least soluble

calcium phosphate mineral at this pH. The low solubility and high stability entails the ability of recrystallization of other CPCs like amorphous calcium phosphate (ACP), DCPA or TTCP to form HA. A great disadvantage of the processing of HA cements for a surgeon are their long setting times. The optimal initial setting time is between three to five minutes. Within that time frame, the formerly moldable paste should set and exhibit a certain mechanical stability. Since the formation of HA takes several minutes to hours [95-97] there is a great need for setting accelerators. Such additives reduce the setting time of HA by enhancing the solubility of the reactant powders. Water soluble orthophosphates like MCPA or phosphoric acid can be employed in the liquid phase. They lower the pH of the liquid phase and, therefore, enhance the solubility of the reactant powders as described in Figure 1. Since there is a linear correlation between the dissolution of the reactants and the formation of the product, the formation of HA is well controlled and does not lead to a higher amount of residues [76]. Another option for the adaption of setting time is milling of the reactant powder to gain an amorphization with increased solubility and hence a faster setting reaction [98-100].

Brushite and monetite

A second very important group of CPC for the biomedical field is forming brushite (DCPD) or monetite (DCPA) as the water free form of brushite. DCPA can either be obtained by the dehydration of brushite cement post-setting or by the reaction with an excess of MCPM [84]. Brushite forms in a hydraulic setting reaction, where water is required not only for mixing but also for a stoichiometric reaction. This also means, that with a very low water content, the formation of monetite is favored [101]. Since brushite and monetite are the least soluble phases at a pH below 4.2 (Figure 1), an acidic environment is essential for their crystal formation. As reactant powders, α-TCP, β-TCP or HA can be used as alkaline calcium source. Since the Ca/P ratio of brushite/monetite is 1, an additional acidic phosphate source is required for the setting. MCPM, MCPA or phosphoric acid can be employed as such a phosphate source.

Possible reactions are the acid-base reaction of β-TCP with MCPM and water (eq. 2.3) or β-TCP with phosphoric acid (eq. 2.4) [101-105].

$$\beta\text{-}Ca_3(PO_4)_2 + Ca(H_2PO_4)_2 \cdot H_2O + 7\ H_2O \rightarrow 4\ CaHPO_4 \cdot 2\ H_2O \quad (2.3)$$

$$\beta\text{-}Ca_3(PO_4)_2 + H_3PO_4 + 6\ H_2O \rightarrow 3\ CaHPO_4 \cdot 2\ H_2O \quad (2.4)$$

The setting time can be controlled by the selection of the basic phase. The limiting factor is the solubility of this basic phase, which is in the order HA < β-TCP < α-TCP. The setting of brushite cements is very fast since compared to HA cements, the crystallization rate for brushite is about three orders of magnitude higher [106] and the setting occurs in the range of seconds [83, 102, 107]. This greatly restricts the handling in the operating room and the application in the patient. To overcome these problems, different setting retarders have been investigated to enlarge the working time for the surgeon. Pyrophosphates are natural inhibitors of mineralization and can be employed to delay the formation of brushite crystals. Due to their strong affinity to calcium orthophosphate surfaces, they bind to the crystal surface and form calcium pyrophosphate. Additionally, pyrophosphate ions reduce the solubility of calcium phosphates leading to a delayed dissolution of the reactant powders, thus limiting the available calcium and phosphate ions [105, 108, 109]. Another group of setting retarders are sulfate ions as they are provided by e.g. sulfuric acid, calcium sulfate dihydrate or sulfate containing substances such as gentamicin sulfate. Since sulfate ions do not reduce the solubility or modify the dissolution rate of the reactant powders, the predominant mechanism for retardation is the inhibition of brushite crystal growth. However, if the concentration of sulfates becomes too high, the effect turns into an accelerated setting. This phenomenon is attributed to the formation of small calcium sulfate dihydrate (CSD) crystals acting as seed crystals for brushite. Since the crystal lattice of brushite and CSD are quite similar, HPO_4^{2-} ions can substitute sulfate ions in the CSD lattice. Due to the concentration dependent nucleation of CSD, a low sulfate addition acts as a retarder, whereas a high concentration accelerates the setting [105]. Carboxylic acids can also act as setting retarders. Their ability to bind calcium

ions enables an interaction between organic acid and growing brushite crystals. The negatively charged carboxyl group interacts with the positively charged calcium biding site at the crystal surface and the formation of a dicalcium phosphate-carboxylic acid complex leads to a slower crystal growth. In addition, the interaction with calcium ions leads to a complexation in the supersaturated solution reducing the supersaturation regarding calcium ions. Carboxylic acids also enhance the nucleation barrier slowing down the crystal formation. All these effects retard the overall setting of brushite cements. Numerous carboxylic acids have been tested in this regard like sodium citrate, citric acid, tartaric acid or glycolic acid [78, 110, 111]. In addition, ions itself can modify the cement setting. This is independent of whether these ions are introduced via the liquid phase or by substitution of the cement raw powder. Magnesium ions can be found in the human body regulating precipitation of calcium phosphates. In the case of brushite, magnesium ions inhibit nucleation and crystal growth. They can be incorporated into the brushite lattice due to their similar atomic dimensions to calcium ions. An additional effect on the setting retardation is the formation of a complex of magnesium with HPO_4^{2-} ions. Since the latter are the limiting factor in brushite formation, the setting is delayed [111].

The addition of substances is not in all cases meant to retard the cement setting reaction. The retarding effects have to be considered for the addition of any additive. Some antibiotics for example gentamicin can contain retarding ions or groups [112]. Bisphosphonates, often used in medical treatment of osteoporosis, are also thought to retard the formation of brushite. They are structurally similar to pyrophosphates but have additional binding sites for functional groups. Etidronate is a representative of bisphosphonates [113]. Although etidronate has a similar structure as pyrophosphates, the retarding effect is much stronger. This could be assigned to the tridentate binding to calcium ions of etidronate compared to the bidentate binding possibility of pyrophosphates [114, 115]. Furthermore, the application as bone replacement material requires in the best case not only cytocompatibility of the setting retarders but also a

promoting effect on bone growth. Here, some setting retarders seem to be more appropriate than others [83, 116].

When implanted *in vivo*, brushite can easily degrade due to its high solubility at physiological pH. However, it was frequently observed, that brushite is converted into the lower soluble HA [117]. As this is not always a desired feature, the addition of Mg^{2+} ions can inhibit this conversion. Mg^{2+} ions adsorb on the surface of converting HA crystals and compete with and replace Ca^{2+} ions. Blocking of the crystallization site inhibits further crystal growth of HA [90, 118, 119]. This is one of the advantages of MPC described in Section 2.4.2.

ACP, OCP and TTCP

Although they are metastable, ACP, OCP and TTCP play a minor but still important role as bone replacement material. After implantation into the human body, they rapidly convert into HA or calcium-deficient hydroxyapatite (CDHA). This property is often exploited by the application as precursor phases with deliberated conversion [35]. In natural bone modelling, ACP cluster form within the vesicles of bone cells. After excretion, the clusters convert fast into OCP and finally into HA. The conversion itself is also a dissolution/precipitation reaction [120]. Due to the amorphous nature of ACP, it exhibits a diverse Ca/P ratio, which also depends on pH and ionic concentration during preparation [121]. This facilitates the substitution with numerous ions like Na^{+}, K^{+}, Mg^{2+}, Cl^{-} or CO_3^{2-} [122]. Due to the fast dissolution, the ions are rapidly released and can induce cellular activity. OCP is hard to produce synthetically since it rapidly converts into HA. Another factor is the slow crystallization rate of OCP [107]. TTCP has antimicrobial properties due to the formation of alkaline $Ca(OH)_2$ during setting that can be used to treat formerly infected bone sites or to prevent infections after implantation [123].

2.4.2 Magnesium phosphate cements (MPC) and magnesium based cements

In the field of biomedical application, magnesium phosphate cements (MPCs) are less exploited compared to CPCs. Originally, MPC were used in construction industries, for example as runway repair [124]. Similar to CPCs, there are different formulations of MPCs depending on pH and foreign ion supplementation during setting reaction (Table 3). The setting reaction itself is similar to brushite. For the acid-base reaction a magnesium oxide or magnesium phosphate is used together with an acidic phosphate solution. After dissolution of the reactant powders, an amorphous gel forms in the supersaturated solution. Crystallization leads to crystal growth and interlocking. The overall reaction is exothermic [125, 126], although quite different maximum temperatures are reported in literature. Measurements are reported with a maximum temperature of 35 – 80 °C [127-130]. Two of the most important MPC for bone replacement material are newberyite and struvite. The possible formation of newberyite is formulated in eq. 2.5 [131, 132].

$$MgO + H_3PO_4 + 2\,H_2O \rightarrow MgHPO_4 \cdot 3\,H_2O \quad (2.5)$$

Struvite can be synthesized by different routes as described in eq. 2.6-2.9 [125, 129, 133-135].

$$MgO + NH_4H_2PO_4 + 5\,H_2O \rightarrow MgNH_4PO_4 \cdot 6\,H_2O \quad (2.6)$$

$$MgO + (NH_4)_2HPO_4 + 5\,H_2O \rightarrow MgNH_4PO_4 \cdot 6\,H_2O + NH_3 \quad (2.7)$$

$$2\,Mg_3(PO_4)_2 + 3\,(NH_4)_2HPO_4 + 36\,H_2O \rightarrow MgNH_4PO_4 \cdot 6\,H_2O + H_3PO_4 \quad (2.8)$$

$$Mg_3(PO_4)_2 + (NH_4)_2HPO_4 + 15\,H_2O \rightarrow 2\,MgNH_4PO_4 \cdot 6\,H_2O + MgHPO_4 \cdot 3\,H_2O \quad (2.9)$$

Table 3:Selection of important MPC formulations and reactant powders for their synthesis for biomedical application [133].

MPC	Chemical formula	Mg/P	Solubility K_{sp}	Solubility / mg/l	Ref.
Magnesium oxide	MgO	-			
Trimagnesium phosphate; farringtonite	$Mg_3(PO_4)_2$	1.5	$6.30 \cdot 10^{-26}$	2.81	[136]
Trimagnesium phosphate octohydrat; bobierrite	$Mg_3(PO_4)_2 \cdot 8\ H_2O$	1.5	$6.31 \cdot 10^{-26}$	4.37	[137]
Trimagnesium phosphate hydrate; cattiite	$Mg_3(PO_4)_2 \cdot 22\ H_2O$	1.5	$7.94 \cdot 10^{-24}$	18.60	[137]
Magnesium hydrogen phosphate	$MgHPO_4$	1.0			
Magnesium phosphate dibasic trihydrate; newberyite	$MgHPO_4 \cdot 3\ H_2O$	1.0	$1.6 \cdot 10^{-6}$	$2.21 \cdot 10^{3}$	[138]
Magnesium ammonium phosphate hexahydrate; struvite	$MgNH_4PO_4 \cdot 6\ H_2O$	1.0	$5.21 \cdot 10^{-15}$ – $2.12 \cdot 10^{-13}$	4.25 – 14.61	[136]
Magnesium potassium phosphate hexahydrate; k-struvite	$MgKPO_4 \cdot 6\ H_2O$	1.0	$2.4 \cdot 10^{-11}$	1.31	[138]
Magnesium hydroxide; brucite	$Mg(OH)_2$	-	$6.92 \cdot 10^{-12}$	7.00	[139]
Magnesium oxychloride (phase 5)	$5\ Mg(OH)_2 \cdot MgCl_2 \cdot 8\ H_2O$	-			

The setting times of struvite cements without any additives are in a range between 1.5 – 16 min (Table 4) [127, 129, 140], which is adequate for surgical procedures. The huge differences in setting times are due to different pretreatments of the raw powder. Grinding, for example, has a huge influence on setting time because smaller powder particles dissolve faster than large ones due to the larger specific surface area. However, a faster setting leads to higher maximum temperature. The setting time can also be adapted by adjusting the PLR, whereby a higher PLR yields in a faster setting reaction [129, 141].

Table 4: Initial setting times of struvite reported in literature.

Equation	Initial setting time / min	Ref.
(2.9)	1.5 – 16	[129]
(2.6)	15	[127]
(2.9)	4	[140]

However, in some cases, additives are necessary to enable a certain application. For minimally invasive surgery, injectable bone cements are required, which entails the application of additives. Moseke et al. successfully used diammonium citrate to enhance the injectability of the cement paste [129]. Borates such as sodium borate decahydrate (borax) [125, 127, 142] and boric acid are popular additives, which retard the cement setting reaction of MPC and decrease the maximum temperature. The mechanism behind the retardation is not a delayed dissolution of the reactant powders but a slower precipitation of the product. Since the deposition of boron on the particle surface could be excluded, it is likely that the slow precipitation is due to a complex formation of $Mg(BOH)_4^+$ [143]. Another form of additives are foreign ion substitutions in MPC. With regard to implant application, Ca^{2+} [136, 144-146] and Sr^{2+} [147, 148] are the most important ones. Here, Ca^{2+} ions in general enhance bone formation by promoting osteoblast proliferation and differentiation and initiating signaling pathways [149]. Furthermore, Ca^{2+} substitution in struvite extends the initial setting time [145]. Sr^{2+} ions also promote bone formation and reduce bone resorption.

A deeper insight into the mechanisms and action of Sr^{2+} ions in mineral bone cements is given in Section 2.7.1. Another advantage of MPC is their fast degradation rate *in vivo*. In contrast to CPC like brushite, MPC do not convert into the lower soluble HA after implantation. The Mg^{2+} ions adsorb on the surface of precipitating HA crystals and, therefore, block the position in the crystal lattice for Ca^{2+}. Due to this competition, a further growth of the HA crystal is inhibited and the remaining MPC has a higher solubility than HA and can be resorbed faster and replaced by new bone [118, 119, 141].

Another group of magnesium based cements are magnesium oxychloride cement (MOC), also called Sorel cements. Similar to MPC but without phosphates, MOCs were first used in construction industries due to their fast setting and high early strength [150]. However, MOCs are fast degrading when in contact with aqueous solutions. This can be utilized for the application as biodegradable bone replacement material. The degradation rate can be tuned by the addition of phosphoric acid or other additives [151, 152]. MOC can exhibit four different phases, where the most common phase is the so-called phase 5: $5\ Mg(OH)_2 \cdot MgCl_2 \cdot 8\ H_2O$ (Table 3). Just two of the four phases are stable at room temperature (phase 3 and phase 5) and are worth to consider for an implant material [153, 154]. The setting reactions of those two phases are shown in eq. 2.10 and 2.11 [135, 151].

$$3\ MgO + MgCl_2 + 11\ H_2O \rightarrow 3\ Mg(OH)_2 \cdot MgCl_2 \cdot 8\ H_2O \quad (2.10)$$

$$5\ MgO + MgCl_2 + 13\ H_2O \rightarrow 5\ Mg(OH)_2 \cdot MgCl_2 \cdot 8\ H_2O \quad (2.11)$$

MOCs also form in a dissolution/precipitation reaction, similar to MPCs. Their setting time can be regulated by the calcination of the MgO reactant powder. A higher calcination temperature leads to an inactivation of MgO and hence longer setting times [155]. During setting MOCs form thin needles that are interlocking, in addition the needles grow into pores and, therefore, reduce the porosity of the solid leading to high strength cementitious materials [156].

2.4.3 Mechanical properties

The mechanical properties of MPC and CPC are quite different, depending on numerous factors regarding processing and composition. However, both belong to ceramic materials and exhibit a typically brittle behavior. The brittleness is due to their inherent ionic structure, where primarily Mg^{2+} and Ca^{2+} ions form ionic bonds with phosphate ions. They exhibit high compressive strength but are prone to failure when loaded in bending mode. There is also only a low capacity for shear stressing, since the translational moving of the ionic lattice leads to repulsive forces within the lattice. The ionic repulsion causes a fast propagation of cracks and always leads to a catastrophic failure of the ceramic [157]. Usually, the compressive strengths that are obtained with CPC or MPC, are about ten-times higher than their bending strengths [76, 158]. Nevertheless, MPC and CPC have high strength when compared to other bone replacement materials based on polymers. The overall goal for an implant material is the simulation of human bone, not only in terms of composition but also with regard to the mechanical properties. This avoids severe problems such as stress-shielding, which is connected to the Young's modulus and often occurs for metal implants. If the Young's modulus of the implant material is much higher than that of bone, external forces are misled. As a consequence, bone tissue adapts to the new loading situation and starts to remodel. Since the implant material absorbs most forces, bone is excessively resorbed in regions of low forces. Due to this weakening, fractures can occur and a total implant failure can follow [159-162]. To avoid stress shielding, the Young's modulus of the implant material has to be considered. An overview of the mechanical performances of different synthetic materials and natural human bone is given in Table 5. Especially for the synthetic materials, there is always a range instead of absolute values. This can be ascribed to several issues. Firstly, the exact composition has a huge influence on mechanics. Setting retarders or accelerators can influence crystal growth and the crystal structure. Since the interlocking of crystals is the main effect on strength, this can alter the overall outcome [163]. A second parameter are additives like foreign ions, which regulate crystal growth and

cement setting, but also can substitute ions in the lattice. Crystallographic defects and dislocations can arise from this ion substitution [164], which subsequently has an impact on the crystal structure and the mechanics. Thirdly, the dissolution/precipitation reaction of low temperature CPC and MPC always requires a liquid phase that is quantified by the powder-to-liquid ratio (PLR). It could be shown that the PLR of those cements is directly associated with the porosity of the set cement [130]. The space between the crystals occupied by the liquid results in pores weakening the ceramic. Compressive strength as well as tensile strength decrease exponentially with increasing porosity [165, 166]. The same phenomenon could be found with the Young's modulus [167]. With the experimental findings in mind, this relationship can be expressed in eq. (2.12) [168, 169].

$$\sigma = \sigma_0 e^{-bP} \tag{2.12}$$

The strength σ depends exponentially on the porosity P. σ_0 is the strength without any porosity (P = 0) and b is an empirical constant. This relation results in a linear correlation between ln(σ) and porosity [74]. The weakening effect of pores within solids can be described with the fracture mechanics. The pores within the matrix act as bulk defects. Pores are the origin of small cracks that can easily propagate through the material. However, for the application as bone replacement material, a certain micro- and macroporosity is essential for bone ingrowth and implant fixation. The nutrient supply and vascularization also need pores within the scaffold for healthy tissue formation [10, 11, 16] (see Section 2.4.4). The design of an implant requires careful weighing of the mechanical performance demanding a low porosity and the biological functionality with a high porosity. Another aspect that has to be considered for an implant material is cyclic mechanical loading. The implant will be continuously stressed in daily life, which could entail fatigue of the material. Bone is a composite with much higher elasticity and less brittleness compared to CPC or MPC. Additionally, bone is self-renewing and self-healing meaning that occurring cracks or defects are defanged before huge damages develop. This issue has to be addressed when thinking of an application in load-bearing regions. Apart from the ultimate

strength of the material, the failure probability is of high importance in such applications. However, just a few studies considered this topic. The Weibull modulus belongs to the statistical theory of the Weibull distribution and is a parameter describing the failure probability of a brittle material under load. A narrow distribution of the ultimate strength, describes a high reliability and yields in high Weibull modulus values, which is favorable for an implant. Similar to the mechanical strength, the Weibull modulus is dependent on different parameters like the porosity. Barralet et al. found an increased Weibull modulus for decreasing porosities and for macropore-free cements. For HA ceramics, values between 1.6 – 18.2 with a porosity of 30 – 54 % are reported [12, 167, 170-172]. Sintered HA exhibits higher Weibull moduli of 3.0 – 7.6 with a lower porosity of 5.0 – 11.7 % [173, 174]. For brushite cements, Weibull moduli of 7.3 – 10.0 were measured for a porosity of 39 – 41 % [175]. Thus, CPC are similar to commonly used PMMA cements with a Weibull modulus of 7 – 14 [176]. The degradation behavior of the CPC and MPC are often neglected in the examination of mechanical properties. Especially fast degrading materials such as brushite or struvite rapidly loose mechanical performance after implantation. When the rate of bone formation is high enough, this effect can be compensated by new bone tissue. However, this often becomes a problem when diseases like osteoporosis are involved and the bone formation is impaired. Therefore, research focused on the improvement of bone replacement materials in terms of supporting bone formation.

Table 5: Mechanical properties of natural and synthetic materials.

Material	Compressive strength / MPa	Flexural strength / MPa	Youngs modulus / GPa	Density / g/cm^3	Ref.
Cortical bone	90 – 193	50 – 197	4.9 – 30	1.85 – 2.05	[27, 44, 177, 178]
Cancellous bone	0.2 – 13	1.2 – 20	0.01 – 0.90	0.4	[27, 44, 178, 179]
PMMA	65 – 100	25 – 50	2.7	-	[44, 180]
HA	300 – 900	9 – 300	80 – 120	3.1 – 3.155	[27, 44, 45, 161]
TCP	450 – 650	40 – 120	90 – 120	2.814 - 3.14	[44, 161]
Brushite	32 – 60	10	4.2	2.319	[16, 44, 76, 107]
Struvite	2 – 65	7.43 – 8.36	20 – 45	1.48 – 2.28	[129, 130, 134]
Newberyite	2 – 67	-	0.2	2.13	[136, 181-183]

2.4.4 Biological behavior *in vivo*

Beside the mechanical performance, the biological behavior of an implant material *in vivo* has to be considered. One of the most important factors is the degradation of the material together with its degradation products and dimensional changes. The degradation of CPC and MPC implants is strongly connected with their respective solubility (Figure 2).

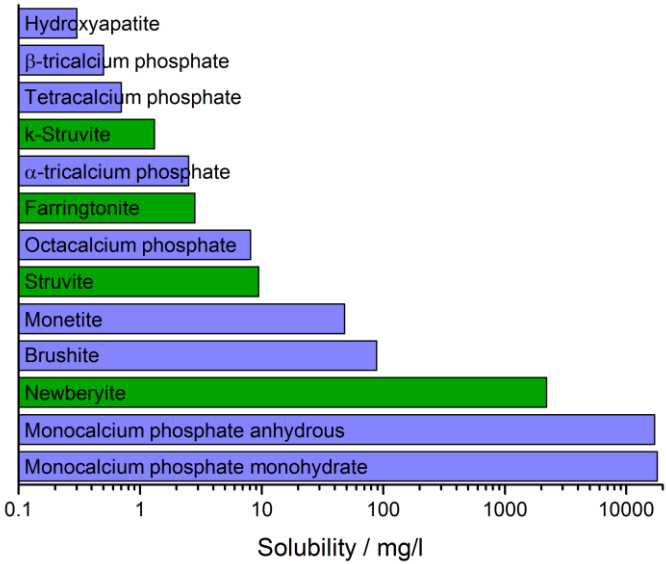

Figure 2: Solubility of different CPC (blue) and MPC (green) according to Table 2 and Table 3.

In general, there are two mechanisms for the resorption of a material *in vivo*: the active and the passive degradation. Resorption by passive degradation mechanism is based on the dissolution of the implant in the surrounding media. At an implantation site, materials are mainly in contact with blood and lymph with a pH around 7.4. In the case of CPC, the dissolution at this pH is quite different for the different formulations (see Figure 1). HA for example is the least soluble CPC and, therefore, hardly degrades via passive mechanism [184]. Since human bone has carbonated HA as main

inorganic phase, a low solubility is of great advantage. However, HA and other CPC and MPC with a low solubility at pH 7.4 can also be resorbed by the human body. The active degradation mechanism by osteoclasts as the bone resorbing cells is based on an increased solubility at lower pH. No matter if endogenous carbonated HA or any other CPC or MPC is resorbed, osteoclasts start their resorption work by the formation of a lacunae. This area is separated from the rest by tight podosomes. The osteoclast secretes a mixture of enzymes and hydrogen ions into the lacunae and decreases the pH locally. At this lower pH the solubility in general is higher leading to a degradation of the CPC or MPC. The degradation products, in the case of CPC and MPC mainly calcium, magnesium and phosphate ions, are processed by the osteoclasts and then secreted into the surrounding fluids [185, 186]. Both, the active and the passive degradation are influenced by numerous intrinsic and extrinsic factors. The natural regulators responsible for bone remodeling also influence the resorption of these biomaterials. For an implantation, the patients' background has to be kept in mind. Diseases like osteoporosis or other metabolic or hormone influencing disorders can alter the resorption behavior of the foreign material. Since the degradation is always connected with the ion release into surrounding fluids or tissue, the degradation products have to be thoroughly investigated. The natural ion concentration in human serum is 2.25 – 2.75 mM for Ca^{2+}, 0.7 – 0.9 mM for Mg^{2+} and 0.8 – 1.4 mM for PO_4^{3-} [187-190]. But not the whole ion amount of the biomaterial will be released into the serum. Bone can act as a storage of Mg^{2+} ions by incorporation of those ions into newly formed bone tissue. By this, bone helps to regulate ion balance (homeostasis) [191, 192]. Also the daily Mg^{2+} uptake (and excretion) should be considered, which is in the range of 265 mg/day to 420 mg/day for adults (depending on age and gender) [192, 193]. Thus hypermagnesemia [193, 194] will improbably happen due to implant degradation of MPC [144, 184]. Habibovic et al. summarized the daily uptake for calcium, magnesium and phosphate ions. The intake was given with 1000 – 4000 mg/day Ca^{2+}, 350 – 420 mg/day Mg^{2+} and 700 – 4000 mg/day PO_4^{3-} [190]. The ionic release of Ca^{2+} and PO_4^{3-} from degrading CPC varies strongly due to the large differences in solubility spanning several orders of magnitude (see Figure 2). In most

studies, *in vitro* experiments are performed in cell culture media (e.g. Dulbecco's Modified Eagle's Medium, DMEM), which contains 36.15 µM Ca^{2+}, 20.90 µM Mg^{2+} and 5.49 µM PO_4^{3-} [145] being far below the concentration found in human serum. Since an adsorption of Ca^{2+} ions was found in studies with CDHA, it can be assumed, that an *in vivo* implantation will also result in an ion adsorption. Even fast degrading cements like brushite or ion substituted cements do not exceed 2 mM Ca^{2+} release per day [184, 195, 196]. However, Liu et al. found an optimum Ca^{2+} concentration for *in vitro* cell proliferation and differentiation at 1.8 mM, which is close to the release during degradation [197]. In general, a highly increased Ca^{2+} concentration can have severe consequences known as hypercalcemia. Since Ca^{2+} is an important ion in the human body, the natural renal secretion system is designed to regulate ion concentrations and hence to secure a constant serum level avoiding hypercalcemia. The exact role of phosphate ions, however, is not fully clear, since there are numerous different phosphate containing species influencing (among others) mineralization, osteoclastic resorption and osteoblast differentiation [190]. Nevertheless, Meleti et al. investigated different concentrations of inorganic phosphate on cell viability. Cells become apoptotic when exposed to high phosphate concentrations (> 4 mM) [122, 197-199]. The release of phosphate ions from CPC and MPC strongly differs in literature. It was found in a range of 0.7 – 18 mM depending on cement composition, solubility and dissolution media [134, 144, 147, 195, 196]. On the other hand, in natural bone forming processes calcium and phosphate concentrations have to be raised by matrix vesicles in order to form new bone. Moreover, phosphate is essential for physiological processes like the initiation of bone formation pathways or collagen mineralization [200-203].

There are numerous factors influencing the degradation rate and the ion release of cements, but a decisive parameter is the porosity and the pore size. Regarding mechanical performance, a completely dense structure would be favorable. However, *in vivo* cells should invade into the implant structure to form new bone matrix and to anchor the implant at the desired site. Cell invasion and bone formation entail

diffusion processes for nutrition supply and the formation of blood vessels for a long-term vascularization of the tissue. The dissolution/precipitation reaction of the mineral bone cements *per se* causes a certain porosity, which can easily be adapted by the PLR. Additionally, porogens can be added to create different pore sizes. The porosity that is commonly achieved with PMMA cements is relatively low with 0 – 40 % and the material is bioinert [204]. In contrast, CPC and MPC can be fabricated with very high porosities of >90 % and interconnected pores [205]. During resorption processes, the porosity and pore sizes change and are not constant over time [206]. The pore sizes can be categorized in micro-, meso- and macropores, although there is no exact definition of the sizes and the terms are used for varying sizes. Undoubtedly, different sizes are required, since they fulfill different tasks in the regeneration (Table 6). It was found, that pores induce osteogenesis [11], which is probably due to several advantages, like the increased surface area. With a greater surface area, the amount of adsorbed proteins is higher, which is favorable for cell adhesion and bone ingrowth [160]. Additionally, pores and the interconnected structure are an ideal scaffold for (micro-)vascularization. The formation of blood vessels is one of the most decisive steps in formation and maintenance of cellular activity of new bone tissue [169, 207-209]. However, osteoconduction and osteoinduction are not able to induce the necessary vascularization [210]. To accelerate the formation of a blood vessel network, growth factors or other cytokines have to be introduced. The pores can be utilized for the incorporation of such drugs into the implantation site. A porous structure facilitates a constant and long-term release of those drugs compared to solid implants, where drugs can just be bound at the surface. The high surface area also enlarges the amount of drug loading [211].

Table 6: Pore sizes and function of different porosities [47, 93, 212-214].

Porosity	Pore size	Function
Microporosity	< 1 – 10 µm	Vascularization, capillaries, cell-matrix interaction
Mesoporosity	1 – 100 µm	Drug loading, cell-matrix interaction
Macroporosity	> 100 µm	Cellular colonization, diffusion, oxygen and nutrition supply

Since the degradation rate of the different CPC and MPC vary strongly, the resorption speed has to be adapted. The implant should be replaced by newly formed bone tissue to maintain mechanical performance and to guarantee a full replacement. Thus, the degradation speed has to match new bone formation. Just a few studies are available quantifying the degradation rate of CPC, e.g. the degradation rate of brushite is about 250 µm/week [215] and of HA about 14.63 µm/week [216]. In contrast, the human bone formation speed is about 7 – 175 µm/week, which is often expressed as the mineral apposition rate [30, 217]. Possible discrepancies have to be overcome to avoid implant loosening. By the addition of ions, polymers or other additives, the degradation rate can be altered. As a result, the degradation rate should be determined for each cement system before taking an *in vivo* study into account. Another aspect during evaluation of a cement system is the choice of the species for an animal study, since the mineral apposition rate can differ from that of humans. For pigs, the mineral apposition rate is 8.4 – 10.5 µm/week, for dogs 10.5 – 14 µm/week [217]. This aspect influences the outcome of the study in terms of bone ingrowth, implant fixation and implant replacement by new bone.

2.5 Processing of mineral bone cements

The mineral bone cements CPC and MPC are designed as bone replacement material *in vivo*. Beside the composition of the material, the fabrication of the implant itself has a decisive influence on the clinical outcome. Sintered ceramics have to be

fabricated prior to implantation, which limits the shape adaption and accuracy. The dissolution/precipitation reaction of mineral bone cements opens a new field of application techniques, like 3D printing, improving the overall implant performance.

2.5.1 Conventional fabrication techniques

The fabrication of monoliths similar to sintered ceramics can also be performed with a dissolution/precipitation reaction. A huge disadvantage of monoliths is the extremely low porosity. However, they can be further modified for example to build up foams with pores ranging from micro to macro scale. Porogens or particles can be added to the cement paste to form pores during dissolution, subsequent burning or chemical reaction [16, 218-220]. The replica technique can also be used to build a ceramic foam. A polymeric foam matrix (e.g. polyurethane) is employed to form the ceramic foam [221, 222]. All of these methods are able to exactly design porosity, pore sizes or pore size distribution to mimic cancellous bone and facilitate bone ingrowth [223]. It should not be dismissed that the high porosity of foams entails weak mechanical strength (see Section 2.4.3). Additional supporting implants like metal plates and screws are required to maintain the mechanical function of the bone. In general, the outer size and the shape of such prefabricated cements can be altered. Granules and nanoparticles are often used in dental applications [224, 225]. Their granular shape favors the adaption to the defect shape. *In vivo* studies already showed, that the intergranular spaces favor angiogenesis, cellular invasion and bone ingrowth [226, 227]. However, small particles or granules tend to agglomerate counteracting their functionality [228]. Furthermore, composites and combinations with already established materials like metals expand the portfolio of bioceramic applications. Metal implants are ideal replacement materials for load-bearing regions, but are inert regarding bone ingrowth [148]. The equipment with a ceramic coating supports bone ingrowth and, therefore, implant fixation [229]. Additionally, the coating reduces friction and the subsequent adverse release of metal ions into surrounding tissue [230, 231]. However, the easiest way for such a cement is a manual molding of the paste *in*

vivo. Solid and liquid phase are poured together, mixed with a spatula until a homogeneous paste forms. This paste can be transferred to the defect site and adapted to the defect shape. Since the setting reaction takes some minutes, there is enough time for molding before the cement sets at the defect site. Additionally, additives for setting acceleration or retardation can be employed for a better handling. The great advantage is the *in situ* adaption to the required shape and a strong bonding to the neighboring bone, as crystals can grow towards the bone faces. However, this technique requires some experience in handling of the cement paste and the mixing procedure. The setting times are restricted to ensure an early loadability, which also restricts the time frame for the implantation. The manual application of the cement paste also requires a relatively large opening and entails a large surgical wound. To minimize the risk of infections, scars and pain, minimally invasive surgery techniques were invented that utilize injectable materials. The cement pastes of mineral bone cements had to be modified to fulfill the requirements of injectability. The huge problem of injecting a cement paste is the so-called filter-pressing effect. By injection through a needle, solid particles separate from the liquid phase resulting in an inhomogeneous, highly liquid phase [232]. Apart from the separation of the two phases, the composition of the paste is endangered leading to non-predictable setting time as well as mechanical and biological behavior [233]. Numerous studies were performed to improve the injectability and reduce filter-pressing. Among others, factors like particle size, distribution and shape can be adapted [234-239] as well as additives can be added [240-244]. Another very powerful tool is the decrease of PLR [129, 232] and the increase of the viscosity of the liquid phase [245, 246]. All of these factors lead to a lower flow rate of the liquid phase through the powder particles and inhibit phase separation.

2.5.2 Additive manufacturing techniques

Beside the conventional application techniques, additive manufacturing (AM) expands and already covers the field of bioceramics. This field has been continuously

growing in the last few decades, since patient specific treatments gain more and more interest in medicine. The different AM techniques are known under several names in literature including combinations and overlapping of those techniques. Some of the most important AM techniques are presented in this section and in Table 7 with the focus on mineral bone cements. The accuracy and layer thickness of the different techniques was reviewed for biomedical applications. For technical constructs, the accuracy and layer thickness can be lowered to the micrometer scale [247]. All techniques have in common the fabrication of a three-dimensional construct based on a computer-aided design. In the biomedical field, data from individual patients are used, e.g. from a computed tomography (CT) scan, or 3D construction and converted into a processible file format. The file slices the three-dimensional object to enable a layer by layer fabrication.

Table 7: Summary of different AM techniques with the respective printing accuracy as well as advantages and drawbacks of the method.

AM technique	Accuracy	Layer thickness	Advantages	Disadvantages	Ref.
Stereolithography	10 – 50 µm	25 – 250 µm	High accuracy	Photopolymer required In some cases support structures necessary Post-curing	[223, 248-251]
Selective laser sintering	150 – 250 µm	80 – 100 µm	No support structures No post-processing Solvent free	High temperatures Powder incorporation in closed architectures	[249, 252-256]
3D Plotting	200 – 610 µm [1]	40 – 1000 µm	Several slurries can be printed Addition of drugs and cells	Support structures Complex geometries are difficult Accuracy limited by strand thickness	[249, 257, 258]
3D powder printing	100 – 500 µm	20 – 200 µm	No support structures Addition of drugs	Post-processing (in some cases) Powder incorporation in closed architectures	[134, 256, 257]

[1] strand thickness

Stereolithography

Stereolithography is an AM technique originating in the fabrication of polymeric components. The typical layer thickness that is used to fabricate the sliced object is typically in the range of 25 – 200 µm [223, 248]. The final part is printed line by line and layer by layer with a laser scanning the layer surface. For stereolithography, a resin is employed that can be locally cured with this laser by a photopolymerization reaction. The thin layers ensure an adhesion between the previously printed layer. The accuracy of this technique is very high with 10 – 50 µm depending on the system and material systems [248, 250, 251]. After the printing process, the excess of resin has to be removed by washing with a suitable organic solvent. Since curing of the resin is in most cases incomplete, a post-curing step is necessary to reach adequate mechanical performance. The resin can also be supplemented with bioceramic particles to form a composite material [259]. After printing, these parts can be sintered to remove the resin and to solidify the ceramic [260, 261]. However, the polymeric component has to fulfill some requirements to be fabricated in stereolithography. One of those requirements is that the resin has to fill the gap when the platform moves after each layer. Therefore, the viscosity of the resin or the resin-bioceramic-composite has to be below 3 Pa·s [262].

Selective laser sintering

Selective laser sintering is a powder based technique, where no additives are required. A powder bed of loose particles is solidified by local melting and subsequent cooling according to the sliced data. After solidification, the next powder layer is spread on top the previous one. The thickness of the single layers is dependent on the powder (e.g. particle size distribution) and ranges between 80 – 100 µm [254, 255]. The energy for the melting of powder particles is provided by a laser beam scanning the powder surface. The accuracy of this process is 150 – 250 µm [252, 253] and several influencing factors like laser focusing or thermal conductivity of the particles. Since the printed part is surrounded by loose powder particles after the printing process, no

support structures are required for overhanging parts. If the powder is directly fused by the laser, a removal of loose powder particles is sufficient as post-processing step. The direct manufacturing of pure ceramic powder with selective laser sintering often requires a pre-heating of the powder due to the high melting point of the material. Nevertheless, the processing of such powders could be demonstrated in several studies [263-265]. However, an indirect method can be applied, where the powder is supplemented with a binder. Instead of melting the powder particles directly, the binder is melted by the laser irradiation, which fuses the particle. Subsequently, the green body has to be sintered to remove the binder and fuse the particles directly. This is done, if the powder particles cannot be fused by the laser due to a high melting point, as it is often found for ceramic particles. The binder can also be chosen to build up a biocompatible bioceramic composite with e.g. polyetheretherketone [266]. The high temperatures induced by the laser beam inhibit the direct modification with pharmaceutical additives like drugs or growth factors, which have to be added after printing or post-processing to ensure their efficacy.

3D Extrusion/plotting

The 3D plotting techniques, also known as robocasting or dispense plotting, use slurries that are extruded through a nozzle. Depending on the number of nozzles and reservoirs available, various different pastes can be extruded to build one construct [267]. Due to solidification of the extruded material, the next layer can be printed on top of the previous one. However, this requires support structures for overhanging parts and specific properties of the paste. The viscosity of the paste is a crucial parameter to enable the extrusion through a nozzle and a subsequent solidification. That means that the slurry has to have a low viscosity during extrusion, but a higher viscosity after deposition to form a solid base for the next layer. This change in viscosity is often achieved by shear thinning pastes or printing into a setting solution [258, 268, 269]. Elevated temperature can also be applied, e.g. for polymeric components, but is not necessarily required for the 3D plotting process [256]. To tune the viscosity of the paste, additives are often employed, although they are not always

advantageous in terms of biological and mechanical performance. Another challenge is the fusion of the solidified single layers to build a three-dimensional construct. The viscosity has to be high enough to ensure the stability and sustainability of the part, but simultaneously has to result in a connection between the layers / strands. Owing to the extruding process, continuous strands are printed. This results in most cases in a grid-like structure of the construct, although the outer shape can be adapted to a specific implant design. It is also possible to interrupt the extrusion to generate single paste droplets positioned one after another [270]. In recent years, the possibilities of 3D plotting especially in the biomedical field were extended. The development of nozzles positioned within each other, as it is already known from microfluidic systems, enabled the extrusion of core/shell strands [271] and, therefore, the encapsulation of e.g. pharmaceutical agents.

3D powder printing

The 3D powder printing (3DP) technique is also known under different names like binder jetting or ink jet printing. It uses loose powder particles that are fused via a binder sprayed on top of the powder layer. Similar to selective laser sintering, the powder layer is spread on top of the previously printed one. Since the layer thickness is about 20 – 200 µm, this requires a good spreadability of the powder, which can be tuned by the particle size and particle size distribution [134, 257, 272]. Reduction of the particle size on the one hand leads to a higher resolution for printing, but on the other hand enhances the risk of particle agglomeration. The best results could be obtained for particles with a medium size of 15 – 35 µm [7, 273]. After layer preparation, binder droplets from a cartridge are sprayed onto the powder bed to locally fuse the particles. Due to capillary forces and diffusion processes, the binder droplet expands within the powder, which restricts the resolution of the printing process [257]. The fusion can be due to either a physical gluing effect of polymeric components or a chemical reaction between powder and binder. In the first case the powder is supplemented or coated with a polymer that becomes sticky when in contact with the liquid (often water), for example cellulose [274-276]. The polymeric

component can also be applied by an organic binder [13, 277]. The second mechanism of particle binding can be achieved by a cement setting reaction as already described in Section 2.4.1 and 2.4.2 for CPC and MPC. The liquid phase is applied by the binder solution that is sprayed onto the reactant powder. The powder dissolves locally and precipitates as the product cement without temperature elevation [278]. This often leads to a 3D part, where post-processing like sintering is not required. Therefore, thermolabile drugs or growth factors can be incorporated in the cement matrix within the processing step [275]. In all cases, a depowdering of the printed sample has to be performed with compressed air to remove loose powder particles that surrounded the part during printing, whereas entrapped powder within the part cannot be removed after printing [279]. Depending on the exact process and the strength of the green body, post-processing steps can become necessary. This can be either a post-hardening by immersion of the parts in the binder solution or a subsequent sintering to remove organic components and densify the printed part [280]. The great advantage of 3DP is the local introduction of different binder solutions when a multi-color printer is used. This facilitates the application of drugs and growth factors as mentioned before [256, 281]. To date, numerous studies investigated the fabrication and properties of 3DP implants made of CPC, MPC or composites of those cements with different materials. This covers fundamental analysis of the printing process and the powder solidification as well as the manufacturing of patient-specific implants [8, 272, 273, 282-287].

2.6 Optimization of mechanical properties

Independent of manufacturing technique, the mechanical properties of CPC and MPC are crucial features, when thinking of the application as bone replacement material. As already described in Section 2.4.3, pure bone cements exhibit a very brittle behavior. This restricts their application to non-load bearing defect sites. However, there is a great need for bone replacement in load bearing bones like the femur or tibia. Due to the significant drawbacks of commonly used bone replacement materials (e.g.

stress-shielding metals or non-degradable PMMA), research has to focus on the improvement of the mechanical properties. Two major strategies are under investigation exhibiting a great potential for this improvement as well as applicability in terms of fabrication and biological behavior. On the one hand, reinforcement with biocompatible fibers can be an appropriate candidate, as it is already established in the field of cements used for civil engineering or building industry [288]. Another possibility is the combination with a second, organic phase that sets simultaneously to the cement reaction (dual setting systems). Both strategies will be described in more detail hereafter.

2.6.1 Fiber reinforcement

The reinforcement of CPC and MPC by the addition of fibers aims to compensate the brittle character of the ceramic matrices. In general, the fibers can be introduced by almost every fabrication technique (e.g. molding, injection, AM), although each technique has its limitations. The reinforcing mechanisms behind a combination of a ceramic with fibers are based on several effects such as an enlarged energy absorption, higher mechanical strength and higher ductility of the composite material. Among others, they include interface debonding, frictional sliding (also known as fiber pull-out), fiber bridging and crack deflection. In all of these cases, the interface between fiber and matrix plays a decisive role. The connection of the fiber surface to the surrounding material can be established either by physical or chemical interaction. The physical interactions can be tuned by e.g. fiber surface roughness or morphology adaption. The fiber surface can also be modified with functional groups to create a chemical bonding to the matrix [9]. After interface debonding, the fibers are pulled out of the matrix resulting in frictional sliding and energy dissipation [289]. Therefore, the fibers (with the length of l) have to exceed a critical length to provide a sufficient surface area for these interactions. This critical fiber length l_c can be calculated on the basis of the fiber strength σ_f and shear stress on the surface τ [9, 290].

$$\sigma_f = \int_0^{l/2} \frac{4}{d} \cdot \tau \cdot dx = 2\frac{l}{d}\tau$$
$$l_c = \frac{d \cdot \sigma_f}{2 \cdot \tau} \tag{2.13}$$

It has to be considered that this equation is a simplified model containing several assumptions: (i) planar crack surfaces, (ii) negligible matrix deformation, (iii) isotropic fiber distribution, (iv) straight and cylindrical fibers, (v) linear elastic behavior of fibers, (vi) fiber rupture after exceeding the ultimate fiber strength, (vii) negligible Poisson effect and (viii) frictional interfacial bond [291]. It becomes obvious from eq. (2.13), that not just the length of the fiber, but also the diameter *d* accounts for the bonding effect. As a whole, the aspect ratio (*l*/*d*) is the influencing parameter, for which a high value is favorable. Another factor is the shear stress occurring at the interface. With a good fiber-matrix interface, the shear stress can be enhanced. This reduces the critical fiber length necessary for an equal overall result. Since some applications are limited in fiber length, like 1 mm maximum length for injection [292], tuning of the fiber surface is an essential tool. For an effective fiber pull-out with energy absorption, the fiber length has to be $\leq 2 \cdot l_c$ [291]. Aside the fiber surface area, the inherent fiber properties regarding defect distance also contribute to the excellent properties of the composite. Even if the fibers used for the reinforcement are of the same material as the matrix, there is a reinforcing effect. This can be attributed to the superior mechanical properties of fibers versus bulk material. Based on their geometrical shape, the defect distance is much higher for fibers than for the bulk. This becomes obvious when the defect distance l_D is calculated for both cases. Eq. 2.14 describes the general dependency of the defect volume V_D from the defect density ρ_D.

$$V_D = \frac{1}{\rho_D} \tag{2.14}$$

For a bulk material (indexed with *B*), the defect distance can be described with eq. 2.15.

$$l_{D,B} = {V_{D,B}}^{1/3} = \frac{1}{{\rho_{D,B}}^{1/3}} \tag{2.15}$$

In contrast, the defect distance of the fiber (indexed with *F*) of the diameter *d* is much greater (eq. 2.16).

$$V_{D,F} = \frac{d^2}{4} \cdot \pi \cdot l_{D,F} = \frac{1}{\rho_{D,F}}$$
$$l_{D,F} = \frac{4}{\pi \cdot d^2 \cdot \rho_{D,F}} \tag{2.16}$$

Since the defect density of a material can be assumed as constant, the defect distance increases with the square of the decreasing fiber diameter. This leads to better mechanical properties and reduced or delayed failure. A high aspect ratio is again favorable for enhanced mechanical properties of the composite. Fiber bridging is another effect that occurs as soon as the fiber exceeds a certain length. Crack opening uncovers the fiber, which is still anchoring in the matrix on both sides of the crack. This avoids a catastrophic failure of the brittle matrix and bridges the crack. A further opening of the crack is delayed and forces can still be borne by the composite. Crack deflection is a phenomenon occurring when additional phases like fibers or particles are introduced into a matrix material. A propagating crack encountering a fiber is deflected and travels a longer distance compared to the direct crack propagation. This enhances the energy consumption due to the formation of new and more surfaces. Crack deflection can be accompanied by interface debonding, also consuming further energy. Fiber bridging and crack deflection are the main mechanisms being responsible for the fracture toughness of human bone since bone is a natural composite of carbonated HA and collagen fibers [293-296]. In practice, several incidents occur, such that the resulting reinforcement differs from the theoretical considerations. These are for example the wettability of the fiber surface or in the case of CPC and MPC a reduced contact area due to pores [297]. As already mentioned earlier, both problems

can be faced by modifications. The fiber surface can be treated prior to incorporation into the matrix, e.g. via surface activation or functional groups [298-300]. Also the porosity can be adapted by the liquid phase, manufacturing technique or post-processing steps [71, 130].

Apart from the interaction between fiber and matrix, the fiber properties play also an important role for the whole composite. The fiber has to have a higher tensile strength than the matrix to lead to a reinforcing effect. Also the fiber volume fraction and the orientation within the matrix are important. On the basis of strength σ and Young's modulus E values of fiber (index f) and matrix (index m), a critical fiber volume fraction V_c can be estimated (eq. 2.17). Above this value, multiple cracking will occur being responsible for a high energy absorption. However, this equation is just valid for parallel aligned and not randomly distributed fibers [301].

$$V_c = \frac{\sigma_m}{\sigma_f + \left(1 - \frac{E_f}{E_m}\right) \cdot \sigma_m} \tag{2.17}$$

With increasing strength or decreasing Young's modulus, the critical fiber volume fraction can be reduced. Since a low fiber volume fraction facilitates handling and manufacturing, strong and ductile fibers are favorable. To date, numerous different fiber types regarding material, length or alignment are used for the reinforcement of biomedical ceramics. For the material, non-degradable and degradable fibers are distinguished depending on the aim of the composite. The fiber material itself can have an influence on the failure mechanism and, therefore, alter the mechanical performance of the composite [291]. Among others, non-degradable fibers are (multi-walled) carbon nanotubes [302-304], carbon fibers [305], polyamide [289, 305, 306]. Those fibers exhibit a high tensile strength (1.8 – 2.6 GPa for carbon fibers and 3.7 GPa for polyamide fibers) and a high Young's modulus (230 – 380 GPa for carbon fibers and 4.0 – 130 GPa for polyamide fibers) [297]. If a degradable composite is desired, polyesters like poly(lactic acid) (PLA) [307], poly(lactic-co-glycolic acid) (PLGA) [308-310] or poly-ε-caprolactone (PCL) [307] can be employed. Apart from

that, natural polymers (collagen [311, 312], chitosan [313]) or glass fibers [305, 314] can reinforce ceramic materials. Due to a higher defect distance in fibers, ceramic materials can be used to reinforce the same bulk material, especially in the form of whiskers [315-317]. Beside the extreme case of whiskers, huge differences in mechanical performance of short and long fiber reinforced cements could be observed. The great advantage of short fibers is their isotropic distribution all over the bulk material [9]. Keeping in mind the structure of natural bone, a certain anisotropy is favorable. In general, isotropic fiber distribution leads to an almost constant Young's modulus but a slightly increased strength, whereas anisotropic distribution decreased the Young's modulus and increased the composite strength [297]. Fiber bundles, meshes or fabrics can also be introduced into ceramic composites, e.g. as laminates, to further enhance the mechanical properties [318].

2.6.2 Dual setting systems

Another reinforcement strategy for mineral bone cements is the application of a dual setting system. The combination of a ceramic matrix interpenetrated by a polymer network mimicking natural bone. There, the main inorganic phase carbonated HA is reinforced by polymeric components such as collagen fibrils. To simulate such an interpenetrating network and make use of the mechanical advantages of such composites, a simultaneous reaction of the mineral bone cement and a polymer can be performed. Since a simultaneous reaction is difficult and depends on numerous factors, many approaches in the past used polymers with ceramic fillers [319, 320] or added non-reactive polymers to a cement matrix [311, 321-323]. In both cases, there is no interpenetration of the polymer within the cement matrix and the connection of the two phases is very weak. The great advantage of the interpenetrating networks obtained by simultaneously occurring cement setting and polymerization reaction is the enhanced failure resistance. Similar to fiber reinforcement, energy consuming effects like crack deflection occur leading to a better mechanical performance as implant material. Owing to the low Young's modulus of most polymers, the polymer

content in dual setting systems has to be much higher than for fiber reinforcement [324]. Similar to the cement setting reaction, also the polymerization can be performed at ambient temperatures. Thus the hybrid material does not harm surrounding tissue during reaction favoring cell survival and bone ingrowth. Different strategies can be pursued to gain a polymeric network within interlocking cement crystals. One approach utilized free Ca^{2+} ions from the CPC raw powder to form a chelate with polymer chains containing e.g. carboxylic or acrylic acid [325-328]. Although no study investigated the combination with MPC so far, a chelating effect with Mg^{2+} could be conceivable. The altered atomic radius can influence the bonding strength but a general complexation could be possible. Another polymeric reinforcement could be achieved by a polymerization within the setting cement slurry (Figure 3). Therefore, water soluble monomers are added to the solid or liquid phase of the cement system. By initiation of the polymerization, which is simultaneously started with the cement reaction, a continuous polymer phase forms within the spaces of cement particles/crystals. In most cases, hydrogel forming polymers are used. Due to the high water consumption of the hydrogel, both reactions compete for water. Secondly, the polymerization is often a radical one, as it is easy to handle and the initiators can be separated in solid and liquid phase prior to setting. Radical polymerizations are very fast compared to the cement reactions, which means that the polymer forms within the cement raw powder particles. If the water consumption of the hydrogel is too high, the cement setting will be retarded or in the worst case inhibited [329]. However, the fast polymerization can be advantageous regarding high initial strength. Especially slow setting HA cements (setting over several days) gain stability within minutes. Since bone remodeling is strongly dependent on external forces (Wolff's law) [37], a bone replacement material with early initial load-bearing capacity is favorable for healing processes and implant fixation. Reinforcement of HA can be realized with different polymer systems. The first attempts were performed by Dos Santos et al. with a polyacrylamide hydrogel in a HA matrix. The setting time could be regulated by polymer addition and the mechanical performance was improved [330-332]. Methacrylates can also be employed for the formation of the

hydrogel phase since the toxicity of acrylamide monomers could be a huge obstacle for clinical applications [333, 334]. Christel et al. used a system, where α-TCP reacted to HA with a simultaneous radical reaction of 2-hydroxyethyl methacrylate (HEMA) to the hydrogel poly-HEMA. HEMA could be added in a concentration of up to 70 % and the work-of-fracture could be enhanced by more than one order of magnitude [335]. In all those dual setting systems there are numerous influencing factors restricting variety of cements and polymers that are suitable for such a dual setting process. One of those factors is the environment of the cement setting reaction. HA is used as the product in most cases, since it sets under ambient pH conditions compared to brushite. Under such conditions, polymers can be integrated without the risk of cleavage or denaturation. However, the acidic setting reaction of brushite forming cements can be exploited for the formation of e.g. silica gel or silk fibroin [336, 337]. Other additives like ammonium phosphate as it is used for the preparation of struvite or setting accelerators or retarders can interact with or harm monomer components or the resulting polymer. But not just the cement components can influence the polymerization. Chelating polymer functionalities can easily lead to the retardation or inhibition of product formation of CPC or MPC (see Section 2.4.1). This weakens the matrix and, therefore, the whole composite material. Therefore, it is essential to tune the single components with respect to the cement setting reaction and polymerization yielding in a damage tolerant composite material.

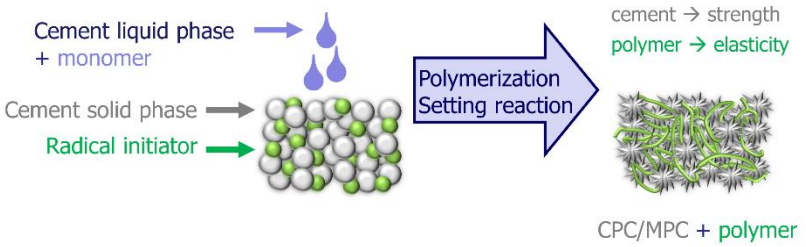

Figure 3: Principle of a dual setting system of a cement (CPC or MPC) with a radical polymerization. Both reactions (polymerization and cement setting reaction) occur simultaneously by mixing solid and liquid phase.

2.7 Optimization of biological properties

The application as implant material requires not only an optimized mechanical performance, but also an adequate biological response. As already mentioned above, the development of biomaterials started with pure cytocompatibility of inert materials and is now heading towards bioactive properties. The osteointegration should be forced to gain a fast implant fixation, bone ingrowth and replacement with native tissue. This effect can be achieved by tuning different parameters. A promising one seems to be the incorporation of foreign ions like Sr^{2+} into the raw materials. Additionally, infections arising during surgery or recovery should be combat at an initial stage to avoid a retarded healing process. Copper [338] and silver ions [339-341] are currently investigated, although a local treatment with drugs would be an effective method. Drug loading with a controlled release is becoming more and more popular as it provides e.g. antibiotics locally without an additional surgery.

2.7.1 Strontium-substitution

The substitution of CPC and MPC with foreign ions can alter the cement properties as well as the biological response of surrounding cells or tissue. This effect can be exploited to improve osteointegration of an implant. A very promising candidate for such a substitution are strontium ions (Sr^{2+}). Due to their chemical similarity to Ca^{2+} and Mg^{2+}, Sr^{2+} can occupy their position in the crystal lattice and thereby introduced to the site of interest. If Ca^{2+} with an ionic radius of 0.99 Å or Mg^{2+} with a radius of 0.69 Å is substituted by Sr^{2+} (ionic radius 1.13 Å) the crystal lattice will be expanded [18, 42, 190, 342]. The effect is concentration dependent but just measureable within the unit cell of the crystals. High substitutions of up to 80 at% were achieved for β-TCP without a rearrangement of the unit cell [343]. The properties of Sr-substituted CPC or MPC can be different. The solubility *in vivo* is enhanced in a Sr-substituted HA compared to pure HA [90]. This makes the new material interesting for a biodegradable implant together with the benefits of Sr^{2+} release. In the human body,

Sr^{2+} has a very high affinity to bone resulting in 99 % of Sr^{2+} being found in bone mineral [344]. Apart from substitution, strontium containing drugs or compounds are already approved by the Food and Drug Administration (FDA), and in clinical use. One example is strontium ranelate, which is used for the treatment of osteoporosis. The effect of such drugs is based on the action of Sr^{2+}, which can be transferred to the Sr-substituted cements. In general, Sr^{2+} has a similar effect *in vivo* due to its chemical similarity to Ca^{2+}. Therefore, new bone formation can be promoted by Sr^{2+} administration [18-24]. Even in natural bone remodeling, the importance of Sr^{2+} becomes obvious as newly formed bone contains $2.5 - 3$ times higher Sr^{2+} concentration than old bone [345]. On the cellular level, Sr^{2+} promotes the proliferation and differentiation of pre-osteoblasts, which could be verified by an enhanced expression of osteoblast genes and markers (collagen I, alkaline phosphatase (ALP), bone sialoprotein (BSP), osteocalcin (OC)). Therefore, the collagen I synthesis and bone mineralization are increased [346-349]. Additionally, bone resorption is reduced by a suppression of osteoclast differentiation and activation. The molecular basis of those effects is only partly understood until now and affects several pathways. The first pathway regards the calcium sensing receptor (CaSR), which can be activated by Ca^{2+}, but also other divalent cations like Sr^{2+} [350, 351]. The activation of CaSR triggers a cascade, where inositol 1,4,5-triphosphate is produced, Wnt, mitogen activated protein kinase (MAPK) signaling and phospholipase Cβ are activated and intracellular Ca^{2+} is released [352]. In the end, this leads to an enhanced osteoblast proliferation and osteoclast apoptosis. The osteoclast apoptosis was found to be potentiated by Sr^{2+} compared to only Ca^{2+} induced apoptosis [353]. Independent of the CaSR pathway, the extracellular signal-regulated kinase 1/2 (ERK1/2) phosphorylation can be activated by Sr^{2+}. The activation or ERK1/2 initiates the expression of cyclooxygenase-2 (COX-2) and prostaglandin E2 [345, 354]. Similar to CaSR, this pathway results in osteoblast proliferation and differentiation of pre-osteoblasts to mature osteoblasts. As a third mechanism osteoclastogenesis is inhibited by additional Sr^{2+}. The Sr^{2+} ions lead to an enhanced expression of OPG and a reduced release of RANKL [348, 355]. As already

described in Section 2.1, osteoclastogenesis is inhibited by the decoy receptor OPG, which binds to the receptor RANK and blocks the fusion of osteoclast progenitor cells [29]. The inhibition of osteoclastogenesis reduces the overall bone resorption. The pathways described are schematically summarized in Figure 4. These three pathways are probably only a small part of the physiological process triggered by an increased Sr^{2+} administration. However, the outcome of an increased bone formation, mass and density together with a reduced bone resorption make Sr^{2+} ions interesting for the support of osteointegrative bone cements.

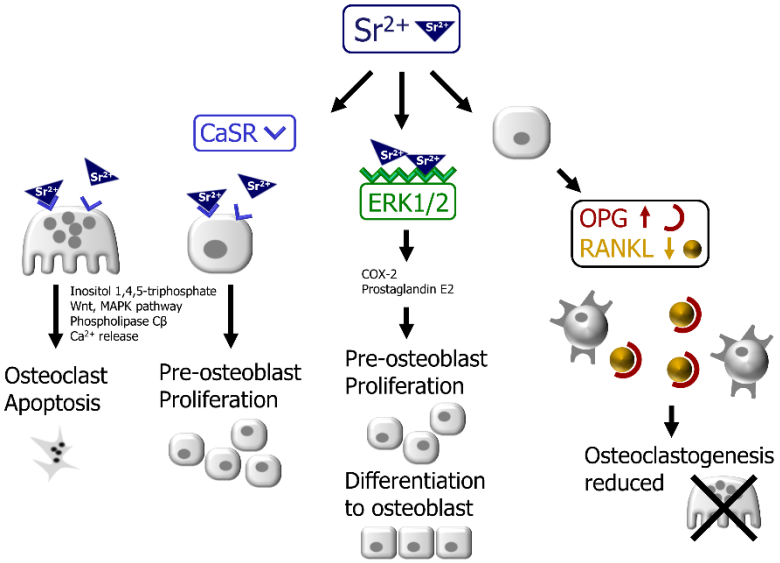

Figure 4: Scheme of the three main pathways triggered by Sr^{2+}. The calcium sensing receptor (CaSR) is activated by Sr^{2+} ions as well as the extracellular signal-regulated kinase 1/2 (ERK1/2) phosphorylation. Additionally an enhanced osteoprotegerin (OPG) expression and a reduced protein receptor activator of the nuclear factor κB ligand (RANKL) release can be observed. All these effects have an impact on osteoblasts and osteoclasts and lead to an enhanced bone formation and reduced bone resorption.

Numerous studies investigated the concentration dependency of Sr^{2+} doping or substitution for an effective dosage. The dose dependency on bone formation is commonly known, but the effective concentrations have a broad range. The

concentrations showing the best results in the different studies ranged from 0.2 – 87.6 ppm [346, 356-360]. However, this range covers concentrations exhibiting adverse effects in other studies. An excess dose of Sr^{2+} can cause hypocalcaemia due to replacement of Ca^{2+} in bone and, therefore, cause a reduced bone mineralization [361]. It is important to investigate different Sr^{2+} contents within the cement and to determine the exact Sr^{2+} release from the cement samples. Apart from the biological response, the addition of Sr^{2+} has another advantage for imaging in clinical practice. Still the most common diagnostic methods for bone analysis are x-ray based methods like CT. Since the composition of bone replacement cements is very similar to the mineral phase of natural bone, the position or degradation of the implant cannot be tracked easily. The radiopacity of bone and implant are too similar to be visually distinguished. By the addition of strontium or strontium compounds, the radiopacity can be enhanced [25, 26]. Therefore, a dual advantageous effect – enhanced bone formation and improvement in diagnostic visualization – could be achieved by Sr^{2+} substitution in CPC and MPC.

2.7.2 Drug delivery systems

Apart from the support of bone regeneration, the treatment of infected implants is getting more and more important. The best treatment is still to avoid a contamination of the implant site. However, aging population with multi-morbidity fuels the problem of implant infections. The systemic administration is the most common treatment including numerous side-effects and high doses. Research is heading toward a local application by so-called DDS. The implant material is equipped with a proteins or drugs like antibiotics, which are released over a period of time to fight infections. Mineral bone cements can also be used as DDS in various forms like blocks, coatings or additively manufactured implants. However, some basic release behaviors have to be considered for the design of DDS. In general, the drug concentration in the blood is observed. For each drug, there is a minimum effective concentration that has to be exceeded to exhibit the desired impact. Additionally, there is a minimum toxic

concentration, which becomes critical especially for high initial release. A single administration of common drugs usually leads to a rapid increase of the drug concentration in the blood. After the administration the human body starts to excrete the substances. This process is concentration dependent, i.e. if there is no depot or a second administration, the process will start fast and slow down over time [362, 363]. Finally, the concentration will fall below the minimum effective concentration. This is problematic especially for antibiotics since bacteria can get resistant when exposed to low concentration of antibiotic. The goal is a constant and concentration independent release of the drug to maintain the drug concentration in the blood over the desired time period. Such an ideal release is called controlled release and follows a zero order kinetic. The mathematical background for the zero order release describes a linear relation between the amount of drug released from the carrier system and the time of dissolution [364]. It can be represented by the linear equation (eq. 2.18):

$$Q_t = Q_0 + K_0 t \tag{2.18}$$

Q_t is the amount of drug dissolved in time t, Q_0 is the initial amount of drug in the dissolution media (in most cases Q_0=0) and K_0 is the zero order release constant. It can be seen, that the drug release is independent of drug concentration in the matrix and, therefore, independent of the concentration gradient between matrix and dissolution media [67, 365]. A generalized example of zero order release is illustrated in Figure 5. To fulfill a zero order release, a DDS has to be equipped with an excess of drug in the matrix to serve as a constant active source. In most cases, this can be just applied in the first stage. After a certain time, the system reaches a state of non-excessive drug source and the release becomes concentration dependent [67]. The release is then comparable to the excretion of the drug by the human body and follows a first order kinetic. Here, the linear relation between the drug still remaining in the matrix and the time can be drawn (eq. 2.19):

$$\frac{dC}{dt} = -K_1 c \tag{2.19}$$

C is the drug concentration, K_1 is the first-order release constant and c is the concentration gradient between the surface and the surrounding media. Eq. (2.19), also known as Noyes-Whitney equation [366], can be rearranged to eq. 2.20:

$$C = C_0 e^{-K_1 t} \quad \text{or} \quad \log C = \log C_0 - K_1 t/2.303 \tag{2.20}$$

with C_0 as the initial concentration of drug. An exemplary first order behavior is depicted in Figure 5. To obtain a linear correlation, such data are usually plotted as log cumulative percentage of drug remaining in the matrix versus time. The resulting slope corresponds to –K/2.303 [365].

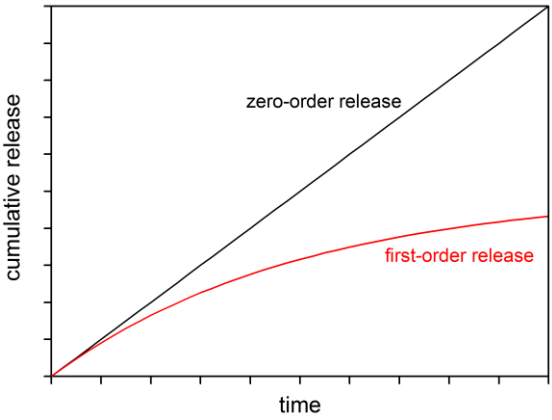

Figure 5: Schematic relationship between cumulative drug release and dissolution time for zero- and first-order release models. For zero-order model there is a linear correlation and for first-order model there is an exponential dependency.

Numerous DDS with various matrix materials and drugs have been developed to match these ideal release behavior. However, observation exhibited different release kinetics that required an adaption or a development of new kinetic models. A lot of drug release kinetic models are based on polymeric matrices. Obviously, polymers behave quite different in terms of swelling, degradation or drug loading and release than ceramics. Nevertheless, basic principles are valid for all materials based on principle laws like Fick's laws of diffusion. The models that will be described

hereafter are just theoretical considerations limited by more or less important factors depending on the individual system under investigation. Some models can just cover a certain state during release or draw restricting assumptions to satisfactory describe the mechanisms.

Power law

A semi-empirical but rather common description of release is the power law, often also called Korsmeyer-Peppas model (eq. 2.21).

$$\frac{M_t}{M_\infty} = Kt^n \tag{2.21}$$

M_t is the absolute cumulative amount of drug released at time t, M_∞ is the absolute cumulative amount of drug release at an infinite time point, K is a constant and n is the so-called release exponent. The constant K includes structural and geometrical parameters of the matrix. The release exponent n can be utilized to characterize the release mechanism of the system. Therefore, just 60 % ($M_t/M_\infty < 0.6$) of the overall drug release should be considered. Table 8 provides an overview of the possible release mechanisms derived from the release exponent [365]. Two special cases can occur: (a) If n = 1 eq. 2.21 becomes zero-order release (eq. 2.18) and the release gets independent of time [367]. (b) If the n = 0.5 the release is diffusion controlled and leads to the so-called Higuchi equation [368]. To obtain a linear correlation log cumulative percentage of drug released versus log time should be plotted [365].

Table 8: Release mechanism derived from the release exponent n of the powder law. Three different matrix geometries are regarded.

Thin film	Cylinder	Sphere	Release mechanism
0.5	0.45	0.43	Fickian diffusion (Higuchi)
0.5<n<1.0	0.45<n<089	0.43<n<0.85	Sub-diffusion (non-Fickian transport)
1.0	0.89	0.85	Zero-order release (Case-II transport)
>1.0	>0.89	>0.85	Super-diffusion (Super Case-II transport)

Super Case-II transport or super-diffusion is a non-linear correlation between the mean squared displacement (MSD) and time. In this anomalous transport the MSD increases with time. Sub-diffusion is the counterpart and an anomalous transport, in which MSD decreases with time. Examples for each diffusion mechanism for thin films is plotted in Figure 6.

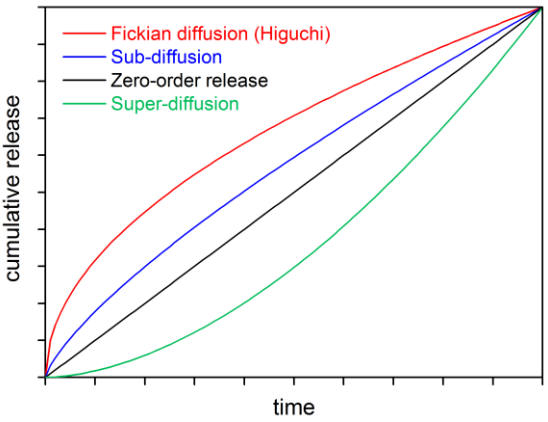

Figure 6: Different release kinetics for each release exponent (Table 8) as an example for thin films.

Higuchi model

The Higuchi model – in its simplified form – is a special case of the general power law with the release exponent n = 0.5 and is therefore based on Fickian diffusion (see Table 8 and Figure 6). Similar to the power law, this model should be applied for up to 60 % of the drug release [369]. Higuchi made some assumptions to maintain the validity of his model [368, 370]: (i) The matrix must not collapse during dissolution. (ii) No partial dissolution or swelling of the matrix occurs so that the geometrical dimensions remain constant during dissolution test. (iii) All of the drug must be equally available within the matrix, i.e. a homogenous distribution and a uniform accessibility of the drug has to be guaranteed. (iv) The release of the drug must be independent on location within the matrix, which means the release at the surface must be the same as in the bulk matrix. (v) The amount of drug loading must be greater

than the solubility in the medium by a factor of at least three, otherwise all of the drug would be solved with no solid drug remaining in the matrix. This assumption is the basis for the pseudo steady-state condition required for the calculation. (vi) Perfect sink conditions are required and have to be maintained during dissolution. (vii) Effects at edges of the matrix are not considered, since this model is based on one-dimensional diffusion. (viii) The drug particles are much smaller than the pores and the diffusion paths. With these assumptions the Higuchi equation for planar systems with a granular matrix can be expressed by eq. (2.22) [370].

$$Q_t = \sqrt{\frac{D\varepsilon}{\tau_t}(2C_0 - \varepsilon C_s)C_s t} \tag{2.22}$$

D is the diffusion coefficient of the drug, ε is the porosity of the matrix, τ_t is the tortuosity and C_s is the drug solubility in the surrounding media. From this equation it becomes obvious that if the porosity changes during drug release, the model suffers applicability [369]. By simplifying eq. (2.21) the square root dependency becomes even more apparent (eq. 2.23).

$$Q = K_H \sqrt{t} = K_H \, t^{0.5} \tag{2.23}$$

K_H is the Higuchi dissolution constant. To get a linear correlation for eq. (2.23) the cumulative percentage of drug release can be plotted versus square root of time. K_H can be determined by the slope of the straight line. Furthermore, Higuchi presented three models (diffusion layer model, interfacial barrier model and Danckwert's model) that describe the dissolution rate mechanisms from solids. These models can occur alone or in combination and are based on the research of Nernst, Wagner, Wurster and Taylor and other scientists [364, 371].

There are numerous models like Baker-Lonsdale, Hixson-Crowell, Weibull or Hopfenberg that can be applied according to the respective system and the assumptions that can or must be drawn. In the end, none of these models will represent

all the kinetic mechanisms behind a drug release process in reality. Additionally, the discrepancy of *in vitro* and *in vivo* behavior has to be taken into account. This includes also factors like drug, matrix and release, which are entangled. Porosity is one of those factors that will always occur for bioceramics due to the preparation. This porosity can be used to introduce drug molecules and simultaneously serves as release path. Surrounding dissolution media or body fluids can invade open porous structures and start diffusion processes for drug liberation. It could be shown that the particle size influenced both the porosity and the tortuosity and, therefore, the drug release [372, 373]. The tortuosity τ_t of a porous sample can be described by the real diffusion path Δl of a particle per unit length Δx (Figure 7).

$$\tau_t = \frac{\Delta l}{\Delta x} \tag{2.24}$$

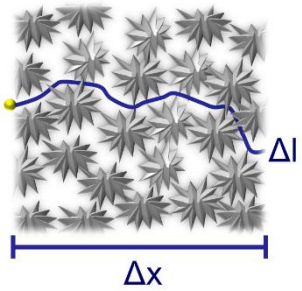

Figure 7: Schematic relationship between diffusion length Δl and the unit length Δx. The ratio of those values describes the tortuosity.

To determine this tortuosity, there are theoretical, experimental (helium pycnometry, mercury intrusion, x-ray microscopy, electrical conductivity, scanning and transmission electron microscopy [374-380]) and empirical (numerical simulations [381]) approaches. Independent on the way of determination, the tortuosity is needed to adapt the diffusion coefficient d_m to larger diffusion paths (eq. 2.25).

$$d'_m = \frac{d_m}{{\tau_t}^2} \tag{2.25}$$

Another influencing factor is a possible interaction between the matrix or an additive and the drug [382]. Desai et al. described the influence of sodium chloride on sodium salicylate. In contrast, potassium chloride showed no impact on the release rate [372]. Chemical interactions like chelation are very likely to occur in CPC or MPC since Ca^{2+} and Mg^{2+} can serve as the central atom. But drugs can also influence matrix properties (e.g. mechanical strength) by interaction with ions or alteration of the porosity. The formation for example of chelation complexes can lead to an altered paste viscosity, setting reaction with smaller crystals and mechanical properties [182]. This again has an impact on processability or injectability of the paste. Moreover, the drug can modify the pH value. Since the dissolution-precipitation process of cement formation is highly dependent on the pH, the product can be changed completely. It can also be the other way round. During dissolution-precipitation, the pH value of the paste changes, which can have an influence on drug solubility or even on drug stability. During degradation of bioceramics, different ions are released into surrounding media. Those ions can again interact with the drug or alter the pH. The specific surface area, which is strongly connected to the porosity, can influence not only drug loading capacity but also the drug release. Qu et al. found a direct correlation between an increase in surface area and an enhanced amount drug adsorption [69]. It is also possible that the surface area changes during degradation or drug release altering again the release rate or even kinetic.

3. Fiber reinforcement during 3D printing

This section was already published as communication in the journal "Materials Letters" in 2015:

Susanne Christ, Martin Schnabel, Elke Vorndran, Jürgen Groll, Uwe Gbureck, Fiber reinforcement during 3D printing, Materials Letters 139 (2015) 165-168.

The experimental procedure as well as the writing of the initial manuscript were performed by Susanne Meininger (née Christ). M. Schnabel and E. Vorndran did some preliminary experiments on the topic (which are not part of the manuscript), whilst J. Groll and U. Gbureck were involved in supervision, submission and proof-reading. For this thesis, figures were adapted due to uniformity of this work.

Abstract

Three-dimensional (3D) printing is an attractive rapid prototyping technology for the fabrication of 3D structures by the localized deposition of a reactive binder liquid onto thin powder layers in predominantly technical applications. A practical limitation is often the low green strength of printed samples, which can lead to a collapse of large and fragile structures during removal from the powder bed and the following depowdering procedure. Fiber reinforcement may improve green mechanical properties of printed samples, which was investigated in this study using a range of different short fibers added to a matrix of cellulose-modified gypsum powder. Mechanical testing of printed samples revealed a bending strength increase of 180 % and up to 10 times higher work of fracture values compared to non-reinforced printed samples.

3.1 Introduction

Three-dimensional powder printing (3DP) is used to create 3D structures of complex shape by localized application of binder into a powder bed [175]. The great advantage of 3DP is an accurate control of the complex structure and a setting at room temperature. Hardening of the structures occurs by either using organic binders, which partially dissolve in contact with printing liquid and bind particles together after drying [277] or hardening can be achieved by using reactive powders showing a hydraulic setting reaction [278]. A practical limitation of 3D printing is the relatively low initial green sample strength, which can lead to a collapse of large structures during removal from the powder bed and the following depowdering procedure [383].

This study aimed at increasing the green strength of 3D printed parts by using a fiber reinforcement approach similar to mineral bone cements [9, 308, 384, 385]. The major challenge for such an approach in 3D printing is the requirement to obtain smooth powder layers (100–200 mm thickness) within the printer. This likely restricts the fiber length and the fiber volume ratio within the powder; in this study we investigated the effect of adding 1 % short fibers with a maximum length of 1–2 mm to a matrix of cellulose-modified gypsum powder. The fiber length was limited by the printing process, as the addition of longer fibers prohibited the preparation of thin and smooth powder layers during printing. Nevertheless, the fiber length was likely above the critical length according to literature for fiber-reinforced ceramic matrix composites [386]. The mechanical properties were determined using a four-point bending test regime in both x and y printing direction, as it is known from previous studies that 3D printing will cause anisotropic mechanical performance of the samples [175].

3.2 Materials & Methods

3D printing of samples was performed on a ZPrinter 310 (ZCorporation, USA) with a layer thickness of 0.1 mm and a binder volume saturation of 100 %. The powder for

printing was prepared by mixing commercially available dental gypsum (GC Fujirock EP, Belgium) with 5 % (hydroxypropyl)methylcellulose (HPMC, Fluka, St. Louis, USA) in a ploughshare mixer (M5R, Lödige, Paderborn, Germany) for 10 min. For reinforcement four different commercially available fibers were tested: polyacrylonitrile fiber fillers (PAN), polyacrylonitrile short cut fiber (PAN-sc), polyamide fiber fillers (PA) and alkali resistant zirconium silicate glass short cut fiber (glass fiber; Heinrich Kautzmann, Germany). All fibers were separated by sieving through a 1 mm mesh size sieve before mixing with the powder for 10 min at a fiber content of 1 %. Samples for bending tests (5 mm x 4 mm x 45 mm) were printed in two different orientations as shown in Figure 8 and incubated for 20 h in water saturated atmosphere. Printing with z orientation was not performed because samples (with or without fiber addition) were not stable enough to be removed from building chamber. Half of the samples were further infiltrated with a self-setting polyurethane resin (Axson technologies, Germany) for additional reinforcement. Mechanical properties were tested by four point bending test with n = 10 using a static mechanical testing device Zwick/Roell Z010 (Zwick GmbH&Co.KG, Ulm, Germany). The 2.5 kN load cell was employed for measurements at a constant cross head speed of 1 mm/min and a pre-load of 0.1 N. To calculate the work of fracture (wof) mechanical testing was stopped when sample was fractured or at a maximum displacement of 3 %. Density measurements were performed by Mohr-Westphal balance based on Archimedean principle using the device Kern ABT 100-5M (Kern & Sohn GmbH, Germany) (n = 3). Porosity characteristics such as pore size distribution and total porosity were measured by mercury (Hg) porosimetry (PASCAL 140/440, Porotec GmbH, Germany) with n = 1. Furthermore, fracture surfaces were examined by scanning electron microscopy (SEM) with a Digital Scanning Microscope DSM 940 (Zeiss, Germany) at an accelerating voltage of 5 kV. Statistical calculations were performed with ANOVA using the software SigmaPlot 12.5 (Systat Software, Inc., 2011).

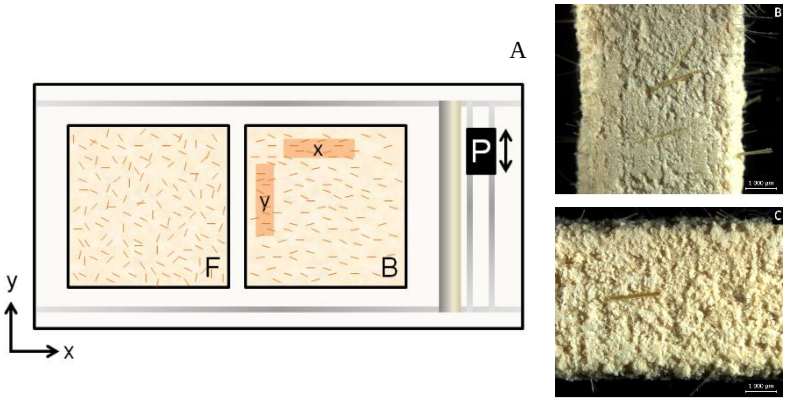

Figure 8: Schematic top view of 3D printing (A). Feed chamber (F) and build chamber (B) are localized in x-y-plane. Samples are labeled with x and y according to their orientation in the building chamber. The print head (P) moves across the building chamber in x-direction where binder is sprayed in y-direction (see arrow next to P). Figure B (y-orientation) and C (x-orientation) show predominant fiber orientation within the samples.

3.3 Results

Samples for bending test were printed in two different orientations (Figure 8) to investigate the influence of fiber orientation within the sample and the influence of binder application due to print head movement. The results for flexural strength showed significantly increased values (up to 180 %) for most of the samples (Figure 9A) with only the flexural strength of PA fibers printed in y direction being comparable to the reference. Regarding standard deviation there was no difference between printing orientations concerning flexural strength; wof calculated by the area underneath stress–strain curves recorded during bending test and the cross sectional area of the sample (Figure 9B) showed a similar behavior like flexural strength. Apart from PA-reinforced samples, wof was also independent of printing orientation and a total increase of up to one order of magnitude could be obtained. Polyurethane infiltration of the samples increased both flexural strength (Figure 9C) as well as wof (Figure 9D) by 10- to 20-fold. After this treatment, however, fiber-reinforced samples showed no significantly higher values compared to unreinforced samples.

Furthermore, fiber content for PAN-reinforced gypsum was optimized with respect to mechanical properties (Figure 9E). Flexural strength could be further increased to more than 400 % with a fiber content of 1.5 % and decreased slightly until 2.5 %. A higher fiber content was not printable.

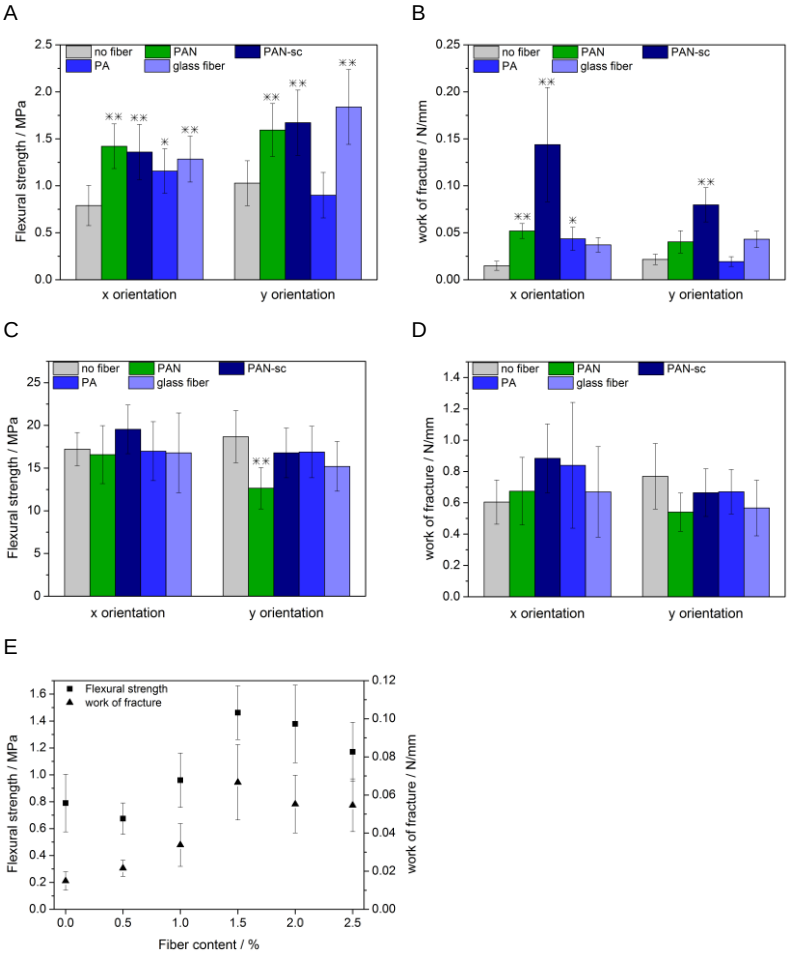

Figure 9: Flexural strength (A) and wof (B) of fiber-reinforced samples printed in x and y direction. (C) Flexural strength and (D) wof of polyurethane infiltrated samples. Fiber content was optimized for PAN in x direction (E). Highly significant ($p < 0.01$) and significant ($p < 0.05$) samples are labelled with ** and *.

Table 9: Porosity and density of fiber-reinforced gypsum was measured with mercury porosimetry and Mohr-Westphal balance, respectively.

Fiber	Porosity (%)	Apparent density (means ± SD) (g/cm³)	Bulk density (means ± SD) (g/cm³)
No fiber	62.35	1.078 ± 0.010	2.10 ± 0.04
PAN	56.10	1.021 ± 0.002	1.95 ± 0.14
PAN-sc	59.10	1.089 ± 0.009	2.27 ± 0.06
PA	58.89	1.030 ± 0.004	2.13 ± 0.04
Glass fiber	57.82	1.060 ± 0.010	2.12 ± 0.01

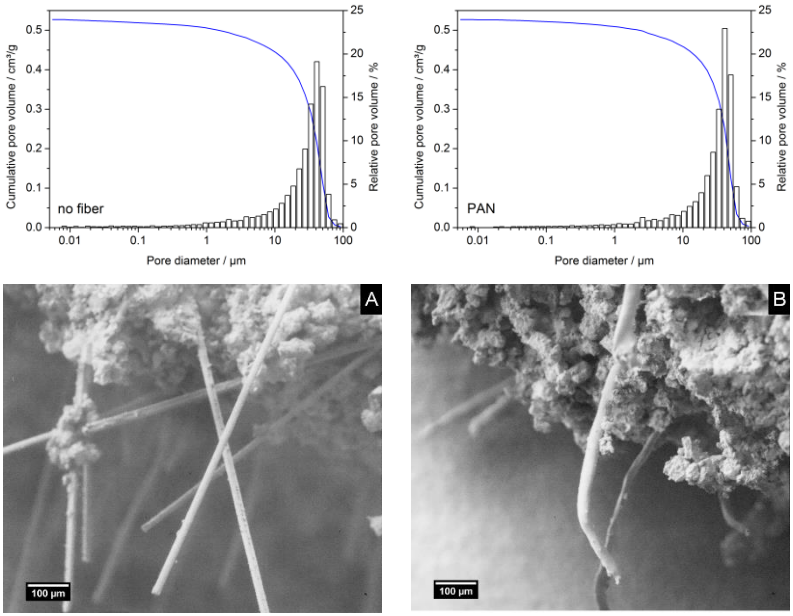

Figure 10: Pore size distribution for gypsum without fibers and PAN-reinforced samples. SEM images (5 kV and 100 times magnification) show gypsum samples reinforced with PAN-sc (A) and PA (B), respectively.

Density and porosity of the composites can have a great influence on mechanical properties. The density, however, was not affected by fiber reinforcement (Table 9). In contrast, porosity of the samples decreased if samples were reinforced (Table 9), but fiber material had no significant effect on porosity and pore size distribution

(Figure 10). Furthermore, fracture surfaces (Figure 10) showed fiber pull out as well as matrix residues on the fiber surfaces. PAN and PA fibers seemed to be deformed, whereas PAN-sc and glass fibers remained intact.

3.4 Discussion

Examination of mechanical properties by four-point bending test revealed higher flexural strengths and wof for reinforced samples (Figure 9), indicating a transfer of mechanical load from matrix into the fiber as well as energy dissipation by frictional forces during fiber pull out [387] resulting in higher strains of the composite. The highest wof values were found for PAN-sc due to its length of 2 mm and therefore its higher surface. Taking into account results of Castilho et al. [175], it can be assumed that orientation of printed fiber-reinforced samples could have an influence on mechanical properties. However, for both flexural strength and wof, there was no difference between printing orientations when samples were fiber reinforced. Due to binder application initial strength of x orientated samples was lower than for y orientated ones. This binder effect was compensated as fibers are predominantly aligned in x direction such that the reinforcement for x orientation is enhanced compared to (initially stronger) samples printed in y direction. Polyurethane infiltration increased mechanical properties enormously but at the same time eliminated the influence of fiber reinforcement. This indicates for this system that polymeric post-hardening has a greater influence on mechanical properties than fiber reinforcement.

Further investigation concerned density and porosity of the reinforced samples (Table 9). Density of all samples did not vary with different fibers. As density of PAN, PAN-sc, and PA is much lower than that of the gypsum mixture (around 1.2 g/cm³), a lower overall density could be expected. However, composite density was not affected due to a low fiber content of 1 %. In contrast, porosity could be decreased by fiber addition from 62 % (no fiber) to a minimum of 56 %. These values are in accordance with printed samples found in literature [213, 249, 388].

Reduced porosity could also have contributed to better mechanical properties such as flexural strength.

The fiber–matrix interface (Figure 10) shows matrix residues on all fiber surfaces indicating good adhesion between fiber and gypsum matrix. Furthermore, fiber pull out can be confirmed, which is typical for polymeric fibers in ceramic matrices [387]. As fiber pull out and interface debonding are the main mechanisms of energy absorption [9], the high wof can be associated with the findings of SEM images. Prior to fiber pull out, fiber bridging of the opening crack leads to a higher deformation of the composite resulting again in a higher wof [9]. Moreover, PAN and PA fibers seem to be deformed, which can be ascribed to the manufacturing process of fiber fillers by grinding. Thus, no fiber fracture could be observed independent of fiber material and length.

3.5 Conclusion

We were able to introduce fiber reinforcement in 3D powder printing for the first time to improve green strength of complex samples. Despite a fiber length being one order of magnitude higher than the powder layer thickness during printing, fabrication quality of samples could be maintained during printing up to a fiber content of 2.5 %. This study focused on materials (fibers and matrix) predominantly used in technical applications to demonstrate the principal reinforcement mechanism during 3D printing. A transfer of the results to biomedical applications, such as hard tissue replacement, would clearly require the use of biocompatible and biodegradable fibers such as polylactic-co-glycolic acid as demonstrated before for fiber-reinforced mineral biocements [389].

4. Fabrication of segmental bone implant with rotationally symmetric negative forms

4.1 Introduction

The diversity of manufacturing techniques for CPC and MPC are already described in Section 2.5. The trend is heading towards the fabrication of patient-specific implants using novel technologies partially borrowed from technical or industrial applications. Centrifugally casting is one of those technologies already established in construction industries, where it is employed for the fabrication of concrete drainpipes [5, 6]. Since human long bones have a tubular structure, the transfer of this technique to the biomedical field is self-evident. The centrifugation, however, can alter the cement setting reaction and properties, as a phase separation of the slurry is likely to occur. On the other hand, the centrifugation could imply some advantages like a reduced porosity and higher mechanical strengths. Human long bones like tibia or femur are based on several segments with specific characteristics. The diaphysis, which is the middle part of the bone, has a tube-like structure with cortical bone as the outer shell enclosing the medullary cavities and bone marrow [390]. By the method of centrifugally casting, tubes with a low porosity can be fabricated analogous to the cortical bone shell. The hollow structure of such constructs enables the invasion of bone marrow and bone marrow derived cells and, therefore, the ingrowth of new bone similar to porous scaffolds [10-15]. The hollow tube can also be filled with the patients' own bone marrow, stem cells or other cells to promote bone formation and ingrowth. Since the formation of bone marrow occurs within 4 – 6 weeks [391], a tubular structure is essential from the very beginning of implantation. Additionally, the design of a hollow tube is derived from nature (long bones), since hollow structures are more lightweight than filled ones in relation to the load they can carry [28]. To date, there are already several additive manufacturing techniques capable of

producing patient-specific implants of CPC and MPC like the 3DP. A comparison of tubular structures manufactured with 3DP and centrifugally cast samples should clarify if the latter could be an adequate alternative and have superior advantages. The transfer from the technical field to new materials always requires the adaption of the parameters for each composition. Therefore, an optimization of those parameters for different CPC and MPC preceded the comparison with 3DP.

The centrifugally cast CPC and MPC showed the possibilities of fabrication with different parameters. However, the brittle character of the cement matrix still remains leading to a very fast crack propagation through the whole part when a single crack event occurs [392]. In the end, they are just suitable for non-load bearing defect sites like in maxillofacial and cranial applications [7, 8, 393]. Due to their high mechanical strength a utilization in load bearing regions comes into mind. When ceramic implants should be transferred to load bearing defect sites, they have to be damage tolerant and need a reinforcement attenuating the brittle character. To date, several reinforcement strategies are possible for CPCs. One of them is the fiber reinforcement with short or long fibers [308, 385]. By the introduction of fibers crack propagation is stopped leading to multiple crack events. Moreover, the energy absorption is enhanced many times due to the lack of catastrophic failure. To tailor the properties like energy absorption or ultimate elongation fiber material, length, content or surface properties can be altered [9, 394] (see Section 2.6.1). The fabrication of tubular structures could also benefit from fiber reinforcement, when thinking of long bone replacement. Whether the centrifugation process alters the fiber distribution in a way that reinforcement is reduced will be analyzed in the following experiments.

Another reinforcement strategy is based on dual setting systems composed of an inorganic phase (CPC) and a polymeric, organic phase. By the process of dual setting, the polymeric component forms an interpenetrating network within the cement pores. There is a huge diversity in polymeric reinforcement materials like acrylamide [330-332, 334] or polyacrylic acid [326, 395], which is just a small selection of possible polymers (see Section 2.6.2). To prove centrifugally casting of a dual setting system,

a non-degradable composite of HA together with poly-HEMA was used. This system was already established for moldable composites [335]. The poly-HEMA hydrogel forms in a radical polymerization reaction and grows into the pores and cavities of HA and HA crystals. This process occurs simultaneously with the cement setting reaction leading to an interpenetrating organic network within an inorganic matrix. Christel et al. could show, that the ultimate bending strength of a composite with 50 % HEMA could be enhanced from 9 MPa to more than 14 MPa. Even more important was the high displacement and, therefore, a wof, which was one order of magnitude higher than for a pure HA [335]. This proved a good damage tolerance and a high energy absorption, which is a key requirement for the application in load bearing defect sites. The work presented hereafter aimed to transfer this material system to a manufacturing technique suitable for the fabrication of segmental bone implants for long bone replacement. It would be also possible to employ 3DP for the fabrication of such patient-specific implants that can be used for molds. To date, there was no successful printing of a dual setting system with 3DP. However, the intermediate step of a mold enables the fabrication of a patient-specific implant by centrifugally casting.

Apart from the mechanical performance, an implant has to be optimized in respect of the biological behavior *in vivo*. This includes the degradation behavior, the loading with drugs to treat infections as well as the fabrication of medically relevant implants. The implantation of a biodegradable material has great advantages over a non-degradable material, which is thought to remain permanently at the application site. This requires an optimal load transmission to avoid stress-shielding and a subsequent implant loss. In contrast, a degradable material gives space for steadily growing bone, which can adapt to varying load situations. This is especially important for young, healthy patients, since the implant material will be replaced by own bone tissue with a full recovery of its metabolic and mechanical function. But also for old, multi-morbid people a degradable implant could be preferable. Here, for permanent implants wear leading to particle release and a reduced mechanical stability have to be considered [396]. Implant failure due to such indications always requires an implant

replacement and a second surgery, which becomes even more dangerous for old patients. The application in different patients (young vs. old, healthy vs. (multi)morbid) already demonstrates the need for perfectly adjusted degradation behavior. This tuning can be achieved by the application or combination of different CPC and MPC as well as by the incorporation of foreign ions. The passive degradation *in vivo* is connected to the solubility of the material, which is quite different for the single CPC and MPC (Figure 2). Also the active degradation can differ for CPC and MPC as already shown in animal studies [141]. Ion incorporation can also alter the degradation behavior. Strontium for example enhances the solubility of a cement and, therefore, the passive degradation [90]. If a fast degrading implant is needed together with the promoting effect for bone growth, Sr^{2+}-substitution would be an adequate method with a dual benefit. Another ion for substitution would be calcium in MPC, which was already tested in terms of material and biological properties [133, 140]. The degradation behavior of those cements can be influenced by the amount of Ca^{2+}-substitution, whereby with a higher amount of Ca^{2+} present in the set cement (e.g. struvite) the active resorption is enhanced [145]. The centrifugally casting technique enables the fabrication of single layers oriented perpendicular to the long axis. Therefore, the degradation speed as well as the ion release can be adapted to each situation or different stages of bone growth. Ions like calcium, magnesium or strontium, which are released during degradation, can further and direct bone growth [19, 21, 86, 87, 149]. The technique allows the fabrication of graded structures, which are already described in literature to combine different properties or to obtain a gradual transition between different properties [324]. Another application of those graded structures in tubes would be the incorporation and encapsulation of drugs into degrading bone cements. Some techniques are not suitable for such an incorporation due to e.g. heat during processing leading to drug denaturation. One of the most common application of drugs are antibiotics for the treatment of bacterial infections, especially when foreign materials are inserted and the risk of infection rises [397, 398]. Such infections can occur during surgery, where bacteria enter the wound, or by the distribution via the blood stream. Either way, an infection at the implant site causes

severe problems often culminating in implant loss [399, 400]. To date, bacterial infections are treated by a systemic application of antibiotics, which has several drawbacks. Firstly, the whole organism is stressed by a relatively high dose of drug to maintain an effective dose at the infection site. As a consequence the secretion of the drug leads to a high activity and stress of different organs like the renal system [401, 402]. Secondly, the application of high amounts of antibiotics furthers the development of resistances against specific stems [401, 403]. Thirdly, it is hardly controllable how much antibiotics really reach the infection site and if a higher dose is necessary or if a lower dose would be sufficient. Such problems could be overcome by a local administration [404]. Therefore, the implant material is equipped with a drug, which is released over a period of time at the infected site. The release of drugs from ceramics can follow different kinetics (see Section 2.7.2) that are more or less convenient for the treatment of a bacterial infection. By the fabrication of centrifugally casting, the single layers can be used to encapsulate antibiotics to control the release kinetics. The aim is to obtain a kinetic of constant release exceeding the minimal dose for efficacy over a long period of time. Since bacterial environment is often more acidic [405, 406], the enhanced solubility of CPC and MPC under acidic conditions can be employed for a release on demand. As a last step, the simplified model of tubes can be transferred to medically relevant implant geometries, with the help of CT data and the fabrication of negative molds. With this last step, the technology demonstrates its superiority over some other AM techniques, as some techniques are limited to certain materials, which can be processed by centrifugally casting.

4.2 Materials & Methods

4.2.1 Parameter optimization and comparison with 3D powder printing

First, an optimization of the setting parameters and conditions for centrifugally casted tubes was performed with a MPC. Therefore, farringtonite ($Mg_3(PO_4)_2$) was used

together with a liquid phase composed of diammonium hydrogen phosphate ($(NH_4)_2HPO_4$; DAHP; Merck, Darmstadt, Germany) and ammonium dihydrogen phosphate ($NH_4H_2PO_4$; AHP; Merck, Darmstadt, Germany). Farringtonite raw powder was obtained by mixing a 2:1 molar ratio of $MgHPO_4 \cdot 3\ H_2O$ (< 125 µm, Sigma-Aldrich, Steinheim, Germany) and $Mg(OH)_2$ (VWR, Radnor, USA) five times in a planetary ball mill (PM400 Retsch, Haan, Germany) for 1 h at 200 rpm. Subsequent sintering of the mixture was performed in a furnace (Oyten Thermotechnic, Oyten, Germany) at 1050 °C in air for 5 h. The sintered cake was crushed with pestle and mortar and sieved < 355 µm. Prior to use, the fabricated farringtonite powder was activated by dry milling for 1 h at 200 rpm in a planetary ball mill.

The tube preparation was performed in 2 ml micro tubes, which were cut longitudinally and sealed with parafilm. A raw powder amount of 1200 mg was used. Mixing of the solid and liquid phase was done within the micro tube with a shaker (Vortex-Genie 2, Scientific Industries, Bohemia, USA). The micro tube was placed in a stirrer (IKA RW16 basic; IKA-Werke GmbH & Co. KG, Staufen, Germany) mounted horizontally for centrifugally casting (see Figure 11). Different parameters were varied to figure out the best set-up for tubes. The parameters are listed in Table 10, where the altered parameter is highlighted in blue. After preparation, supernatant liquid was removed and the sample was dried in a cabinet at 37 °C.

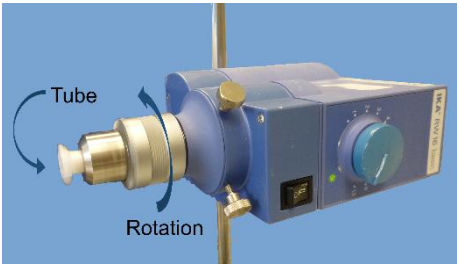

Figure 11: Stirrer mounted horizontally for centrifugally casting of cement tubes within a micro tube.

Table 10: Summary of the parameter variation. The altered parameter compared to the first composition is marked in blue.

Liquid phase	Post-hardening	PLR / g/ml	Setting condition	Rotation speed & time
3 M DAHP + 0.5 M AHP	-	1	-	5 min 1600 rpm + 20 min 160 rpm
3 M DAHP + 0.5 M AHP	2x1 min in 0.5 M AHP + 3 M DAHP	1	-	5 min 1600 rpm + 20 min 160 rpm
2 M DAHP + 1.5 M AHP	-	1	-	5 min 1600 rpm + 20 min 160 rpm
3 M DAHP + 0.5 M AHP	-	1.3	-	5 min 1600 rpm + 20 min 160 rpm
3 M DAHP + 0.5 M AHP	-	0.7	-	5 min 1600 rpm + 20 min 160 rpm
3 M DAHP + 0.5 M AHP	-	1	1 d water bath storage	5 min 1600 rpm + 20 min 160 rpm
3 M DAHP + 0.5 M AHP	-	1	1 d storage in H_2O	5 min 1600 rpm + 20 min 160 rpm
3 M DAHP + 0.5 M AHP	-	1	-	1 min 1600 rpm + 24 min 160 rpm
3 M DAHP + 0.5 M AHP	-	1	-	10 min 1600 rpm + 15 min 160 rpm
3 M DAHP + 0.5 M AHP	-	1	-	5 min 1600 rpm

After evaluation of the parameters with MPC, brushite samples were fabricated with the following set-up: PLR = 1 g/ml, rotation for 5 min at 1600 rpm followed by 20 min at 160 rpm, storage at 37 °C and 100 % humidity for 1 d, no post-hardening step. Brushite samples were prepared by mixing β-TCP stoichiometrically with MCPA (Chemische Fabrik Budenheim, Budenheim, Germany) in a coffee mill (Privileg, Quelle GmbH, Fürth, Germany) and 0.1 M citric acid as setting retardant. The raw powder β-TCP was manufactured by a 2:1 mixture of $CaHPO_4$ (Baker, Fisher Scientific GmbH, Schwerte, Germany) and $CaCO_3$ (Merck, Darmstadt, Germany). The mixture was sintered in a furnace at 1400 °C for 5 h followed by annealing at 1100 °C for 5 h to obtain phase pure β-TCP. The sintered cake was crushed with mortar and pestle and sieved < 125 µm. Finally, the β-TCP raw powder was ground in a planetary ball mill for 10 min at 200 rpm.

Mechanical testing was performed with a static universal testing machine (Zwick/Roell Z010, Zwick GmbH & Co. KG, Ulm, Germany) with a 10 kN load-cell. The cross-head speed was set to 1 mm/min at a pre-load of 1 N. Brushite as well as struvite were tested for axial compression and diametral tension. The axial compression strength was calculated according to equation (4.1):

$$\sigma = \frac{F}{\pi * ({r_a}^2 - {r_i}^2)} \tag{4.1}$$

with σ as the strength, F as the ultimate force, r_a as the outer radius and r_i as the inner radius. For the diametral tensile strength (DTS) the brittle ring test was used. Tensile strength was calculated using the following equation:

$$\sigma = \frac{F * (3 * d_i + 5 * s)}{h * \pi * s^2} \tag{4.2}$$

where d_i is the inner diameter, h is the height of the tube and s is the wall thickness defined as

$$s = \frac{d_a - d_i}{2} \tag{4.3}$$

with d_a as the outer diameter [407]. Moreover, density of the brushite and struvite samples was measured by Mohr-Westphal balance (Kern ABT-A01, Kern & Sohn GmbH, Balingen, Germany). The density ρ was calculated according to the following equation:

$$\rho = \frac{m_{air}}{m_{air} - m_{EtOH}} \rho_{EtOH} \tag{4.4}$$

m_{air} is mass in air, m_{EtOH} is mass in ethanol and ρ_{EtOH} is the density of ethanol. Ethanol had a temperature of 22 °C and, therefore, a density of 0.7876 g/cm³. Weight was recorded after 1 min or after stabilization, if the latter was within 1 min.

Since tubular structures can also be achieved by 3DP, a comparison between 3DP tubes and centrifugally cast tubes was drawn. For centrifugally cast samples brushite was prepared as described above. The 3DP was performed on the printer ZCorporation Spectrum Z310 (Burlington, USA) in three different directions. The orientation of the tube could alter the mechanical performance caused by a different layer structure due to fabrication. As raw powder α/β-TCP was used. The preparation of α/β-TCP was done by a 2:1 molar mixture of $CaHPO_4$ and $CaCO_3$ (both Merck, Darmstadt, Germany). It was sintered in a furnace at 1400 °C for 5 h. Crushing with mortar and pestle was followed by grinding in a planetary ball mill for 10 min at 200 rpm. The powder was set with 20 % phosphoric acid solution as binder with a layer thickness of 100 µm. The dimensions for the tubes given by the .stl file were the height 25 mm, r_a = 4.50 and r_i = 3.35 mm. After printing, the samples were removed and depowdered with compressed air. Post-hardening was performed twice for 30 s also in 20 % phosphoric acid solution. Mechanical testing was performed in dry state with a universal testing machine in brittle ring testing mode with the settings described above. Strength was calculated according to eq. 4.2 and 4.3. Finally, the toughness was calculated by integration of strength-elongation curve until an elongation of 0.25 or until the force dropped below the pre-load of 1 N.

4.2.2 Fiber reinforcement and dual setting system

The fiber reinforced tubes were fabricated of glass fiber reinforced brushite and struvite. For the brushite samples, a stoichiometric β-TCP and MCPA mixture was used as raw powder. The fabrication of β-TCP raw powder was already described in Section 4.2.1. The raw powder for struvite samples was farringtonite ($Mg_3(PO_4)_2$), where the preparation is also mentioned in Section 4.2.1. The tube formation was performed according to the previously optimized set-up. This means for brushite a liquid phase composed of 0.1 M citric acid and for struvite 3 M DAHP + 0.5 M AHP. The fabrication parameters were chosen according to the previous optimization: PLR = 1 g/ml, rotation for 5 min at 1600 rpm followed by 20 min at 160 rpm, storage at

37 °C and 100 % humidity for 1 d, no post-hardening step. For reinforcement alkali resistant zirconium silicate glass short fibers (Schwarzwälder Textilwerke Heinrich Kautzmann GmbH, Schenkenzell, Germany) were employed as well as glass fiber meshes. Glass fibers were mixed in a content of 3 % with the cement raw powder before mixing with the liquid phase to obtain a homogenous fiber distribution. Glass fiber meshes (glass filament fabric, Faserverbundwerkstoffe Composite Technology, Waldenbuch, Germany) were cut and introduced to the micro tube inner surface before adding the cement slurry. Calculations revealed a fiber content for the meshes of 15.7 ± 1.3 wt%. After centrifugation, supernatant liquid was removed. The fiber reinforced samples were compared to pure ceramic samples in terms of mechanical performance and density. The DTS was measured as well as the compressive strength by a universal testing machine with a 10 kN load-cell, a cross-head speed of 1 mm/min and a pre-load of 1 N. From these measurements the area under the strength-displacement curve was calculated representing the toughness and energy absorption ability of the sample. Additionally, the density of the pure and reinforced tubes was measured by Mohrs balance (Kern ABT-A01, Kern & Sohn GmbH, Balingen, Germany). Weighing was performed in ethanol (temperature 21 °C, density 0.7884 g/cm^3) and recorded after 1 min of stabilization. The density of the tubes was calculated according to eq. (4.4). Highly significant differences (**, $p < 0.001$) were tested with SigmaPlot 12.5 (Systat Software, Inc., 2011) in a t-test between two groups and Mann-Whitney Rank Sum test.

A second reinforcement strategy is a dual setting system composed of an inorganic cement and an organic polymer undergoing a simultaneous setting/polymerization reaction. As a model, the already established system HA + poly-HEMA was used for tube formation [335]. The inorganic component HA was built using α-TCP and a 5 % Na_2HPO_4 solution. α-TCP was produced by mixing 10.75 mol $CaHPO_4$ (J.T. Baker, Griesheim, Germany) and 5 mol $CaCO_3$ (Merck, Darmstadt, Germany) and sintering in a furnace (Oyten Thermotechnic, Oyten, Germany) for 5 h at 1400 °C. After quenching, the sinter cake was crushed with mortar and pestle and sieved <355 µm.

Prior to cement setting, α-TCP was activated by dry milling in a planetary ball mill for 4 h at 200 rpm. For the polymeric component, poly-HEMA was formed by a mixture of HEMA, ammonium peroxodisulfate (APS) and tetramethylethylenediamine (TEMED). In detail, 99.5 % α-TCP was mixed with 0.5 % APS as powder phase. The HEMA content was varied between 20 % and 50 % with respect to the liquid phase and compared to cement without HEMA addition. For a HEMA content < 20 % no stable tube could be formed, that means 20 % is the minimum HEMA content required for reinforcement. TEMED (0.25 %) and 5 % Na_2HPO_4 solution (99.75 % – HEMA content) concentration were mixed with HEMA as the liquid phase. The PLR for HEMA reinforced samples was set to 1 g/ml. For pure HA, α-TCP with 5 % Na_2HPO_4 solution was mixed at a PLR of 2.2 g/ml, which is the optimum PLR to get a uniform tube. After rotation for 5 min at 1600 rpm and 20 min at 160 rpm the tube was filled with ultrapure water and stored at 37 °C and 100 % humidity. The samples were demolded after 1 day and stored in ultrapure water for additional 6 days. The resulting samples had the dimensions 6.7 mm (inner diameter), 9 mm (outer diameter) and 27 mm (tube length). Morphological analysis of pure HA and samples with HEMA was performed with a scanning electron microscope (SEM, Zeiss CB 340, Oberkochen, Germany) at an acceleration voltage of 5 kV and a magnification of 10 000-fold. DTS of wet samples was measured with the universal testing machine with a 10 kN load-cell at a testing speed of 1 mm/min and a pre-load of 1 N (see eq. 4.2 and 4.3). The area under the strength-displacement curve as equivalent to the toughness was calculated up to an elongation of 0.25 or when the force dropped below 1 N set as the pre-load. The formation of HA was approved by x-ray diffraction (XRD; Siemens D5005, Bruker AXS, Karlsruhe, Germany) measurements and comparison with the ICDD (International Centre for Diffraction Data) database for α-TCP (PDF Ref. 29-0359) and HA (PDF Ref. 09-0432). The measurement was performed with a step size of 0.02 °/step and a scan speed of 1.5 s/step. A Cu-K_α radiation was used with a wavelength of $\lambda = 0.15418$ nm. Statistical analysis was again performed with SigmaPlot 12.5 (Systat Software, Inc.,

2011) and a t-test. Significant (*, $p \leq 0.05$) and highly significant differences (**, $p \leq 0.001$) were marked.

4.2.3 Improvement of biological properties

After the successful fabrication of single walled tubes by centrifugally casting, multi-walled tubes with different cement components could be manufactured. Ion substitution alters the cement properties and can be used for radially graded structures. Therefore, struvite was produced with different amounts of Ca^{2+}- and Sr^{2+}-substitution, respectively, in the single layers. For Ca^{2+} graded samples, Ca^{2+} doped farringtonite was used with two different Ca^{2+} contents: $Mg_3(PO_4)_2$, $Mg_{2.25}Ca_{0.75}(PO_4)_2$ and $Mg_{1.5}Ca_{1.5}(PO_4)_2$. For Sr^{2+} graded samples also farringtonite and two different Sr^{2+} doped magnesium phosphates were applied: $Mg_3(PO_4)_2$, $Mg_{2.67}Sr_{0.33}(PO_4)_2$ and $Mg_{2.33}Sr_{0.67}(PO_4)_2$. Cements were set with 3 M DAHP + 0.5 M AHP at a PLR of 1 g/mL and prepared with the optimized parameters (rotation for 5 min at 1600 rpm + 20 min at 160 rpm, storage at 37 °C and 100 % humidity for 1 d, no post-hardening step). The outermost tube was formed by struvite (out of $Mg_3(PO_4)_2$) followed by $Mg_{2.25}Ca_{0.75}(PO_4)_2$ and $Mg_{1.5}Ca_{1.5}(PO_4)_2$ or $Mg_{2.67}Sr_{0.33}(PO_4)_2$ and $Mg_{2.33}Sr_{0.67}(PO_4)_2$, respectively, for the innermost layer (see Figure 12). To achieve a fluent transition between the three layers the rotation speed was varied to 5 min at 1600 rpm + 0 min at 160 rpm before adding the next slurry. The surface ratio of the three different layers was calculated from light microscopy images (Carl Zeiss Discovery V.20, Oberkochen, Germany). Three different cross-sections along the long axis were used for calculation of the perimeter. With these values the centrifugal forces F_c could be calculated for each layer (eq. 4.5).

$$F_c = m \cdot \omega^2 \cdot r \tag{4.5}$$

Mass m of the sample and angular velocity ω are constant for each layer, whereas the radius r varies. The mass was 2400 mg and rotation speed was 1600 rpm. Accordingly, the centrifugal acceleration could be determined by eq. 4.6.

$$a = \omega^2 \cdot r \tag{4.6}$$

Surface morphology was investigated with a scanning electron microscope (SEM; Zeiss CB 340, Oberkochen, Germany) at an acceleration voltage of 2.0 kV. Elemental distribution of Ca^{2+}, Mg^{2+} and Sr^{2+} on the cross-section surface was evaluated with the attached EDX INCA Energy 350 AzTec Advanced system using a silicon drift detector (Oxford Instruments, Abingdon, UK) at an acceleration voltage of 15 kV and an aperture of 30 µm. For the preparation of cross-sections, tubes were embedded in Technovit 4071 (Heraeus Kulzer, Wehrheim, Germany) and cut in radial discs before sputtering with 4 nm platinum.

Figure 12: Layer assembly of the Ca^{2+}- (left) and Sr^{2+}-substituted (right) struvite tubes in graded samples. View along the tube axis.

With the help of those graded structures, the combination of CPC and MPC is possible. This opens up new application possibilities, since the setting conditions are different. Therefore, the combination of struvite (for the outermost and innermost layer) and brushite (for the middle layer) facilitates the incorporation of the antibiotic vancomycin. The antibiotic can be entrapped in the middle layer and act as a depot with altered release behavior. The struvite layers were made of $Mg_3(PO_4)_2$ with 3 M DAHP + 0.5 M AHP as liquid phase. Brushite was composed of β-TCP supplemented with an equimolar ratio of MCPA and 0.1 M citric acid as liquid phase. The preparation of the raw powders farringtonite as well as β-TCP are described in Section 4.2.1. For each layer the PLR was set to 1 g/mL and it was rotated for 5 min at 1600 rpm + 20 min at 160 rpm. After rotation samples were stored for 1 d at 37 °C and 100 % humidity before drying for 1 d at 37 °C. Vancomycin (CP 500 mg, active

substance: vancomycin hydrochloride, Hikma Pharma GmbH, Germany, batch: 252/16) was added to the brushite layer and struvite served as barrier (Figure 13A). For preliminary tests, 2 % vancomycin were added to the liquid phase (citric acid solution) and the solid phase (β-TCP + MCPA), respectively. Since the layered structure was exposed to outer media at the tube ends, they were sealed with silicone (Dublisil 15, Dreve Dentamid GmbH, Unna, Germany). The hollow pipe shape stayed intact (see Figure 13B). Investigation of vancomycin release was observed by static immersion in 10 ml phosphate buffered saline (PBS) at 37 °C for a total of 15 days. PBS was composed of 8 g/l NaCl, 0.2 g/l KH_2PO_4, 1.1 g/l Na_2HPO_4 and 0.2 g/l KCl, which was dissolved in ultrapure water. For analysis, PBS was exchanged completely and measured via high performance liquid chromatography (HPLC; LC-20AT, Shimadzu, Kyoto, Japan). The HPLC was operated isocratic and equipped with an autosampler (SIL-20AC, Shimadzu, Kyoto, Japan), a column oven (CTO-20AC, Shimadzu, Kyoto, Japan) at 40 °C and the column (Luna 5u C18(2) 100 A, 150*4.60 mm, 5 micro, P.No 00F-4252-E0, phenomenex). The mobile phase was 0.05 M $NH_4H_2PO_4$ (pH 4) – acetonitrile (92:8, v/v) with a flow rate of 1 ml/min. UV detection (Photodiode Array Detector) was used at a wavelength of $\lambda = 220$ nm together with the Software LabSolutions. After the dissolution study, the overall vancomycin content was determined by crushing the dried samples and immersion in PBS together with ultrasonication. Samples with the same cement assembly but without vancomycin addition served as negative control. Measurements were quantified with a calibration curve created by Michaela Rödel. The linear correlation had a slope of 21 662.78089 and an intercept of -32 765.12151. This intercept already indicates an uncertainty leading to deviations. Nevertheless, the setup is sufficient for a first assessment of the release behavior of such systems. Although a splitting of the signals occurred during dissolution, all signals were considered for the calculation of the cumulative vancomycin release. Based on the preliminary test, a second investigation over a period of 50 days was performed with $n = 7$. Therefore, vancomycin was only added to the solid phase in a concentration of 2 %. The static dissolution was performed at 37 °C in 5 ml PBS before measurement with HPLC and

calculation as described for the preliminary tests. For the evaluation of the release behavior, the power law was applied until a maximum of 60 % of cumulative release to estimate the release exponent as described in Section 2.7.2.

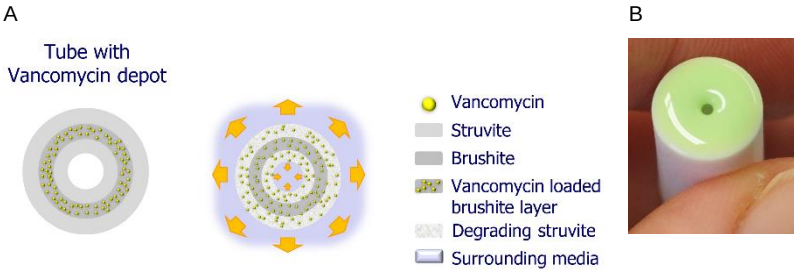

Figure 13: Assembly of vancomycin loaded tubes (A). The antibiotic is entrapped in a brushite layer in the middle. The outermost and innermost layers of struvite regulate the release kinetics. For dissolution tests, the tube ends were sealed with silicone to avoid antibiotic leakage (B).

The advantage of centrifugally casting is that not only symmetric tubes can be produced but also medically relevant implant geometries. To demonstrate this, a section of a long bone from a CT scan was reproduced. The resulting .stl file was used for 3DP of a model with α/β-TCP and 20 % phosphoric acid as binder and post-hardened 3 times for 30 s in 20 % phosphoric acid. The preparation of α/β-TCP raw powder is described in Section 4.2.1. The desired part of the diaphysis was cut and molded in silicone to get a negative of the bone segment. Analogous to the tube fabrication previously described, the silicone mold was filled with the cement paste and rotated at 1600 rpm. The cement paste was composed of farringtonite (for raw powder preparation see Section 4.2.1) and set with 3.5 M DAHP at a PLR of 1 g/ml. The resulting tube replicates the desired bone segment.

4.3 Results

4.3.1 Parameter optimization and comparison with 3D powder printing

Since the fabrication of centrifugally cast cement tubes was performed for the first time, an optimization of the parameters had to be conducted. This included parameters of the process (e.g. rotation speed and time) as well as of the cement slurry (e.g. PLR or post-processing). The optimization was done with a struvite forming MPC, where a summary of the variables and the respective values is given in Table 10. For each composition, the ultimate strength in compression mode was evaluated (Figure 14). Although just a small number of samples could be tested, it is striking that all samples except one composition exhibited similar strengths with medium values of around 12 – 20 MPa. The exception was a composition that was stored in the water bath with 37 °C and 100 % humidity for 1 d. The strength values highly scattered, but reached a medium compressive strength of ~20 MPa with maximum values of up to 42.1 MPa. For following tests, the composition of $Mg_3(PO_4)_2$ with the liquid phase of 3 M DAHP + 0.5 M AHP in a PLR of 1 g/ml without post-hardening was centrifuged for 5 min at 1600 rpm + 20 min at 160 rpm and subsequently stored at 37 °C and 100 % humidity for 1 d. Since the storage of the cast cement tube was the reason for an enhanced strength, this was adapted to other cement tubes based on brushite.

Additional to the compressive strength, the density of the tubes and the influence of the parameters on the density was evaluated (Figure 15). As a comparison, a brushite tube was manufactured according to the optimized parameters. The density varied between 1.89 – 2.02 g/cm³ for struvite samples and was 2.24 g/cm³ for brushite. For the optimized parameters regarding compressive strength, the struvite tube reached almost the highest density with 2.00 g/cm³. The compressive strength of brushite tubes was only 7.7 ± 3.4 MPa, although the density was higher than for struvite.

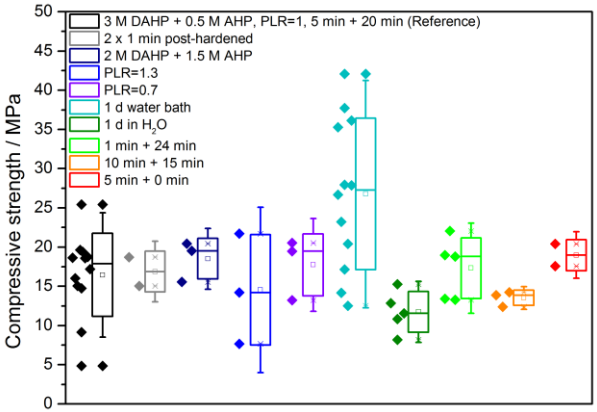

Figure 14: Optimization of preparation parameters for centrifugally cast struvite in compression test.

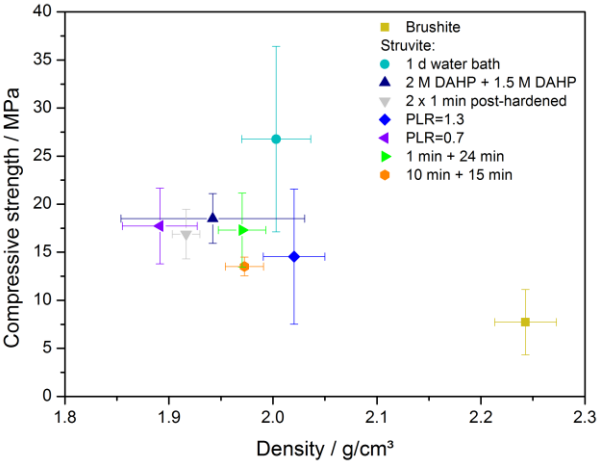

Figure 15: Compressive strength of tubular struvite and brushite depending on the cement density. Parameter optimization was performed for struvite samples. As a comparison, one brushite composition was added.

To obtain patient-specific implants, the 3DP technique is capable to process CPC as well as MPC. Based on free-form fabrication, also tubes can be produced. 3DP leads

to laminated structures due to processing (see Section 2.5.2), but after the post-hardening those structures are hardly visible any more (Figure 16).

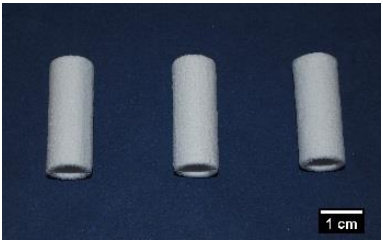

Figure 16: Tubes fabricated by 3DP. Printing was performed in three different directions (from the left: x-, y- and z-direction). After post-hardening, laminated structure is hardly visible.

The mechanical testing was done in a DTS mode, as bone and, therefore, an implant is predominantly exposed to bending forces [408] and is more fragile when loaded in bending. The diametral tensile strength for 3DP and rotationally casted samples is shown in Figure 17A. The printing direction did not influence the ultimate strength and ranged around 7.4 – 8.5 MPa. The ultimate strength of centrifugally casted samples is about 4-times lower (2.2 ± 0.7 MPa) than for the 3DP ones. In the case of energy absorption during mechanical testing, represented by the area under the strength-elongation curve, (Figure 17B) only x- and y-direction (0.04 ± 0.00 and 0.03 ± 0.00, respectively) of the 3DP samples was similar, whereas z-direction was higher (0.07 ± 0.02). In contrast to the ultimate strength, the energy absorption of the centrifugally cast samples was comparable to the 3DP ones in x- and y-direction. The reason for both phenomena can be found in the strength-elongation curve shown in Figure 17C. The high energy absorption for 3DP samples in z-direction was caused by a multiple cracking event. In contrast to the printed samples in x- and y-direction, the centrifugally cast tubes underwent a high deformation before failure. Phase analysis of printed and centrifugally cast samples revealed hardly any differences between the treatments during fabrication (Figure 17D). Brushite (b) and monetite (m) formed and only a small amount of the raw powder β-TCP (β) was left. The setting reaction in both cases can be considered as complete.

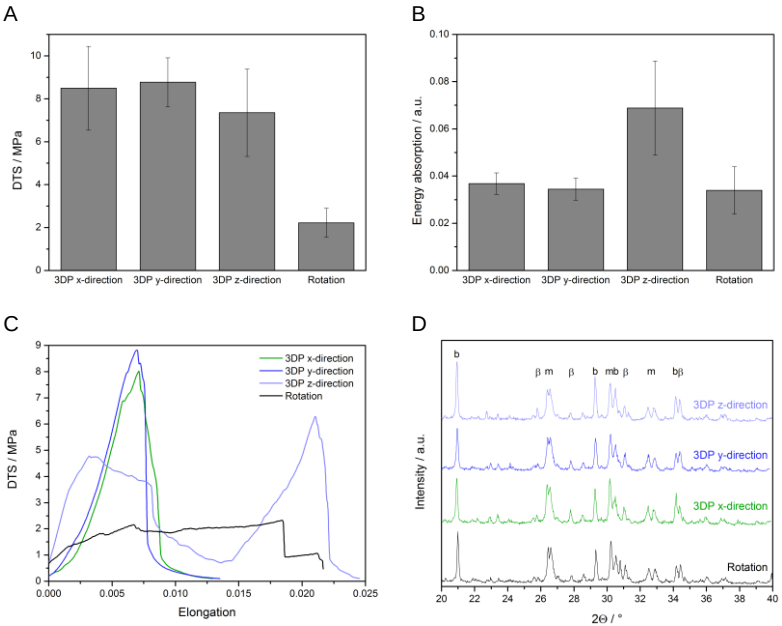

Figure 17: Diametral tensile strength (A) and energy absorption (B) for 3DP and rotationally fabricated samples. 3DP was performed in three different directions to exclude an influence of layer fabrication. For each fabrication a representative strength-elongation curve is shown (C). Phase analysis was performed with XRD to identify brushite (b), monetite (m) and β-TCP (β) (D).

4.3.2 Fiber reinforcement and dual setting system

For the previously optimized centrifugation parameters, reinforced struvite tubes were fabricated to reach a damage tolerance instead of a brittle fracture behavior. Pure struvite served as control for short fiber and fiber mesh reinforced struvite. In both cases, glass fibers were employed as model fiber, although the interface can be assumed to be not the optimum. However, after mechanical testing, a huge difference became even macroscopically obvious (Figure 18A). The pure struvite tube broke into numerous small pieces as it is typical for a catastrophic failure of a brittle material (left). The short fiber reinforced sample remained predominantly intact with just single pieces breaking out at the edge (middle). The best damage tolerance could be observed for the fiber mesh reinforced sample (right). There the edge of the tube was

deformed but not catastrophic failure occurred. This macroscopic observation is represented in the force-displacement curves for each case (Figure 18B). Reinforced samples had a huge displacement reflected in the energy absorption represented by the area under the curve. The ultimate strength was not increased by fiber addition, but a catastrophic failure was prevented and the tube stayed intact even after this high displacement.

A

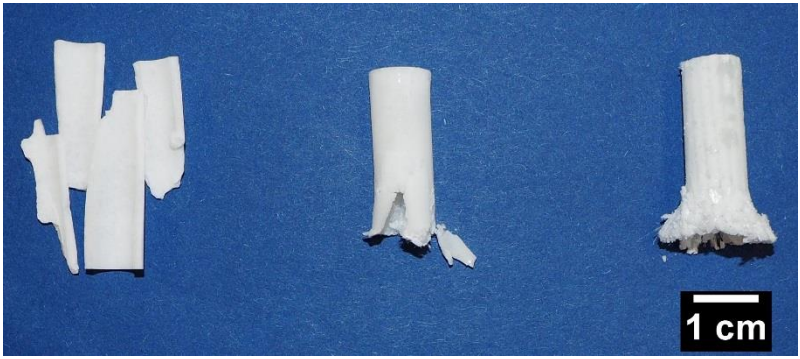

B

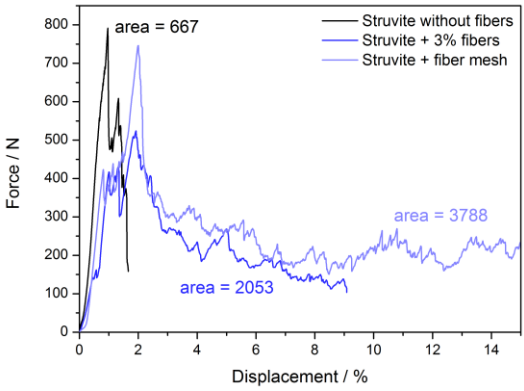

Figure 18: Unreinforced, short fiber reinforced and fiber mesh reinforced struvite tube after mechanical testing (from the left; A).Representative force-displacement curves show the reinforcing effect of fiber and fiber mesh addition (B).

As the fiber mesh reinforcement exhibited the best results in terms of damage tolerance, these samples were further investigated under different types of load. A pure brushite and a pure struvite matrix were tested under compressive and diametral tensile load. Additionally, the fiber mesh reinforced samples of each cement matrix were tested under diametral tensile load (Figure 19A). Since long bone in human and other mammals are predominantly loaded in flexural mode, the DTS seemed to be more meaningful for a long bone implant [408]. The DTS for both matrices was lower than the compressive strength. However, this could be increased by the fiber mesh reinforcement. The ultimate DTS of struvite could be almost doubled from 6.9 ± 0.7 MPa for unreinforced struvite to 11.3 ± 2.0 MPa for fiber mesh reinforced struvite. Brushite exhibited lower mechanical strength in general, but the reinforcing effect was even greater and the strength could be more than tripled: 1.8 ± 0.6 MPa (unreinforced) could be enhanced to 5.8 ± 1.8 MPa (fiber mesh). Due to the damage tolerance and the previously observed high displacement during testing, the energy absorption for the diametral tensile test showed the same trend (Figure 19B). Since the mechanical performance of bone cements strongly depends on the sample porosity and, therefore, the density, the DTS and the energy absorption was analyzed with respect to the sample density (Figure 19C and D). Since glass fibers have a higher density (2.5 g/cm³) than struvite or brushite, an increased overall density of the composite was expected. However, measurements exhibited even a reduced density for the composite material of 1.94 ± 0.03 g/cm³ for struvite and 2.18 ± 0.04 g/cm³ for brushite with fiber mesh. The differences in strength and density as well as in energy absorption and density are highly significant ($p < 0.001$).

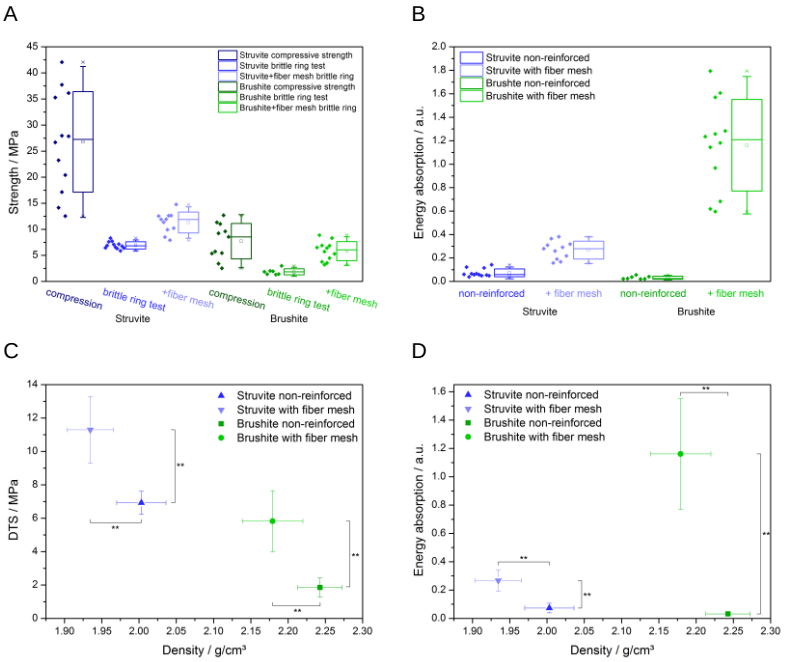

Figure 19: Strength (A) and energy absorption (B) of fiber mesh reinforced brushite and struvite under different types of load. DTS (C) and the energy absorption thereof (D) is dependent on the composite density. Highly significant differences ($p < 0.001$) are marked with **.

A further reinforcement strategy was pursued with a dual setting system with HA and poly-HEMA. The fabrication of poly-HEMA reinforced HA by centrifugation resulted in centrosymmetric tubes. HA tubes without HEMA addition served as control for all analysis methods. However, for a HEMA content below 20 % the samples were instable and broke unexceptional during demolding. Therefore, 20 % is the lowest HEMA addition that resulted in stable and measurable tubes. The morphology analyzed by SEM images (Figure 20) revealed a gradually altering structure with increasing HEMA addition. Without any HEMA, the typical morphology of nanocrystalline HA could be found. When HEMA content was enhanced, a smooth structure occurred between the single HA crystals, which can be ascribed to the poly-HEMA hydrogel. Especially for high HEMA contents (> 40 %

HEMA) the interpenetration of the organic network becomes visible. Although the two components are chemically different (organic polymer in an inorganic matrix), there was a certain contact between the phases.

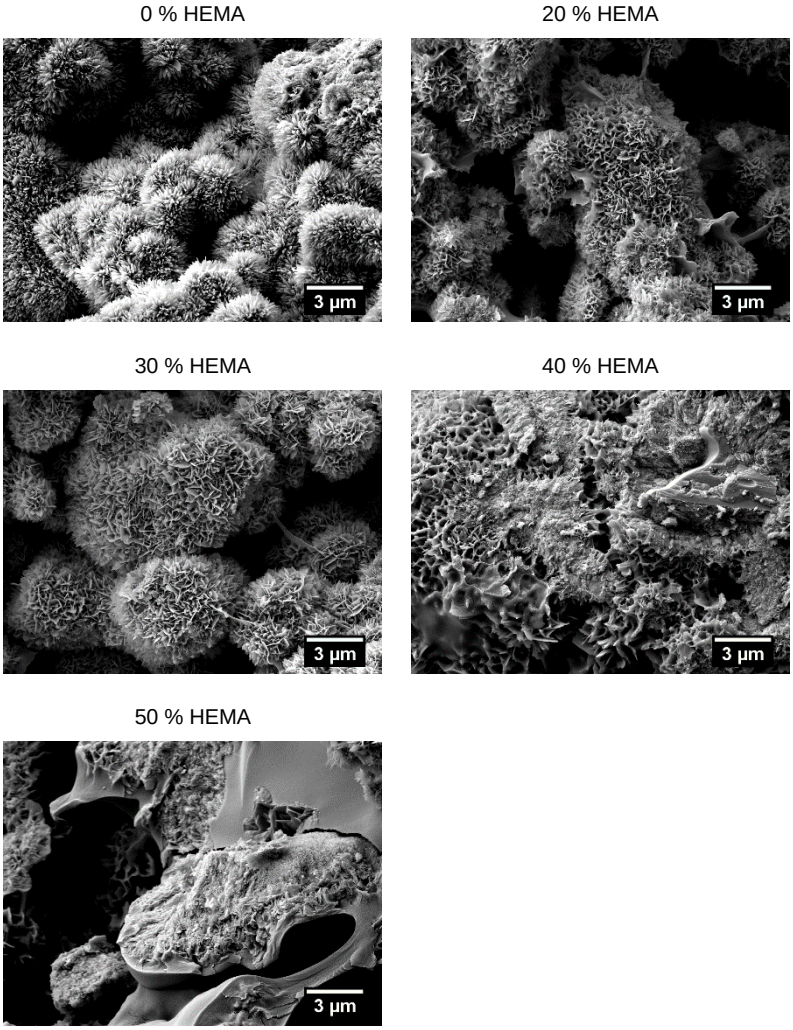

Figure 20: SEM images of dual set HA + HEMA samples at an acceleration voltage of 5 kV and a magnification of 10 000-fold.

The focus of this study was on the improvement of mechanical behavior such as damage tolerance. By the addition of the hydrogel poly-HEMA occurring cracks within the cement matrix should be bridged leading to a more elastic behavior (Figure 21A). The addition of only 20 – 40 % HEMA to the cement matrix caused a drop in ultimate tensile strength from 1.6 ± 0.3 MPa for pure HA to 0.7 ± 0.2 MPa for 20 % HEMA content. However, the strength could be more than doubled (3.4 ± 2.1 MPa) when a very high HEMA content of 50 % was added. Even though the deviation increased with higher HEMA content, the enhanced mechanical strength was statistically significant ($p < 0.05$). The energy absorption during mechanical loading is even more important, since absorbed energy will not contribute to crack formation or propagation (Figure 21B). With the help of this dual setting system, the energy absorption corresponding to the toughness could be improved by a factor of 24 from 0.02 ± 0.01 (pure HA) to 0.41 ± 0.25 MPa (50 % HEMA). Both the increased strength after an initial drop and the enhanced energy absorption could also be monitored in the strength-elongation curves recorded during testing (Figure 21C). The pure HA matrix showed the typical brittle behavior of a ceramic. It exhibited a high modulus and a high strength. However, after an initial crack, catastrophic failure occurred at a very low elongation. This means that the deformation was very small and a single crack event led to total failure of the sample. An increasing HEMA addition (20 – 40 %) resulted in lower ultimate strength but the sample deformation increased. Also the initial slope representing the modulus became flatter. At high HEMA contents (> 45 %) the deformation reached the limits of measurement. At an elongation around 0.25 the sample cross-section became elliptic until the tube walls touched each other. This of course would lead to measuring errors and the test was stopped at an elongation of 0.25 (Figure 21D and E).

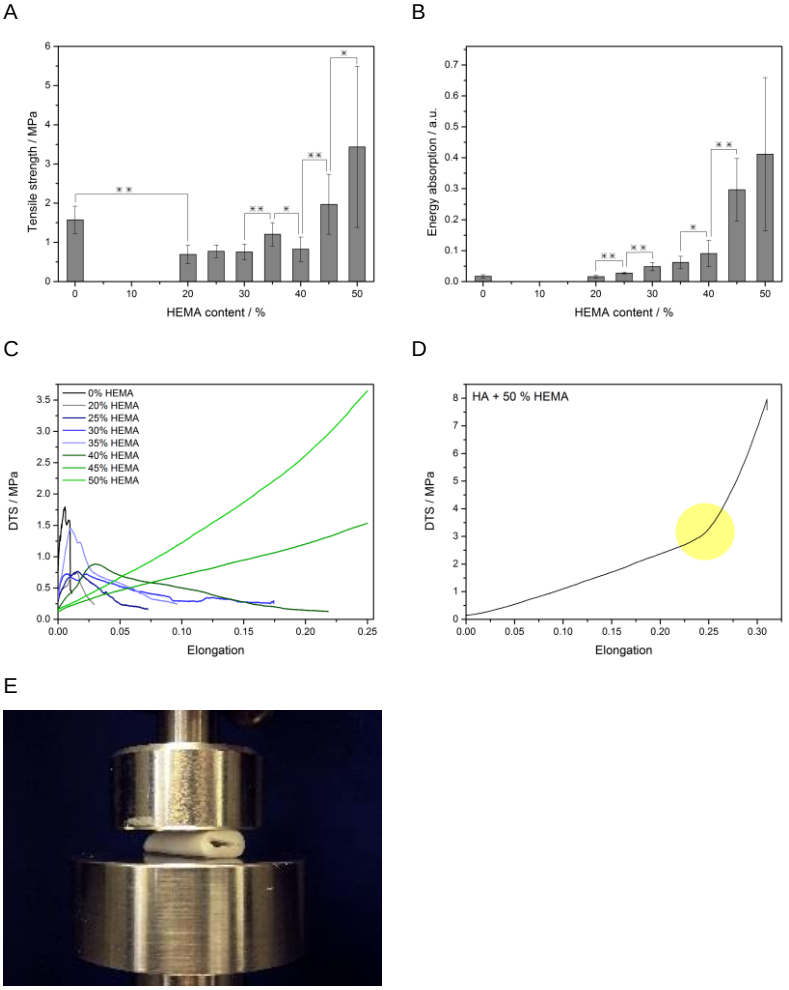

Figure 21: Diametral tensile strength (A) and energy absorption corresponding to the toughness (B) of tubes made of the dual setting system HA + poly-HEMA. Significant (*, $p < 0.05$) and highly significant (**, $p < 0.001$) differences between the HEMA concentrations are marked. Representative examples of a strength-elongation curve for each composition is shown in C. Measuring errors occurring after an elongation of 0.25 (D) can be traced back to the high deformation of the samples during testing (E).

Phase analysis with XRD exhibited a partial conversion of α-TCP to HA, that means there are still raw powder residues left in the sample (Figure 22). However, the amount of raw powder residue was independent of HEMA addition. Even for samples without

a polymeric component α-TCP could be found. Therefore, the polymeric phase had no obvious influence on HA formation as well as on crystallinity or crystal size, in contrast to the findings of Christel et al. [335].

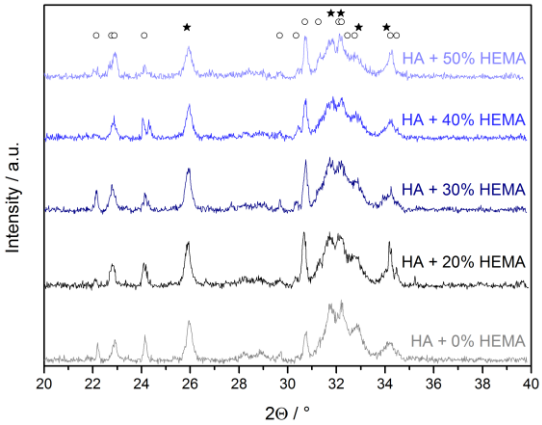

Figure 22: XRD of dual set HA + HEMA samples with different HEMA concentrations. α-TCP (°) and HA (*) reflections are marked.

4.3.3 Improvement of biological properties

The preparation of graded structures within a single tube could be performed with Ca^{2+}- and Sr^{2+}-substituted MPCs. First, the Ca^{2+}-substituted samples were investigated by light microscopy as well as SEM. Light microscopy revealed a sharp transition between the single cement compositions (Figure 23). This might be due to different centrifugal forces leading to different porosities, which could probably be investigated further by e.g. micro-CT analysis. Moreover, a fluent transition instead of sharp single layers could be achieved when the following cement layer would be added earlier during processing so that the previous layer is not fully set.

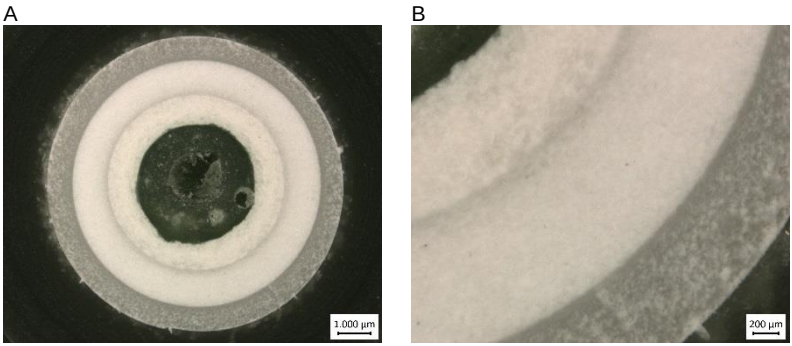

Figure 23: Light microscopy images of Ca^{2+} graded samples embedded in Technovit. The outermost layer is a pure struvite cement and the Ca^{2+} content increases towards the tube center.

The investigation of surface morphology of radially cut tubes was performed with SEM (Figure 24). The overview in the SEM images still shows three single layers as was previously observed in the light microscopy images. However, close-ups of each layer did not reveal any differences regarding topography or porosity. Planar, smooth surfaces in 2000-fold magnification can be ascribed to preparation. To obtain a cross-section the tube was embedded in Technovit and sawed radially producing flat surfaces. In the 15000-fold magnification single crystal structures could be found having the same size all over the cross-section independent of Ca^{2+}-substitution. Furthermore, just very small porous structures not exceeding 5 µm could be detected in all layers.

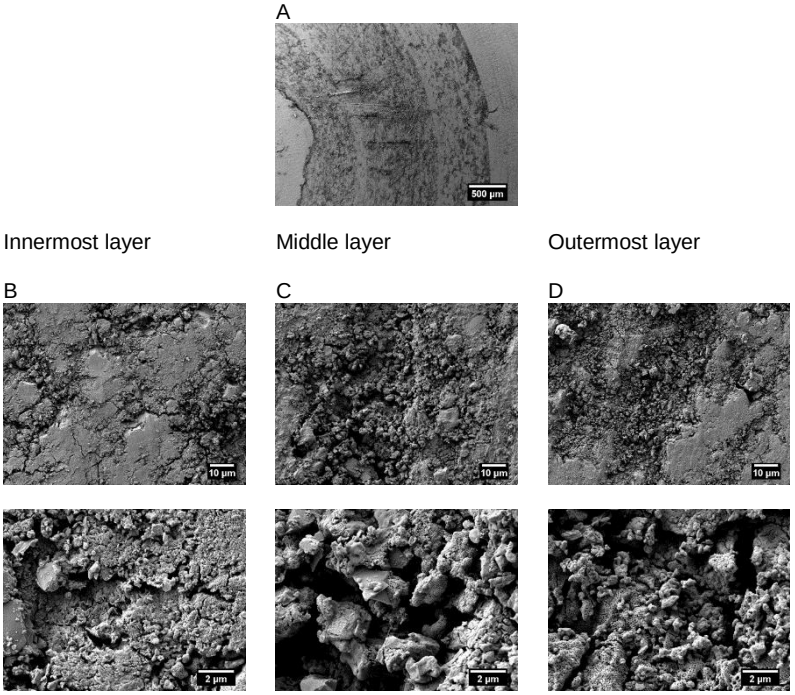

Figure 24: SEM images of all three layers with an overview (A) and close-ups (B-D) with two different magnifications (2000-fold and 15000-fold). The innermost and middle layer were substituted with Ca^{2+} ions. No significant differences between the compositions could be observed topographically.

The elemental distribution of Mg^{2+} (green) and Ca^{2+} (blue) within the single layers was detected by EDX measurements (Figure 25 and Table 11). As already observed in light microscopy images, the single layers are sharply separated from each other. However, the Ca^{2+}-substitution could be observed, which increased towards the tube center. With the help of elemental quantification, the Mg:Ca ratio could be compared to the theoretical values gained from the composition of the reactant powders. As they are well in accordance with each other, a loss of ions by e.g. leaching can be excluded.

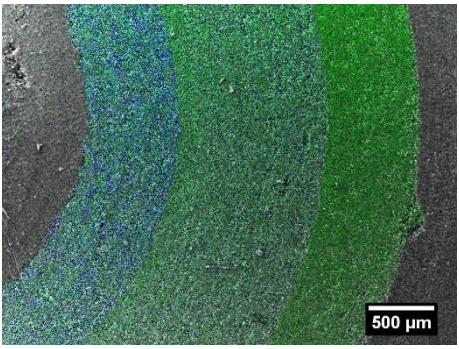

Figure 25: EDX measurements of cross-section showing all three rings. Mg^{2+} (green) and Ca^{2+} (blue) are color coded, where the color intensity corresponds to single counts. The set cement tube still represents the Mg:Ca ratio that was given by the reactant powders: $Mg_3(PO_4)_2$, $Mg_{2.5}Ca_{0.75}(PO_4)_2$ and $Mg_{1.5}Ca_{1.5}(PO_4)_2$ (from outermost to innermost layer).

Table 11: Results of EDX measurements of all three layers regarding Mg^{2+} and Ca^{2+} content. The experimentally (exp.) determined mass ratio comply with the theoretical (theo.) value calculated from the reactant composition.

	Innermost ring	Middle ring	Outermost ring
EDX wt% Mg^{2+}	7.8 ± 0.1	12.5 ± 0.1	22.0 ± 0.1
EDX wt% Ca^{2+}	11.3 ± 0.1	7.0 ± 0.1	0.2 ± 0.0
Exp. mass ratio Mg:Ca	0.690 ± 0.011	1.786 ± 0.029	110 ± 0.25
Theo. mass ratio Mg:Ca	0.606	1.819	∞

Since the sharp separation of the single layers as well as the cement porosity are strongly influenced by the centrifugal acceleration and forces during processing, those values were calculated for each layer according to eq. 4.5 and 4.6 (Table 12). The forces were calculated for the outer and inner diameter of each layer. The angular velocity at a rotation speed of 1600 rpm was 167.6 rad/s for a mass of 2400 mg. This resulted in centrifugal acceleration of 51 – 123 m/s² and centrifugal forces of 122 – 296 mN for the whole tube. This means, the forces of the outermost layer were more than double compared to the inside of the innermost layer.

Table 12: Centrifugal forces F_c and centrifugal acceleration a were calculated from each layer on the inside and outside of the layer with radius r according to eq. 4.5 and 4.6.

	Innermost layer		Middle layer		Outermost layer	
	Inside	Outside	Inside	Outside	Inside	Outside
r in mm	1.806	2.605	2.605	3.676	3.676	4.394
F_c in mN	122	176	176	248	248	296
a in m/s²	51	73	73	103	103	123

To create a gradient rather than a graded structure, the rotation protocol was altered to 5 min at 1600 rpm + 0 min at 160 rpm. By the reduction of the time for setting, the single layer should fuse at the edges to achieve a fluent transition between those single layers. So the previous layer could set for just 5 min before the next slurry was added. An EDX of a cross-section revealed the elemental distribution (Figure 26). The single layers are still separated and can easily be distinguished. Therefore, there was no fluent transition between the layers and no difference to the previous rotation parameters. However, there was no delamination of the layers neither for the optimized rotation parameters nor for the shortened setting time. This indicates a good cohesion between the layers.

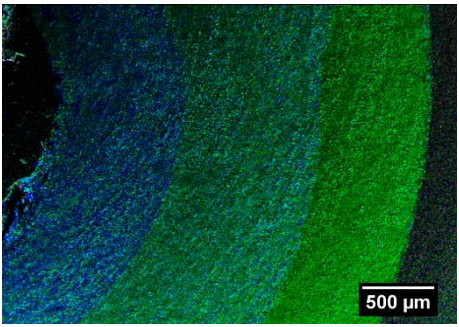

Figure 26: EDX measurement of Ca^{2+}-substituted MPC with adapted rotation parameters. The aim was a fluent transition of the single layers. However, there are still sharp separations. Ca^{2+} is depicted in blue, Mg^{2+} in green.

The same procedure was performed with a Sr^{2+}-substituted MPC. First, the optimized parameters with a rotation of 5 min at 1600 rpm + 20 min at 160 rpm were employed. Light microscopy images were similar to that of Ca^{2+}-substituted tubes (Figure 27). The single layers were easily distinguishable, which means there is no transition zone between the layers.

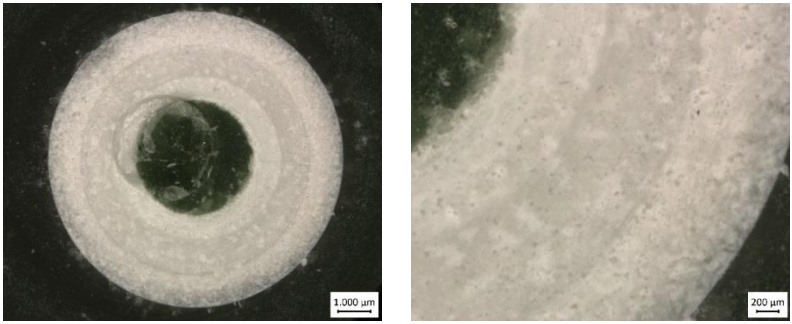

Figure 27: Light microscopy images of Sr^{2+}-substituted tubes. The outermost layer is a pure struvite cement with an increasing Sr^{2+} content towards the tube center.

A closer insight to the surface morphology and the elemental distribution was gained by SEM images (Figure 28) and EDX measurements (Figure 29 and Table 13). In an overview, the single layers were hard to distinguish, in contrast to the Ca^{2+}-substitution. The close-ups of the single layers exhibited the same trend as for the Ca^{2+}-substitution. The surfaces were rather smooth, which can be ascribed to the sample preparation. Additionally, there was no difference between the single layers topographically as well as for the porosity.

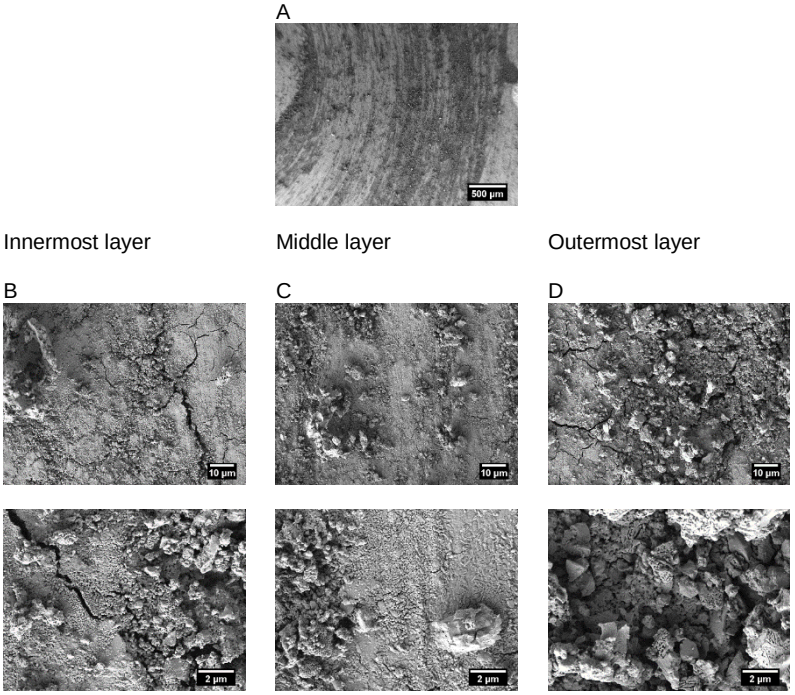

Figure 28: SEM images of all three layers with an overview (A) and close-ups (B-D) with two different magnifications (2000-fold and 15000-fold). The innermost and middle layer are substituted with Sr^{2+} ions. No differences between the compositions could be observed topographically.

Analysis of elemental distribution was performed again with EDX measurements for Mg^{2+} (green) and Sr^{2+} (red) (Figure 29). Since the Mg:Sr ratio of the raw powders was higher than Mg:Ca ratio, the signal for Sr^{2+} was pretty low compared to the Mg^{2+} signal. Therefore, the separation of the single layers seemed to be not as strict as for Ca^{2+} graded samples. However, the single layers were still clearly visible with the Sr^{2+} content being highest in the innermost layer. This became even more striking for the quantitative analysis of the two elements within each layer in comparison with the theoretical values of the raw powder (Table 13). For substituted cements Mg:Sr ratio was slightly higher in the set cement than theoretically calculated. However, the

deviation was small and a graded assembly with increasing Sr^{2+} content towards the tube center could be proved.

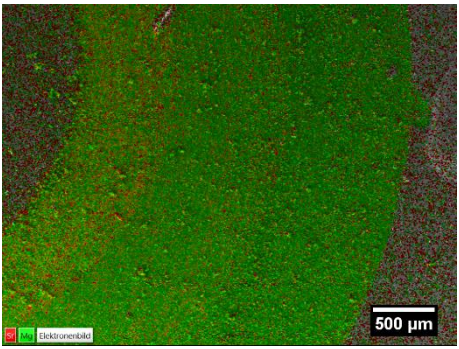

Figure 29: EDX measurement of a cross-section showing all three rings. Mg^{2+} (green) and Sr^{2+} (red) are color coded, where the color intensity corresponds to signal counts.

Table 13: Results of EDX measurements of all three layers regarding Mg^{2+} and Sr^{2+} content. The experimentally (exp.) determined mass ratio comply with the theoretical (theo.) value calculated from the reactant composition.

	Innermost ring	Middle ring	Outermost ring
EDX wt% Mg^{2+}	13.3 ± 0.1	16.1 ± 0.1	14.8 ± 0.1
EDX wt% Sr^{2+}	11.8 ± 0.1	6.2 ± 0.1	0.0 ± 0.0
Exp. mass ratio Mg:Sr	1.127 ± 0.013	2.597 ± 0.045	∞
Theo. mass ratio Mg:Sr	0.965	2.244	∞

To achieve a better transition between the layers, as already tried for Ca^{2+}-substitution, rotation protocol was again varied to 5 min at 1600 rpm + 0 min at 160 rpm. The setting of the previous layer should not be completed due to a shorter time period. This could enable a fusion with the next layer. However, light microscopy images of such samples also exhibited the single layers similar to the previous rotation parameters (Figure 30A and B). To exclude a pure porosity difference as a cause of the visually separated layers, EDX measurements of a cross-section were performed (Figure 30C). Mg^{2+} (green) and Sr^{2+} (red) were distributed similar to the previous settings with increasing Sr^{2+} content towards the tube center. Again single layers were

visible and no smooth transition between these layers could be observed. The initial setting time of the cements seemed to be short enough to form a stable tube within 5 min, which inhibited diffusion processes between the different cements. Nevertheless, delamination never occurred indicating that cohesion between the layers was very high due to interpenetrating crystals or probably local precipitation.

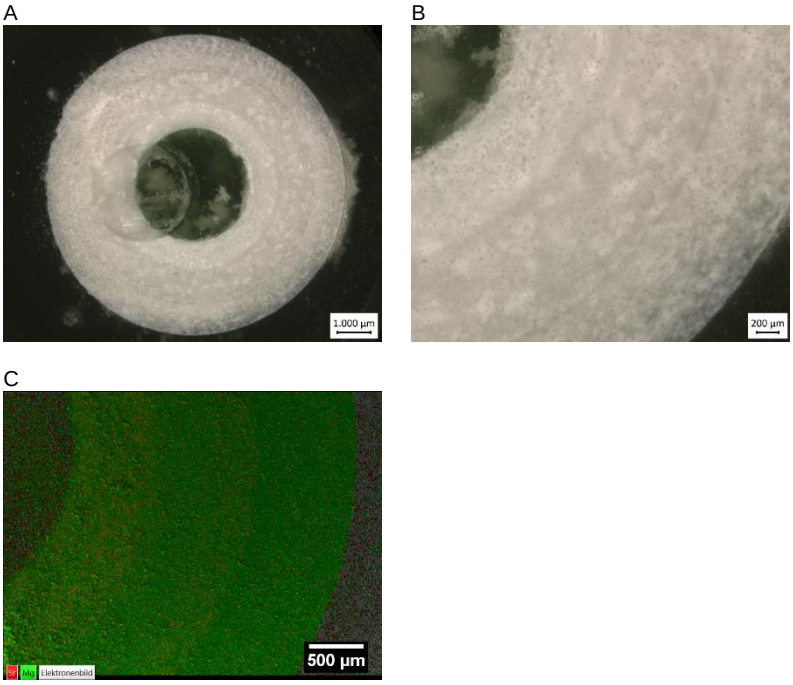

Figure 30: Light microscopy images of Sr^{2+}-substituted tubes with altered rotation parameters (A, B). The aim was a fluent transition between single layers. However, the layers are still separated. EDX measurement of Sr^{2+}-substituted tube with altered rotation parameters for a fluent transition. Mg^{2+} (green) and Sr^{2+} (red) are color coded, where the color intensity corresponds to signal counts.

The strict separation of the single layers can be utilized for entrapping of antibiotics with a controlled release by degradation of the outer layers. As a model drug, vancomycin was used for cement loading in a brushite layer. A loading of struvite would not be possible, since there is an adverse interaction of vancomycin with the

ammonium phosphate solution. However, as already shown for Ca^{2+}-substituted MPC, a combination of CPC and MPC is possible without delamination (Figure 31A). For a preliminary test, samples were loaded by addition of vancomycin to the liquid phase and the solid phase, respectively. During 15 days of immersion in PBS, no degradation was macroscopically visible and the samples were still mechanically stable in both cases. A pure cement tube without vancomycin served as negative control to exclude any influence of the cement or the silicone sealing on the HPLC measurement (Figure 31B). Both loading cases exhibited the same release trend during dissolution time. After 15 days, about 24 % of the vancomycin added to the solid phase was released, whereas 41 % were released in the case of liquid phase loading. Therefore, the depot function could be better exploited when the drug was added to the solid phase. Moreover, the loading capacity for the solid phase is higher than for the liquid phase, which makes the first case more attractive for drug release systems.

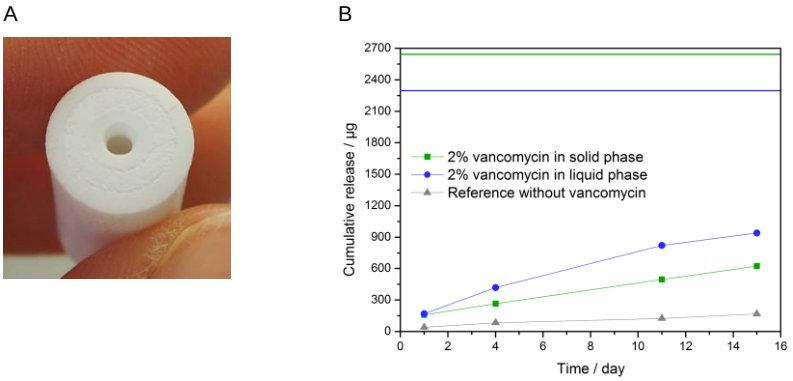

Figure 31: Cross-section of a tube with brushite as middle layer and struvite for the outermost and innermost layer, respectively (A). No delamination occurred after fabrication and the brushite layer could be loaded with vancomycin. Vancomycin release for preliminary tests, where the antibiotic was added to the liquid and the solid phase, respectively (B). The solid line indicates the absolute amount of vancomycin entrapped in the sample.

For the long-term study, the addition of vancomycin to the solid phase was chosen to determine the release during 50 days (Figure 32A). The total amount of vancomycin in the sample that could be theoretically released was about 2200 µg/ml. In the first

few days (until about day 10) there was a linear cumulative release following zero-order release kinetic. After that, the release decreased resulting in a flattened release curve. About one third of the total vancomycin amount was release during this first linear stage, whereas after 50 days the release was just 58 %. The power law (see Section 2.7.2) was applied to calculate the release exponent and with that to determine the mode of release (Figure 32B). In general, the power law is just valid for a cumulative release of 60 %, which is in accordance with the release until day 50. The resulting release exponent is 0.35. Table 8 summarized the mode of release for different release exponents and sample geometries. For cylindrical systems the lowest value for the release exponent was 0.45 for a Fickian diffusion, which can be described by the Higuchi model. To determine the degradation of the cement matrix, samples were weighed before and after 50 days of dissolution and the vancomycin release was considered. This resulted in a weight loss of the pure matrix between 45 and 85 mg, representing 3 to 5 % of the initial weight.

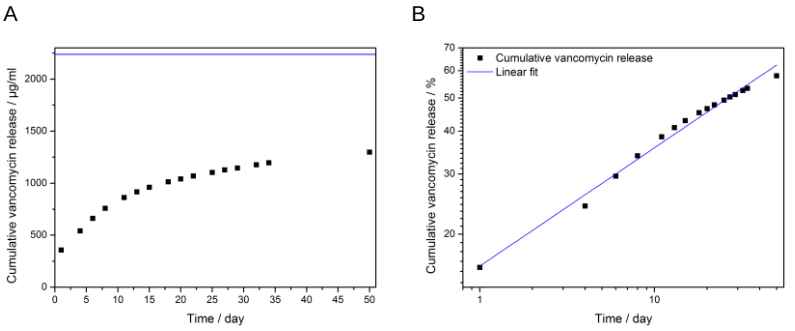

Figure 32: Cumulative vancomycin release over a dissolution period of 50 days. The solid blue line indicates the total amount of vancomycin entrapped in the sample corresponding to 100 % (A). The cumulative vancomycin release was fitted with the power law to obtain the release exponent and the mode of release (B).

All investigations regarding parameters, cement formulations or property optimization were performed with simple tubes to obtain standardized conditions for the tests. However, when thinking of the application, an individual, patient-specific implant has to be fabricated. To demonstrate the possibilities, a CT scan of a human

femur was used for 3DP of a scaled down model. This model was cut to obtain the diaphysis, which should be replaced by a new implant. The cut diaphysis was molded and served as a negative for the rotation of the cement slurry. After processing, the centrifugally cast implant perfectly fitted into the defect site. The single steps as well as the resulting implant are illustrated in Figure 33. This enables the patient-specific processing of materials that are not suitable for 3DP like the dual setting cements.

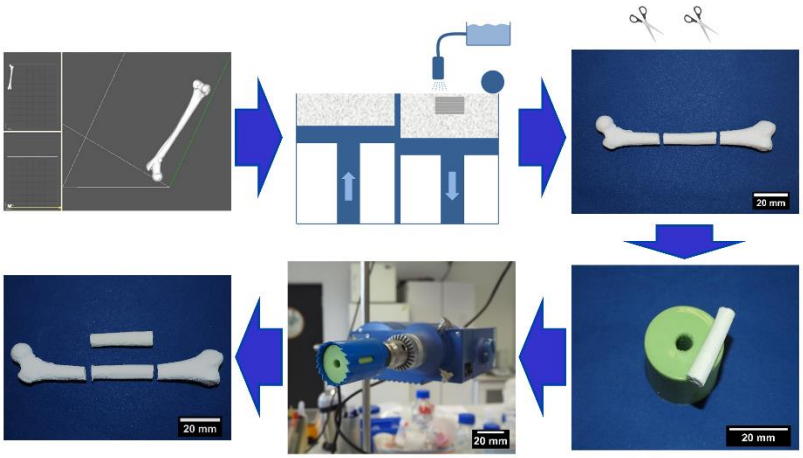

Figure 33: Fabrication of a segmental bone by 3DP of a bone model, molding of a negative form and fabrication of a long bone segment by centrifugally casting.

4.4 Discussion

For the optimization of the new fabrication process of centrifugally casting of CPC and MPC, parameters regarding the process and the cement composition were varied. The evaluation was performed by compression tests to reach the best mechanical performance (Figure 14). The low sample number inhibited a reasonable test for significant differences between the parameters. However, the subsequent storage for 1 d in a water bath at 37 °C and 100 % humidity could double the compressive strength of the tubes. Such an increase was not possible by varying other parameters. This indicates that after processing, the cement still underwent a setting reaction,

where single crystals grew and interlock to form a stable solid. Initial setting times for struvite are reported to be 1.5 – 16 min [127, 129, 140]. Although the process of centrifugally casting took 25 min, the setting reaction was not completed and the cement gained further strength. The elevated temperature of 37 °C (compared to room temperature) accelerated the setting reaction and the high humidity prevented the cement from desiccation and water shortage. Since water is needed for the setting reaction to struvite (see Section 2.4.2), the latter aspect is probably predominant. Therefore, this treatment was adapted for all cements prepared by centrifugally casting to obtain a good mechanical performance. Since the density of a ceramic is strongly connected to its mechanical strength [165, 166], it was investigated for all parameters of struvite samples as well as for a brushite sample produced under the optimized condition with storage in a water bath for 1 d (Figure 15). For the optimized settings, struvite reached a density of 2.00 g/cm³ and brushite 2.24 g/cm³. The brushite samples were well in accordance with literature (density of 2.319 g/cm³ [44]) and the theoretical density of 2.257 g/cm³ [409]. For struvite, measured densities in literature varied between 1.48 and 2.28 g/cm³ [129, 130], whereas the theoretical density is just 1.706 g/cm³ [410]. The discrepancy between theoretical density and experimental values probably occur due to an incomplete reaction or incorporation of foreign phases with a density higher than 1.706 g/cm³. This influences the overall density of the sample and can lead to density values higher than the theoretical value, which was calculated for pure struvite being free from defects.

3DP is a technique that can be used for the fabrication of patient-specific implants. Since this is also the aspiration of centrifugally casting, a comparison of those two techniques was pursued. It is already known that the printing direction has a strong influence on the mechanical performance of a printed part [175]. Therefore, tests were performed with tubes printed in x-, y- and z-direction. However, after the post-hardening step, the laminated structure, which is typical for 3DP samples, was smoothened (Figure 16). During post-hardening, the raw powder particles still remaining on the surface and within the bulk dissolve and undergo a setting reaction.

The dissolved particles precipitate as brushite crystals and form a smooth surface. Additionally, the precipitation of brushite crystals reduces the porosity and the crystal growth leads to a further interlocking of the single crystals. This enhances the mechanical strength of the tubes for all directions (Figure 17). For this investigation, the DTS was chosen, because it is closer to the real loading situation [408]. The centrifugally cast tubes exhibited a DTS of only 2.2 ± 0.7 MPa, which is 4-times lower than the 3DP samples. Since the optimization was done only for struvite samples, the influence of post-hardening of brushite tubes is unclear. The centrifugally cast tubes could be expected to have still raw powder left, which not fully reacted to brushite. In contrast, the post-hardening of printed samples could have led to a full conversion of the raw powder and, therefore, a high degree of crystal interlocking, which would explain a higher mechanical strength. However, XRD analysis of printed and centrifugally cast samples revealed hardly any difference in composition (Figure 17D). Therefore, both processes can be considered to result in a complete conversion from β-TCP to brushite and monetite, which excludes different phases to be the cause of different mechanical behavior. Additionally, centrifugation could have influenced the crystal structure and growth so that just small crystals formed, which could hardly interlock. In contrast to the findings for the strength, the energy absorption of x- and y-direction are comparable to the centrifugally cast tubes. Just the printed samples in z-direction exhibited an energy absorption, which was almost double. The strength-elongation curve can explain that discrepancy. The centrifugally cast samples had a very high elongation until failure compared to the printed samples. Therefore, the energy absorption was very high. This would support the theory of small crystals that hardly interlocked. They can be moved relatively to each other without a catastrophic failure event, which makes them less brittle. The 3DP samples in z-direction could adsorb much energy, because their mechanical behavior is based on a multiple cracking event. Due to the orientation within the printer, the tube was built of single rings stacked on top of each other. Probably these rings have to be considered individually, so that some parts can bear higher load or can be stronger deformed. Additionally, the connection between those rings is not as strong as for the x- and y-

direction. Crack propagation along the tube is therefore hindered by the single segments, which makes the whole tube more resistant against catastrophic failure.

The overall aim of the reinforcement was the fabrication of a damage tolerant material manufactured by centrifugally casting. Therefore, the mechanical performance was evaluated in different types of loading. Although glass fibers are not an optimum reinforcement material for CPC, they can serve as a model fiber as already shown in Section 3. The reinforcing effect could be observed macroscopically as well as in the force-displacement curves (Figure 18). The fiber reinforced samples had a much higher displacement than the pure cement. This is due to the well-known mechanisms of fiber reinforcement like fiber bridging, pull-out or crack deflection (see Section 2.6.1). The fiber mesh yielded in an even better mechanical reinforcement than the short fibers. This is on the one hand due to a higher fiber content of 15.7 wt% compared to 3 % for the short fibers. On the other hand, the fiber mesh has a woven structure, which further contributes to an energy absorption during loading. Therefore, the fiber mesh reinforced brushite and struvite tubes were further investigated under different loading modes (Figure 19). Comparing the two different cements, struvite exhibited a higher strength and energy absorption than brushite independent of loading situation. This can be traced back to the material inherent mechanical properties as already known from literature [141]. Interestingly, the tubular structure had no influence on the mechanical performance and is comparable to cuboid samples [129, 317]. Independent of material composition, the DTS was lower than the compressive strength. This is a typical behavior of brittle materials like ceramics [76, 158], although in this case the DTS was less than one order of magnitude lower. By the addition of a fiber mesh, the DTS could be increased by a factor of two to three, which indicates a good transfer of external forces from the matrix to the fiber. As this transfer requires a stable interface with a certain matrix-fiber-bonding, it can be concluded that even the glass fibers are an adequate reinforcement fiber material for MPC and CPC. Similar to that, the energy absorption could be increased by incorporation of a fiber mesh. While struvite samples underwent an increase by a

factor of 3.6, especially brushite samples benefited from a higher elongation before failure with more than one order of magnitude higher energy absorption. This enormous enhancement can again be traced back to the mechanisms of fiber reinforcement with crack deflection, fiber pull-out etc. However, the scattering of energy absorption values raised rapidly by fiber mesh reinforcement, which will be to the expense of implant reliability. This phenomenon indicates the introduction of hardly predictable defects into the ceramic matrix by the fiber addition. However, the effect of an enhanced catastrophic failure resistance and energy absorption overbalances the drawback of a higher value scattering. Another phenomenon of fiber mesh addition was a reduced density of the composite material. For both struvite and brushite, the density of the composite was lower than the density of the pure matrix. With a fiber mesh content of 15.7 wt% and a material density of the fiber of 2.5 g/cm³ an overall higher density was expected. In contrast, the density could be reduced to 97 % of the former density, which was a highly significant difference. The density reduction has to be related to a higher porosity or a higher amount of closed pores. However, the high porosity did not lead to a lower strength, as would be expected from pure ceramics [165, 166]. The reinforcing effect of the fiber mesh was prevailing and led to an increased strength. In the end, a light weight implant with a high mechanical strength and toughness can be achieved with this composition.

The second reinforcement strategy used a simultaneous setting of a cement matrix and an organic, polymeric network. The interpenetrating network of the dual set HA + HEMA could be found within the fracture surfaces (Figure 20). Depending on the HEMA addition, the nanocrystalline HA is more or less embedded in the hydrogel. This morphology was already found for molded samples [335, 411], which means that the centrifugation process did not hinder the formation of two interpenetrating phases. Additionally, the contact between the inorganic crystals and the organic polymer seemed to be as close as for the molded samples. In contrast to the molded samples described in literature [335, 411], the centrifugally cast tubes exhibited the same crystal size independent of HEMA concentration. Therefore, the HA formation could

be decoupled from the hydrogel formation, which is in accordance with the phase analysis. There was no evidence from the XRD measurements for the influence of the polymeric phase on cement formation, crystallinity and crystal size (Figure 22). In contrast, Christel et al. found a reduced conversion of α-TCP to HA with increasing HEMA addition [335]. Hurle et al. further investigated this reduced HA formation [411]. They found a delayed HA formation, although this occurred within the first few hours with and without HEMA. With the help of *in situ* XRD, they traced this back to a lower α-TCP dissolution during setting. Two possible explanations were presented for this phenomenon: first, by introduction of a hydrogel, a competition for water between organic and inorganic phase occurs. The reduced water available lowered the dissolution of the raw powder. Second, the hydrogel network impedes ionic diffusion of Ca^{2+} and PO_4^{3-}, which is necessary for HA formation. In this experiment, the same system was employed for the fabrication of tubes, but the HA formation was independent of HEMA addition. Hence the manufacturing technique could have influenced the cement setting reaction. It can be assumed that the centrifugation and, therefore, the partial separation of solid and liquid phase led to a uniform HA formation independent of HEMA addition. This would also explain an incomplete HA formation for the pure cement tubes without HEMA. In the previous studies, they found a phase conversion of 95 % [411] and 96 % [335], respectively. However, the mechanical performance is comparable to those studies. At low HEMA contents (20 – 40 %) the mechanical strength decreased (Figure 21A). The crystal interlocking is probably disturbed by the polymeric phase, as the interlocking is the main reason for the high strength of ceramic materials [163]. Under load, the crystals cannot interlock as they would do in a pure HA matrix. Thus, the crystals start to slip, which in the end decreases the load-bearing behavior of the whole composite. This hypothesis is supported by the fragile behavior with a HEMA content below 20 % resulting in broken samples only by demolding. Therefore, the damage tolerance of those low content samples was lower than the reference and all other samples measured. Although the ultimate strength suffered from a low HEMA content, the polymeric network for 20 – 40 % HEMA addition was sufficient to bridge the cracks in the

matrix and absorb energy during deformation (Figure 21B). However, the deformation for low HEMA contents is still limited. A HEMA content of at least 45 % is required to reach deformations of 25 % without an accelerated failure (Figure 21C). In these cases, the polymeric network seemed to span the whole construct and exceed the disturbance of crystal interlocking. This becomes even more obvious, when considering the initial slope. For high HEMA contents, the slope became flatter being a sign of an enhanced elasticity. The effect of the polymeric phase overwhelms that of the brittle ceramic matrix. Simultaneously, the inorganic matrix serves as a structuring element that can still bear high loads.

The combination of different cements within a single tube can be employed to tune the biological properties of such implants. With a Ca^{2+}-substitution, the degradation of the tube can be altered or Sr^{2+}-substitution supports new bone formation. Firstly, those systems have to be investigated regarding material properties. Light microscopy images as well as SEM images revealed surface morphologies and connection of the single layers. It became apparent that the single layers were easily visible and distinguishable in a cross-section. This could point to different densities and, therefore, different porosities of the cement layers. When calculating the centrifugal forces, the outermost layer exhibited about twice as high forces compared to the innermost layer. Since there is always a separation of liquid and solid phase during centrifugation and the porosity of CPC and MPC is influenced by the PLR [130], it is highly probable that the outermost layer had a different porosity and density than the innermost layer. In the SEM images, there was hardly any difference between the layers regarding surface morphology, which is partially attributed to the preparation of sawed cross-sections. Beside the smooth surfaces, some pores could be detected, which were in the range of about 5 µm. However, these were very small pores, which were at least one order of magnitude smaller than osteoclasts needed for active degradation [412, 413]. Thus, invasion of cells and penetration of body fluids are inhibited or at least strongly reduced leading to surface degradation processes. Since the surface degradation rate is dependent on the surface area, the degradation of an

implant can be accelerated with an increased surface area. In this case, the surface ratios of the three different layers were: 1.7 : 1.4 : 1. By incorporation of Ca^{2+} ions into struvite, the degradation can be adapted to the respective surface area to reach a constant degradation, whereby fluent transition between the single layers would be favorable. However, even for shorter centrifugation times, no transition could be achieved. Here, the initial setting time for the cements was probably too short, such that a stable cement matrix was formed before the next slurry was added and there was no fusion with this next layer. Another reason that inhibits a fusion could be the high density due to centrifugal forces, which impedes a diffusion between the layers. Nevertheless, a good adhesion between the layers was achieved and no delamination occurred. During setting, crystal interlocking leads to mechanical stability within and between the layers [163]. The lattice parameters are altered by the ion substitution, since Ca^{2+} (0.99 Å), Mg^{2+} (0.69 Å) and Sr^{2+} (1.13 Å) ions have different ionic radii [18, 42, 190, 342]. However, the differences were too small to inhibit a sufficient interlocking. This provides the opportunity to combine different CPC and MPC, in general, for further property improvements. The ratio of the different ions was determined by EDX measurements of cross-sections. The Mg:Ca ratio was well in accordance with the theoretical value calculated from the raw powder. However, for Mg:Sr the ratio measured experimentally was slightly higher than the theoretical value. Since the Sr^{2+}-substitution was lower than the Ca^{2+}-substitution, the signal for Sr^{2+} was much weaker in relation to the Mg^{2+} signal. This small amount of data could have influenced the calculated Mg:Sr ratio, although it was quite similar to the theoretical values. The selection of a foreign ion doped cement can be assumed to result in graded structures with the same ionic doping ratio.

Such graded structures could be employed for drug delivery systems by loading a middle brushite layer with the antibiotic vancomycin. This middle layer was separated from surrounding media by struvite layers at each side of the tube. The fabrication of such tubes could be performed without any delamination, although CPC and MPC with different lattice parameters were combined. This indicates that the main

mechanism behind mechanical stability is the interlocking of single crystals [163]. Additionally, the application of a brushite layer enabled the loading with vancomycin. A loading of a struvite layer was not possible due to an interaction of vancomycin with the ammonium phosphate solution needed for the setting of struvite. Thus, for new systems with different components like antibiotics or growth factors, possible interactions of cement components and drug have to be considered. Preliminary tests showed a successful release of vancomycin over a period of 15 days with more than half of the vancomycin left in the samples (Figure 31B). Samples that were loaded in the solid phase, exhibited a higher overall loading and a slower release of the antibiotic. On the one hand, this could be assigned to the fabrication technique. During centrifugation, a separation of solid and liquid phase occurred, where the solid particles are spun outwards and the liquid components remained inwards. After fabrication, the supernatant was discarded. When added to the solid, more of the vancomycin could be transported to the solid tube wall. In contrast, when added to the liquid, a lot of vancomycin was discarded yielding in a lower overall loading. On the other hand, the slower release could be explained by a better vancomycin distribution within the samples. Since vancomycin was added as a solid, a more homogeneous mixture could be achieved. However, the quantification of vancomycin via HPLC exhibited some problems. During dissolution at 37 °C, vancomycin started to degrade, which could be detected by a splitting of the signal. The main signal of fresh vancomycin appeared at a retention time of 7 – 7.5 min. Several degraded parts of vancomycin, however, could be detected at lower retention times between 3 and 6 min pointing to a cleavage of the molecule. In the end, it has to be investigated, if vancomycin fragments are still effective against bacteria. This would be decisive, which signals should be regarded for the quantification of release. Nevertheless, all peaks including vancomycin fragments were used for this quantification, since the system should be only a model for a drug delivery system. The long-term study over 50 days was then performed with the solid phase loading, as it had the greatest potential for a long-term release. Initially, there was a linear release over ~10 days followed by a flattening of the release curve until day 50 (Figure 32A). After 50 days,

~58 % of vancomycin was released, which made a fitting with the power law possible until day 50 (Figure 32B) [365, 368]. The release exponent could be determined with 0.35, which is lower than the release exponent for cylinders in Fickian diffusion processes (0.45). According to the power law, the Fickian diffusion is the most suitable release model for the vancomycin release observed in this test. The Fickian diffusion was described by Higushi, but just for thin polymeric films. Moreover, Higushi made several assumptions to simplify the model (see Section 2.7.2). While some assumptions like the pseudo steady-state condition or the perfect sink conditions could be maintained, the degradation of the cement matrix could interfere with the release model. The system of struvite and brushite is designed to degrade during implantation actively and passively. In this set-up, only the passive degradation could be considered, which resulted in a weight loss of 3 – 5 % with respect to the initial weight. The degrading matrix, however, influences the release kinetic due to larger pores or a thinner matrix barrier with shorter diffusion paths and better perfusion. These altered conditions are not considered in the Higushi model and the power law resulting in a slightly different release exponent and perhaps an altered release kinetic. Apart from a theoretical description of such degrading systems, the fabrication as well as a long-term release could be achieved. Furthermore, the system provides the opportunity of a higher release in acidic environment, as it is often found for bacterial infections [405, 406].

Centrifugally casting of medically relevant implants is the ultimate goal for this fabrication technique. The fundamental feasibility could be shown even for non-centrosymmetric implant for long bone replacement of a femur. It has to be taken into account, that this was only a first proof of principle with a single material, which is not optimized for load bearing defects. Nevertheless, it demonstrates that the ultimate goal could be achieved with this technique and that the processing of materials that were not suitable for other AM techniques is possible.

4.5 Conclusion

The parameters for the centrifugally casting process could be optimized for struvite tubes and transferred to the fabrication of brushite tubes. The comparison of those tubes with the well-established process of 3DP showed a further need for improvements regarding mechanical strength but a comparable energy absorption during loading. Therefore, this process can be adapted to the biomedical field for patient-specific implants. It can be utilized for further improvements of various properties including those not tunable in 3DP processes.

The reinforcement with fibers as well as a dual setting system could successfully be transferred to a new fabrication technique. Due to the forces involved during centrifugation of the cement slurry, the overall mechanical performance of the composite could be altered. However, with this study it could be shown that the goal of reinforcement was achieved for both strategies. The formerly brittle ceramics of CPC and MPC were modified to obtain damage tolerant composites paving the way to patient-specific implants for load-bearing applications.

With the help of ionic substitution, graded structures with increasing Ca^{2+}- and Sr^{2+}-substitution could be fabricated with centrifugally casting. A good adhesion between the single layers ensured mechanical stability during the time of implantation. With this tool bar, the biological properties regarding degradation and new bone formation can be tuned to obtain an optimal implant for each patient. Beside those properties, such graded cement tubes can be loaded with drugs or growth factors together with a controlled local release of the substances. The model of vancomycin loaded brushite tube flanked by struvite exhibited the possibilities for a long-term release, although a description with common release kinetic models turned out to be difficult. Apart from these tubes employed as a model for long bone replacement, an implant replacing the diaphysis of a human femur was manufactured. This proved that also non-centrosymmetric implants could be fabricated, as this is the general case for patient-specific implants.

5. Strontium substituted magnesium phosphate cements

5.1 Strength reliability and *in vitro* degradation of three-dimensional powder printed strontium-substituted magnesium phosphate scaffolds

This section was already published as full length article in the journal "Acta Biomaterialia" in 2016:

Susanne Meininger, Sourav Mandal, Alok Kumar, Jürgen Groll, Bikramjit Basu, Uwe Gbureck, Strength reliability and *in vitro* degradation of three-dimensional powder printed strontium-substituted magnesium phosphate scaffolds, Acta Biomater 31 (2016) 401-11.

The practical work as well as the writing of the article were performed by Susanne Meininger (née Christ). Micro-computed tomography imaging was pursued by S. Mandal, which is marked in the following article. B. Basu and U. Gbureck supervised the work and helped with final corrections of the manuscript. For this thesis, figures and abbreviations were adapted due to uniformity of this work.

Abstract

Strontium ions (Sr^{2+}) are known to prevent osteoporosis and also encourage bone formation. Such twin requirements have motivated researchers to develop Sr-substituted biomaterials for orthopedic applications. The present study demonstrates a new concept of developing Sr-substituted $Mg_3(PO_4)_2$ – based biodegradable scaffolds. In particular, this work reports the fabrication, mechanical properties with

an emphasis on strength reliability as well as *in vitro* degradation of highly biodegradable strontium-incorporated magnesium phosphate cements. These implantable scaffolds were fabricated using three-dimensional powder printing, followed by high temperature sintering and/or chemical conversion, a technique adaptable to develop patient-specific implants. A moderate combination of strength properties of 36.7 MPa (compression), 24.2 MPa (bending) and 10.7 MPa (tension) were measured. A reasonably modest Weibull modulus of up to 8.8 was recorded after uniaxial compression or diametral tensile tests on 3D printed scaffolds. A comparison among scaffolds with varying compositions or among sintered or chemically hardened scaffolds reveals that the strength reliability is not compromised in Sr-substituted scaffolds compared to baseline $Mg_3(PO_4)_2$. The micro-computed tomography analysis reveals the presence of highly interconnected porous architecture in three-dimension with lognormal pore size distribution having median in the range of 17.74–26.29 µm for the investigated scaffolds. The results of extensive *in vitro* ion release study revealed passive degradation with a reduced Mg^{2+} release and slow but sustained release of Sr^{2+} from strontium-substituted magnesium phosphate scaffolds. Taken together, the present study unequivocally illustrates that the newly designed Sr-substituted magnesium phosphate scaffolds with good strength reliability could be used for biomedical applications requiring consistent Sr^{2+}- release, while the scaffold degrades in physiological medium.

Statement of significance

The study investigates the additive manufacturing of scaffolds based on different strontium-substituted magnesium phosphate bone cements by means of three-dimensional powder printing technique (3DP). Magnesium phosphates were chosen due to their higher biodegradability compared to calcium phosphates, which is due to both a higher solubility as well as the absence of phase changes (to low soluble hydroxyapatite) *in vivo*. Since strontium ions are known to promote bone formation by stimulating osteoblast growth, we aimed to establish such a highly degradable magnesium phosphate ceramic with an enhanced bioactivity for new bone ingrowth.

After post-processing, mechanical strengths of up to 36.7 MPa (compression), 24.2 MPa (bending) and 10.7 MPa (tension) could be achieved. Simultaneously, the failure reliability of those bioceramic implant materials, measured by Weibull modulus calculations, were in the range of 4.3–8.8. Passive dissolution studies *in vitro* proved an ion release of Mg^{2+} and PO_4^{3-} as well as Sr^{2+}, which is fundamental for *in vivo* degradation and a bone growth promoting effect. In our opinion, this work broadens the range of bioceramic bone replacement materials suitable for additive manufacturing processing. The high biodegradability of MPC ceramics together with the anticipated promoting effect on osseointegration opens up the way for a patient-specific treatment with the prospect of a fast and complete healing of bone fractures.

5.1.1 Introduction

One of the treatment approaches for healing of critical size bone defects caused by trauma or tumor resection involves the implantation of bioceramics to maintain skeleton functionality. Among the many synthetic calcium phosphate ceramics and cements, farringtonite ($Mg_3(PO_4)_2$) and struvite ($MgNH_4PO_4 \cdot 6\,H_2O$) based on magnesium phosphate chemistry have attracted wider interest due to the fact that biodegradation is enhanced compared to calcium phosphate bone compounds [136, 141]. This aspect is decisive as autologous bone is still the gold standard in hard tissue replacement [43, 414, 415]. A second advantage of magnesium based bone cements is the lack of phase conversion into low soluble hydroxyapatite (HA; $Ca_{10}(PO_4)_6(OH)_2$), since Mg^{2+} ions are adsorbed on the surface of newly formed HA crystals by competing with and replacing Ca^{2+} ions. By blocking the crystallization site, further crystal growth of HA is then inhibited [118, 119].

Several studies have already proved that HA can hardly be resorbed under physiological conditions compared to other calcium and magnesium phosphate bone cements [78, 136, 141, 416]. Thus, the restriction of HA formation is favorable for bone substitutes and overall healing of bone defects. The inhibition of HA by incorporation of Mg^{2+} and degradation of magnesium-based cements also leads to

Mg^{2+} ion release into surrounding tissue, serum and circulating blood, whereas bone serves as a storage of Mg^{2+} and also helps in regulating ion balance [191, 192]. It is worthwhile to mention that the daily uptake (and excretion) of Mg^{2+} is in the range of 265 mg/day to 420 mg/day for adults (depending on age and gender) [192, 193], and side effects such as hypermagnesemia [193, 194] are unlikely to happen as a result of implanted magnesium phosphate ceramics. Recent calculations indicated an Mg^{2+} ion release of degrading struvite cement of only 22.8 mg/day [184] and 1.08 µg/day (for a 1 g implant) [144] and such release can unlikely lead to hypermagnesemia.

Following the degradation of bone substitute implants, new bone formation is essential for the replacement by fully regenerated bone. Several studies have already proved that strontium ions (Sr^{2+}) promote new bone formation due to their chemically similar behavior compared to Ca^{2+} [18-24]. The influence of Sr^{2+} is based on a cellular level, affecting both osteoblast and osteoclast cell fate processes [42, 352]. In particular, the Sr^{2+} ions are reported to promote the proliferation of osteoblast precursor cells and the differentiation into mature osteoblasts [348, 349]. Furthermore, strontium induces the activation of calcium sensing receptors within osteoblasts [350, 351]. This aspect has two major implications – (i) stimulation of osteoprotegerin production and (ii) release of receptor activator of the nuclear factor κB ligand (RANKL), which is responsible for osteoclastogenesis [417]. Osteoprotegerin binds to RANKL, which is expressed by osteoblasts [352]. Therefore, osteoprotegerin reduces the amount of free RANKL for osteoclastogenesis [418] and hence leads to a reduced cellular mediated bone resorption. Apart from that, Sr^{2+} exponentiates the effect of Ca^{2+} in terms of inducing osteoclast apoptosis, leading to a decreased bone resorption [353].

In addition to designing the formulation for bone reconstructive cements, processing of these materials is an important aspect to facilitate therapeutically successful results. In recent years, numerous additive manufacturing processes were developed for, or adapted to the fabrication of anatomically tailored patient-specific implants. Most important techniques involve stereolithography [248], selective laser sintering [255,

419], three-dimensional (3D) plotting and 3D printing [134, 247, 250, 270, 271, 277, 420-424]. The 3D powder printing (3DP) technology serves as an excellent tool for the fabrication of patient-specific ceramic implants with geometrically complex shape [7]. Computed tomography provides computer aided design (CAD) data of a patients individual defect structure. These data are digitally converted into a laminated structure that can be printed via a layer-by-layer technique. The use of a reactive binder leads to a hydraulic setting reaction, whereas the powder undergoes a phase transition and forms a solid by crystal growth [272, 278, 285]. Apart from this, a polymeric binder or a polymeric powder component can be utilized to act as glue leading to adhesion of powder particles [13, 277]. The latter technique includes a post-processing by sintering of the printed samples. During sintering, polymeric additives will be removed and simultaneously powder particles will be sintered and densified. Biocompatible implants for bone replacement manufactured by 3DP mainly used calcium phosphate cements (CPC) such as brushite, tricalcium phosphate or HA [8, 13, 276, 285, 286]. These bone cements, however, are either only slowly degradable or they may undergo a phase transformation during *in vivo* into lower soluble phases and therefore are not suitable for a non-permanent implant. Magnesium phosphate cements (MPC) are an adequate alternative due to their biodegradation and mechanical stability. To the best of our knowledge, only Vorndran et al. and Klammert et al. fabricated MPC using 3DP [134, 272] by employing an ammonium phosphate dibasic solution as binder to facilitate a phase conversion from farringtonite to struvite. In the above perspective, the present work aimed to fabricate degradable freeform implants with enhanced bioactivity by 3DP of MPC and strontium-substituted MPC (SrMPC) using 3D printing route with degassed ultrapure water as binder. Since the antiosteoporotic effect of strontium strongly depends on the extent of Sr^{2+} doping/incorporation [358], studies on such material, i.e. SrMPC need to consider different amounts of Sr^{2+} ions introduced to the implantation site. Accordingly, the magnesium phosphate powders ($Mg_3(PO_4)_2$) were supplemented with two different Sr^{2+} concentrations: $Mg_{2.5}Sr_{0.5}(PO_4)_2$ and $Mg_2Sr_1(PO_4)_2$. Fabrication was accomplished by particle adhesion with cellulose powder addition followed by

sintering, leading to mechanically stable three-dimensional parts. In addition, a phase conversion was obtained after sintering by immersion in ammonium phosphate dibasic solution. Apart from the extensive mechanical property measurements including critical analysis of strength reliability, *in vitro* degradation products of MPC were also investigated. An emphasis has been placed to evaluate strength reliability as well as microcomputed analysis of pore architecture and a comparison is made consistently between the sintered and chemically hardened scaffolds with different levels of Sr-substitution.

5.1.2 Materials & Methods

Powder synthesis and 3D powder printing

We used magnesium phosphate with three different concentrations for Sr-substitution, $Mg_3(PO_4)_2$, $Mg_{2.5}Sr_{0.5}(PO_4)_2$ and $Mg_2Sr_1(PO_4)_2$. All raw powders for material synthesis were mixed five times in a planetary ball mill (PM400 Retsch, Haan, Germany) for 1 h at 200 rpm. Farringtonite ($Mg_3(PO_4)_2$) was sintered with a 2:1 molar ratio of $MgHPO_4 \cdot 3\,H_2O$ (< 125 µm, Sigma-Aldrich, Steinheim, Germany) and $Mg(OH)_2$ (VWR, Radnor, USA). The composition for $Mg_{2.5}Sr_{0.5}(PO_4)_2$ was a 4:1:1 molar ratio of $MgHPO_4 \cdot 3\,H_2O$, $Mg(OH)_2$ and $SrCO_3$ (Sigma-Aldrich, Steinheim, Germany) respectively; similarly a 2:1 molar ratio of $MgHPO_4 \cdot 3\,H_2O$ and $SrCO_3$ yielded the composition $Mg_2Sr_1(PO_4)_2$. Powders were sintered in a furnace (Oyten Thermotechnic, Oyten, Germany) at 1050 °C in air for 5 h. The sintered cakes were crushed with pestle and mortar and sieved < 355 µm, to obtain the powder mix for three-dimensional printing experiments.

The three dimensional printing of the powder mix was performed on a spectrum Z510 printer (Z-Corporation, Burlington, USA). Each powder was supplemented with 5 wt% (hydroxypropyl)methylcellulose (HPMC; Fluka, Steinheim, Germany) and degassed ultrapure water served as binder. After depowdering, samples were sintered in a furnace (Nabertherm L08/14, Lilienthal, Germany) for 4 h in air. $Mg_3(PO_4)_2$ was

sintered at 1175 °C, whereas $Mg_{2.5}Sr_{0.5}(PO_4)_2$ and $Mg_2Sr_1(PO_4)_2$ were sintered at 1100 °C. Subsequently, the sintered samples were post-hardened by immersion in 3.5 M ammonium phosphate dibasic solution (DAHP; Merck, Darmstadt, Germany). By post-hardening, a conversion into struvite ($MgNH_4PO_4 \cdot 6\ H_2O$) was expected.

Mechanical properties

Compressive strength (CS), flexural strength (FS) and diametral tensile strength (DTS) of both groups of printed samples (sintered and post-hardened) were measured using the universal testing machine Zwick/Roell Z010 (Zwick GmbH&Co.KG, Ulm, Germany) with a 10 kN load-cell, a cross-head speed of 1 mm/min and a pre-load of 0.1 N. The sample dimensions were 12 x 6 x 6 mm, 45 x 5 x 4 mm and 10 x 20 mm for uniaxial compression, three-point bending/flexural and diametral compression experiments, respectively. The Weibull modulus (m), a measure of strength reliability of brittle solids, like ceramics/glass/cements, was calculated based on at least 30 samples. Based on weakest link statistics, the probability of failure, P_f represents the reliability of the ceramic on the basis of following equation:

$$P_f(\sigma) = 1 - \exp\left[-\int_V \left(\frac{\sigma - \sigma_t}{\sigma_0}\right)^m dV\right] \tag{5.1}$$

where V is the stressed volume, σ is the stress at failure, σ_0 is the scale parameter with a failure probability of 63.2 %, σ_t is the threshold stress and m is the Weibull modulus. Since σ_t is the stress below which the probability of failure is zero, it can be set to zero for brittle ceramics [172]. This assumption leads to the following expression (eq. 5.2):

$$P_f(\sigma) = 1 - \exp\left[-\left(\frac{\sigma}{\sigma_0}\right)^m\right] \tag{5.2}$$

Applying natural logarithm results in equation (4.8), which can be plotted and fitted. The slope of the fitted curve provides an estimate of the Weibull modulus (m).

$$\ln\left[\ln\left(\frac{1}{1-P_f(\sigma)}\right)\right] = m * ln\frac{\sigma}{\sigma_0} \quad (5.3)$$

In the present case, estimation of the probability of failure, P_f was performed according to equation (5.4):

$$P_f = \frac{n_R - 0.5}{N} \quad (5.4)$$

where, n_R is the rank number of the strength data and N is the number of tested samples [172, 425].

Phase assemblage

The phase composition of sintered and post-hardened samples was investigated by X-ray diffraction (XRD; PANalytical, X'Pert Pro, Almelo, Netherlands) in the range of 2 θ = 12.5° - 40°. XRD device was operated with a Cu-K_α radiation (λ = 0.15418 nm), a scan rate of 1 s/step and a step size of 0.02°. The phase identification was checked using ICDD (International Centre for Diffraction Data) database for farringtonite (PDF Ref. 33-0876), $Mg_2Sr_1(PO_4)_2$ (PDF Ref. 14-0206) and struvite (PDF Ref. 03-0240). The surface morphology was observed by scanning electron microscopy (SEM, Inspect F50, FEI, Hillsboro, USA) at an accelerating voltage of 10 kV after sputtering of the samples with gold to avoid the charging during scanning.

Micro-computed tomography[1]

Microporosity of 3D printed/sintered samples was measured by micro-computed tomography (micro-CT) with a VersaXRM-500 (Xradia, Zeiss, Jena, Germany). For different sample composition, the X-ray source energy was ranging between 40 – 110 kV. A 4x objective with 5 – 15 s exposure time and suitable filters for single image acquisition was employed to get an ideal transmission of at least 25 – 35 %.

[1] The micro-CT measurements were performed by the co-author Sourav Mandal.

Total 3201 2D transmission images were captured within 360° sample rotation. The collected 2D images were reconstructed into a 3D tomogram in XMReconstructor software (Xradia, Zeiss, Jena, Germany) using standard beam hardening correction with 0.7 kernal size. Manual reconstruction was done visually in the case of failure of auto-reconstruction by adjusting center-shift and beam-hardening values. Image processing, analysis and visualization were performed with commercially available software (Avizo Fire 8.1, FEI, France). First, the 3D images were calibrated into same grey level using 'match contrast' module and when the histogram was narrow, it was stretched to get better contrast range with 'histogram equalization'. Non-local-means filter was applied for noise reduction. Subsequently, images were binarised and separated with suitable connectivity and marker extent parameters. The application of opening module with kernel size 1 discarded all the pores below voxel size 1. Then label analysis was carried out to identify connected and separated objects. The obtained results were visualized with orthoslice and volume rendering module in 2D and 3D respectively. To quantify the pore size distribution of the non-interconnected pores, the equivalent pore diameters (EqD) obtained from micro-CT analysis was plotted in histograms with a bin size of 5 µm and fitted with suitable function. Porosity measurement by micro-CT has the advantage over conventional techniques e.g. Mercury porosimetry as the former provides the detail of both open and closed pores. All these quantification was performed considering both interconnected and non-interconnected pores i.e. for open and closed porosity, respectively. Limited by the voxel size for the measurement only pores with a size of 4.5 µm or bigger were included into calculation.

In vitro dissolution study

The *in vitro* dissolution experiments with cylindrical samples (diameter 15 mm and height 5 mm) was performed in Dulbecco's Modified Eagle's Medium (DMEM; 4.5 g/l Glucose, L-Glutamine, Sodium Pyruvate, L-Cystine, 3.7 g/l $NaHCO_3$, Gibco, Carlsbad, USA) for 10 days. The inductively coupled plasma mass spectrometry (ICP-MS; Varian, Darmstadt, Germany) was used for the quantification of ion release and

adsorption. Magnesium ions, strontium ions and phosphate ions as well as calcium ions have been detected in solution after experiments against standard solutions (5 ppm and 10 ppm). Dissolution media was changed after every 24 h and samples were stored at 37 °C. The ion concentration was calculated with respect to fresh DMEM.

Statistics were performed with ANOVA using the program SigmaPlot 12.5 (Systat Software, Inc., 2011). Sintered and post-hardened samples were compared among each other.

5.1.3 Results

In reference to the additive manufacturing of MPC/SrMPC, the present study reveals that ultrapure water can be reproducibly used as binder for 3D printing of different sized/shaped samples. We could not measure any significant dimensional changes or distortion of the as-printed scaffolds with respect to the respective .stl files. Microscopic measurements of all geometries employed for mechanical testing revealed a deviation of less than ± 0.4 mm.

Subsequently, the as-printed samples were sintered at 1100 °C (SrMPC) or 1175 °C (MPC), followed by chemical hardening in $(NH_4)_2HPO_4$ (DAHP) solution. In this section, we present illustrative results to elaborate how post-printing treatment together with compositional variation influences the phase stability, porous architecture development, mechanical strength reliability and *in vitro* ion release.

Phase assemblage analysis using XRD

While analyzing the X-ray diffraction patterns, plotted in Figure 34, we observed that pure MPC predominantly contain farringtonite (f). The characteristic peaks of the farringtonite phase lie at $2\theta = 26$ and 23.25° and other lower intensity peaks are located in the range of 20 – 22° or at 24.5°. Importantly, a clear difference in the evolution of X-ray peak at $2\theta = 23.25°$ is recorded after sintering in SrMPC samples.

Apart from a clear peak shift, either a shoulder peak or a broadened peak appears in the range of 2θ = 23 – 23.25° for the sintered SrMPC. Simultaneously, the intensity of the farringtonite peak at 2θ = 26° is either significantly reduced or the peak disappears in SrMPC. Such observations are also made with lower intensity X-ray peaks of f-phase in SrMPC, with respect to MPC. All these observations together indicate a progressive phase conversion of farringtonite into $Mg_2Sr_1(PO_4)_2$ phase, indicated as x-phase in Figure 34, in the as-sintered SrMPC samples.

In the post-hardened samples, the characteristic peak of struvite (s) appears at 2θ = 21°, irrespective of sample composition. In summary, the post-hardened $Mg_2Sr_1(PO_4)_2$ predominantly contains targeted phase of $Mg_2Sr_1(PO_4)_2$ together with struvite, indicating a complete phase conversion. In contrast, $Mg_{2.5}Sr_{0.5}(PO_4)_2$ sample contains a mixture of f, x and s-phases. Such a difference in the phase assemblage should have an influence on mechanical strength or *in vitro* ion release properties. The results summarized below will either contradict or support this hypothesis.

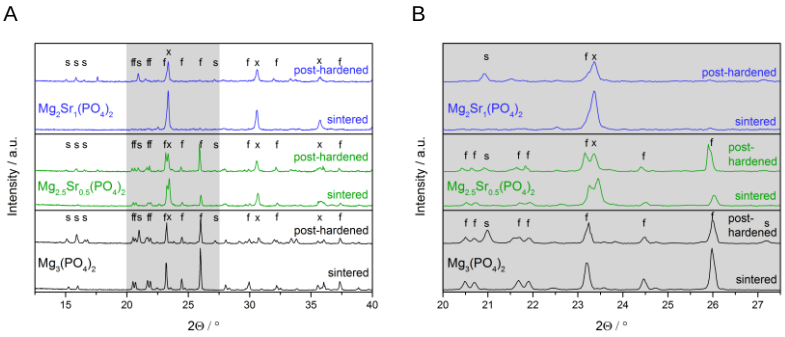

Figure 34: XRD spectra of sintered and post-hardened MPC and SrMPC (A) and a section of this spectra (grey area) for 2θ = 20 – 27.5° (B). Post-hardening in DAHP leads to a conversion of farringtonite (f) into struvite (s). SrMPC contain $Mg_2Sr_1(PO_4)_2$ (x), depending on the overall strontium content.

SEM and micro-CT analysis[2]

SEM observation of the surface topography revealed that the round shaped particles were sintered together (Figure 35). With increasing strontium content, particles seem to become smaller due to recrystallization. Additionally, porosity and the specific surface area were increased after sintering, which was confirmed using micro-CT (Figure 36). During post-hardening, the phase conversion into struvite led to a densification of the material revealing a decrease in porosity. Since samples were dried at room temperature after immersion, sharp edged ammonium phosphate (DAHP) crystals were formed as a consequence of water evaporation.

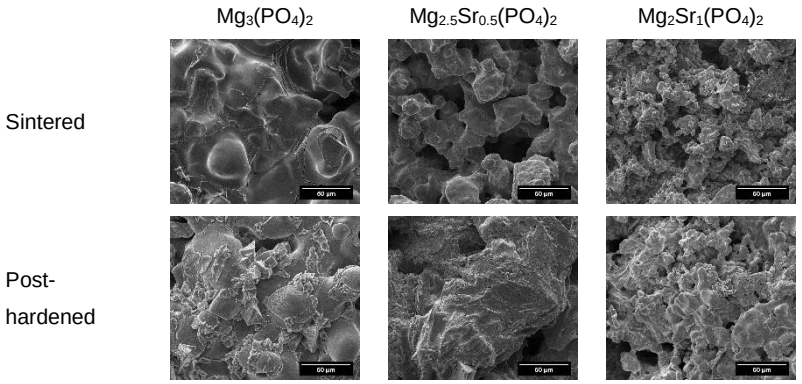

Figure 35: SEM images revealing surface morphology of sintered and post-hardened MPC and SrMPC.

As a part of three-dimensional microstructure evaluation, micro-CT study revealed the phases within the cement samples (Figure 36). Different grey levels for Sr-substituted scaffolds revealed a second phase, apart from that already observed for pure MPC. For Sr-substituted samples, pores were highly interconnected, whereas MPC had mostly closed pores. It was found that the pores are homogenously distributed throughout the sample volume, and this aspect was confirmed from

[2] Data from micro-CT measurements, visualization and calculation of the pore equivalent diameter were pursued by Sourav Mandal. Analysis and interpretation of the results were performed by myself.

volume rendered images of representative 3D volume of 1416 x 2718 x 1217 µm^3 (see Figure 36, colored images). The porosity of all compositions was in the range of 15–25 % and was independent of post-hardening, as shown in Figure 37. The pore size distribution is monomodal and narrow and also very similar for all compositions with a main pore fraction in the range of 4.5–25 µm (see Figure 37 and Table 14).

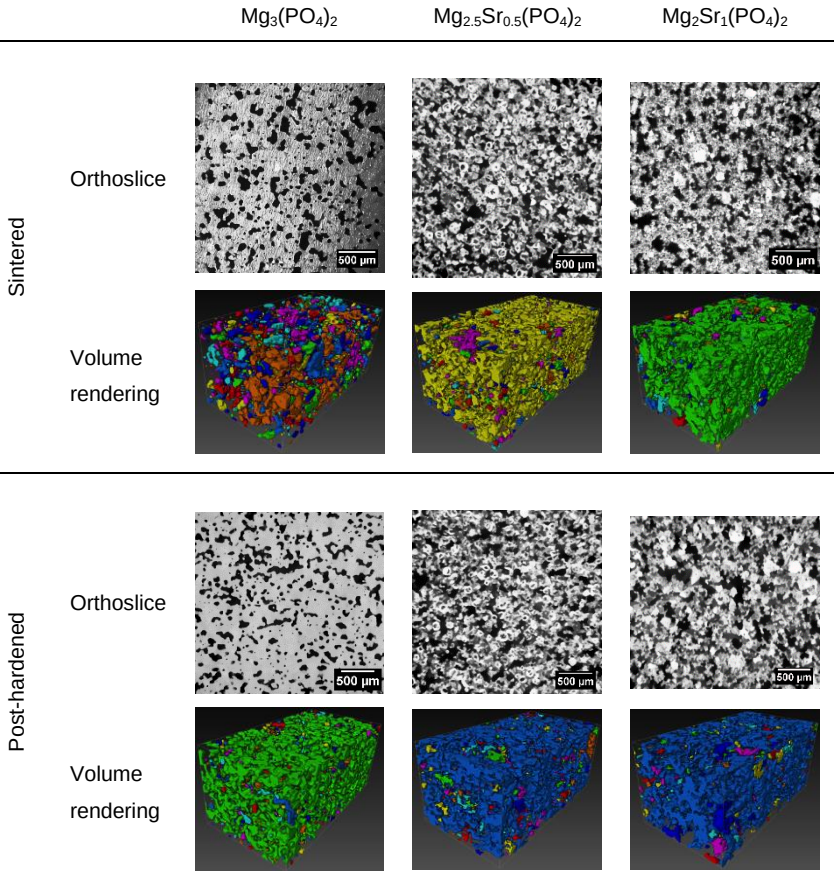

Figure 36: 2D and 3D micro-CT images of sintered and post-hardened MPC and SrMPC samples. The orthoslice views show porosity in black and bright grey levels as material composing different compounds. Different colors in the volume rendered 3D sections are representative of pores with varying level of interconnectivity.

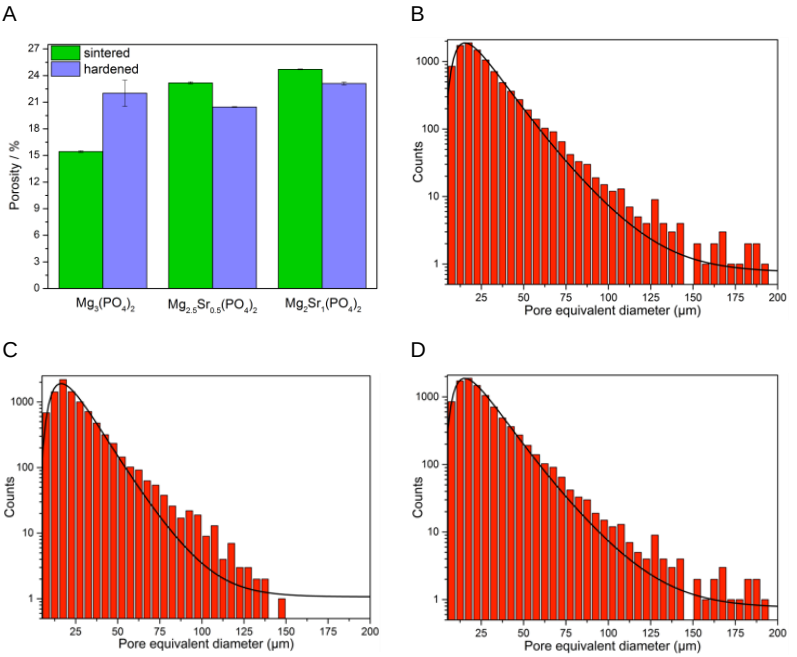

Figure 37: Porosity of sintered and post-hardened MPC and SrMPC calculated from micro-CT data. (A) Measurement includes pores down to a size of 4 µm. (B)-(D) are representative distribution of pore equivalent diameter for $Mg_3(PO_4)_2$ post-hardened, $Mg_{2.5}Sr_{0.5}(PO_4)_2$ sintered and post-hardened.

Table 14: The mode and median of pore size distribution for cements without strontium and with two different strontium concentrations was evaluated by micro-CT for sintered and post-hardened samples (±standard deviation). The equivalent pore diameters for all the samples follow lognormal distribution with a correlation coefficient of 0.97 – 0.99, irrespective of scaffold composition.

		Pore size distribution	
		Mode in µm	Median in µm
$Mg_3(PO_4)_2$	Sintered	11.48 ± 3.17	26.29 ± 3.93
	Hardened	9.63 ± 0.00	21.00 ± 0.40
$Mg_{2.5}Sr_{0.5}(PO_4)_2$	Sintered	9.59 ± 0.00	19.73 ± 1.16
	Hardened	10.12 ± 1.08	21.26 ± 0.86
$Mg_2Sr_1(PO_4)_2$	Sintered	8.42 ± 1.87	17.74 ± 2.00
	Hardened	11.30 ± 3.12	25.67 ± 2.85

Mechanical properties

The sintered as well as post-hardened samples of each composition were tested for the compressive, flexural and tensile strength (Figure 38). Interestingly, post-hardened samples revealed a higher strength than the respective sintered counterpart. Among all the tested samples, $Mg_{2.5}Sr_{0.5}(PO_4)_2$ had the highest strength with a compressive strength of 36.7 MPa, flexural strength of 24.2 MPa and tensile strength of 10.7 MPa. The measured strength values indicate that MPC or SrMPC is stronger in compression and weaker in tension with flexural strength lying in between tensile and compression values. This is consistent with the mechanical behavior of any brittle ceramic. The weakest samples for both sintering and post-hardening contained the highest strontium content, i.e. $Mg_2Sr_1(PO_4)_2$. Additionally, the strength reliability of ceramic samples under tension and compression was evaluated by determination of the Weibull modulus (m) according to eq. (5.1) – (5.4) (Figure 39). In contrast to the maximum strength, Weibull moduli were independent of both strontium content and post-hardening and this has been one of the important observations (see Table 15). Furthermore, the m values were in the same range between 5.3 and 8.8 for uniaxial-compression tests and 4.3 – 7.4 for diametral tensile tests (tensile strength). Such observations therefore indicate the absence of any significant difference between tensile/compressive moduli for MPC/SrMPC.

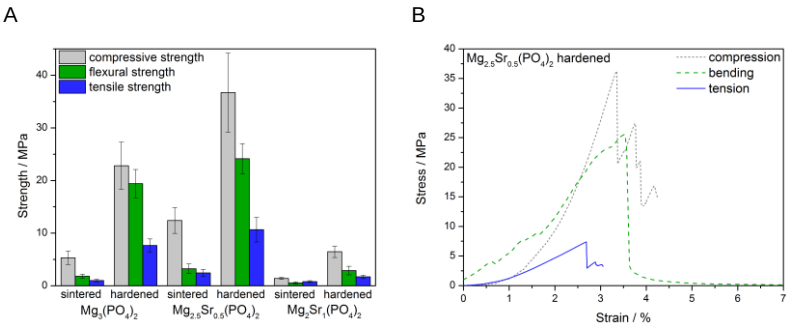

Figure 38: Plot of the strength properties of three compositionally different scaffolds under uniaxial compression, diametral compression and three point flexural mode (A). A representative plot of stress-strain response of SrMPC under these three different modes is also shown (B).

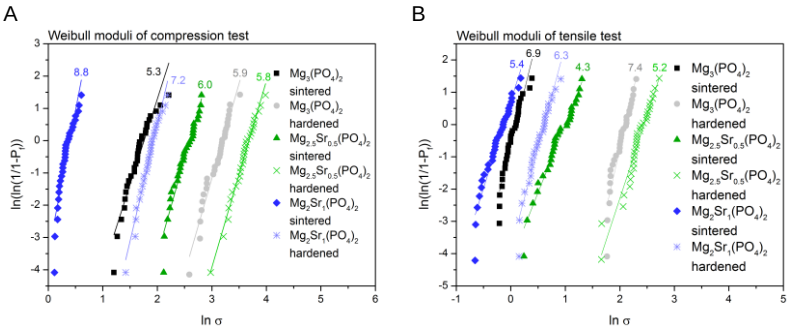

Figure 39: Weibull plots for determination of Weibull moduli from compression (A) and diametral tensile test (B), respectively, for pure MPC and SrMPC. Weibull moduli were calculated according to eq. (5.1)-(5.4).

Table 15: Summary of Weibull moduli (m ± standard deviation) obtained from compressive strength (m_{CS}) and diametral tensile strength (m_{DTS}) for cement without strontium and with two different strontium concentrations.

		Weibull modulus m (R^2)	
		m_{CS}	m_{DTS}
$Mg_3(PO_4)_2$	Sintered	5.3 ± 0.3 (0.91)	6.9 ± 0.4 (0.92)
	Hardened	5.9 ± 0.2 (0.96)	7.4 ± 0.5 (0.90)
$Mg_{2.5}Sr_{0.5}(PO_4)_2$	Sintered	6.0 ± 0.3 (0.94)	4.3 ± 0.2 (0.97)
	Hardened	5.8 ± 0.1 (0.99)	5.2 ± 0.2 (0.95)
$Mg_2Sr_1(PO_4)_2$	Sintered	8.8 ± 0.6 (0.88)	5.4 ± 0.2 (0.94)
	Hardened	7.2 ± 0.2 (0.97)	6.3 ± 0.3 (0.95)

Dissolution study

The results of the release and adsorption of Mg^{2+}, Ca^{2+}, PO_4^{3-} and Sr^{2+} during *in vitro* dissolution are shown in Figure 40. The release of Mg^{2+} in solution was highest for MPC and almost constant over the whole period of dissolution. In contrast, PO_4^{3-} and Sr^{2+} release were dependent on the scaffold composition and the post-hardening step. Both MPC (sintered and post-hardened) and sintered SrMPC had a very low but consistently slow release. Post-hardened SrMPC showed a very high release within

the first 6 days and remained high with a constant release afterwards. Among all ions investigated, PO_4^{3-} was released most with the highest release of 540 mg/l for the first day. The cumulative ion release of the cements was calculated for the whole period of 10 days and referred to the total mass of each sample. Again, the highest Mg^{2+} release was observed for MPC and it decreased with strontium substitution. Since cements did not contain any Ca^{2+}, both sintered and post-hardened samples adsorbed Ca^{2+} ions from surrounding DMEM. Using XRD, no phase conversion was observed after 10 days (data not shown). The release and adsorption of PO_4^{3-} depend on the cement composition. After post-hardening, PO_4^{3-} ions were released whereas sintered samples revealed an adsorption during dissolution. Furthermore, the amount of PO_4^{3-} release depends on strontium substitution with a higher strontium content leading to a higher release of PO_4^{3-}. This phenomenon can also be observed for Sr^{2+} release which reached a maximum of 127 mg/l over 10 days.

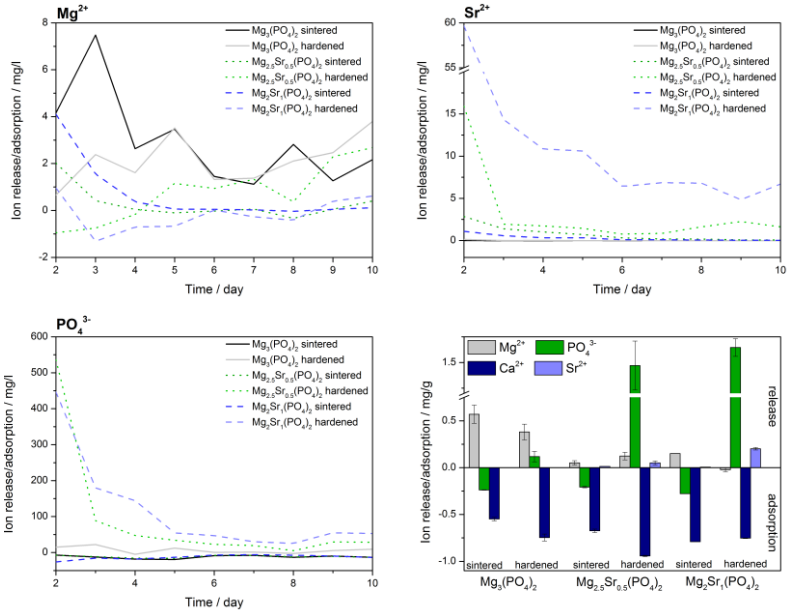

Figure 40: Cumulative ion release for the dissolution study in DMEM culture medium for 10 days. Mg^{2+}, PO_4^{3-}, Ca^{2+} and Sr^{2+} were detected by ICP-MS.

5.1.4 Discussion

Phase stability

For the present study, MPC was substituted by strontium ions to enhance the bone formation and therefore support the regeneration of critical size bone defects. The XRD results confirm the substitution of Mg^{2+} by Sr^{2+} with increasing $Mg_2Sr_1(PO_4)_2$ content (Figure 34). For the scaffold composition $Mg_{2.5}Sr_{0.5}(PO_4)_2$, both farringtonite and $Mg_2Sr_1(PO_4)_2$ phases were present, whereas farringtonite completely disappeared for the composition $Mg_2Sr_1(PO_4)_2$. This means that $Mg_{2.5}Sr_{0.5}(PO_4)_2$ is just a theoretical composition, actually being a mixture of farringtonite and $Mg_2Sr_1(PO_4)_2$.

Additionally, MPC and SrMPC were investigated in two different modifications: sintered and post-hardened. Post-hardening was performed by immersion of sintered samples in diammonium phosphate (DAHP) solution. The observation of phase composition (see Figure 34A and B) revealed the formation of struvite for both MPC and SrMPC according to eq. (5.5):

$$2\ Mg_3(PO_4)_2 + 3\ (NH_4)_2HPO_4 + 6\ H_2O \rightarrow 6\ MgNH_4PO_4 \cdot 6\ H_2O + H_3PO_4 \qquad (5.5)$$

Struvite formation was independent of strontium content, suggesting that SrMPC can also be converted into fast degrading struvite. The absence of a new strontium containing phase revealed that either an amorphous strontium phosphate was formed during conversion or that strontium ions were incorporated into the struvite lattice.

Surface morphology analysis using SEM

SEM images of the post-sintered MPC showed round shaped particles fused together (Figure 35). The round structure on the surface is favorable since sharp edged particles are known to lead to inflammation of surrounding tissue *in vivo* [144, 224, 426]. In our experiments, the lowest possible temperature was chosen for the sintering process to avoid shrinkage and stresses within the sample such that an optimal mechanical performance can be achieved. Typical necks between the particles indicate the

signature of diffusional mass transport during sintering. Also, low sintering temperatures (i.e. 1100 °C and 1175 °C, respectively) lead to limited grain growth, which is confirmed by the porous structure of the sintered samples. Importantly, no signature of phase or lattice conversion was found, as analyzed by the XRD. Interestingly, phase conversion into struvite due to post-processing results in increase in particle size. As XRD reveals this conversion to struvite was not completed even for post-hardened samples, where farringtonite and $Mg_2Sr_1(PO_4)_2$ were found in samples. Although SEM analysis confirmed the presence of large particles of converted phase on the surface, we are expecting non-converted inner core with MPC and SrMPC phases.

3D microstructural analysis from micro-CT[3]

Importantly, micro-CT data reveal the presence of different phases in three dimension in highly interconnected porous scaffolds. For SrMPC, two different phases were found, illustrating a phase mixture of $Mg_2Sr_1(PO_4)_2$ and farringtonite. From the 3D volume rendered image, we can also visualize the amount of interconnectivity. With the help of 'labelling' module, the pore spaces connected with each other are considered as single object and shown with same color, whereas each non-connected pores are colored with different color as they are different 'objects'. Although the color code is arbitrary, all the samples show one majorly interconnected pore space and small fraction of non-connected pores throughout, except in MPC samples. This can be attributed to the different sintering temperature. For example, MPC samples were sintered at higher temperature than were SrMPC samples, leading to more separated pores with least interconnectivity in case of MPC. Although, we see the presence of more than one material phase qualitatively, there is not enough difference in X-ray opacity between the converted and non-converted phases to distinguish them quantitatively. It is important to mention that a homogenous distribution of pores was

[3] Data from micro-CT measurements were collected by Sourav Mandal. Analysis and interpretation of the results were performed by myself.

noticed and this indicates the efficacy of the adopted printing parameters to generate homogeneous scaffolds. In addition, pore size and pore size distribution seem not to be layer dependent such that the manufacturing process of 3DP did not lead to an anisotropic structure.

The specific surface area of a porous scaffold depends on the pore size and the degradation is a surface dependent mechanism. Thus, an open porosity and a high specific surface will lead to a faster and more homogeneous resorption of the scaffold, *in vivo*. Interconnectivity, especially found for Sr-substituted samples, will provide a sufficient nutrient supply, which is essential for the cell invasion and tissue formation. The extensive analyses of pore sizes in 3D for MPC or SrMPC scaffolds reveal lognormal distribution with correlation coefficient > 0.98 of pore equivalent diameter (EqD) (Figure 37 and Table 14). The general mathematical formula of the distribution is shown here, in terms of probability density function (*y*, PDF)

$$y = \frac{1}{x s_p \sqrt{2\pi}} \exp\left(-\frac{(\ln x - \mu)^2}{2 {s_p}^2}\right) \tag{5.6}$$

where, x is lognormally distributed variable (here, EqD), μ and s_p are location and scale parameters respectively and the median and mode of the above distribution function is e^{μ} and $e^{\mu - sp^2}$ respectively. This kind of distribution is frequently observed for various natural phenomena e.g. disease models [427], measure of sizes of living tissue [428] etc. The median (value that divides the higher and lower half of the distribution) and mode (value with highest number of data points) of the EqD are quite close for all the samples with values of 17.74 – 26.29 µm and 8.42 – 11.48 µm, respectively (see Table 14). In general, the pore size of interconnected pores is quite high, especially in case of SrMPC. Although the microporosity of non-connected pores is too small for osteoblasts or blood vessel ingrowth [208, 210, 383, 429], the interconnected pore space will have more influence due to high cumulative volume than non-interconnected micropores, as previously discussed. Moreover, the high

specific surface area and a fast degradation will probably widen up the micropores, enabling ingrowth of surrounding tissue at later time point when the implant degrades.

Mechanical strength reliability

Sintered and post-hardened samples were investigated for their mechanical properties under different loading situations. Similar to a classical brittle ceramic, the strengths of MPC/SrMPC materials were higher in uniaxial compression, three-point flexural and diametral tensile mode of loading. This order is also consistent with calcium phosphate based bioceramics [78]. The compressive strength as well as the tensile strength is in the range or even exceeds that of cancellous bone, but is still lower than the strength of cortical bone [430-434]. Pittet and Lemaitre reported that the diametral tensile strength underestimates the real tensile strength by 85 % [435], which would lead to a true tensile strength of up to 12.5 MPa for post-hardened $Mg_{2.5}Sr_{0.5}(PO_4)_2$. Thus, mechanical properties of all cement compositions reported here are in accordance with the mechanical properties of a cancellous bone. To further increase the mechanical properties of the cements like strength or failure resistance, samples might be infiltrated with other materials (e.g. polymers) (see Section 3). Another very important parameter for implanted biomaterials is the reliability under different loading situations. Here, the Weibull modulus quantifies the failure probability with data obtained from mechanical tests, when weakest link fracture statistics is assumed [436]. However, determination of Weibull moduli for bioceramics is rare and not much data are available. For MPC and SrMPC, Weibull moduli were calculated with data from compression and diametral tensile tests ranging from 5.3 to 8.8 for compression-based moduli and 4.3–7.4 for tensile-based moduli (see Figure 39 and Table 15). Since ceramic materials typically exhibit Weibull moduli between 5 and 20 [425], MPC and SrMPC are in the lower half but still within this range. Cordell et al. [12] observed a relationship between microporosity and the reliability of bioceramics, which could not be proved by our results. Thus, the failure mechanisms seem to be much more complex, especially for a system of printed, sintered and post-hardened samples. Nevertheless, the reliability of magnesium-based ceramics is not

compromised to any extent by Sr-substitution, enabling the application of these biomaterials as implant materials.

In vitro dissolution

A dissolution study was performed in order to investigate passive degradation of MPC and SrMPC in sintered and post-hardened state. Ion release into and adsorption from surrounding body fluids can directly influence ion balance that is required for the bone healing. A main degradation product of MPC and SrMPC are Mg^{2+} ions. These ions can be incorporated into newly formed bone equivalently to Ca^{2+} ions [191, 192]. Nevertheless, the buffering effect of bone to a large amount of Mg^{2+} ions is limited, thus an overdose may lead to hypermagnesemia with severe consequences. The average daily Mg^{2+} release found in this study was far lower than the maximum daily uptake for adults [192, 193]. Thus, the release during degradation will likely not have side effects even for very large implants. The Mg^{2+} release further decreased for SrMPC with increasing strontium content (Figure 40). This might be either due to stoichiometric reasons (lower Mg^{2+} ion content in SrMPC) or to a reduced solubility of SrMPC. Since the PO_4^{3-} release for post-hardened samples is much higher for SrMPC than pure MPC, it seems more likely that Mg^{2+} ions were replaced by Sr^{2+} in the crystal lattice of struvite. The release of PO_4^{3-} ions was observed only for post-hardened samples, whereas sintered MPC and SrMPC adsorbed PO_4^{3-} from the medium. This can be explained by the changes of the Mg:P ratio, which was 3:2 for farringtonite and decreased to 1:1 for struvite after conversion. Hence, during degradation of struvite, more PO_4^{3-} ions will be released into the dissolution media than during degradation of farringtonite. Additionally, struvite has a higher degradation rate than farringtonite [141] and, therefore, this increases the ion concentration. This phenomenon was even more evident for SrMPC samples. However, compared to Mg^{2+} and PO_4^{3-}, the release of Sr^{2+} ions was very low with a maximum cumulative release of 0.2 mg/g after 10 days, even for post-hardened $Mg_2Sr_1(PO_4)_2$. The released Sr^{2+} ions can be incorporated into bone tissue [437] and

can promote bone remodeling or bone formation directly at the implant site [42, 348-353, 417].

The results obtained in this study indicated that Sr-substitution overall enhanced the degradation of the magnesium phosphate scaffolds and will likely promote the ingrowth of new bone tissue. Although Ca^{2+} ions were adsorbed to all sample surfaces, independent of strontium content in a range of 0.55–0.94 mg/g, XRD analyses did not show any phase conversion to HA or any other calcium phosphate on the sample surface. This can be due to several reasons: (1) phase conversion may have occurred only in a very thin layer which was not detectable by XRD. (2) An amorphous layer of calcium phosphate was built on the surface. Since no amorphous background could be detected by XRD, either no phase conversion occurred or the amorphous layer again was too thin for detection. (3) Beside phase conversion, Ca^{2+} ions could just be physically adsorbed onto the cement surface. The latter possibility is supported by the inhibiting effect of Mg^{2+} ions on phase conversion to HA [118, 119] and a continuing degradation even after 10 days of dissolution.

5.1.5 Conclusion

On the basis of the experimental results analyzed in this paper, the following key points can be summarized:

(a) Three-dimensional powder printing together with sintering followed by chemical conversion has been established as a viable processing strategy to fabricate mechanically reliable $Mg_3(PO_4)_2$ or Sr-substituted $Mg_3(PO_4)_2$ based biodegradable scaffolds. Also, our results illustrate that ultrapure water can be used as binder.

(b) The critical analysis of micro-computed tomography results clearly infers that 3D printed SrMPC scaffolds are characterized by highly interconnected porous architecture with lognormal pore size distribution. The median and mode of such distribution varies in the range of 8.42 – 26.29 µm, depending on the scaffold composition or the post-printing treatment.

(c) The compositional design approach followed by combinatorial post-printing treatment allows targeted phase of $Mg_2Sr_1(PO_4)_2$ in higher Sr-substituted MPC. Also, the chemical hardening treatment favors the struvite phase formation.

(d) A combination of moderate compressive strength around 40 MPa and flexural strength of 10 MPa can be obtained in $Mg_{2.5}Sr_{0.5}(PO_4)_2$.

(e) The extensive analysis of strength measurements in the light of the weakest-link fracture statistics reveals that the Weibull modulus is not compromised to any extent in Sr-substituted MPC. More importantly, $Mg_2Sr_1(PO_4)_2$ scaffolds exhibit higher Weibull modulus in compression (m_{cs} = 8.8) compared to other scaffold compositions.

(f) The *in vitro* dissolution experiments revealed slow but consistent release of Sr^{2+} or PO_4^{3-} ions together with reduced release of Mg^{2+} ions from chemically hardened $Mg_2Sr_1(PO_4)_2$ scaffolds.

The above-described property combination can be useful in application of SrMPC as bioresorbable scaffolds.

5.2 *In vitro* cell study of three-dimensional powder printed strontium-substituted magnesium phosphate scaffolds

5.2.1 Introduction

The evaluation of the mechanical performance (as described in Section 5.1) is a fundamental requirement when thinking of the application as implant material. Since the material should be used within the human body, the biological response is also a crucial feature. Although MPC are relatively new in the field of bone replacement material, they exhibit several advantages over the already established CPC, like a fast degradation *in vivo* or the phase stability [118, 119, 141] (see Section 2.4.2 – 2.4.4). Additionally, the substitution with strontium ions can further support new bone formation by the intervention in signaling pathways (see Section 2.7.1). For the

composition tested in terms of mechanical performance in Section 5.1 ($Mg_3(PO_4)_2$, $Mg_{2.5}Sr_{0.5}(PO_4)_2$ and $Mg_2Sr_1(PO_4)_2$), a biological investigation was performed. As a first step, *in vitro* test with different cell lines in different testing modes are necessary to investigate such biological responses to the modified MPC. Osteoblast cell lines were employed, since the strontium addition is said to have a promoting effect on the proliferation of such cells. On the one hand, cells were seeded directly on the cement surface, which simulates a cellular colonization *in vivo*. However, the degradation of MPC is enhanced by strontium substitution [90] making another indirect test method necessary. For the indirect cytotoxicity test, cements were immersed in cell culture media as it was performed for the dissolution study of ion release. After dissolution, cell response to the altered ion concentration in cell culture media was observed.

5.2.2 Materials & Methods

The evaluation of biological properties was performed by a direct seeding of cement samples as well as an indirect cytotoxicity test with eluate. For direct cell seeding samples (n = 4; 11 x 5 mm) with different strontium content were cultured with two different osteoblast cell lines MG63 and human fetal osteoblast cell line 1.19 (hFOB), respectively, in a 48-well plate. Prior to testing, cement samples were disinfected with 70 % ethanol. Dulbecco's Modified Eagle's Medium (DMEM, Cat.No.: 31966-021, Gibco, Carlsbad, USA) supplemented with 1 % Penicillin-Streptomycin (Cat.No.: 15140-122, Gibco, Carlsbad, USA), 1 % HEPES 1M (Cat.No.: 15630-056, Gibco, Carlsbad, USA) and 10 % fetal calf serum (FCS; Cat.No.: 10270-106, Gibco, Carlsbad, USA) was applied for MG63. hFOB was cultured in Dulbecco's Modified Eagle's Medium (DMEM/F12, Cat.No.: 313311-028, Gibco, Carlsbad, USA) supplemented with 1 % Penicillin-Streptomycin, 0.3 g/L Geneticin G-418 Sulphate (Cat.No.: 11811-064, Gibco, Carlsbad, USA) and 10 % FCS. Polystyrene (PS) served as reference to control the behavior of MG63 and hFOB during culture and was seeded with $5 \cdot 10^4$ cells/ml, whereas cement samples were seeded with $10 \cdot 10^4$ cells/ml. Incubation was performed at 37 °C (MG63) and 34 °C (hFOB) and 5 % CO_2 over 10

days, while media was exchanged every 2 – 3 days. After day 3, 7 and 10 cell number and cell activity were evaluated using a Neubauer chamber and water-soluble tetrazolium salt (WST) test, respectively. Prior to counting, cells were detached from scaffold surfaces by incubation with accutase (Cat.No.: L11-007, PAA, Boston, USA). For WST test cells were incubated with WST-1 reagent (dilution 1:10) and the supernatant was analyzed with a spectrometer (Tecan SpectraFluor Plus, Tecan, Maennedorf, Switzerland) at a wavelength of 450 nm. Samples were tested of highly significant differences (*, $p < 0.01$) with SigmaPlot 12.5 (Systat Software, Inc., 2011) in a two way ANOVA and a Tukey test.

Indirect cytotoxicity test was performed with the eluate from cement samples. Therefore, hFOB were cultured in 48-well plate with a cell density of $83 \cdot 10^3$ cells/ml. Cement samples were again disinfected with 70 % ethanol. Samples were immersed in 412 µl (equal to 1.05 µl/mm³) DMEM/F12 supplemented with 1 % Penicillin-Streptomycin, 0.3 g/l Geneticin G-418 Sulphate and 10 % FCS. Medium was exchanged daily and added to cells for cultivation. For each cement n = 4 wells were seeded and cultivated at 34 °C and 5 % CO_2. Culture media with the same composition was used for the reference. Prior to immersed media exposure, cells were cultivated for 1 day in as-prepared medium, whereas day 0 was defined as the day of first exposure. Just as for the direct seeding, after day 3, 7 and 10 cell number and cell activity were evaluated using a cell counter (Casy, Roche innovates AG, Germany) and WST test, respectively. Prior to counting, cells were detached from well plate surfaces by incubation with accutase. For WST test, cells were incubated with WST-1 reagent (dilution 1:10) and the supernatant was analyzed with a spectrometer.

5.2.3 Results

Biocompatibility was investigated regarding cell number and cell activity over 10 days with MG63 and hFOB (Figure 41) first in a direct seeding of the cement samples. The results of cultivation with MG63 are shown in Figure 41A and B. Cell number varied between all three cement compositions especially after 10 days. After 3 days a

reduction of cells could be observed for all cements. Cells on pure MPC and $Mg_{2.5}Sr_{0.5}(PO_4)_2$ proliferated during culture, whereas on cement with the highest Sr^{2+} concentration cell number remained lower than the seeding density. In general, it can be stated that with increasing Sr^{2+} content cell proliferation decreased for culture over 10 days. A comparison of sintered and post-hardened samples showed no significant difference for all three compositions. Evaluation of the cell activity by WST test also revealed differences between MPC and SrMPC. Activity increased dramatically after 7 days for almost all cements. For pure MPC, sintered and post-hardened samples were comparable. In contrast, post-hardening decreased cell activity for both SrMPC cements and again a higher Sr^{2+} content led to a reduced activity. For post-hardened $Mg_2Sr_1(PO_4)_2$ cement no cell activity was recorded over the whole period of culture. Cells on PS exhibited a normal behavior. With regard to the reference, cell proliferation was reduced on cement samples but cell activity remained high. That means a higher cell activity per cell when compared to the reference PS indicating an active metabolism. To verify the findings from MG63 cell test, the same investigation was performed with hFOB (Figure 41C and D). The cell number was highest on sintered MPC over the whole period of cultivation. As already observed with MG63, cell number dropped below the seeding density for all samples except sintered MPC. However, cells on post-hardened MPC and sintered $Mg_{2.5}Sr_{0.5}(PO_4)_2$ proliferated during the following days. In contrast, all other samples remained with low cell numbers, which became also obvious for the cell activity. $Mg_2Sr_1(PO_4)_2$ and post-hardened $Mg_{2.5}Sr_{0.5}(PO_4)_2$ showed hardly any activity over 10 days. The cell activity of pure MPC and sintered $Mg_{2.5}Sr_{0.5}(PO_4)_2$ was in accordance with the cell number. The proliferation on PS reference was too high, such that cells became confluent and agglomerated during culture. Furthermore, cell agglomeration was also observed on pure MPC samples revealing a high proliferation.

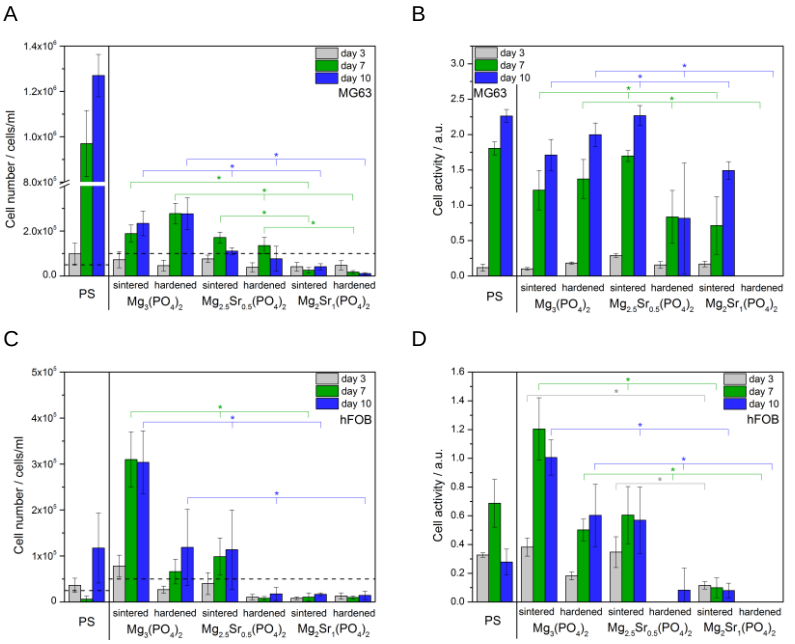

Figure 41: Cell number and cell activity of MG63 (A,B) and hFOB (C,D), respectively, after 10 days of cultivation. Dashed line indicates the cell number seeded on the samples on day 0. Polystyrene (PS) served as reference. For post-hardened $Mg_2Sr_1(PO_4)_2$ and in the beginning for post-hardened $Mg_{2.5}Sr_{0.5}(PO_4)_2$ no cell activity could be detected. Statistical analysis was performed for sintered and post-hardened samples among each other. Highly significant ($p < 0.001$) samples are marked with *.

To avoid the influence of degrading cement surfaces, an indirect test was performed with eluate from immersed samples. In contrast to direct seeding, the cell number as well as cell activity of $Mg_2Sr_1(PO_4)_2$ sintered was comparable to $Mg_3(PO_4)_2$ and $Mg_{2.5}Sr_{0.5}(PO_4)_2$ sintered. But for the post-hardened samples of $Mg_{2.5}Sr_{0.5}(PO_4)_2$ and $Mg_2Sr_1(PO_4)_2$ hardly any cells and activity was detected. This is in accordance with the observation from the direct cell seeding. Just $Mg_{2.5}Sr_{0.5}(PO_4)_2$ hardened showed a slow regeneration after 10 days indicating cytocompatibility in long-term application. Since the reference supplied with fresh media showed no noticeable findings, cells have to be influenced by the eluate.

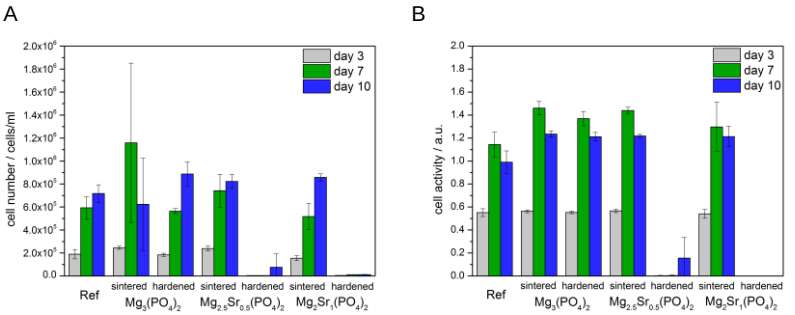

Figure 42: Cell number (A) and cell activity (B) of hFOB during an indirect cytotoxicity test with eluate over 10 days with MPC and SrMPC.

5.2.4 Discussion

Strontium substitution of bioceramics was previously demonstrated to have a promoting effect on osteoblast activity and proliferation [18, 19, 24]. Hence, 3D printed SrMPC samples were investigated using the osteoblastic cell lines MG63 and hFOB compared to the references of pure MPC and PS (Figure 41). Additionally, an indirect test was performed with the eluate from immersed cement samples. First, the results of both cell lines directly cultivated exhibited the same tendency of a decreased proliferation and cell activity for an increasing Sr^{2+} content. Since these findings are contradictory to numerous *in vitro* and *in vivo* tests found in literature [18, 19, 21, 361, 438, 439], it is obvious that the contradictive influence observed is not directly assigned to the Sr^{2+} content. Post-hardened $Mg_{2.5}Sr_{0.5}(PO_4)_2$ and $Mg_2Sr_1(PO_4)_2$ showed a very low or no cell activity and the cell number ranged below the seeding density when cultured with both MG63 and hFOB cells. One of the reasons for cell death and a reduced metabolism could be due to the tremendous phosphate release (Figure 40). Meleti et al. [198] investigated different phosphate concentrations with regard to their effect on osteoblasts. The down regulation of osteoblast activity was observed for a phosphate content as low as 3 mmol/l and a concentration of 7 mmol/l caused apoptosis of almost all cells within 96 h. The initial release of phosphate ions for the post-hardened $Mg_{2.5}Sr_{0.5}(PO_4)_2$ and $Mg_2Sr_1(PO_4)_2$ cements was 5.6 and

4.7 mmol/l and the cumulative release reached 8.5 and 10.9 mmol/l, respectively. Thus, a negative influence on the cultured osteoblasts cannot be excluded. However, this theory is still controversial and the influencing mechanisms are not completely understood [440]. Another reason could be found in the modified surface morphology of SrMPC (Figure 35). The single particles of SrMPC were smaller compared to those of pure MPC, which could lead to an altered cell response. Furthermore, during cell culture SrMPC scaffolds degraded and cement particles were released into surrounding media. This again can have two effects: (1) Loose particles can influence osteoblast function such as proliferation or production of extracellular matrix as it is already known from CPC particles [441]. (2) Due to surface degradation cell attachment is either directly inhibited or attached cells are removed together with the particle. Since lots of cement particles were observed during cell counting via microscopy, the latter mechanism seems to have the strongest impact on the results. Taking into account that strontium-substituted bone cements are already proved to have beneficial effects on bone remodeling and tissue ingrowth [18-21] a highly resorbable implant material supports the replacement of bone substitutes by new bone tissue.

To exclude an influence of loose powder particles, an indirect test was performed. For all sintered samples the cell number as well as the cell activity were comparable to the reference supplied with fresh media. In these cases, it could be assumed that the high degradation rate is the predominant factor leading to low cell numbers for the direct cell seeding. However, the post-hardened samples of $Mg_{2.5}Sr_{0.5}(PO_4)_2$ and $Mg_2Sr_1(PO_4)_2$ exhibited very low to no cell numbers and activities. This is in accordance with the results from the direct cell seeding, which excludes the effect of degradation. The reason for the cell death could be the extremely high phosphate release during culture (see Figure 40), as already observed in literature [122, 197-199] and described above. The post-hardened $Mg_{2.5}Sr_{0.5}(PO_4)_2$, however, showed a slow regeneration after 10 days of cultivation. This gives a hint that not all cells were killed

by the phosphate release and that a recovery was possible. Especially for long-term applications, the cytocompatibility could be sufficient.

Taken both direct and indirect seeding into account, strontium-substituted MPC that were only sintered were cytocompatible over the period of 10 days without any adverse effect of ion release. The high degradation rate has to be considered in *in vitro* tests and further tested *in vivo*. Post-hardening of the SrMPC seemed to increase the degradation rate and, therefore, the ion release in a way that the phosphate release has a negative impact on cell proliferation and activity. In all cases, a promoting effect on osteoblast proliferation, as it is described in literature, could not be confirmed. This could be due to the low Sr^{2+} concentrations that have been released. The initial release was only high for post-hardened $Mg_{2.5}Sr_{0.5}(PO_4)_2$ and $Mg_2Sr_1(PO_4)_2$ (16 mg/l and 60 mg/l, respectively) compared to the other samples (< 2.8 mg/l). In literature controversial in vitro results are found for different Sr^{2+} concentrations. The effective dose for an increased cell proliferation was in the range of 4500 – 10500 mg/l [442], whereas no effect could be found for concentrations between 16 and about 2500 ppm [442-444]. Since the beneficial effects on bone growth are often shown, just further *in vivo* test can clarify this discrepancy.

5.2.5 Conclusion

The substitution with Sr^{2+} enhanced the degradation of the pure MPC, which entails technical challenges for *in vitro* studies. The direct seeding of cement samples is on the one hand reasonable in terms of an implant material, but on the other hand just valid for non-degradable or very slowly degradable materials. This could be found in the differences in direct and indirect seeding, especially for the sintered $Mg_{2.5}Sr_{0.5}(PO_4)_2$ and $Mg_2Sr_1(PO_4)_2$. Nevertheless, a fast degradation involves a high ion release, which could influence cellular behavior. The post-hardened $Mg_{2.5}Sr_{0.5}(PO_4)_2$ and $Mg_2Sr_1(PO_4)_2$ had such high phosphate release that almost all cells became apoptotic. Although, a promoting effect of Sr^{2+} on osteoblast proliferation could not be verified, the degradation could be tuned by Sr^{2+} addition.

Apart from that, these *in vitro* tests cannot be directly transferred to *in vivo* outcomes without further investigation.

6. Future perspectives

Different processing techniques with numerous materials and additives have been demonstrated to optimize mechanical as well as biological properties of CPC and MPC. However, these were only basic investigations and often poof of principles, which have to be further tuned for a specific application. For some studies, already established techniques were combined or transferred. One of those studies examined the fiber reinforcement during 3DP, an established reinforcing technique transferred to an AM technique for the processing of cement raw powders. Basically, gypsum was used together with non-degradable polymeric fibers and glass fibers as a model material. The green strength could be enhanced, although the system was not optimized regarding interfacial bonding. As a next step, these findings can be used to reinforce a biomedically relevant material like CPC or MPC with biocompatible fibers. As those matrix materials undergo a setting reaction during the printing process [278], the mechanical performance of the finished construct can be improved. Therefore, an optimization of the interface between fiber and matrix would be necessary to exploit the potential of energy absorbing effects like debonding, fiber pull-out or crack deflection [9, 289, 293, 294]. The treatment of the fibers would be analogous to conventionally fabricated composites by means of a chemical or physical pretreatment [9, 298-300]. According to the application and the patients' needs, the components can be selected regarding degradable or non-degradable use. Biodegradable materials open up further possibilities apart from a steady and complete replacement by new bone tissue. By the combination of a fast degrading fiber with a slowly degrading cement matrix, channels or porous structures can be created that form after a certain temporal offset. Especially for polymeric fibers, this time offset can be tuned e.g. via chain length to guarantee an initial osseous integration of the implant. After fiber dissolution remaining channels are favorable for vascularization [17, 308, 445] and further bone ingrowth [297, 318] into the implant. This ensures a long-term nutrition supply of newly formed tissue and the invasion of

bone forming cells [17]. Furthermore, a combination of two different fiber types and a CPC or MPC matrix could be employed. If the fibers differ in terms of dissolution rate, channels or pores appear at different time points of degradation. Therefore, after the dissolution of one fiber type vascularization and bone ingrowth can take place and simultaneously another fiber type can maintain the mechanical properties [318]. This further supports the implant integration and the mechanical stability of a patient-specific implant that was fabricated by 3DP.

The principle of fiber reinforcement was also employed for centrifugally casting. This technique was adapted from construction industries, where tubular structures like drainpipes are fabricated by the centrifugation of a curing slurry [5, 6]. In medicine, the replacement of the diaphysis of long bone is also based on tubular structures that can be fabricated by centrifugally casting of a bioceramic slurry. The hollow shape of the tube is favorable for the ingrowth of bone marrow and the invasion of bone marrow derived cells [10-15]. However, such defects often occur in load-bearing regions like the femur or tibia and need a treatment with damage tolerant materials. The brittle bioceramics could be reinforced with fibers and fiber meshes, although the interface was again not optimized for the matrix. Numerous parameters can be adapted to further enhance the damage tolerance of the composite including the fiber material, content, length and arrangement. Again, degradable and permanent implants can be realized with different material combinations. However, each change in composition entails an adaption of the parameters regarding the components (e.g. cement composition) as well as the processing set-up (e.g. rotation time). As could be shown for a pure MPC, such an optimization can be easily performed within the same device resulting in the desired composite.

Apart from the fiber reinforcement, another strategy to obtain a damage tolerant composite can be employed. The already established dual setting system of HA and HEMA was used to demonstrate the feasibility of tube production with centrifugally casting. In contrast, a transfer of such a dual setting system to the 3DP was not attained yet. The 3DP technique uses commercially available cartridges for binder application.

Those cartridges are chemically not resistant against some components of the dual setting system, which makes a binder application impossible. For centrifugally casting, the cement slurry is prepared prior to processing, which is similar to conventional molding. As HA and HEMA are a non-degradable model for a dual setting system, the application of degradable and more biocompatible dual setting systems would be desirable [336, 337]. However, a problem that will always occur for such damage tolerant materials is the high deformation and measurement errors in mechanical tests. Different tests that are closer to the real load situation *in vivo* should be established for such composites to not distort the performance evaluation. Furthermore, the test conditions have to be considered, as such dual setting systems often contain hydrogels, whose mechanical performance is highly dependent on the water content and the temperature [446]. Also graded structures are hard to produce with other AM techniques, since different raw materials are involved. The variety of graded structures already studied [324] illustrates the need for such constructs with superior properties. With centrifugally casting, different ion substituted cements can be combined as well as CPC and MPC, which offers a versatile tool box to tune mechanical and biological properties. Since centrifugally casting is also capable of fabricating patient-specific implants, this technique can be not just an adequate alternative to common AM techniques but an extension of fabrication possibilities. Thus for materials undergoing a dissolution/precipitation reaction or even for polymers hardly any limitations exist for this process, whereas the processing parameters have to be adapted to each composition.

The incorporation of vancomycin as a model drug demonstrated that also different drugs, growth factors or proteins can be added to such graded structures within the process. The additive selection is just limited by the combination with the cement matrix, as it would also be for conventionally molded samples. The process itself implies no further limitations like denaturation due to heat or adverse interactions with machine components. The graded structures in combination with drug loading introduced new features and even a long-term release became possible. Since the drug

could be combined with a cement matrix, pH-dependency of cement solubility can be exploited for the drug release. Bacterial environment is often acidic [405, 406] resulting in an enhanced cement matrix solubility (Figure 1) and, therefore, an enhanced drug release through enlarged pores. By this method, a drug release on demand can be reached to even more efficiently fight local infections, while minimizing adverse effects on the patients' organism. Other drugs, growth factors or proteins have to be tested with this manufacturing technique with respect to different applications. However, the study with vancomycin already showed that for a long-term release the degradation of the additive has to be considered and further investigated. Since vancomycin disintegrated in several fragments, the efficacy of those fragments against bacteria has to be evaluated. When thinking of other additives, a disintegration with the loss of efficacy during a long-term exposition at 37 °C has to be taken into account. However, such considerations just rose due to the possibility of a long-term release being the first step towards a local treatment of implant infections.

3DP as a commercially available AM technique can be applied for numerous applications and materials. In contrast to centrifugally casting, 3DP entails the introduction of pores in double-digit to low triple-digit micrometer range together with a high interconnectivity. These are ideal conditions for nutrition supply, cellular invasion, vascularization and bone ingrowth [17]. Additionally to the biological advantages, such implants exhibit a high mechanical reliability. With the help of Weibull statistics such reliabilities can be calculated, which should be performed for all biomedical applications, as the reliability is one of the most important features of an implant. Since 3DP is a uniform process independent of the operator, the reliability of the implant will be ensured, which is even more important for a transfer to commercial products. The Sr^{2+}-substitution in this study was not yet optimized for an osteoblast promoting effect, although the impact of Sr^{2+} ions on bone formation is already well investigated [18-24]. As Sr^{2+} ions also enhance the degradation of the substituted cement, the release has to be considered for each degree of substitution to obtain a maximum promoting effect and a minimum adverse effect of released

phosphate ions. Therefore, the study showed that there is always a discrepancy between direct and indirect cell seeding especially for fast degrading cements. This makes the combination of both tests indispensable for an evaluation of cell response and with that an optimization of the biological behavior *in vivo*.

7. Summary

The main focus of this thesis was the processing of different calcium and magnesium phosphate cements together with an optimization of mechanical and biological properties. Therefore, different manufacturing techniques like 3D powder printing and centrifugally casting were employed for the fabrication of reinforced or biomedically improved implants.

One of the main problems during 3D powder printing is the low green strength of many materials, especially when they are only physically bonded and do not undergo a setting reaction. Such materials need post-treatments like sintering to exhibit their full mechanical performance. However, the green bodies have to be removed from the printer requiring a certain stability. With the help of fiber reinforcement, the green strength of printed gypsum samples could be increased by the addition of polymeric and glass fibers within the printing process. The results showed that fiber reinforcement during 3D powder printing is possible and opens up diverse opportunities to enhance the damage tolerance of green bodies as well as directly printed samples. The transfer to biomedically relevant materials like calcium and magnesium phosphate cements and biocompatible fibers would be the next step towards reinforced patient-specific implants.

In a second approach, centrifugally casting derived from construction industries was established for the fabrication of hollow bioceramic cylinders. The aim was the replacement of the diaphysis of long bones, which exhibit a tubular structure with a high density of cortical bone on the fringe. By centrifugation, cement slurries with and without additives could be fabricated to tubes. As a first establishment, the processing parameters regarding the material (e.g. cement composition) as well as the set-up (e.g. rotation times) had to be optimized for each system. In respect of mechanics, such tubes can keep up with 3D powder printed tubes, although the mechanical performance of 3D printed tubes is strongly dependent on printing

directions. Additionally, some material compositions like dual setting systems cannot be fabricated by 3D powder printing. Therefore, a transfer of such techniques to centrifugally casting enabled the fabrication of tubular structures with an extremely high damage tolerance due to high deformation ability. A similar effect was achieved by fiber (mesh) addition, as already shown for 3D powder printing. Another possibility of centrifugally casting is the combination of different materials resulting in graded structures to adjust implant degradation or bone formation. This became especially apparent for the incorporation of the antibiotic vancomycin, which is used for the treatment of bacterial implant infections. A long-term release could be achieved by the entrapment of the drug between magnesium phosphate cement layers. Therefore, the release of the drug could be regulated by the degradation of the outer shell, which supports the release into an acidic bacterial environment. The centrifugally casting technique exhibited to be a versatile tool for numerous materials and applications including the fabrication of non-centrosymmetric patient-specific implants for the reconstruction of human long bones.

The third project aimed to manufacture strontium-substituted magnesium phosphate implants with improved biological behavior by 3D powder printing. As the promoting effect of strontium on bone formation and the inhibitory impact on bone resorption is already well investigated, the incorporation of strontium into a degradable magnesium phosphate cement promised a fast integration and replacement of the implant. Porous structures were obtained with a high pore interconnectivity that is favorable for cell invasion and bone ingrowth. Despite the porosity, the mechanical performance was comparable to pure magnesium phosphate cement with a high reliability of the printed samples as quantitatively determined by Weibull statistics. However, the biological testing was impeded by the high degradation rate and the relating ion release. The high release of phosphate ions into surrounding media and the detachment of cement particles from the surface inhibited osteoblast growth and activity. To distinguish those two effects, a direct and indirect cell seeding is always required for degradable materials. Furthermore, the high phosphate release compared to the strontium release

has to be managed during degradation such that the adverse effect of phosphate ions does not overwhelm the bone promoting effect of the strontium ions.

The manufacturing techniques presented in this thesis together with the material property improvement offer a diverse tool box for the fabrication of patient-specific implants. This includes not just the individual implant shape but also the application like bone growth promotion, damage tolerance and local drug delivery. Therefore, this can act as the basis for further research on specific medical indications.

8. Zusammenfassung

Der Fokus dieser Dissertation lag auf der Verarbeitung von Calcium- und Magnesiumphosphatzementen zusammen mit der Optimierung mechanischer und biologischer Eigenschaften. Dazu wurden verschiedene Produktionsverfahren wie beispielsweise der 3D Pulverdruck und der Schleuderguss verwendet, um mechanisch verstärkte oder biomedizinisch verbesserte Implantate herzustellen.

Eines der Hauptprobleme des 3D Pulverdrucks ist die geringe Festigkeit des Grünkörpers vieler Materialien, besonders wenn diese lediglich physikalisch gebunden sind und keine Abbindereaktion durchlaufen. Solche Materialien müssen nachbearbeitet werden, beispielsweise durch Sintern, um ihre volle mechanische Leistungsfähigkeit zu entfalten. Die Grünkörper müssen jedoch aus dem 3D Drucker entnommen werden können, was eine gewisse Stabilität erfordert. Mit Hilfe der Faserverstärkung konnte die Festigkeit von gedruckten Grünkörper aus Gips erhöht werden, indem Polymer- und Glasfasern innerhalb des Druckprozesses eingebracht wurden. Die Ergebnisse zeigten, dass Faserverstärkung innerhalb des 3D Pulverdrucks möglich ist und dabei vielfältige Möglichkeiten eröffnet, um die Schadenstoleranz von Grünkörpern wie auch von direkt gedruckten Proben zu verbessern. Der nächste Schritt hin zu verstärkten, patientenspezifischen Implantaten wäre die Übertragung auf biomedizinisch relevante Materialien wie Calcium- und Magnesiumphosphatzemente und biokompatible Fasern.

In einem zweiten Ansatz wurde der aus dem Baugewerbe stammende Schleuderguss für die Herstellung hohler Zylinder aus Biokeramik etabliert. Das Ziel war es, die Diaphyse von Röhrenknochen zu ersetzen, die eine tubuläre Struktur mit einer hohen Dichte an kortikalem Knochen am Rand aufweist. Durch Zentrifugieren konnten Zementpasten mit und ohne Additive zu Röhren verarbeitet werden. Zunächst mussten dabei die Prozessparameter bezüglich Material (z.B. Zementzusammensetzung) ebenso wie bezüglich der Einstellungen (z.B.

Rotationszeiten) für jedes System optimiert werden. Im Hinblick auf ihre mechanischen Eigenschaften können solche Röhren mit 3D pulvergedruckten Röhren mithalten, obwohl die mechanische Leistungsfähigkeit von 3D gedruckten Röhren stark von der Druckrichtung abhängt. Zusätzlich können einige Materialkombinationen wie dual-abbindende Systeme nicht mit 3D Pulverdruck verarbeitet werden. Daher ermöglicht eine Übertragung solcher Techniken auf den Schleuderguss die Fertigung tubulärer Strukturen mit extrem hoher Schadenstoleranz aufgrund hoher Verformbarkeit. Wie bereits für das 3D Pulverdrucken gezeigt, konnte ein ähnlicher Effekt durch die Zugabe von Fasern (Geweben) erzielt werden. Eine weitere Möglichkeit des Schleudergusses ist die Kombination verschiedener Materialien zu gradientenartigen Strukturen, um den Implantatabbau oder die Knochenbildung anzupassen. Dies war besonders wichtig für die Einbringung des Antibiotikums Vancomycin, das für die Behandlung bakterieller Implantatinfektionen eingesetzt wird. Eine Langzeitfreisetzung konnte durch den Einbau des Arzneistoffs zwischen Magnesiumphosphatschichten erreicht werden. Dadurch konnte die Freisetzung des Wirkstoffs durch den Abbau der äußeren Hülle geregelt werden, was die Freisetzung in das saure Milieu von Bakterien unterstützt. Der Schleuderguss erwies sich als vielseitiges Werkzeug für viele Materialien und Anwendungen, was die Herstellung von nicht-zentrosymmetrischen, patientenspezifischen Implantaten zur Rekonstruktion von menschlichem Röhrenknochen einschließt.

Das dritte Projekt zielte auf die Herstellung Strontium-substituierter Magnesiumphosphatimplantaten mittels 3D Pulverdruck mit verbessertem biologischen Verhalten ab. Da die unterstützende Wirkung von Strontium auf die Knochenbildung und die Hemmung des Knochenabbaus bereits eingehend untersucht sind, versprach die Einbringung von Strontium in den abbaubaren Magnesiumphosphatzement eine schnelle Integration und Ersatz des Implantats. Es konnten poröse Strukturen mit einer hohen Poreninterkonnektivität erhalten werden, was förderlich für die Einwanderung von Zellen und das Einwachsen von Knochen ist. Neben der Porosität waren auch die mechanischen Eigenschaften vergleichbar mit

reinem Magnesiumphosphatzement mit einer hohen Verlässlichkeit der gedruckten Proben, was quantitativ durch eine Weibullstatistik bestimmt wurde. Die biologische Testung wurde allerdings durch die hohe Degradationsrate und der damit einhergehenden Ionenfreisetzung erschwert. Die hohe Freisetzung von Phosphationen in das umgebende Medium und die Ablösung von Zementpartikeln von der Oberfläche verhinderten das Wachstum und Aktivität der Osteoblasten. Um diese beiden Effekte voneinander unterscheiden zu können, war eine direkte und indirekte Zellbesiedelung der abbaubaren Materialien notwendig. Des Weiteren muss die hohe Phosphatfreisetzung im Vergleich zur Strontiumfreisetzung während des Abbaus derart gesteuert werden, dass die negativen Effekte der Phosphationen nicht die Förderung des Knochenaufbaus durch Strontiumionen überwiegen.

Die in dieser Dissertation dargestellten Fertigungstechniken zusammen mit der Verbesserung der Materialeigenschaften bieten eine vielfältige Palette zur Herstellung patientenspezifischer Implantate. Dies beinhaltet nicht nur eine individuelle Implantatgeometrie, sondern auch eine Verbesserung der Schadenstoleranz, die Förderung des Knochenwachstums sowie eine lokale Wirkstofffreisetzung. Daher kann diese Arbeit als Grundlage für weitere Forschung im Bereich spezifischer, medizinischer Indikationen dienen.

References

[1] J.O. Hollinger, J.C. Kleinschmidt, The Critical Size Defect as an Experimental Model To Test Bone Repair Materials, Journal of Craniofacial Surgery 1 (1990) 60-68.
[2] L.L. Hench, The future of bioactive ceramics, Journal of Materials Science: Materials in Medicine 26 (2015) 86.
[3] D. Arcos, I. Izquierdo-Barba, M. Vallet-Regí, Promising trends of bioceramics in the biomaterials field, Journal of Materials Science: Materials in Medicine 20 (2009) 447-455.
[4] J. Mahamid, A. Sharir, D. Gur, E. Zelzer, L. Addadi, S. Weiner, Bone mineralization proceeds through intracellular calcium phosphate loaded vesicles: A cryo-electron microscopy study, Journal of Structural Biology 174 (2011) 527-535.
[5] V.Y. Kopeiko, Production and use of pipe piles, Soil Mechanics and Foundation Engineering 7 (1970) 34-39.
[6] G. De Schutter, D. Feys, R. Verhoeven, Ecological profit for a cocnrete pipe factory due to self-compacting concrete technology, Second international conference on sustainable construction materials and technologies, Proceedings 2 (2010) 1281-1287.
[7] E. Vorndran, C. Moseke, U. Gbureck, 3D printing of ceramic implants, MRS Bulletin 40 (2015) 127–136.
[8] U. Klammert, U. Gbureck, E. Vorndran, J. Rödiger, P. Meyer-Marcotty, A.C. Kübler, 3D powder printed calcium phosphate implants for reconstruction of cranial and maxillofacial defects, Journal of Cranio-Maxillofacial Surgery 38 (2010) 565-570.
[9] R. Krüger, J. Groll, Fiber reinforced calcium phosphate cements – On the way to degradable load bearing bone substitutes?, Biomaterials 33 (2012) 5887-5900.
[10] O. Gauthier, J.-M. Bouler, E. Aguado, P. Pilet, G. Daculsi, Macroporous biphasic calcium phosphate ceramics: influence of macropore diameter and macroporosity percentage on bone ingrowth, Biomaterials 19 (1998) 133–139.
[11] V. Karageorgiou, D. Kaplan, Porosity of 3D biomaterial scaffolds and osteogenesis, Biomaterials 26 (2005) 5474-5491.
[12] J.M. Cordell, M.L. Vogl, A.J. Wagoner Johnson, The influence of micropore size on the mechanical properties of bulk hydroxyapatite and hydroxyapatite scaffolds, Journal of the Mechanical Behavior of Biomedical Materials 2 (2009) 560-570.
[13] B. Leukers, H. Gülkan, S.H. Irsen, S. Milz, C. Tille, M. Schieker, H. Seitz, Hydroxyapatite scaffolds for bone tissue engineering made by 3D printing, Journal of Materials Science: Materials in Medicine 16 (2005) 1121-1124.
[14] H. Yoshikawa, A. Myoui, Bone tissue engineering with porous hydroxyapatite ceramics, Journal of Artificial Organs 8 (2005) 131-136.

[15] R.M. Hoerth, B.M. Seidt, M. Shah, C. Schwarz, B.M. Willie, G.N. Duda, P. Fratzl, W. Wagermaier, Mechanical and structural properties of bone in non-critical and critical healing in rat, Acta Biomaterialia 10 (2014) 4009-4019.
[16] G. Cama, F. Barberis, R. Botter, P. Cirillo, M. Capurro, R. Quarto, S. Scaglione, E. Finocchio, V. Mussi, U. Valbusa, Preparation and properties of macroporous brushite bone cements, Acta Biomaterialia 5 (2009) 2161-2168.
[17] F.M. Klenke, Y. Liu, H. Yuan, E.B. Hunziker, K.A. Siebenrock, W. Hofstetter, Impact of pore size on the vascularization and osseointegration of ceramic bone substitutes in vivo, Journal of Biomedical Materials Research Part A 85A (2008) 777-786.
[18] S. Tarafder, W.S. Dernell, A. Bandyopadhyay, S. Bose, SrO- and MgO-doped microwave sintered 3D printed tricalcium phosphate scaffolds: Mechanical properties and in vivo osteogenesis in a rabbit model, Journal of Biomedical Materials Research Part B: Applied Biomaterials 103 (2015) 679-690.
[19] U. Thormann, S. Ray, U. Sommer, T. ElKhassawna, T. Rehling, M. Hundgeburth, A. Henß, M. Rohnke, J. Janek, K.S. Lips, C. Heiss, G. Schlewitz, G. Szalay, M. Schumacher, M. Gelinsky, R. Schnettler, V. Alt, Bone formation induced by strontium modified calcium phosphate cement in critical-size metaphyseal fracture defects in ovariectomized rats, Biomaterials 34 (2013) 8589-8598.
[20] G.X. Ni, K.Y. Chiu, W.W. Lu, Y. Wang, Y.G. Zhang, L.B. Hao, Z.Y. Li, W.M. Lam, S.B. Lu, K.D.K. Luk, Strontium-containing hydroxyapatite bioactive bone cement in revision hip arthroplasty, Biomaterials 27 (2006) 4348-4355.
[21] M. Baier, P. Staudt, R. Klein, U. Sommer, R. Wenz, I. Grafe, P.J. Meeder, P.P. Nawroth, C. Kasperk, Strontium enhances osseointegration of calcium phosphate cement: a histomorphometric pilot study in ovariectomized rats, Journal of orthopaedic surgery and research 8 (2013) 16.
[22] S. Ray, Strontium Modified Calcium Phosphate Cement (SRCPC) Enhances Bone Formation In Critical-size Metaphyseal Osteoporotic Fracture Defects In Rats, Bone & Joint Journal Orthopaedic Proceedings Supplement 96-B (2014) 88-88.
[23] A. Sabareeswaran, B. Basu, S.J. Shenoy, Z. Jaffer, N. Saha, A. Stamboulis, Early osseointegration of a strontium containing glass ceramic in a rabbit model, Biomaterials 34 (2013) 9278-9286.
[24] B. Basu, A. Sabareeswaran, S.J. Shenoy, Biocompatibility property of 100% strontium-substituted SiO2–Al2O3–P2O5–CaO–CaF2 glass ceramics over 26 weeks implantation in rabbit model: Histology and micro-Computed Tomography analysis, Journal of Biomedical Materials Research Part B: Applied Biomaterials 103 (2015) 1168-1179.
[25] T. Yu, J. Ye, Y. Wang, Preparation and characterization of a novel strontium-containing calcium phosphate cement with the two-step hydration process, Acta Biomaterialia 5 (2009) 2717-2727.
[26] X. Wang, J. Ye, Y. Wang, Influence of a novel radiopacifier on the properties of an injectable calcium phosphate cement, Acta Biomaterialia 3 (2007) 757-763.
[27] K.A. Hing, Bone repair in the twenty–first century: biology, chemistry or engineering?, Philosophical Transactions of the Royal Society of London A: Mathematical, Physical and Engineering Sciences 362 (2004) 2821-2850.

[28] A.G. Robling, A.B. Castillo, C.H. Turner, Biomechanical and molecular regulation of bone remodeling, Annual Review of Biomedical Engineering 8 (2006) 455–498.
[29] N. Udagawa, N. Takahashi, H. Yasuda, A. Mizuno, K. Itoh, Y. Ueno, T. Shinki, M.T. Gillespie, T.J. Martin, K. Higashio, T. Suda, Osteoprotegerin Produced by Osteoblasts Is an Important Regulator in Osteoclast Development and Function, Endocrinology 141 (2000) 3478-3484.
[30] S.C. Manolagas, Birth and Death of Bone Cells: Basic Regulatory Mechanisms and Implications for the Pathogenesis and Treatment of Osteoporosis, Endocrine Reviews 21 (2000) 115-137.
[31] N.A. Sims, J.H. Gooi, Bone remodeling: Multiple cellular interactions required for coupling of bone formation and resorption, Seminars in Cell & Developmental Biology 19 (2008) 444-451.
[32] F.C.M. Driessens, J.A. Planell, M.G. Boltong, I. Khairoun, M.P. Ginebra, Osteotransductive bone cements, Proceedings of the Institution of Mechanical Engineers, Part H: Journal of Engineering in Medicine 212 (1998) 427-435.
[33] R. Detsch, H. Mayr, G. Ziegler, Formation of osteoclast-like cells on HA and TCP ceramics, Acta Biomaterialia 4 (2008) 139-148.
[34] J. Mahamid, B. Aichmayer, E. Shimoni, R. Ziblat, C. Li, S. Siegel, O. Paris, P. Fratzl, S. Weiner, L. Addadi, Mapping amorphous calcium phosphate transformation into crystalline mineral from the cell to the bone in zebrafish fin rays, Proceedings of the National Academy of Sciences 107 (2010) 6316-6321.
[35] W. Habraken, P. Habibovic, M. Epple, M. Bohner, Calcium phosphates in biomedical applications: materials for the future?, Materials Today 19 (2016) 69-87.
[36] G. Boivin, P.J. Meunier, Changes in Bone Remodeling Rate Influence the Degree of Mineralization of Bone, Connective Tissue Research 43 (2002) 535-537.
[37] A. Schindeler, M.M. McDonald, P. Bokko, D.G. Little, Bone remodeling during fracture repair: The cellular picture, Seminars in Cell & Developmental Biology 19 (2008) 459-466.
[38] K. Anselme, Osteoblast adhesion on biomaterials, Biomaterials 21 (2000) 667-681.
[39] R. Pérez-Tanoira, X. Han, A. Soininen, A.A. Aarnisalo, V.-M. Tiainen, K.K. Eklund, J. Esteban, T.J. Kinnari, Competitive colonization of prosthetic surfaces by staphylococcus aureus and human cells, Journal of Biomedical Materials Research Part A 105 (2017) 62-72.
[40] K. Wang, C. Zhou, Y. Hong, X. Zhang, A review of protein adsorption on bioceramics, Interface Focus 2 (2012) 259-277.
[41] M. Lampin, R. Warocquier-Clérout, C. Legris, M. Degrange, M.F. Sigot-Luizard, Correlation between substratum roughness and wettability, cell adhesion, and cell migration, Journal of Biomedical Materials Research 36 (1997) 99-108.
[42] S. Bose, G. Fielding, S. Tarafder, A. Bandyopadhyay, Understanding of dopant-induced osteogenesis and angiogenesis in calcium phosphate ceramics, Trends in Biotechnology 31 (2013) 594-605.
[43] P.V. Giannoudis, H. Dinopoulos, E. Tsiridis, Bone substitutes: An update, Injury 36 (2005) S20-S27.

[44] N. Eliaz, N. Metoki, Calcium Phosphate Bioceramics: A Review of Their History, Structure, Properties, Coating Technologies and Biomedical Applications, Materials 10 (2017) 334.
[45] E.M. Bueno, J. Glowacki, Cell-free and cell-based approaches for bone regeneration, Nature Reviews Rheumatology 5 (2009) 685-697.
[46] N. Reznikov, R. Shahar, S. Weiner, Bone hierarchical structure in three dimensions, Acta Biomaterialia 10 (2014) 3815-3826.
[47] A.J. Salinas, P. Esbrit, M. Vallet-Regí, A tissue engineering approach based on the use of bioceramics for bone repair, Biomaterials Science 1 (2013) 40-51.
[48] L.L. Hench, J.M. Polak, Third-Generation Biomedical Materials, Science 295 (2002) 1014-1017.
[49] F. Baino, S. Fiorilli, C. Vitale-Brovarone, Bioactive glass-based materials with hierarchical porosity for medical applications: Review of recent advances, Acta Biomaterialia 42 (2016) 18-32.
[50] J.R. Jones, L.L. Hench, Factors affecting the structure and properties of bioactive foam scaffolds for tissue engineering, Journal of Biomedical Materials Research Part B: Applied Biomaterials 68B (2004) 36-44.
[51] J.R. Jones, L.L. Hench, Effect of surfactant concentration and composition on the structure and properties of sol-gel-derived bioactive glass foam scaffolds for tissue engineering, Journal of Materials Science 38 (2003) 3783-3790.
[52] J.R. Jones, Reprint of: Review of bioactive glass: From Hench to hybrids, Acta Biomaterialia 23, Supplement (2015) S53-S82.
[53] G. Kaur, O.p. Pandey, K. Singh, D. Homa, B. Scott, G. Pickrell, A review of bioactive glasses: Their structure, properties, fabrication and apatite formation, Journal of Biomedical Materials Research Part A 102 (2014) 254-274.
[54] L.L. Hench, Bioceramics: From Concept to Clinic, Journal of the American Ceramic Society 74 (1991) 1487-1510.
[55] J.R. Jones, P. Sepulveda, L.L. Hench, Dose-dependent behavior of bioactive glass dissolution, Journal of Biomedical Materials Research Part A 58 (2001) 720–726.
[56] I.D. Xynos, A.J. Edgar, L.D.K. Buttery, L.L. Hench, J.M. Polak, Ionic Products of Bioactive Glass Dissolution Increase Proliferation of Human Osteoblasts and Induce Insulin-like Growth Factor II mRNA Expression and Protein Synthesis, Biochemical and Biophysical Research Communications 276 (2000) 461-465.
[57] I.D. Xynos, M.V.J. Hukkanen, J.J. Batten, L.D. Buttery, L.L. Hench, J.M. Polak, Bioglass ®45S5 Stimulates Osteoblast Turnover and Enhances Bone Formation In Vitro: Implications and Applications for Bone Tissue Engineering, Calcified Tissue International 67 (2000) 321-329.
[58] A.M. Pietak, J.W. Reid, M.J. Stott, M. Sayer, Silicon substitution in the calcium phosphate bioceramics, Biomaterials 28 (2007) 4023-4032.
[59] I.D. Xynos, A.J. Edgar, L.D.K. Buttery, L.L. Hench, J.M. Polak, Gene-expression profiling of human osteoblasts following treatment with the ionic products of Bioglass® 45S5 dissolution, Journal of Biomedical Materials Research 55 (2001) 151-157.

[60] T. Waltimo, D. Mohn, F. Paqué, T.J. Brunner, W.J. Stark, T. Imfeld, M. Schätzle, M. Zehnder, Fine-tuning of Bioactive Glass for Root Canal Disinfection, Journal of Dental Research 88 (2009) 235-238.
[61] A.J. Salinas, J.M. Merino, N. Hijón, A.I. Martín, M. Vallet-Regí, Bioactive organic-inorganic hybrids based on CaO-SiO2 sol-gel glasses, Trans Tech Publications, 2004, pp. 481–484.
[62] Q. Chen, F. Miyaji, T. Kokubo, T. Nakamura, Apatite formation on PDMS-modified CaO–SiO2–TiO2 hybrids prepared by sol–gel process, Biomaterials 20 (1999) 1127-1132.
[63] K. Tsuru, C. Ohtsuki, A. Osaka, T. Iwamoto, J.D. Mackenzie, Bioactivity of sol–gel derived organically modified silicates: Part I: In vitro examination, Journal of Materials Science: Materials in Medicine 8 (1997) 157-161.
[64] B.M. Novak, Hybrid Nanocomposite Materials—between inorganic glasses and organic polymers, Advanced Materials 5 (1993) 422-433.
[65] A. Corma, From microporous to mesoporous molecular sieve materials and their use in catalysis, Chemical reviews 97 (1997) 2373–2420.
[66] A. Taguchi, F. Schüth, Ordered mesoporous materials in catalysis, Microporous and Mesoporous Materials 77 (2005) 1-45.
[67] M. Vallet-Regí, F. Balas, D. Arcos, Mesoporous Materials for Drug Delivery, Angewandte Chemie International Edition 46 (2007) 7548-7558.
[68] M. Vallet-Regí, I. Izquierdo-Barba, M. Colilla, Structure and functionalization of mesoporous bioceramics for bone tissue regeneration and local drug delivery, Philosophical Transactions of the Royal Society A: Mathematical, Physical and Engineering Sciences 370 (2012) 1400-1421.
[69] F. Qu, G. Zhu, S. Huang, S. Li, J. Sun, D. Zhang, S. Qiu, Controlled release of Captopril by regulating the pore size and morphology of ordered mesoporous silica, Microporous and Mesoporous Materials 92 (2006) 1-9.
[70] V. Mamaeva, C. Sahlgren, M. Lindén, Mesoporous silica nanoparticles in medicine—Recent advances, Advanced Drug Delivery Reviews 65 (2013) 689-702.
[71] E. Champion, Sintering of calcium phosphate bioceramics, Acta Biomaterialia 9 (2013) 5855-5875.
[72] R. Trombetta, J.A. Inzana, E.M. Schwarz, S.L. Kates, H.A. Awad, 3D Printing of Calcium Phosphate Ceramics for Bone Tissue Engineering and Drug Delivery, Annals of Biomedical Engineering 45 (2017) 23-44.
[73] M. Bohner, U. Gbureck, J.E. Barralet, Technological issues for the development of more efficient calcium phosphate bone cements: A critical assessment, Biomaterials 26 (2005) 6423-6429.
[74] K. Ishikawa, K. Asaoka, Estimation of ideal mechanical strength and critical porosity of calcium phosphate cement, Journal of Biomedical Materials Research 29 (1995) 1537-1543.
[75] C. Liu, Y. Huang, J. Chen, The physicochemical properties of the solidification of calcium phosphate cement, Journal of Biomedical Materials Research Part B: Applied Biomaterials 69B (2004) 73-78.

[76] S.V. Dorozhkin, Self-Setting Calcium Orthophosphate Formulations: Cements, Concretes, Pastes and Putties, International Journal of Materials and Chemistry 1 (2012) 1-48.
[77] Y. Song, Z. Feng, T. Wang, In situ study on the curing process of calcium phosphate bone cement, Journal of Materials Science: Materials in Medicine 18 (2007) 1185-1193.
[78] F. Tamimi, Z. Sheikh, J. Barralet, Dicalcium phosphate cements: Brushite and monetite, Acta Biomaterialia 8 (2012) 474-487.
[79] C. Migliaresi, L. Fambri, J. Kolarik, Polymerization kinetics, glass transition temperature and creep of acrylic bone cements, Biomaterials 15 (1994) 875–881.
[80] H. Deramond, N.T. Wright, S.M. Belkoff, Temperature elevation caused by bone cement polymerization during vertebroplasty, Bone 25 (1999) 17S-21S.
[81] J.C.J. Webb, R.F. Spencer, The role of polymethylmethacrylate bone cement in modern orthopaedic surgery, Bone & Joint Journal 89 (2007) 851–857.
[82] T. Golz, C.R. Graham, L.C. Busch, J. Wulf, R.J. Winder, Temperature elevation during simulated polymethylmethacrylate (PMMA) cranioplasty in a cadaver model, Journal of Clinical Neuroscience 17 (2010) 617-622.
[83] S. Meininger, C. Blum, M. Schamel, J.E. Barralet, A. Ignatius, U. Gbureck, Phytic acid as alternative setting retarder enhanced biological performance of dicalcium phosphate cement in vitro, Scientific Reports 7 (2017) 558.
[84] M. Bohner, U. Gbureck, Thermal reactions of brushite cements, Journal of Biomedical Materials Research Part B: Applied Biomaterials 84B (2008) 375–385.
[85] A. Farzadi, F. Bakhshi, M. Solati-Hashjin, M. Asadi-Eydivand, N.A.a. Osman, Magnesium incorporated hydroxyapatite: Synthesis and structural properties characterization, Ceramics International 40 (2014) 6021-6029.
[86] J. Zhang, X. Ma, D. Lin, H. Shi, Y. Yuan, W. Tang, H. Zhou, H. Guo, J. Qian, C. Liu, Magnesium modification of a calcium phosphate cement alters bone marrow stromal cell behavior via an integrin-mediated mechanism, Biomaterials 53 (2015) 251-264.
[87] J. Cabrejos-Azama, M.H. Alkhraisat, C. Rueda, J. Torres, L. Blanco, E. López-Cabarcos, Magnesium substitution in brushite cements for enhanced bone tissue regeneration, Materials Science and Engineering: C 43 (2014) 403-410.
[88] Y. Wang, X. Yang, Z. Gu, H. Qin, L. Li, J. Liu, X. Yu, In vitro study on the degradation of lithium-doped hydroxyapatite for bone tissue engineering scaffold, Materials Science and Engineering: C 66 (2016) 185-192.
[89] S. Vahabzadeh, V.K. Hack, S. Bose, Lithium-doped β-tricalcium phosphate: Effects on physical, mechanical and *in vitro* osteoblast cell-material interactions: in vitro osteoblast cell-Li doped TCP interactions, Journal of Biomedical Materials Research Part B: Applied Biomaterials 105 (2017) 391-399.
[90] J.T.B. Ratnayake, M. Mucalo, G.J. Dias, Substituted hydroxyapatites for bone regeneration: A review of current trends, Journal of Biomedical Materials Research Part B: Applied Biomaterials 105(5) (2016) 1285-1299.
[91] K. Cameron, P. Travers, C. Chander, T. Buckland, C. Campion, B. Noble, Directed osteogenic differentiation of human mesenchymal stem/precursor cells on

silicate substituted calcium phosphate, Journal of Biomedical Materials Research Part A 101A (2013) 13-22.
[92] A.F. Khan, M. Saleem, A. Afzal, A. Ali, A. Khan, A.R. Khan, Bioactive behavior of silicon substituted calcium phosphate based bioceramics for bone regeneration, Materials Science and Engineering: C 35 (2014) 245-252.
[93] A. Manchón, M. Alkhraisat, C. Rueda-Rodriguez, J. Torres, J.C. Prados-Frutos, A. Ewald, U. Gbureck, J. Cabrejos-Azama, A. Rodriguez-González, E. López-Cabarcos, Silicon calcium phosphate ceramic as novel biomaterial to simulate the bone regenerative properties of autologous bone, Journal of Biomedical Materials Research Part A 103 (2015) 479-488.
[94] K. Kuroda, M. Okido, Hydroxyapatite Coating of Titanium Implants Using Hydroprocessing and Evaluation of Their Osteoconductivity, Bioinorganic Chemistry and Applications 2012 (2012) 1-7.
[95] J.E. Barralet, K.J. Lilley, L.M. Grover, D.F. Farrar, C. Ansell, U. Gbureck, Cements from nanocrystalline hydroxyapatite, Journal of Materials Science: Materials in Medicine 15 (2004) 407-411.
[96] F.C.M. Driessens, M.G. Boltong, O. Bermudez, J.A. Planell, Formulation and setting times of some calcium orthophosphate cements: a pilot study, Journal of Materials Science: Materials in Medicine 4 (1993) 503-508.
[97] E. Fernández, M.P. Ginebra, M.G. Boltong, F.C.M. Driessens, J.A. Planell, J. Ginebra, E.a.P. De Maeyer, R.M.H. Verbeeck, Kinetic study of the setting reaction of a calcium phosphate bone cement, Journal of Biomedical Materials Research 32 (1996) 367-374.
[98] U. Gbureck, O. Grolms, J.E. Barralet, L.M. Grover, R. Thull, Mechanical activation and cement formation of β-tricalcium phosphate, Biomaterials 24 (2003) 4123-4131.
[99] U. Gbureck, J.E. Barralet, L. Radu, H.G. Klinger, R. Thull, Amorphous α-Tricalcium Phosphate: Preparation and Aqueous Setting Reaction, Journal of the American Ceramic Society 87 (2004) 1126-1132.
[100] M. Bohner, A.K. Malsy, C.L. Camiré, U. Gbureck, Combining particle size distribution and isothermal calorimetry data to determine the reaction kinetics of α-tricalcium phosphate–water mixtures, Acta Biomaterialia 2 (2006) 343-348.
[101] U. Gbureck, S. Dembski, R. Thull, J.E. Barralet, Factors influencing calcium phosphate cement shelf-life, Biomaterials 26 (2005) 3691-3697.
[102] A.A. Mirtchi, J. Lemaître, E. Hunting, Calcium phosphate cements: action of setting regulators on the properties of the β-tricalcium phosphate-monocalcium phosphate cements, Biomaterials 10 (1989) 634-638.
[103] A.A. Mirtchi, J. Lemaitre, N. Terao, Calcium phosphate cements: study of the β-tricalcium phosphate — monocalcium phosphate system, Biomaterials 10 (1989) 475-480.
[104] M. Bohner, P.V. Landuyt, H.P. Merkle, J. Lemaitre, Composition effects on the pH of a hydraulic calcium phosphate cement, Journal of Materials Science: Materials in Medicine 8 (1997) 675-681.
[105] M. Bohner, J. Lemaitre, T.A. Ring, Effects of Sulfate, Pyrophosphate, and Citrate Ions on the Physicochemical Properties of Cements Made of β-Tricalcium

Phosphate-Phosphoric Acid-Water Mixtures, Journal of the American Ceramic Society 79 (1996) 1427–1434.
[106] C. Oliveira, A. Ferreira, F. Rocha, Dicalcium Phosphate Dihydrate Precipitation: Characterization and Crystal Growth, Chemical Engineering Research and Design 85 (2007) 1655-1661.
[107] M. Bohner, Calcium orthophosphates in medicine: from ceramics to calcium phosphate cements, Injury 31, Supplement 4 (2000) D37-D47.
[108] L.M. Grover, U. Gbureck, A.M. Young, A.J. Wright, J.E. Barralet, Temperature dependent setting kinetics and mechanical properties of β-TCP–pyrophosphoric acid bone cement, Journal of Materials Chemistry 15 (2005) 4955.
[109] F.T. Mariño, J. Torres, M. Hamdan, C.R. Rodríguez, E.L. Cabarcos, Advantages of using glycolic acid as a retardant in a brushite forming cement, Journal of Biomedical Materials Research Part B: Applied Biomaterials 83B (2007) 571–579.
[110] M.H. Alkhraisat, F.T. Mariño, J.R. Retama, L.B. Jerez, E. López-Cabarcos, Beta-tricalcium phosphate release from brushite cement surface, Journal of Biomedical Materials Research Part A 84A (2008) 710–717.
[111] J.L. Giocondi, B.S. El-Dasher, G.H. Nancollas, C.A. Orme, Molecular mechanisms of crystallization impacting calcium phosphate cements, Philosophical Transactions of the Royal Society A: Mathematical, Physical and Engineering Sciences 368 (2010) 1937-1961.
[112] M. Bohner, J. Lemaître, P.V. Landuyt, P.-Y. Zambelli, H.P. Merkle, B. Gander, Gentamicin-loaded hydraulic calcium phosphate bone cement as antibiotic delivery system, Journal of Pharmaceutical Sciences 86 (1997) 565-572.
[113] S.E. Papapoulos, Bisphosphonates: how do they work?, Best Practice & Research Clinical Endocrinology & Metabolism 22 (2008) 831-847.
[114] P.-T. Cheng, K.P.H. Pritzker, S.C. Nyburg, alpha-Calcium Disodium Pyrophosphate Tetrahydrate, Acta Crystallographica Section B 36 (1980) 921-924.
[115] F. Grases, M. Ramis, A. Costa-Bauzá, Effects of phytate and pyrophosphate on brushite and hydroxyapatite crystallization, Urological Research 28 (2000) 136-140.
[116] P. Jamshidi, R.H. Bridson, A.J. Wright, L.M. Grover, Brushite cement additives inhibit attachment to cell culture beads, Biotechnology and Bioengineering 110 (2013) 1487–1494.
[117] M. Bohner, F. Theiss, D. Apelt, W. Hirsiger, R. Houriet, G. Rizzoli, E. Gnos, C. Frei, J.A. Auer, B. von Rechenberg, Compositional changes of a dicalcium phosphate dihydrate cement after implantation in sheep, Biomaterials 24 (2003) 3463-3474.
[118] Z. Amjad, P.G. Koutsoukos, G.H. Nancollas, The crystallization of hydroxyapatite and fluorapatite in the presence of magnesium ions, Journal of Colloid and Interface Science 101 (1984) 250-256.
[119] M.H. Salimi, J.C. Heughebaert, G.H. Nancollas, Crystal growth of calcium phosphates in the presence of magnesium ions, Langmuir 1 (1985) 119-122.
[120] O. Suzuki, Octacalcium phosphate: Osteoconductivity and crystal chemistry, Acta Biomaterialia 6 (2010) 3379-3387.

[121] J.D. Termine, E.D. Eanes, Comparative chemistry of amorphous and apatitic calcium phosphate preparations, Calcified Tissue Research 10 (1972) 171-197.
[122] S. Samavedi, A.R. Whittington, A.S. Goldstein, Calcium phosphate ceramics in bone tissue engineering: A review of properties and their influence on cell behavior, Acta Biomaterialia 9 (2013) 8037-8045.
[123] C. Moseke, U. Gbureck, Tetracalcium phosphate: Synthesis, properties and biomedical applications, Acta Biomaterialia 6 (2010) 3815-3823.
[124] Q. Yang, B. Zhu, X. Wu, Characteristics and durability test of magnesium phosphate cement-based material for rapid repair of concrete, Materials and Structures 33 (2000) 229–234.
[125] N. Yang, C. Shi, J. Yang, Y. Chang, Research Progresses in Magnesium Phosphate Cement–Based Materials, Journal of Materials in Civil Engineering 26(10) (2014) 04014071.
[126] R. Neiman, A.C. Sarma, Setting and Thermal Reactions of Phosphate Investments, Journal of Dental Research 59 (1980) 1478-1485.
[127] G. Mestres, M.-P. Ginebra, Novel magnesium phosphate cements with high early strength and antibacterial properties, Acta Biomaterialia 7 (2011) 1853-1861.
[128] A.-j. Wang, J. Zhang, J.-m. Li, A.-b. Ma, L.-t. Liu, Effect of liquid-to-solid ratios on the properties of magnesium phosphate chemically bonded ceramics, Materials Science and Engineering: C 33 (2013) 2508-2512.
[129] C. Moseke, V. Saratsis, U. Gbureck, Injectability and mechanical properties of magnesium phosphate cements, Journal of Materials Science: Materials in Medicine 22 (2011) 2591-2598.
[130] D.A. Hall, R. Stevens, B.E. Jazairi, Effect of water content on the structure and mechanical properties of magnesia-phosphate cement mortar, Journal of the American Ceramic Society 81 (1998) 1550–1556.
[131] A.S. Wagh, S.Y. Jeong, Chemically Bonded Phosphate Ceramics: I, A Dissolution Model of Formation, Journal of the American Ceramic Society 86 (2003) 1838-1844.
[132] T. Finch, J.H. Sharp, Chemical reactions between magnesia and aluminium orthophosphate to form magnesia-phosphate cements, Journal of materials science 24 (1989) 4379–4386.
[133] N. Ostrowski, A. Roy, P.N. Kumta, Magnesium Phosphate Cement Systems for Hard Tissue Applications: A Review, ACS Biomaterials Science & Engineering 2 (2016) 1067-1083.
[134] U. Klammert, E. Vorndran, T. Reuther, F.A. Müller, K. Zorn, U. Gbureck, Low temperature fabrication of magnesium phosphate cement scaffolds by 3D powder printing, Journal of Materials Science: Materials in Medicine 21 (2010) 2947-2953.
[135] S.A. Walling, J.L. Provis, Magnesia-Based Cements: A Journey of 150 Years, and Cements for the Future?, Chemical Reviews 116 (2016) 4170-4204.
[136] U. Klammert, A. Ignatius, U. Wolfram, T. Reuther, U. Gbureck, In vivo degradation of low temperature calcium and magnesium phosphate ceramics in a heterotopic model, Acta Biomaterialia 7 (2011) 3469-3475.

[137] A.W. Taylor, A.W. Frazier, E.L. Gurney, J.P. Smith, Solubility products of di- and trimagnesium phosphates and the dissociation of magnesium phosphate solutions, Transactions of the Faraday Society 59 (1963) 1585–1589.
[138] M. Le Rouzic, T. Chaussadent, G. Platret, L. Stefan, Mechanisms of k-struvite formation in magnesium phosphate cements, Cement and Concrete Research 91 (2017) 117-122.
[139] M.I.H. Bhuiyan, D.S. Mavinic, F.A. Koch, Thermal decomposition of struvite and its phase transition, Chemosphere 70 (2008) 1347-1356.
[140] E. Vorndran, A. Ewald, F.A. Müller, K. Zorn, A. Kufner, U. Gbureck, Formation and properties of magnesium–ammonium–phosphate hexahydrate biocements in the Ca–Mg–PO4 system, Journal of Materials Science: Materials in Medicine 22 (2011) 429-436.
[141] B. Kanter, M. Geffers, A. Ignatius, U. Gbureck, Control of in vivo mineral bone cement degradation, Acta Biomaterialia 10 (2014) 3279-3287.
[142] G. Mestres, F.S. Aguilera, N. Manzanares, S. Sauro, R. Osorio, M. Toledano, M.P. Ginebra, Magnesium phosphate cements for endodontic applications with improved long-term sealing ability, International Endodontic Journal 47 (2014) 127-139.
[143] H. Lahalle, C. Cau Dit Coumes, A. Mesbah, D. Lambertin, C. Cannes, S. Delpech, S. Gauffinet, Investigation of magnesium phosphate cement hydration in diluted suspension and its retardation by boric acid, Cement and Concrete Research 87 (2016) 77-86.
[144] T. Christel, M. Geffers, U. Klammert, B. Nies, A. Höß, J. Groll, A.C. Kübler, U. Gbureck, Fabrication and cytocompatibility of spherical magnesium ammonium phosphate granules, Materials Science and Engineering: C 42 (2014) 130-136.
[145] C. Blum, T. Brückner, A. Ewald, A. Ignatius, U. Gbureck, Mg:Ca ratio as regulating factor for osteoclastic in vitro resorption of struvite biocements, Materials Science and Engineering: C 73 (2017) 111-119.
[146] U. Klammert, T. Reuther, M. Blank, I. Reske, J.E. Barralet, L.M. Grover, A.C. Kübler, U. Gbureck, Phase composition, mechanical performance and in vitro biocompatibility of hydraulic setting calcium magnesium phosphate cement, Acta Biomaterialia 6 (2010) 1529-1535.
[147] S. Meininger, S. Mandal, A. Kumar, J. Groll, B. Basu, U. Gbureck, Strength reliability and in vitro degradation of three-dimensional powder printed strontium-substituted magnesium phosphate scaffolds, Acta Biomaterialia 31 (2016) 401-411.
[148] M. Meininger, C. Wolf-Brandstetter, J. Zerweck, F. Wenninger, U. Gbureck, J. Groll, C. Moseke, Electrochemically assisted deposition of strontium modified magnesium phosphate on titanium surfaces, Materials Science and Engineering: C 67 (2016) 65-71.
[149] A. Hoppe, N.S. Güldal, A.R. Boccaccini, A review of the biological response to ionic dissolution products from bioactive glasses and glass-ceramics, Biomaterials 32 (2011) 2757-2774.
[150] A.K. Misra, R. Mathur, Magnesium oxychloride cement concrete, Bulletin of materials science 30 (2007) 239–246.

[151] D. Deng, The mechanism for soluble phosphates to improve the water resistance of magnesium oxychloride cement, Cement and Concrete Research 33 (2003) 1311-1317.
[152] Y. Tan, Y. Liu, L. Grover, Effect of phosphoric acid on the properties of magnesium oxychloride cement as a biomaterial, Cement and Concrete Research 56 (2014) 69-74.
[153] Y. Tan, Y. Liu, Z. Zhao, J.Z. Paxton, L.M. Grover, Synthesis and in vitro degradation of a novel magnesium oxychloride cement, Journal of Biomedical Materials Research Part A 103 (2015) 194-202.
[154] Z. Li, C.K. Chau, Influence of molar ratios on properties of magnesium oxychloride cement, Cement and Concrete Research 37 (2007) 866-870.
[155] F.C. Harper, Effect of calcination temperature on the properties of magnesium oxides for use in magnesium oxychloride cements, Journal of Chemical Technology and Biotechnology 17 (1967) 5–10.
[156] B. Matkovic, J.F. Young, Microstructure of Magnesium Oxychloride Cements, Nature 246 (1973) 79-80.
[157] B.R. Lawn, D.B. Marshall, Hardness, toughness, and brittleness: an indentation analysis, Journal of the American ceramic society 62 (1979) 347–350.
[158] M. Bohner, Design of ceramic-based cements and putties for bone graft substitution, European Cells & Materials 20 (2010) 1-12.
[159] C.K. Seal, K. Vince, M.A. Hodgson, Biodegradable surgical implants based on magnesium alloys ? A review of current research, IOP Conference Series: Materials Science and Engineering 4 (2009) 012011.
[160] B.M. Holzapfel, J.C. Reichert, J.-T. Schantz, U. Gbureck, L. Rackwitz, U. Nöth, F. Jakob, M. Rudert, J. Groll, D.W. Hutmacher, How smart do biomaterials need to be? A translational science and clinical point of view, Advanced Drug Delivery Reviews 65 (2013) 581-603.
[161] M. Pilia, T. Guda, M. Appleford, Development of Composite Scaffolds for Load-Bearing Segmental Bone Defects, BioMed Research International 2013 (2013) 458253.
[162] E. Wintermantel, S.-W. Ha, Medizintechnik Life Science Engineering, 4. ed., Springer Berlin Heidelberg, Berlin, Heidelberg, 2008.
[163] M. Bohner, Physical and chemical aspects of calcium phosphates used in spinal surgery, European Spine Journal 10 (2001) S114-S121.
[164] F.C. Frank, LXXXIII. Crystal dislocations.-Elementary concepts and definitions, The London, Edinburgh, and Dublin Philosophical Magazine and Journal of Science 42 (1951) 809-819.
[165] T. Takahashi, M. Yamamoto, K. Ioku, S. Goto, Relationship between compressive strength and pore structure of hardened cement pastes, Advances in Cement Research 9 (1997) 25-30.
[166] B. Feng, M. Guolin, Y. Yuan, L. Changshen, W. Zhen, L. Jian, Role of macropore size in the mechanical properties and in vitro degradation of porous calcium phosphate cements, Materials Letters 64 (2010) 2028-2031.

[167] J.e. Barralet, T. Gaunt, A.J. Wright, I.R. Gibson, J.C. Knowles, Effect of porosity reduction by compaction on compressive strength and microstructure of calcium phosphate cement, Journal of Biomedical Materials Research 63 (2002) 1-9.
[168] Y. Zhang, H.H.K. Xu, S. Takagi, L.C. Chow, In-situ hardening hydroxyapatite-based scaffold for bone repair, Journal of Materials Science: Materials in Medicine 17 (2006) 437-445.
[169] I. Ajaxon, Y. Maazouz, M.-P. Ginebra, C. Öhman, C. Persson, Evaluation of a porosity measurement method for wet calcium phosphate cements, Journal of Biomaterials Applications 30(5) (2015) 526-536.
[170] J.E. Barralet, L. Grover, T. Gaunt, A.J. Wright, I.R. Gibson, Preparation of macroporous calcium phosphate cement tissue engineering scaffold, Biomaterials 23 (2002) 3063-3072.
[171] J.P. Morgan, R.H. Dauskardt, Notch strength insensitivity of self-setting hydroxyapatite bone cements, Journal of Materials Science: Materials in Medicine 14 (2003) 647–653.
[172] M. Castilho, B. Gouveia, I. Pires, J. Rodrigues, M. Pereira, The role of shell/core saturation level on the accuracy and mechanical characteristics of porous calcium phosphate models produced by 3Dprinting, Rapid Prototyping Journal 21 (2015) 43-55.
[173] M.A. Lopes, F.J. Monteiro, J.D. Santos, others, Glass-reinforced hydroxyapatite composites: Secondary phase proportions and densification effects on biaxial bending strength, Journal of biomedical materials research 48 (1999) 734–740.
[174] M.G.S. Murray, J. Wang, C.B. Ponton, P.M. Marquis, An improvement in processing of hydroxyapatite ceramics, Journal of materials science 30 (1995) 3061–3074.
[175] M. Castilho, M. Dias, U. Gbureck, J. Groll, P. Fernandes, I. Pires, B. Gouveia, J. Rodrigues, E. Vorndran, Fabrication of computationally designed scaffolds by low temperature 3D printing, Biofabrication 5(3) (2013) 035012.
[176] C.I. Vallo, Flexural strength distribution of a PMMA-based bone cement, Journal of Biomedical Materials Research 63 (2002) 226-236.
[177] M.P. Staiger, A.M. Pietak, J. Huadmai, G. Dias, Magnesium and its alloys as orthopedic biomaterials: a review, Biomaterials 27 (2006) 1728–1734.
[178] K.A. Athanasiou, C.-F. Zhu, D.R. Lanctot, C.M. Agrawal, X. Wang, Fundamentals of biomechanics in tissue engineering of bone, Tissue engineering 6 (2000) 361–381.
[179] A. Rohlmann, H. Zilch, G. Bergmann, R. Kolbel, Material properties of femoral cancellous bone in axial loading, Archives of orthopaedic and traumatic surgery 97 (1980) 95–102.
[180] U. Gbureck, J.E. Barralet, K. Spatz, L.M. Grover, R. Thull, Ionic modification of calcium phosphate cement viscosity. Part I: hypodermic injection and strength improvement of apatite cement, Biomaterials 25 (2004) 2187-2195.
[181] H. Zhou, A.K. Agarwal, V.K. Goel, S.B. Bhaduri, Microwave assisted preparation of magnesium phosphate cement (MPC) for orthopedic applications: A

novel solution to the exothermicity problem, Materials Science and Engineering: C 33 (2013) 4288-4294.
[182] T. Christel, S. Christ, J.E. Barralet, J. Groll, U. Gbureck, M.P. Ginebra, Chelate Bonding Mechanism in a Novel Magnesium Phosphate Bone Cement, Journal of the American Ceramic Society 98(3) (2015) 694-697.
[183] F. Tamimi, D.L. Nihouannen, D.C. Bassett, S. Ibasco, U. Gbureck, J. Knowles, A. Wright, A. Flynn, S.V. Komarova, J.E. Barralet, Biocompatibility of magnesium phosphate minerals and their stability under physiological conditions, Acta Biomaterialia 7 (2011) 2678-2685.
[184] C. Grossardt, A. Ewald, L.M. Grover, J.E. Barralet, U. Gbureck, Passive and active in vitro resorption of calcium and magnesium phosphate cements by osteoclastic cells, Tissue Engineering. Part A 16 (2010) 3687-3695.
[185] W.J. Boyle, W.S. Simonet, D.L. Lacey, Osteoclast differentiation and activation, Nature 423 (2003) 337-342.
[186] J.F. Charles, A.O. Aliprantis, Osteoclasts: more than 'bone eaters', Trends in Molecular Medicine 20 (2014) 449-459.
[187] L.A. Hebert, J. Lemann Jr, J.R. Petersen, E.J. Lennon, Studies of the mechanism by which phosphate infusion lowers serum calcium concentration, Journal of Clinical Investigation 45 (1966) 1886.
[188] J.R. Weisinger, E. Bellorín-Font, Magnesium and phosphorus, The Lancet 352 (1998) 391–396.
[189] L. Lind, S. Jakobsson, H. Lithell, B. Wengle, S. Ljunghall, Relation of serum calcium concentration to metabolic risk factors for cardiovascular disease, BMJ 297 (1988) 960-963.
[190] P. Habibovic, J.E. Barralet, Bioinorganics and biomaterials: Bone repair, Acta Biomaterialia 7 (2011) 3013-3026.
[191] M.E. Maguire, J.A. Cowan, Magnesium chemistry and biochemistry, Biometals 15 (2002) 203-210.
[192] J. Vormann, Magnesium: nutrition and metabolism, Molecular Aspects of Medicine 24 (2003) 27-37.
[193] G.A. Quamme, C. de Rouffignac, Epithelial magnesium transport and regulation by the kidney, Frontiers in Bioscience 5 (2000) 15.
[194] J.M. Topf, P.T. Murray, Hypomagnesemia and Hypermagnesemia, Reviews in Endocrine and Metabolic Disorders 4 (2003) 195-206.
[195] C. Knabe, W. Ostapowicz, R.J. Radlanski, R. Gildenhaar, G. Berger, R. Fitzner, U. Gross, In vitro investigation of novel calcium phosphates using osteogenic cultures, Journal of Materials Science: Materials in Medicine 9 (1998) 337-345.
[196] S.S. Singh, A. Roy, B. Lee, S. Parekh, P.N. Kumta, Murine osteoblastic and osteoclastic differentiation on strontium releasing hydroxyapatite forming cements, Materials Science and Engineering: C 63 (2016) 429-438.
[197] Y.K. Liu, Q.Z. Lu, R. Pei, H.J. Ji, G.S. Zhou, X.L. Zhao, R.K. Tang, M. Zhang, The effect of extracellular calcium and inorganic phosphate on the growth and osteogenic differentiation of mesenchymal stem cells in vitro : implication for bone tissue engineering, Biomedical Materials 4(2) (2009) 025004.

[198] Z. Meleti, I.M. Shapiro, C.S. Adams, Inorganic phosphate induces apoptosis of osteoblast-like cells in culture, Bone 27 (2000) 359-366.
[199] Y. Liu, P.R. Cooper, J.E. Barralet, R.M. Shelton, Influence of calcium phosphate crystal assemblies on the proliferation and osteogenic gene expression of rat bone marrow stromal cells, Biomaterials 28 (2007) 1393-1403.
[200] R. Zhang, Y. Lu, L. Ye, B. Yuan, S. Yu, C. Qin, Y. Xie, T. Gao, M.K. Drezner, L.F. Bonewald, J.Q. Feng, Unique roles of phosphorus in endochondral bone formation and osteocyte maturation, Journal of Bone and Mineral Research 26 (2011) 1047-1056.
[201] P. Habibovic, D.C. Bassett, C.J. Doillon, C. Gerard, M.D. McKee, J.E. Barralet, Collagen Biomineralization In Vivo by Sustained Release of Inorganic Phosphate Ions, Advanced Materials 22 (2010) 1858-1862.
[202] B. Houston, A.J. Stewart, C. Farquharson, PHOSPHO1—A novel phosphatase specifically expressed at sites of mineralisation in bone and cartilage, Bone 34 (2004) 629-637.
[203] M.D. Polewski, K.A. Johnson, M. Foster, J.L. Millán, R. Terkeltaub, Inorganic pyrophosphatase induces type I collagen in osteoblasts, Bone 46 (2010) 81-90.
[204] J. Kwarcinski, P. Boughton, A. Ruys, A. Doolan, J. van Gelder, Cranioplasty and Craniofacial Reconstruction: A Review of Implant Material, Manufacturing Method and Infection Risk, Applied Sciences 7 (2017) 276.
[205] S.-I. Roohani-Esfahani, S. Nouri-Khorasani, Z. Lu, R. Appleyard, H. Zreiqat, The influence hydroxyapatite nanoparticle shape and size on the properties of biphasic calcium phosphate scaffolds coated with hydroxyapatite–PCL composites, Biomaterials 31 (2010) 5498-5509.
[206] M. Bohner, Y. Loosli, G. Baroud, D. Lacroix, Commentary: Deciphering the link between architecture and biological response of a bone graft substitute, Acta Biomaterialia 7 (2011) 478-484.
[207] R.K. Jain, P. Au, J. Tam, D.G. Duda, D. Fukumura, Engineering vascularized tissue, Nature Biotechnology 23 (2005) 821-823.
[208] J. Rouwkema, N.C. Rivron, C.A. van Blitterswijk, Vascularization in tissue engineering, Trends in Biotechnology 26 (2008) 434-441.
[209] L.E. Rustom, T. Boudou, S. Lou, I. Pignot-Paintrand, B.W. Nemke, Y. Lu, M.D. Markel, C. Picart, A.J. Wagoner Johnson, Micropore-induced capillarity enhances bone distribution in vivo in biphasic calcium phosphate scaffolds, Acta Biomaterialia 44 (2016) 144-154.
[210] S. Bose, M. Roy, A. Bandyopadhyay, Recent advances in bone tissue engineering scaffolds, Trends in Biotechnology 30 (2012) 546-554.
[211] M. Espanol, R.A. Perez, E.B. Montufar, C. Marichal, A. Sacco, M.P. Ginebra, Intrinsic porosity of calcium phosphate cements and its significance for drug delivery and tissue engineering applications, Acta Biomaterialia 5 (2009) 2752-2762.
[212] J.M. Bouler, P. Pilet, O. Gauthier, E. Verron, Biphasic calcium phosphate ceramics for bone reconstruction: A review of biological response, Acta Biomaterialia 53 (2017) 1-12.

[213] J. Will, R. Melcher, C. Treul, N. Travitzky, U. Kneser, E. Polykandriotis, R. Horch, P. Greil, Porous ceramic bone scaffolds for vascularized bone tissue regeneration, Journal of Materials Science: Materials in Medicine 19 (2008) 2781-2790.
[214] P. Habibovic, H. Yuan, C.M. van der Valk, G. Meijer, C.A. van Blitterswijk, K. de Groot, 3D microenvironment as essential element for osteoinduction by biomaterials, Biomaterials 26 (2005) 3565-3575.
[215] K. Ohura, M. Bohner, P. Hardouin, J. Lemaître, G. Pasquier, B. Flautre, Resorption of, and bone formation from, new β-tricalcium phosphate-monocalcium phosphate cements: An in vivo study, Journal of Biomedical Materials Research 30 (1996) 193–200.
[216] J. Zhao, G. Shen, C. Liu, S. Wang, W. Zhang, X. Zhang, X. Zhang, D. Ye, J. Wei, Z. Zhang, X. Jiang, Enhanced Healing of Rat Calvarial Defects with Sulfated Chitosan-Coated Calcium-Deficient Hydroxyapatite/Bone Morphogenetic Protein 2 Scaffolds, Tissue Engineering Part A 18 (2012) 185-197.
[217] M. Thorwarth, S. Rupprecht, S. Falk, E. Felszeghy, J. Wiltfang, K.A. Schlegel, Expression of bone matrix proteins during de novo bone formation using a bovine collagen and platelet-rich plasma (prp) - an immunohistochemical analysis, Biomaterials 26 (2005) 2575-2584.
[218] R.P. del Real, J.G.C. Wolke, M. Vallet-Regí, J.A. Jansen, A new method to produce macropores in calcium phosphate cements, Biomaterials 23 (2002) 3673-3680.
[219] D.-M. Liu, Influence of porosity and pore size on the compressive strength of porous hydroxyapatite ceramic, Ceramics International 23 (1997) 135–139.
[220] M. Bohner, G.H. van Lenthe, S. Grünenfelder, W. Hirsiger, R. Evison, R. Müller, Synthesis and characterization of porous β-tricalcium phosphate blocks, Biomaterials 26 (2005) 6099-6105.
[221] C.M.S. Ranito, F.A. Costa Oliveira, J.P. Borges, Hydroxyapatite Foams for Bone Replacement, Key Engineering Materials 284-286 (2005) 341-344.
[222] U. Deisinger, F. Stenzel, G. Ziegler, Development of Hydroxyapatite Ceramics with Tailored Pore Structure, Key Engineering Materials 254-256 (2004) 977-980.
[223] U. Deisinger, Generating Porous Ceramic Scaffolds: Processing and Properties, Key Engineering Materials 441 (2010) 155-179.
[224] C. Moseke, C. Bayer, E. Vorndran, J.E. Barralet, J. Groll, U. Gbureck, Low temperature fabrication of spherical brushite granules by cement paste emulsion, Journal of Materials Science: Materials in Medicine 23 (2012) 2631-2637.
[225] P. Weiss, P. Layrolle, L.P. Clergeau, B. Enckel, P. Pilet, Y. Amouriq, G. Daculsi, B. Giumelli, The safety and efficacy of an injectable bone substitute in dental sockets demonstrated in a human clinical trial, Biomaterials 28 (2007) 3295-3305.
[226] O. Gauthier, J.-M. Bouler, P. Weiss, J. Bosco, E. Aguado, G. Daculsi, Short-term effects of mineral particle sizes on cellular degradation activity after implantation of injectable calcium phosphate biomaterials and the consequences for bone substitution, Bone 25 (1999) 71S–74S.

[227] O. Gauthier, E. Goyenvalle, J.-M. Bouler, J. Guicheux, P. Pilet, P. Weiss, G. Daculsi, Macroporous biphasic calcium phosphate ceramics versus injectable bone substitute: a comparative study 3 and 8 weeks after implantation in rabbit bone, Journal of materials science: materials in medicine 12 (2001) 385–390.
[228] M. Bohner, S. Tadier, N. van Garderen, A. de Gasparo, N. Döbelin, G. Baroud, Synthesis of spherical calcium phosphate particles for dental and orthopedic applications, Biomatter 3 (2013) e25103.
[229] R.A. Surmenev, M.A. Surmeneva, A.A. Ivanova, Significance of calcium phosphate coatings for the enhancement of new bone osteogenesis – A review, Acta Biomaterialia 10 (2014) 557-579.
[230] K.W. Jennette, The role of metals in carcinogenesis: biochemistry and metabolism., Environmental Health Perspectives 40 (1981) 233-252.
[231] X. Liu, S. Zhu, J. Cui, H. Shao, W. Zhang, H. Yang, Y. Xu, D. Geng, L. Yu, Strontium ranelate inhibits titanium-particle-induced osteolysis by restraining inflammatory osteoclastogenesis in vivo, Acta Biomaterialia 10 (2014) 4912-4918.
[232] I. Khairoun, M.G. Boltong, F.M. Driessens, J.A. Planell, Some factors controlling the injectability of calcium phosphate bone cements, Journal of Materials Science: Materials in Medicine 9 (1998) 425–428.
[233] R. O'Neill, H.O. McCarthy, E.B. Montufar, M.-P. Ginebra, D.I. Wilson, A. Lennon, N. Dunne, Critical review: Injectability of calcium phosphate pastes and cements, Acta Biomaterialia 50 (2017) 1-19.
[234] K. Ishikawa, Effects of spherical tetracalcium phosphate on injectability and basic properties of apatitic cement, Key Engineering Materials 240 (2003) 369–372.
[235] V. Jack, F.J. Buchanan, N.J. Dunne, Particle attrition of α-tricalcium phosphate: effect on mechanical, handling, and injectability properties of calcium phosphate cements, Proceedings of the Institution of Mechanical Engineers, Part H: Journal of Engineering in Medicine 222 (2008) 19-28.
[236] E.B. Montufar, Y. Maazouz, M.P. Ginebra, Relevance of the setting reaction to the injectability of tricalcium phosphate pastes, Acta Biomaterialia 9 (2013) 6188-6198.
[237] U. Gbureck, K. Spatz, R. Thull, J.E. Barralet, Rheological enhancement of mechanically activated α-tricalcium phosphate cements, Journal of Biomedical Materials Research Part B: Applied Biomaterials 73B (2005) 1–6.
[238] S. Tadier, L. Galea, B. Charbonnier, G. Baroud, M. Bohner, Phase and size separations occurring during the injection of model pastes composed of β-tricalcium phosphate powder, glass beads and aqueous solutions, Acta Biomaterialia 10 (2014) 2259-2268.
[239] P.M.C. Torres, S. Gouveia, S. Olhero, A. Kaushal, J.M.F. Ferreira, Injectability of calcium phosphate pastes: Effects of particle size and state of aggregation of β-tricalcium phosphate powders, Acta Biomaterialia 21 (2015) 204-216.
[240] E.F. Burguera, H.H.K. Xu, M.D. Weir, Injectable and rapid-setting calcium phosphate bone cement with dicalcium phosphate dihydrate, Journal of Biomedical Materials Research Part B: Applied Biomaterials 77B (2006) 126-134.

[241] W. Liu, J. Zhang, P. Weiss, F. Tancret, J.-M. Bouler, The influence of different cellulose ethers on both the handling and mechanical properties of calcium phosphate cements for bone substitution, Acta Biomaterialia 9 (2013) 5740-5750.
[242] S. Sarda, E. Fernandez, M. Nilsson, M. Balcells, J.A. Planell, Kinetic study of citric acid influence on calcium phosphate bone cements as water-reducing agent, Journal of Biomedical Materials Research Part A 61 (2002) 653–659.
[243] J.E. Barralet, L.M. Grover, U. Gbureck, Ionic modification of calcium phosphate cement viscosity. Part II: hypodermic injection and strength improvement of brushite cement, Biomaterials 25 (2004) 2197-2203.
[244] H.H.K. Xu, M.D. Weir, E.F. Burguera, A.M. Fraser, Injectable and macroporous calcium phosphate cement scaffold, Biomaterials 27 (2006) 4279-4287.
[245] M. Bohner, G. Baroud, Injectability of calcium phosphate pastes, Biomaterials 26 (2005) 1553-1563.
[246] J. Franco, P. Hunger, M.E. Launey, A.P. Tomsia, E. Saiz, Direct write assembly of calcium phosphate scaffolds using a water-based hydrogel, Acta Biomaterialia 6 (2010) 218-228.
[247] M. Vaezi, H. Seitz, S. Yang, A review on 3D micro-additive manufacturing technologies, The International Journal of Advanced Manufacturing Technology 67 (2013) 1721-1754.
[248] F.P.W. Melchels, J. Feijen, D.W. Grijpma, A review on stereolithography and its applications in biomedical engineering, Biomaterials 31 (2010) 6121-6130.
[249] A. Butscher, M. Bohner, S. Hofmann, L. Gauckler, R. Müller, Structural and material approaches to bone tissue engineering in powder-based three-dimensional printing, Acta Biomaterialia 7 (2011) 907-920.
[250] S. Yang, K.-F. Leong, Z. Du, C.-K. Chua, The Design of Scaffolds for Use in Tissue Engineering. Part II. Rapid Prototyping Techniques, Tissue Engineering 8 (2002) 1-11.
[251] J.W. Halloran, Ceramic Stereolithography: Additive Manufacturing for Ceramics by Photopolymerization, Annual Review of Materials Research 46 (2016) 19-40.
[252] K.F. Leong, C.M. Cheah, C.K. Chua, Solid freeform fabrication of three-dimensional scaffolds for engineering replacement tissues and organs, Biomaterials 24 (2003) 2363-2378.
[253] S.L. Sing, W.Y. Yeong, F.E. Wiria, B.Y. Tay, Z. Zhao, L. Zhao, Z. Tian, S. Yang, Direct selective laser sintering and melting of ceramics: a review, Rapid Prototyping Journal 23 (2017) 611-623.
[254] K.H. Tan, C.K. Chua, K.F. Leong, M.W. Naing, C.M. Cheah, Fabrication and characterization of three-dimensional poly(ether-ether-ketone)/-hydroxyapatite biocomposite scaffolds using laser sintering, Proceedings of the Institution of Mechanical Engineers, Part H: Journal of Engineering in Medicine 219 (2005) 183-194.
[255] J.M. Williams, A. Adewunmi, R.M. Schek, C.L. Flanagan, P.H. Krebsbach, S.E. Feinberg, S.J. Hollister, S. Das, Bone tissue engineering using polycaprolactone scaffolds fabricated via selective laser sintering, Biomaterials 26 (2005) 4817-4827.

[256] H.N. Chia, B.M. Wu, Recent advances in 3D printing of biomaterials, Journal of Biological Engineering 9 (2015).
[257] A. Kumar, S. Mandal, S. Barui, R. Vasireddi, U. Gbureck, M. Gelinsky, B. Basu, Low temperature additive manufacturing of three dimensional scaffolds for bone-tissue engineering applications: Processing related challenges and property assessment, Materials Science and Engineering: R: Reports 103 (2016) 1-39.
[258] M. Houmard, Q. Fu, M. Genet, E. Saiz, A.P. Tomsia, On the structural, mechanical, and biodegradation properties of HA/β-TCP robocast scaffolds: Bone-Substitute Material in Various Tissue-Engineering Applications, Journal of Biomedical Materials Research Part B: Applied Biomaterials 101 (2013) 1233-1242.
[259] V.K. Popov, A.V. Evseev, A.L. Ivanov, V.V. Roginski, A.I. Volozhin, S.M. Howdle, Laser stereolithography and supercritical fluid processing for custom-designed implant fabrication, Journal of Materials Science: Materials in Medicine 15 (2004) 123–128.
[260] N.L. Porter, R.M. Pilliar, M.D. Grynpas, Fabrication of porous calcium polyphosphate implants by solid freeform fabrication: a study of processing parameters and in vitro degradation characteristics, Journal of Biomedical Materials Research Part A 56 (2001) 504–515.
[261] W. Bian, D. Li, Q. Lian, W. Zhang, L. Zhu, X. Li, Z. Jin, Design and fabrication of a novel porous implant with pre-set channels based on ceramic stereolithography for vascular implantation, Biofabrication 3 (2011) 034103.
[262] M.L. Griffith, J.W. Halloran, Freeform Fabrication of Ceramics via Stereolithography, Journal of the American Ceramic Society 79 (2005) 2601-2608.
[263] S.F.S. Shirazi, S. Gharehkhani, M. Mehrali, H. Yarmand, H.S.C. Metselaar, N.A. Kadri, N.A.A. Osman, A review on powder-based additive manufacturing for tissue engineering: selective laser sintering and inkjet 3D printing, Science and Technology of Advanced Materials 16 (2015) 033502.
[264] C. Shuai, P. Feng, C. Cao, S. Peng, Processing and characterization of laser sintered hydroxyapatite scaffold for tissue engineering, Biotechnology and Bioprocess Engineering 18 (2013) 520-527.
[265] C. Shuai, P. Li, J. Liu, S. Peng, Optimization of TCP/HAP ratio for better properties of calcium phosphate scaffold via selective laser sintering, Materials Characterization 77 (2013) 23-31.
[266] K.H. Tan, C.K. Chua, K.F. Leong, C.M. Cheah, P. Cheang, M.S. Abu Bakar, S.W. Cha, Scaffold development using selective laser sintering of polyetheretherketone–hydroxyapatite biocomposite blends, Biomaterials 24 (2003) 3115-3123.
[267] Y. Luo, A. Lode, F. Sonntag, B. Nies, M. Gelinsky, Well-ordered biphasic calcium phosphate–alginate scaffolds fabricated by multi-channel 3D plotting under mild conditions, Journal of Materials Chemistry B 1 (2013) 4088.
[268] Y. Maazouz, E.B. Montufar, J. Guillem-Marti, I. Fleps, C. Öhman, C. Persson, M.P. Ginebra, Robocasting of biomimetic hydroxyapatite scaffolds using self-setting inks, J. Mater. Chem. B 2 (2014) 5378-5386.
[269] A. Kumar, A.R. Akkineni, B. Basu, M. Gelinsky, Three-dimensional plotted hydroxyapatite scaffolds with predefined architecture: comparison of stabilization

by alginate cross-linking versus sintering, Journal of Biomaterials Applications 30 (2016) 1168-1181.
[270] R. Landers, R. Mülhaupt, Desktop manufacturing of complex objects, prototypes and biomedical scaffolds by means of computer-assisted design combined with computer-guided 3D plotting of polymers and reactive oligomers, Macromolecular Materials and Engineering 282 (2000) 17-21.
[271] Y. Luo, A. Lode, C. Wu, J. Chang, M. Gelinsky, Alginate/Nanohydroxyapatite Scaffolds with Designed Core/Shell Structures Fabricated by 3D Plotting and in Situ Mineralization for Bone Tissue Engineering, ACS Applied Materials & Interfaces 7 (2015) 6541-6549.
[272] E. Vorndran, K. Wunder, C. Moseke, I. Biermann, F.A. Müller, K. Zorn, U. Gbureck, Hydraulic setting Mg3(PO4)2 powders for 3D printing technology, Advances in Applied Ceramics 110 (2011) 476-481.
[273] A. Butscher, M. Bohner, C. Roth, A. Ernstberger, R. Heuberger, N. Doebelin, P. Rudolf von Rohr, R. Müller, Printability of calcium phosphate powders for three-dimensional printing of tissue engineering scaffolds, Acta Biomaterialia 8 (2012) 373-385.
[274] A. Pfister, R. Landers, A. Laib, U. Hübner, R. Schmelzeisen, R. Mülhaupt, Biofunctional rapid prototyping for tissue-engineering applications: 3D bioplotting versus 3D printing, Journal of Polymer Science Part A: Polymer Chemistry 42 (2004) 624–638.
[275] E. Vorndran, U. Klammert, A. Ewald, J.E. Barralet, U. Gbureck, Simultaneous Immobilization of Bioactives During 3D Powder Printing of Bioceramic Drug-Release Matrices, Advanced Functional Materials 20 (2010) 1585-1591.
[276] E. Vorndran, M. Klarner, U. Klammert, L.M. Grover, S. Patel, J.E. Barralet, U. Gbureck, 3D Powder Printing of β-Tricalcium Phosphate Ceramics Using Different Strategies, Advanced Engineering Materials 10 (2008) B67–B71.
[277] H. Seitz, W. Rieder, S. Irsen, B. Leukers, C. Tille, Three-dimensional printing of porous ceramic scaffolds for bone tissue engineering, Journal of Biomedical Materials Research Part B: Applied Biomaterials 74B (2005) 782-788.
[278] U. Gbureck, T. Hölzel, U. Klammert, K. Würzler, F.A. Müller, J.E. Barralet, Resorbable Dicalcium Phosphate Bone Substitutes Prepared by 3D Powder Printing, Advanced Functional Materials 17 (2007) 3940–3945.
[279] A. Butscher, M. Bohner, N. Doebelin, S. Hofmann, R. Müller, New depowdering-friendly designs for three-dimensional printing of calcium phosphate bone substitutes, Acta Biomaterialia 9 (2013) 9149-9158.
[280] U. Gbureck, T. Hölzel, I. Biermann, J.E. Barralet, L.M. Grover, Preparation of tricalcium phosphate/calcium pyrophosphate structures via rapid prototyping, Journal of Materials Science: Materials in Medicine 19 (2008) 1559-1563.
[281] N. Sandler, A. Määttänen, P. Ihalainen, L. Kronberg, A. Meierjohann, T. Viitala, J. Peltonen, Inkjet printing of drug substances and use of porous substrates-towards individualized dosing, Journal of Pharmaceutical Sciences 100 (2011) 3386-3395.
[282] E.L. Nyberg, A.L. Farris, B.P. Hung, M. Dias, J.R. Garcia, A.H. Dorafshar, W.L. Grayson, 3D-Printing Technologies for Craniofacial Rehabilitation,

Reconstruction, and Regeneration, Annals of Biomedical Engineering 45 (2017) 45-57.
[283] R. Vasireddi, B. Basu, Conceptual design of three-dimensional scaffolds of powder-based materials for bone tissue engineering applications, Rapid Prototyping Journal 21 (2015) 716-724.
[284] H. Seitz, U. Deisinger, B. Leukers, R. Detsch, G. Ziegler, Different Calcium Phosphate Granules for 3-D Printing of Bone Tissue Engineering Scaffolds, Advanced Engineering Materials 11 (2009) B41-B46.
[285] M. Castilho, C. Moseke, A. Ewald, U. Gbureck, J. Groll, I. Pires, J. Teßmar, E. Vorndran, Direct 3D powder printing of biphasic calcium phosphate scaffolds for substitution of complex bone defects, Biofabrication 6 (2014) 015006.
[286] J.A. Inzana, D. Olvera, S.M. Fuller, J.P. Kelly, O.A. Graeve, E.M. Schwarz, S.L. Kates, H.A. Awad, 3D printing of composite calcium phosphate and collagen scaffolds for bone regeneration, Biomaterials 35 (2014) 4026-4034.
[287] U. Klammert, H. Böhm, T. Schweitzer, K. Würzler, U. Gbureck, J. Reuther, A. Kübler, Multi-directional Le Fort III midfacial distraction using an individual prefabricated device, Journal of Cranio-Maxillofacial Surgery 37 (2009) 210-215.
[288] V.C. Li, On engineered cementitious composites (ECC), Journal of advanced concrete technology 1 (2003) 215–230.
[289] H.H.K. Xu, J.B. Quinn, S. Takagi, L.C. Chow, F.C. Eichmiller, Strong and macroporous calcium phosphate cement: Effects of porosity and fiber reinforcement on mechanical properties, Journal of Biomedical Materials Research 57 (2001) 457–466.
[290] D.A. Norman, R.E. Robertson, The effect of fiber orientation on the toughening of short fiber-reinforced polymers, Journal of applied polymer science 90 (2003) 2740–2751.
[291] V.C. Li, Y. Wang, S. Backer, A micromechanical model of tension-softening and bridging toughening of short random fiber reinforced brittle matrix composites, Journal of the Mechanics and Physics of Solids 39 (1991) 607–625.
[292] S. Maenz, E. Kunisch, M. Mühlstädt, A. Böhm, V. Kopsch, J. Bossert, R.W. Kinne, K.D. Jandt, Enhanced mechanical properties of a novel, injectable, fiber-reinforced brushite cement, Journal of the Mechanical Behavior of Biomedical Materials 39 (2014) 328-338.
[293] M.E. Launey, R.O. Ritchie, On the Fracture Toughness of Advanced Materials, Advanced Materials 21 (2009) 2103-2110.
[294] R.O. Ritchie, The conflicts between strength and toughness, Nature Materials 10 (2011) 817-822.
[295] R.K. Nalla, J.J. Kruzic, J.H. Kinney, R.O. Ritchie, Mechanistic aspects of fracture and R-curve behavior in human cortical bone, Biomaterials 26 (2005) 217-231.
[296] H. Peterlik, P. Roschger, K. Klaushofer, P. Fratzl, From brittle to ductile fracture of bone, Nature Materials 5 (2006) 52-55.
[297] C. Canal, M.P. Ginebra, Fibre-reinforced calcium phosphate cements: A review, Journal of the Mechanical Behavior of Biomedical Materials 4 (2011) 1658-1671.

[298] V.C. Li, H. Stang, Interface property characterization and strengthening mechanisms in fiber reinforced cement based composites, Advanced Cement Based Materials 6 (1997) 1-20.
[299] V.C. Li, H.-C. Wu, Y.-W. Chan, Effect of Plasma Treatment of Polyethylene Fibers on Interface and ementitious Composite Properties, Journal of the American Ceramic Society 79 (1996) 700-704.
[300] P. Payrow, M.R. Nokken, D. Banu, D. Feldman, Effect of surface treatment on the post-peak residual strength and toughness of polypropylene/polyethylene-blended fiber-reinforced concrete, Journal of Composite Materials 45(20) (2011) 2047-2054.
[301] V.C. Li, H.-C. Wu, Conditions for Pseudo Strain-Hardening in Fiber Reinforced Brittle Matrix Composites, Applied Mechanics Reviews 45 (1992) 390-398.
[302] A.A. White, S.M. Best, I.A. Kinloch, Hydroxyapatite–carbon nanotube composites for biomedical applications: a review, International Journal of Applied Ceramic Technology 4 (2007) 1–13.
[303] K.-K. Chew, K.-L. Low, S.H. Sharif Zein, D.S. McPhail, L.-C. Gerhardt, J.A. Roether, A.R. Boccaccini, Reinforcement of calcium phosphate cement with multi-walled carbon nanotubes and bovine serum albumin for injectable bone substitute applications, Journal of the Mechanical Behavior of Biomedical Materials 4 (2011) 331-339.
[304] X. Wang, J. Ye, Y. Wang, L. Chen, Reinforcement of Calcium Phosphate Cement by Bio-Mineralized Carbon Nanotube, Journal of the American Ceramic Society 90 (2007) 962-964.
[305] H.H.K. Xu, F.C. Eichmiller, A.A. Giuseppetti, Reinforcement of a self-setting calcium phosphate cement with different fibers, Journal of Biomedical Materials Research 52 (2000) 107–114.
[306] L.A. Dos Santos, L.C. De Oliveira, E.C. Da Silva Rigo, R.G. Carrodéguas, A.O. Boschi, A.C. Fonseca de Arruda, Fiber Reinforced Calcium Phosphate Cement, Artificial Organs 24 (2000) 212–216.
[307] Y. Zuo, F. Yang, J.G.C. Wolke, Y. Li, J.A. Jansen, Incorporation of biodegradable electrospun fibers into calcium phosphate cement for bone regeneration, Acta Biomaterialia 6 (2010) 1238-1247.
[308] H.H.K. Xu, J.B. Quinn, Calcium phosphate cement containing resorbable fibers for short-term reinforcement and macroporosity, Biomaterials 23 (2002) 193-202.
[309] E.F. Burguera, H.H.K. Xu, S. Takagi, L.C. Chow, High early strength calcium phosphate bone cement: Effects of dicalcium phosphate dihydrate and absorbable fibers, Journal of Biomedical Materials Research Part A 75A (2005) 966-975.
[310] A.S. Von Gonten, J.R. Kelly, J.M. Antonucci, Load-bearing behavior of a simulated craniofacial structure fabricated from a hydroxyapatite cement and bioresorbable fiber-mesh, Journal of Materials Science: Materials in Medicine 11 (2000) 95–100.

[311] J.L. Moreau, M.D. Weir, H.H.K. Xu, Self-setting collagen-calcium phosphate bone cement: Mechanical and cellular properties, Journal of Biomedical Materials Research Part A 91A (2009) 605–613.
[312] R.M. O'Hara, J.F. Orr, F.J. Buchanan, R.K. Wilcox, D.C. Barton, N.J. Dunne, Development of a bovine collagen–apatitic calcium phosphate cement for potential fracture treatment through vertebroplasty, Acta Biomaterialia 8 (2012) 4043-4052.
[313] T.-Y. Wu, Z.-B. Zhou, Z.-W. He, W.-P. Ren, X.-W. Yu, Y. Huang, Reinforcement of a new calcium phosphate cement with RGD-chitosan-fiber, Journal of Biomedical Materials Research Part A 102 (2014) 68-75.
[314] N. Nezafati, F. Moztarzadeh, S. Hesaraki, M. Mozafari, Synergistically reinforcement of a self-setting calcium phosphate cement with bioactive glass fibers, Ceramics International 37 (2011) 927-934.
[315] F.A. Müller, U. Gbureck, T. Kasuga, Y. Mizutani, J.E. Barralet, U. Lohbauer, Whisker-Reinforced Calcium Phosphate Cements, Journal of the American Ceramic Society 90 (2007) 3694–3697.
[316] M. Kon, L.M. Hirakata, Y. Miyamoto, H. Kasahara, K. Asaoka, Strengthening of calcium phosphate cement by compounding calcium carbonate whiskers, Dental materials journal 24 (2005) 104–110.
[317] K. Zorn, E. Vorndran, U. Gbureck, F.A. Müller, Reinforcement of a Magnesium-Ammonium-Phosphate Cement with Calcium Phosphate Whiskers, Journal of the American Ceramic Society 98 (2015) 4028-4035.
[318] J. Zhang, W. Liu, V. Schnitzler, F. Tancret, J.-M. Bouler, Calcium phosphate cements for bone substitution: Chemistry, handling and mechanical properties, Acta Biomaterialia 10 (2014) 1035-1049.
[319] M. Dziadek, E. Stodolak-Zych, K. Cholewa-Kowalska, Biodegradable ceramic-polymer composites for biomedical applications: A review, Materials Science and Engineering: C 71 (2017) 1175-1191.
[320] A. Pandey, E. Jan, P.B. Aswath, Physical and mechanical behavior of hot rolled HDPE/HA composites, Journal of Materials Science 41 (2006) 3369-3376.
[321] F. Tamimi, B. Kumarasami, C. Doillon, U. Gbureck, D.L. Nihouannen, E.L. Cabarcos, J.E. Barralet, Brushite–collagen composites for bone regeneration, Acta Biomaterialia 4 (2008) 1315-1321.
[322] M.H. Alkhraisat, C. Rueda, F.T. Mariño, J. Torres, L.B. Jerez, U. Gbureck, E.L. Cabarcos, The effect of hyaluronic acid on brushite cement cohesion, Acta Biomaterialia 5 (2009) 3150-3156.
[323] R.A. Perez, H.-W. Kim, M.-P. Ginebra, Polymeric additives to enhance the functional properties of calcium phosphate cements, Journal of tissue engineering 3(1) (2012) 1-20.
[324] S.V. Dorozhkin, Calcium Orthophosphate-Containing Biocomposites and Hybrid Biomaterials for Biomedical Applications, Journal of Functional Biomaterials 6 (2015) 708-832.
[325] Y.E. Greish, P.W. Brown, J.D. Bender, H.R. Allcock, S. Lakshmi, C.T. Laurencin, Hydroxyapatite–Polyphosphazane Composites Prepared at Low Temperatures, Journal of the American Ceramic Society 90 (2007) 2728-2734.

[326] W.-C. Chen, C.-P. Ju, J.-C. Wang, C.-C. Hung, J.-H. Chern Lin, Brittle and ductile adjustable cement derived from calcium phosphate cement/polyacrylic acid composites, Dental Materials 24 (2008) 1616-1622.
[327] R.M. Khashaba, M. Moussa, C. Koch, A.R. Jurgensen, D.M. Missimer, R.L. Rutherford, N.B. Chutkan, J.L. Borke, Preparation, Physical-Chemical Characterization, and Cytocompatibility of Polymeric Calcium Phosphate Cements, International Journal of Biomaterials 2011 (2011) 1-13.
[328] K.E. Watson, K.S. Tenhuisen, P.W. Brown, The formation of hydroxyapatite–calcium polyacrylate composites, Journal of Materials Science: Materials in Medicine 10 (1999) 205–213.
[329] A. Sugawara, J.M. Antonucci, S. Takagi, L.C. Chow, M. Ohashi, Formation of hydroxyapatite in hydrogels from tetracalcium phosphate/dicalcium phosphate mixtures, The Journal of Nihon University School of Dentistry 31 (1989) 372–381.
[330] L.A. Dos Santos, L.C. De Oliveira, E.C.S. Rigo, R.G. Carrodeguas, A.O. Boschi, A.C.F. De Arruda, Influence of polymeric additives on the mechanical properties of α-tricalcium phosphate cement, Bone 25 (1999) 99S-102S.
[331] L.A. Dos Santos, R.G. Carrodeguas, A.O. Boschi, A.C. De Arruda, Dual-Setting Calcium Phosphate Cement Modified with Ammonium Polyacrylate, Artificial Organs 27 (2003) 412-418.
[332] L.A. Dos Santos, R.G. Carrodéguas, A.O. Boschi, A.C. Fonseca de Arruda, Fiber-enriched double-setting calcium phosphate bone cement, Journal of Biomedical Materials Research Part A 65A (2003) 244-250.
[333] J. Wang, C. Liu, Y. Liu, S. Zhang, Double-Network Interpenetrating Bone Cement via in situ Hybridization Protocol, Advanced Functional Materials 20 (2010) 3997-4011.
[334] E.C.S. Rigo, D. Santos, L. A, L.C.O. Vercik, R.G. Carrodeguas, A.O. Boschi, alpha-tricalcium phosphate- and tetracalcium phosphate/dicalcium phosphate-based dual setting cements, Latin American applied research 37 (2007) 267-274.
[335] T. Christel, M. Kuhlmann, E. Vorndran, J. Groll, U. Gbureck, Dual setting α-tricalcium phosphate cements, Journal of Materials Science: Materials in Medicine 24 (2013) 573-581.
[336] M. Geffers, J.E. Barralet, J. Groll, U. Gbureck, Dual-setting brushite–silica gel cements, Acta Biomaterialia 11 (2015) 467-476.
[337] M. Schamel, J.E. Barralet, M. Gelinsky, J. Groll, U. Gbureck, Intrinsic 3D Prestressing: A New Route for Increasing Strength and Improving Toughness of Hybrid Inorganic Biocements, Advanced Materials 29(35) (2017).
[338] S. Shanmugam, B. Gopal, Copper substituted hydroxyapatite and fluorapatite: Synthesis, characterization and antimicrobial properties, Ceramics International 40 (2014) 15655-15662.
[339] G.A. Fielding, M. Roy, A. Bandyopadhyay, S. Bose, Antibacterial and biological characteristics of silver containing and strontium doped plasma sprayed hydroxyapatite coatings, Acta Biomaterialia 8 (2012) 3144-3152.
[340] J.V. Rau, M. Fosca, V. Graziani, A.A. Egorov, Y.V. Zobkov, A.Y. Fedotov, M. Ortenzi, R. Caminiti, A.E. Baranchikov, V.S. Komlev, Silver-Doped Calcium

Phosphate Bone Cements with Antibacterial Properties, Journal of Functional Biomaterials 7 (2016) 10.
[341] O. Gokcekaya, K. Ueda, K. Ogasawara, H. Kanetaka, T. Narushima, In vitro evaluation of Ag-containing calcium phosphates: Effectiveness of Ag-incorporated β-tricalcium phosphate, Materials Science and Engineering: C 75 (2017) 926-933.
[342] M.H. Alkhraisat, F.T. Mariño, C.R. Rodríguez, L.B. Jerez, E.L. Cabarcos, Combined effect of strontium and pyrophosphate on the properties of brushite cements, Acta Biomaterialia 4 (2008) 664-670.
[343] A. Bigi, E. Foresti, M. Gandolfi, M. Gazzano, N. Roveri, Isomorphous substitutions in β-tricalcium phosphate: The different effects of zinc and strontium, Journal of Inorganic Biochemistry 66 (1997) 259-265.
[344] S.G. Dahl, P. Allain, P.J. Marie, Y. Mauras, G. Boivin, P. Ammann, Y. Tsouderos, P.D. Delmas, C. Christiansen, Incorporation and distribution of strontium in bone, Bone 28 (2001) 446–453.
[345] M. Pilmane, K. Salma-Ancane, D. Loca, J. Locs, L. Berzina-Cimdina, Strontium and strontium ranelate: Historical review of some of their functions, Materials Science and Engineering: C 78 (2017) 1222-1230.
[346] E. Bonnelye, A. Chabadel, F. Saltel, P. Jurdic, Dual effect of strontium ranelate: Stimulation of osteoblast differentiation and inhibition of osteoclast formation and resorption in vitro, Bone 42 (2008) 129-138.
[347] A. Barbara, P. Delannoy, B.G. Denis, P.J. Marie, Normal matrix mineralization induced by strontium ranelate in MC3T3-E1 osteogenic cells, Metabolism 53 (2004) 532-537.
[348] T. Brennan, M. Rybchyn, W. Green, S. Atwa, A. Conigrave, R. Mason, Osteoblasts play key roles in the mechanisms of action of strontium ranelate, British Journal of Pharmacology 157 (2009) 1291-1300.
[349] E. Canalis, M. Hott, P. Deloffre, Y. Tsouderos, P.J. Marie, The divalent strontium salt S12911 enhances bone cell replication and bone formation in vitro, Bone 18 (1996) 517-523.
[350] J. Coulombe, H. Faure, B. Robin, M. Ruat, In vitro effects of strontium ranelate on the extracellular calcium-sensing receptor, Biochemical and Biophysical Research Communications 323 (2004) 1184-1190.
[351] A.D. Conigrave, D.T. Ward, Calcium-sensing receptor (CaSR): Pharmacological properties and signaling pathways, Best Practice & Research Clinical Endocrinology & Metabolism 27 (2013) 315-331.
[352] Z. Saidak, P.J. Marie, Strontium signaling: Molecular mechanisms and therapeutic implications in osteoporosis, Pharmacology & Therapeutics 136 (2012) 216-226.
[353] A.S. Hurtel-Lemaire, R. Mentaverri, A. Caudrillier, F. Cournarie, A. Wattel, S. Kamel, E.F. Terwilliger, E.M. Brown, M. Brazier, The Calcium-sensing Receptor Is Involved in Strontium Ranelate-induced Osteoclast Apoptosis: new insights into the associated signaling pathways, Journal of Biological Chemistry 284 (2009) 575-584.
[354] S. Choudhary, S. Wadhwa, L.G. Raisz, C. Alander, C.C. Pilbeam, Extracellular Calcium Is a Potent Inducer of Cyclo-oxygenase-2 in Murine

Osteoblasts Through an ERK Signaling Pathway, Journal of Bone and Mineral Research 18 (2003) 1813-1824.
[355] G.J. Atkins, K.J. Welldon, P. Halbout, D.M. Findlay, Strontium ranelate treatment of human primary osteoblasts promotes an osteocyte-like phenotype while eliciting an osteoprotegerin response, Osteoporosis International 20 (2009) 653-664.
[356] J.Y. Reginster, D. Felsenberg, I. Pavo, J. Stepan, J. Payer, H. Resch, C.C. Glüer, D. Mühlenbacher, D. Quail, H. Schmitt, T. Nickelsen, Effect of raloxifene combined with monofluorophosphate as compared with monofluorophosphate alone in postmenopausal women with low bone mass: a randomized, controlled trial, Osteoporosis International 14 (2003) 741-749.
[357] S. Murphy, D. Boyd, S. Moane, M. Bennett, The effect of composition on ion release from Ca–Sr–Na–Zn–Si glass bone grafts, Journal of Materials Science: Materials in Medicine 20 (2009) 2207.
[358] S.C. Verberckmoes, M.E. De Broe, P.C. D'Haese, Dose-dependent effects of strontium on osteoblast function and mineralization, Kidney International 64 (2003) 534-543.
[359] J. Braux, F. Velard, C. Guillaume, S. Bouthors, E. Jallot, J.-M. Nedelec, D. Laurent-Maquin, P. Laquerrière, A new insight into the dissociating effect of strontium on bone resorption and formation, Acta Biomaterialia 7 (2011) 2593-2603.
[360] M. Sila-Asna, A. Bunyaratvej, S. Maeda, H. Kitaguchi, N. Bunyaratavej, Osteoblast differentiation and bone formation gene expression in strontium-inducing bone marrow mesenchymal stem cell, The Kobe journal of medical sciences 53 (2007) 25-35.
[361] M.D. Grynpas, E. Hamilton, R. Cheung, Y. Tsouderos, P. Deloffre, M. Hott, P.J. Marie, Strontium increases vertebral bone volume in rats at a low dose that does not induce detectable mineralization defect, Bone 18 (1996) 253-259.
[362] D. Arcos, M. Vallet-Regí, Bioceramics for drug delivery, Acta Materialia 61 (2013) 890-911.
[363] M. Manzano, Ceramics for Drug Delivery, in: r. Vallet-Regí (Ed.), Bio-Ceramics with Clinical Applications, John Wiley & Sons, Ltd2014, pp. 343-382.
[364] G. Singhvi, M. Singh, Review: in-vitro drug release characterization models, International Journal of Pharmaceutical Sciences and Research 2 (2011) 77–84.
[365] S. Dash, P.N. Murthy, L. Nath, P. Chowdhury, Kinetic modeling on drug release from controlled drug delivery systems, Acta Poloniae Pharmaceutica 67 (2010) 217–23.
[366] P. Costa, J.M. Sousa Lobo, Modeling and comparison of dissolution profiles, European Journal of Pharmaceutical Sciences 13 (2001) 123-133.
[367] R.W. Korsmeyer, R. Gurny, E. Doelker, P. Buri, N.A. Peppas, Mechanisms of solute release from porous hydrophilic polymers, International journal of pharmaceutics 15 (1983) 25–35.
[368] J. Siepmann, N.A. Peppas, Modeling of drug release from delivery systems based on hydroxypropyl methylcellulose (HPMC), Advanced Drug Delivery Reviews 64, Supplement (2012) 163-174.

[369] M.P. Ginebra, T. Traykova, J.A. Planell, Calcium phosphate cements as bone drug delivery systems: A review, Journal of Controlled Release 113 (2006) 102-110.
[370] T. Higuchi, Mechanism of sustained-action medication. Theoretical analysis of rate of release of solid drugs dispersed in solid matrices, Journal of Pharmaceutical Sciences 52 (1963) 1145-1149.
[371] W.I. Higuchi, Diffusional models useful in biopharmaceutics - Drug release rate processes, Journal of Pharmaceutical Sciences 56 (1967) 315-324.
[372] S.J. Desai, A.P. Simonelli, W.I. Higuchi, Investigation of factors influencing release of solid drug dispersed in inert matrices, Journal of Pharmaceutical Sciences 54 (1965) 1459-1464.
[373] D. Pastorino, C. Canal, M.-P. Ginebra, Drug delivery from injectable calcium phosphate foams by tailoring the macroporosity–drug interaction, Acta Biomaterialia 12 (2015) 250-259.
[374] M.M. Crowley, B. Schroeder, A. Fredersdorf, S. Obara, M. Talarico, S. Kucera, J.W. McGinity, Physicochemical properties and mechanism of drug release from ethyl cellulose matrix tablets prepared by direct compression and hot-melt extrusion, International Journal of Pharmaceutics 269 (2004) 509-522.
[375] P.A. Webb, An introduction to the physical characterization of materials by mercury intrusion porosimetry with emphasis on reduction and presentation of experimental data, Micromeritics Instrument Corp, Norcross, Georgia (2001).
[376] S.S. Manickam, J. Gelb, J.R. McCutcheon, Pore structure characterization of asymmetric membranes: Non-destructive characterization of porosity and tortuosity, Journal of Membrane Science 454 (2014) 549-554.
[377] S. Mauran, L. Rigaud, O. Coudevylle, Application of the Carman–Kozeny Correlation to a High-Porosity and Anisotropic Consolidated Medium: The Compressed Expanded Natural Graphite, Transport in Porous Media 43 (2001) 355-376.
[378] P. Aggarwal, V. Asthana, J.S. Lawson, H.D. Tolley, D.R. Wheeler, B.A. Mazzeo, M.L. Lee, Correlation of chromatographic performance with morphological features of organic polymer monoliths, Journal of Chromatography A 1334 (2014) 20-29.
[379] C. Labbez, P. Fievet, A. Szymczyk, C. Simon, A. Vidonne, A. Foissy, J. Pagetti, Hydraulic resistance measurements combined with electrical or diffusional resistance measurements for determination of pore size in MF membranes, Desalination 141 (2001) 291–299.
[380] E. Mahmoud, R.F. Lobo, Recent advances in zeolite science based on advance characterization techniques, Microporous and Mesoporous Materials 189 (2014) 97-106.
[381] L. Pisani, Simple Expression for the Tortuosity of Porous Media, Transport in Porous Media 88 (2011) 193-203.
[382] M. Parent, H. Baradari, E. Champion, C. Damia, M. Viana-Trecant, Design of calcium phosphate ceramics for drug delivery applications in bone diseases: A review of the parameters affecting the loading and release of the therapeutic substance, Journal of Controlled Release 252 (2017) 1-17.

[383] A.J. Salgado, O.P. Coutinho, R.L. Reis, Bone Tissue Engineering: State of the Art and Future Trends, Macromolecular Bioscience 4 (2004) 743-765.
[384] N.J.S. Gorst, Y. Perrie, U. Gbureck, A.L. Hutton, M.P. Hofmann, L.M. Grover, J.E. Barralet, Effects of fibre reinforcement on the mechanical properties of brushite cement, Acta Biomaterialia 2 (2006) 95-102.
[385] Y. Zhang, H.H.K. Xu, Effects of synergistic reinforcement and absorbable fiber strength on hydroxyapatite bone cement, Journal of Biomedical Materials Research Part A 75A (2005) 832–840.
[386] Cheremisinoff, Handbook of Ceramics and Composites: Mechanical Properties and Specialty Applications, CRC Press1991.
[387] V.C. Li, M. Maalej, Toughening in cement based composites. Part II: Fiber reinforced cementitious composites, Cement and Concrete Composites 18 (1996) 239-249.
[388] U. Gbureck, T. Hölzel, C.J. Doillon, F.A. Müller, J.E. Barralet, Direct Printing of Bioceramic Implants with Spatially Localized Angiogenic Factors, Advanced Materials 19 (2007) 795–800.
[389] W.D. Losquadro, S.A. Tatum, M.J. Allen, K.A. Mann, Polylactide-co-glycolide Fiber–Reinforced Calcium Phosphate Bone Cement, Archives of Facial Plastic Surgery 11 (2009) 104.
[390] R. Baron, Anatomy and Ultrastructure of Bone – Histogenesis, Growth and Remodeling, (2008).
[391] K.J.L. Burg, S. Porter, J.F. Kellam, Biomaterial developments for bone tissue engineering, Biomaterials 21 (2000) 2347-2359.
[392] R. Dugnani, R.J. Zednik, Quantitative Characterization of Mechanical Stress Field and Fracture Strength in Isotropic Brittle Materials During Crack Tip Propagation, Journal of the American Ceramic Society 97(12) (2014) 3853-3856.
[393] F. Rengier, A. Mehndiratta, H. von Tengg-Kobligk, C.M. Zechmann, R. Unterhinninghofen, H.-U. Kauczor, F.L. Giesel, 3D printing based on imaging data: review of medical applications, International Journal of Computer Assisted Radiology and Surgery 5 (2010) 335-341.
[394] V.C. Li, D.K. Mishra, H.-C. Wu, Matrix design for pseudo-strain-hardening fibre reinforced cementitious composites, Materials and Structures 28 (1995) 586-595.
[395] A.O. Majekodunmi, S. Deb, J.W. Nicholson, Effect of molecular weight and concentration of poly(acrylic acid) on the formation of a polymeric calcium phosphate cement, Journal of Materials Science: Materials in Medicine 14 (2003) 747-752.
[396] J.M. Anderson, Biological Responses to Materials, Annual Review of Materials Research 31 (2001) 81-110.
[397] S.D. Elek, P.E. Conen, The Virulence of Staphylococcus pyogenes for Man. A Study of the Problems of Wound Infection, British Journal of Experimental Pathology 38 (1957) 573-586.
[398] W. Petty, S. Spanier, J.J. Shuster, C. Silverthorne, The influence of skeletal implants on incidence of infection. Experiments in a canine model., The Journal of bone and joint surgery. American volume 67 (1985) 1236-1244.

[399] N. Renz, C. Perka, A. Trampuz, Management periprothetischer Infektionen des Kniegelenks, Der Orthopäde 45 (2016) 65-71.
[400] T. Gehrke, P. Alijanipour, J. Parvizi, The management of an infected total knee arthroplasty, Bone Joint J 97-B (2015) 20-29.
[401] C. Liu, A. Bayer, S.E. Cosgrove, R.S. Daum, S.K. Fridkin, R.J. Gorwitz, S.L. Kaplan, A.W. Karchmer, D.P. Levine, B.E. Murray, M.J. Rybak, D.A. Talan, H.F. Chambers, Clinical Practice Guidelines by the Infectious Diseases Society of America for the Treatment of Methicillin-Resistant Staphylococcus aureus Infections in Adults and Children, Clinical Infectious Diseases 52 (2011) e18-e55.
[402] J. Chandrananth, A. Rabinovich, A. Karahalios, S. Guy, P. Tran, Impact of adherence to local antibiotic prophylaxis guidelines on infection outcome after total hip or knee arthroplasty, Journal of Hospital Infection 93 (2016) 423-427.
[403] K.L. Garvin, S.H. Hinrichs, J.A. Urban, Emerging antibiotic-resistant bacteria. Their treatment in total joint arthroplasty, Clinical Orthopaedics and Related Research (1999) 110-123.
[404] N.J. Hickok, I.M. Shapiro, Immobilized antibiotics to prevent orthopaedic implant infections, Advanced Drug Delivery Reviews 64 (2012) 1165-1176.
[405] H.-P. Simmen, J. Blaser, Analysis of pH and pO2 in abscesses, peritoneal fluid, and drainage fluid in the presence or absence of bacterial infection during and after abdominal surgery, The American Journal of Surgery 166 (1993) 24-27.
[406] V. Albright, I. Zhuk, Y. Wang, V. Selin, B. van de Belt-Gritter, H.J. Busscher, H.C. van der Mei, S.A. Sukhishvili, Self-defensive antibiotic-loaded layer-by-layer coatings: Imaging of localized bacterial acidification and pH-triggering of antibiotic release, Acta Biomaterialia 61 (2017) 66-74.
[407] T. Frey, A. Haubenreich, F.B. Werkstofftechnik, R. Girmscheid, P.E. Metzler, Vergleichende Festigkeitsuntersuchungen an Mg-PSZ und Aluminimoxid, (2003).
[408] J.E.A. Bertram, A.A. Biewener, Bone curvature: Sacrificing strength for load predictability?, Journal of Theoretical Biology 131 (1988) 75-92.
[409] Brushite, in: J.W. Anthony, R.A. Bideaux, K.W. Bladh, M.C. Nicholas (Eds.), Handbook of Mineralogy, Mineralogical Society of America2001.
[410] Struvite, in: J.W. Anthony, R.A. Bideaux, K.W. Bladh, M.C. Nicholas (Eds.), Handbook of Mineralogy, Mineralogical Society of America2001.
[411] K. Hurle, T. Christel, U. Gbureck, C. Moseke, J. Neubauer, F. Goetz-Neunhoeffer, Reaction kinetics of dual setting α-tricalcium phosphate cements, Journal of Materials Science: Materials in Medicine 27 (2016).
[412] R.F.M. van Oers, R. Ruimerman, E. Tanck, P.A.J. Hilbers, R. Huiskes, A unified theory for osteonal and hemi-osteonal remodeling, Bone 42 (2008) 250-259.
[413] M.S. Cheung, F.H. Glorieux, F. Rauch, Large Osteoclasts in Pediatric Osteogenesis Imperfecta Patients Receiving Intravenous Pamidronate, Journal of Bone and Mineral Research 24 (2009) 669-674.
[414] U. Kneser, D.J. Schaefer, E. Polykandriotis, R.E. Horch, Tissue engineering of bone: the reconstructive surgeon's point of view, Journal of Cellular and Molecular Medicine 10 (2006) 7-19.

[415] C.J. Damien, J.R. Parsons, Bone graft and bone graft substitutes: A review of current technology and applications, Journal of Applied Biomaterials 2 (1991) 187-208.
[416] F. Tamimi, D.L. Nihouannen, H. Eimar, Z. Sheikh, S. Komarova, J. Barralet, The effect of autoclaving on the physical and biological properties of dicalcium phosphate dihydrate bioceramics: Brushite vs. monetite, Acta Biomaterialia 8 (2012) 3161-3169.
[417] S.K. Tat, J.-P. Pelletier, F. Mineau, J. Caron, J. Martel-Pelletier, Strontium ranelate inhibits key factors affecting bone remodeling in human osteoarthritic subchondral bone osteoblasts, Bone 49 (2011) 559-567.
[418] P. Kostenuik, v. Shalhoub, Osteoprotegerin A Physiological and Pharmacological Inhibitor of Bone Resorption., Current Pharmaceutical Design 7 (2001) 613-635.
[419] E. Berry, J.M. Brown, M. Connell, C.M. Craven, N.D. Efford, A. Radjenovic, M.A. Smith, Preliminary experience with medical applications of rapid prototyping by selective laser sintering, Medical Engineering & Physics 19 (1997) 90-96.
[420] E. Sachs, M. Cima, J. Cornie, D. Brancazio, J. Bredt, A. Curodeau, M. Esterman, T. Fan, C. Harris, K. Kremmin, S.J. Lee, B. Pruitt, P. Williams, Three Dimensional Printing: Rapid Tooling and Prototypes Directly from CAD Representation, CIRP Annals 39(1) (1990) 201-204.
[421] V. Ramakrishna, B. Basu, Conceptual Design of Three-Dimensional Scaffolds of powder-based materials for Bone Tissue Engineering Applications, Rapid Prototyping 21(6) (2015) 716-724.
[422] Y. Luo, A. Lode, C. Wu, M. Gelinsky, 3D-plotting of bioceramic scaffolds under physiological conditions for bone tissue engineering, CRC Press (2013).
[423] C. Wu, Y. Luo, G. Cuniberti, Y. Xiao, M. Gelinsky, Three-dimensional printing of hierarchical and tough mesoporous bioactive glass scaffolds with a controllable pore architecture, excellent mechanical strength and mineralization ability, Acta Biomaterialia 7 (2011) 2644-2650.
[424] Y. Luo, C. Wu, A. Lode, M. Gelinsky, Hierarchical mesoporous bioactive glass/alginate composite scaffolds fabricated by three-dimensional plotting for bone tissue engineering, Biofabrication 5 (2013) 015005.
[425] C.B. Carter, M.G. Norton, Ceramic materials: science and engineering, Springer, New York, 2007.
[426] D.J. Misiek, J.N. Kent, R.F. Carr, Soft tissue responses to hydroxylapatite particles of different shapes, Journal of Oral and Maxillofacial Surgery 42 (1984) 150-160.
[427] W. Wang, Z. Wu, C. Wang, R. Hu, Modelling the spreading rate of controlled communicable epidemics through an entropy-based thermodynamic model, Science China Physics, Mechanics and Astronomy 56 (2013) 2143-2150.
[428] J. Huxley, Problems of relative growth, (1932).
[429] M. Lipowiecki, M. Ryvolová, Á. Töttösi, N. Kolmer, S. Naher, S.A. Brennan, M. Vázquez, D. Brabazon, Permeability of rapid prototyped artificial bone scaffold structures, Journal of Biomedical Materials Research Part A 102 (2014) 4127-4135.

[430] L. Røhl, E. Larsen, F. Linde, A. Odgaard, J. Jørgensen, Tensile and compressive properties of cancellous bone, Journal of Biomechanics 24 (1991) 1143-1149.
[431] E.B.W. Giesen, M. Ding, M. Dalstra, T.M.G.J. van Eijden, Mechanical properties of cancellous bone in the human mandibular condyle are anisotropic, Journal of Biomechanics 34 (2001) 799-803.
[432] A.J. Wagoner Johnson, B.A. Herschler, A review of the mechanical behavior of CaP and CaP/polymer composites for applications in bone replacement and repair, Acta Biomaterialia 7 (2011) 16-30.
[433] R.W. McCalden, J.A. McGeough, C.M. Court-Brown, Age-Related Changes in the Compressive Strength of Cancellous Bone. The Relative Importance of Changes in Density and Trabecular Architecture, The Journal of Bone & Joint Surgery 79 (1997) 421-7.
[434] K. Rezwan, Q.Z. Chen, J.J. Blaker, A.R. Boccaccini, Biodegradable and bioactive porous polymer/inorganic composite scaffolds for bone tissue engineering, Biomaterials 27 (2006) 3413-3431.
[435] C. Pittet, J. Lemaître, Mechanical characterization of brushite cements: A Mohr circles' approach, Journal of Biomedical Materials Research 53 (2000) 769-780.
[436] B. Basu, D. Tiwari, D. Kundu, R. Prasad, Is Weibull distribution the most appropriate statistical strength distribution for brittle materials?, Ceramics International 35 (2009) 237-246.
[437] X.B. Chen, D.R. Nisbet, R.W. Li, P.N. Smith, T.B. Abbott, M.A. Easton, D.-H. Zhang, N. Birbilis, Controlling initial biodegradation of magnesium by a biocompatible strontium phosphate conversion coating, Acta Biomaterialia 10 (2014) 1463-1474.
[438] C. Lindahl, S. Pujari-Palmer, A. Hoess, M. Ott, H. Engqvist, W. Xia, The influence of Sr content in calcium phosphate coatings, Materials Science and Engineering: C 53 (2015) 322-330.
[439] H. Valiense, M. Barreto, R.F. Resende, A.T. Alves, A.M. Rossi, E. Mavropoulos, J.M. Granjeiro, M.D. Calasans-Maia, In vitro and in vivo evaluation of strontium-containing nanostructured carbonated hydroxyapatite/sodium alginate for sinus lift in rabbits, Journal of Biomedical Materials Research Part B: Applied Biomaterials 104(2) (2015) 274-282.
[440] G.R. Beck, Inorganic phosphate as a signaling molecule in osteoblast differentiation, Journal of Cellular Biochemistry 90 (2003) 234-243.
[441] D.P. Pioletti, H. Takei, T. Lin, P. Van Landuyt, Q. Jun Ma, S. Yong Kwon, K.-L. Paul Sung, The effects of calcium phosphate cement particles on osteoblast functions, Biomaterials 21 (2000) 1103-1114.
[442] Y. Shen, J. Liu, K. Lin, W. Zhang, Synthesis of strontium substituted hydroxyapatite whiskers used as bioactive and mechanical reinforcement material, Materials Letters 70 (2012) 76-79.
[443] S. Tadier, R. Bareille, R. Siadous, O. Marsan, C. Charvillat, S. Cazalbou, J. Amédée, C. Rey, C. Combes, Strontium-loaded mineral bone cements as sustained release systems: Compositions, release properties, and effects on human

osteoprogenitor cells, Journal of Biomedical Materials Research Part B: Applied Biomaterials 100B (2012) 378-390.
[444] M.H. Alkhraisat, C. Moseke, L. Blanco, J.E. Barralet, E. Lopez-Carbacos, U. Gbureck, Strontium modified biocements with zero order release kinetics, Biomaterials 29 (2008) 4691-4697.
[445] H.H.K. Xu, C.G. Simon, Self-hardening calcium phosphate cement–mesh composite: Reinforcement, macropores, and cell response, Journal of Biomedical Materials Research Part A 69A (2004) 267–278.
[446] K.S. Anseth, C.N. Bowman, L. Brannon-Peppas, Mechanical properties of hydrogels and their experimental determination, Biomaterials 17 (1996) 1647-1657.

Danksagung

Zunächst möchte ich Prof. Dr. Jürgen Groll danken, dass ich diese Arbeit nach meiner Bachelor- und Masterarbeit ebenfalls am Lehrstuhl für Funktionswerkstoffe der Medizin und der Zahnheilkunde (FMZ) anfertigen konnte. Die Bereitstellung des Themas, sowie die für die Bearbeitung nötige Infrastruktur machten diese Doktorarbeit erst möglich. Außerdem möchte ich mich für die Betreuung und Gespräche während meiner Arbeiten und die letztendliche Begutachtung und Prüfung dieser Doktorarbeit bedanken.

Mein Dank geht auch an Prof. Dr. Frank A. Müller für die Begutachtung und Prüfung meiner Arbeit. Die erfolgreiche Kooperation am gemeinsamen Projekt, sowie konstruktive Besprechungen während meiner Arbeiten zu dieser Dissertation haben für mich sehr viele neue Erfahrungen und Anregungen gebracht.

Ein ganz herzlicher Dank geht an Prof. Dr. Uwe Gbureck. Die hervorragende Betreuung während meiner Bachelor- und Masterarbeit und das wahnsinnig interessante Thema der Calcium- und Magnesiumphosphate waren schon Grund genug auch meine Promotion diesem Gebiet zu widmen. Seine Tür war für uns „Zementies“ immer offen und man konnte stets mit theoretischer und auch praktischer Hilfe im Labor rechnen. Die Unterstützung beim Verfassen von Papern, bei Vorträgen und Konferenzen war sehr gut, was mit vielen Veröffentlichungen und immer besseren Vorträgen belohnt wurde. Mein Dank geht aber auch über das fachliche hinaus.

Für die finanzielle Unterstützung meiner Arbeiten am Lehrstuhl danke ich der Deutschen Forschungsgemeinschaft für das Projekt DFG SPP 1568, das von Prof. Dr. Uwe Gbureck erfolgreich eingeworben wurde. Diese Finanzierung machte eine mehrjährige Beschäftigung mit dem Thema erst möglich. In diesem Rahmen danke ich auch unseren Kooperationspartnern auf diesem Projekt Prof. Dr. Frank A. Müller und Anne Böhm von der Friedrich Schiller Universität Jena.

Die rasterelektronischen Aufnahmen wurden mit dem Gerät Zeiss CB 340 erstellt, das durch die DFG über den Antrag INST 105022/58-1 FUGG finanziert wurde.

Ein besonderer Dank geht natürlich an alle Mitarbeiter des FMZ, die mich all die Jahre hier begleitet und unterstützt haben. Danke an Isabell Biermann für die Hilfe ab dem ersten Tag. Die gute Seele des Anorganik-Labor weiß einfach wo was ist und wie was

funktioniert, von den Zementen über Bestellungen und Geräte bis zu allen alltäglichen Fragen. Außerdem danke ich Dr. Andrea Ewald, Maria Aniolek und Simone Werner, die mich bei meinen Zellversuchen unterstützt und mir immer weiter geholfen haben. Ein offenes Ohr für alle handwerklichen und IT Angelegenheiten hatten auch Harald Hümpfer und Anton Hofmann für mich. Sie hatten immer kreative Lösungen und unkonventionelle Vorschläge parat, die dann auch unkompliziert umgesetzt wurden. Für die Einweisung und Unterstützung der REM-Aufnahmen bedanke ich mich bei Judith Friedlein und Dr. Claus Moseke. Dr. Claus Moseke war auch immer zur Stelle, wenn das XRD mal wieder gestreikt hat. Danke auch an Dr. Elke Vorndran, die mir den 3D-Pulverdrucker erklärt und auch bei Problemen weiter geholfen hat. Bei Dr. Jörg Teßmar und Tanja Dambach möchte ich mich bedankten, da sie stets für organisatorische, fachliche und sonstige Probleme da waren.

Danke auch an meine zahlreichen Kollegen, die im Laufe der Jahre eher zu Freunden geworden sind. Besonders meine Bürokollegen Theresa Brückner und Gernot Hochleitner, sowie Michaela Rödel möchte ich hier erwähnen. Sie alle hatten immer ein offenes Ohr für die großen und kleinen Probleme, sei es bei Experimenten im Labor, dem üblichen Durchhänger während der Promotion oder organisatorischem Irrsinn und haben mich immer wieder aufgebaut, um weiter zu machen. Danke für die vielen schönen, lustigen Stunden, die ich mit euch verbringen durfte.

Vielen Dank an meine Freunde, Familie, an meinen Mann Markus und meinen Sohn Matthias, die mich immer unterstützt und wieder aufgebaut haben. Ihr habt wesentlichen Anteil daran, dass diese Arbeit existiert und es mich so gibt, wie ich heute bin.

Abschließend bedanke ich mich bei allen, die ich vergessen habe, die mir aber bei den vielen großen und kleinen Dingen im Leben geholfen haben.